Tsunamis in south central Chile

Evidence from coastal lakes

Tsunamis in zuid-centraal Chili

Een studie van de sedimentaire opvulling van kustmeren

PHILIPP KEMPF

Dissertation submitted for the degree of
Doctor of Science: Geology

March, 2016

Promoter: Prof. Dr. Marc De Batist
Co-promoter: Dr. Jasper Moernaut

Members of the reading committee:
Prof. Dr. Marc De Batist (promoter, Ghent University, Belgium)
Dr. Jasper Moernaut (co-promoter, University of Innsbruck, Austria)

Members of the examination committee:
Prof. Dr. Stephen Louwye (Ghent University, Belgium)
Prof. Dr. Sébastien Bertrand (Ghent University, Belgium)
Prof. Dr. Vanessa Heyvaert (Ghent University, Belgium)
Dr. Maarten Van Daele (Ghent University, Belgium)
Prof. Dr. Helmut Brückner (University of Cologne, Germany)
Prof. Dr. Klaus Reicherter (RWTH Aachen University, Germany)
Dr. Ed Garrett (Royal Belgian Institute of Natural Sciences, Belgium)

Philipp Kempf carried out the research with financial support by the Special Research Fund (BOF) of Ghent University.

This research was conducted at the Renard Centre of Marine Geology (RCMG), Department of Geology, Ghent University, Ghent, Belgium.

This thesis should be referred to as:
Kempf, P., 2016. Tsunamis in south central Chile – Evidence from coastal lakes. PhD Thesis, Ghent University, Belgium.

”Like dwarves perched on the shoulders of giants, [...]
we are able to see more and farther than the latter.”

AD 1159, John of Salisbury in *Metalogicon*

Summary

The south central Chilean coast lies on the Peru-Chile subduction zone. As a result, the area is prone to megathrust earthquakes. The convergent motion of the oceanic Nazca Plate and the South American Plate during these earthquakes causes co-seismic vertical deformation on the seafloor, which in turn generates tsunamis. The tsunamis propagate across the Pacific Ocean and eventually inundate the South American and other coasts, where they sometimes cause catastrophic damage. Alongside the destruction of infrastructure and the loss of life, tsunamis deposit distinct sediments. This thesis focuses on tsunami deposits in two coastal lakes, Lake Cucao and Lake Huelde, on the west coast of Isla de Chiloé, south central Chile (42.6° S), and their immediate surroundings.

The thesis establishes the sedimentary characteristics of the most recent tsunami deposit in the lakes' sedimentary records. The tsunami in question was caused by the AD 1960 Great Chilean Earthquake (M_W 9.5). The AD 1960 tsunami inundated both lakes, which are located ~2 km apart and ~1.2 km behind the present coastline. The stratigraphy of both lakes features gyttja, interrupted by the abrupt emplacement of a sandy layer with mud rip-up clasts and a mud cap. This sandy layer reflects a sudden change in the sedimentary environment. Using grain size analysis and comparisons with samples from modern environments, it is demonstrated that the proximal (seaward) part of the tsunami deposit consists of a mixture of sand derived from subaerial sources and reworked lacustrine gyttja. In the distal (landward) part of Lake Cucao, the tsunami deposit lacks the sand component and consists entirely of remobilised lake sediments. The repetition of tsunami deposit sequences (or subsets thereof) in Lake Huelde suggests a minimum of three inundating waves. Sub-bottom profiles and side scan sonar mosaics reveal tsunami inundation over the barrier and more prominently through the outlet river channel. The dominant role of the river channel as a pathway for sediment transport is also described in core samples by tsunami deposits that are fining away from the channel mouth. The identification and description of the AD 1960 deposit provide important insights into tsunami sedimentation in coastal lakes and set a baseline as to what tsunami deposits should look like in the deeper sedimentary record of the two coastal lakes.

In Lake Huelde, the established expectation of the sedimentary characteristics of tsunami deposits is used to investigate the exceptionally long and continuous sedimentary record. Lake Huelde's sedimentary record contains 17 distinct detrital layers from the last 5500 yrs, which are interpreted as tsunami deposits. With the unusually high number of tsunami deposits in a single sedimentary record it is possible to analyse the recurrence pattern. Recurrence rates and pattern are an integral part to tsunami hazard assessment. In probabilistic tsunami hazard assessment tsunami recurrences are typically modelled with a Poisson distribution, which, as I demonstrate, does not necessarily represent the hazard correctly. Results of ^{137}Cs- and ^{210}Pb-dating, infrared stimulated luminescence (IRSL) dating and radiocarbon dating are used as input for Bayesian age-depth modelling. The resulting age-depth relationship is used to estimate the age of tsunami deposits. The inferred mean recurrence time of ~325 yrs broadly agrees with the existing regional paleoseismic and paleotsunami records. However, our record reveals a large tem-

poral variability between tsunami events, which forms a bimodal probability density function for the recurrence pattern with modes at ~115 and ~490 yrs. As the mean recurrence time coincides with the lowest probability between the two modes, we conclude that the sense of safety in coastal communities in south central Chile, 55 yrs after the last catastrophe, may be deceiving. A tsunamigenic earthquake in the near future would not redefine the extremes of the presented record.

Lake Cucao's sedimentary history is more complex than Lake Huelde's, however, its sedimentary record holds valuable paleotsunami information, too. The area of the lake basin has been submerged since the postglacial sea-level rise and may have recorded tsunami inundations in its sedimentary record since then. A radiocarbon date from a sediment core and internal acoustic reflections, which converge towards a tidal channel, indicate that tidal currents were active at least sporadically over the last 3700 yrs. Little vertical displacement over the last 3700 yrs maintained the ability of Lake Cucao to record tsunamis in its sedimentary record. In total 15 detrital layers are interpreted as tsunami deposits with a varying level of confidence. The level of confidence depends on five criteria; there are site-specific criteria, i.e. i) high magnetic susceptibility of the sediment indicating high detrital content in contrast to the organic-rich gyttja, ii) core-to-core correlation, and iii) acoustic reflection correlation to the sedimentary record (the latter two indicate traceability of the detrital layer in the sedimentary record), and general criteria, i.e. iv) presence of mud clasts indicating an episode of extreme flow conditions in an otherwise calm environment and v) age correlation to known paleotsunamis in the area. The neighbouring Lake Huelde contains 14 or 15 tsunami deposits in the same time interval as Lake Cucao, suggesting that both lakes may have been equally reliable in recording tsunami inundation. This study adds a long paleotsunami record on a coastline, where extreme tsunamis occur relatively frequently and where long paleotsunami records are still sparse. Many important sedimentary features were revealed by side scan sonar data and sub-bottom profiles, which demonstrates how indispensible acoustic imagery can be in understanding the depositional environment, especially in lakes as dynamic as the coastal Lake Cucao. Imaging tsunami deposits in coastal lakes with sidescan sonars and sub-bottom profiles can now be added to the growing list of tools in the toolkit to observe, describe and recognise tsunami deposits.

The amount of data collected about the numerous tsunami deposits in both lakes allows a ranking of tsunami deposits according to multiple criteria, which may represent the size of the associated tsunami. These criteria are i) maximum magnetic susceptibility, ii) average magnetic susceptibility, iii) traceability (lateral extent), iv) average tsunami deposit thickness and v) percentage of mud rip-up clast intervals. Integrating the two coastal lake records, it is evident that the AD 1960 tsunami was one of the major events in both lakes in the last ~4000 yrs. Two older tsunami deposits of similar characteristics as the AD 1960 tsunami deposit are tentatively correlated across both lakes. Their ages are ~3740 and ~3890 cal. yrs BP. However, the relative ranking of tsunamis only compares the sedimentary effect in both lakes and cannot be translated directly to relative tsunami size, because environmental changes are not accounted for. For example, landscape evolution, horizontal and vertical shoreline displacement all affect how and where an environment records a tsunami inundation. Models that could quantify the tsunami size in absolute terms need this information. These models can be physical or numerical, however, physical models of tsunamis focus on subaerial landslide-induced tsunamis. Of the numerical models, there are forward models and inverse models. Forward models are extremely complex dynamic models and can include all aspects of tsunamis from fault slip simulation during the causative earthquake to vertical seafloor deformation, tsunami generation, propagation and inundation, and eventually erosion and deposition of coastal sediments. Inverse models try to infer tsunami inundation parameters, e.g. flow depth, from characteristics of tsunami deposits. However, none of the existing inverse tsunami models are applicable to tsunami sediments in coastal lakes. Furthermore, only little is known of how the environment changed around Lake Cucao and Lake Huelde, e.g. relative sea-level change, vegetation changes, horizontal shoreline displacement and more. Further investigation towards the environmental history and application of numerical forward models could facilitate quantitative paleotsunami research.

Samenvatting

De zuid-centraal Chileense kust ligt aan de Peru-Chili subductiezone. Hierdoor loopt dit gebied een hoog risico op subductie-aardbevingen. De convergente beweging van de oceanische Nazcaplaat en de Zuid-Amerikaanse Plaat tijdens deze aardbevingen veroorzaakt co-seismische verticale vervorming van de zeebodem, die op zijn beurt tsunami's kan veroorzaken. De tsunami's breiden zich uit over de Stille Oceaan en kunnen uiteindelijk de Zuid-Amerikaanse westkust en andere kustgebieden overstromen, hetgeen voor de kustgemeenschappen catastrofale gevolgen kan hebben. Naast het veroorzaken van vele slachtoffers en de vernietiging van infrastructuur, zetten tsunami's ook specifieke sedimenten af. Dit proefschrift richt zich op de tsunamiafzettingen in twee kustmeren, Lake Cucao en Lake Huelde, aan de westkust van Isla de Chiloé, in zuid-centraal Chili (42.6° S), en hun directe omgeving.

Dit proefschrift beschrijft de sedimentaire kenmerken van de recentste tsunamiafzettingen in de sedimentaire archieven van de kustmeren, met een focus op de tsunamiafzetting van de AD 1960 Grote Chileense Aardbeving (M_W 9.5). De AD 1960 tsunami overstroomde beide meren. De meren bevinden zich ~2 km uit elkaar en liggen ~1.2 km achter de kust. De sedimentaire opvulling van beide meren bestaat uit gyttja, met daarin geïntercaleerde zandlagen, die ook klei-klasten ("mud rip-up clasts") kunnen bevatten en gekenmerkt worden door een siltige toplaag. Deze zandlaag vertegenwoordigt een plotselinge verandering in het sedimentaire milieu. Met behulp van korrelgrootte-analyse en vergelijkingen met oppervlaktemonsters uit de omgeving van het meer, tonen we aan dat het proximale (zeewaarts) deel van de tsunamiafzetting uit een mengsel van zand en geremobiliseerde lacustriene gyttja bestaat. Het zand is afkomstig van niet-aquatische ("subaerial") bronnen. In het distale (landzijde) deel van Lake Cucao, bevat de tsunamiafzetting geen zandfractie en bestaat ze volledig uit geremobiliseerde meersedimenten. Herhalingen van sequenties van tsunamiafzettingen (of delen daarvan) in Lake Huelde suggereren dat er minstens drie overstromende tsunamigolven moeten geweest zijn. Seismische profielen en side scan sonar mozaïeken onthullen dat de tsunami-golven hoofdzakelijk doorheen het rivierkanaal vloeiden, maar ook over de barrière tussen de meren en de Stille Oceaan. De dominante rol van het kanaal als route voor sediment-transport wordt ook aangetoond door de samenstelling van de tsunamiafzetting, die fijner wordt verder weg van de monding van het kanaal. De identificatie en beschrijving van de AD 1960 tsunamiafzetting geeft belangrijke inzichten in tsunamisedimentatie in kustmeren en geeft een duidelijke indicatie van hoe tsunamiafzettingen eruit zouden moeten zien in het sedimentaire archief van de twee kustmeren.

De beschreven sedimentaire kenmerken van de tsunamiafzettingen in Lake Huelde worden aangewend om het uitzonderlijk lange en continue sedimentaire archief te onderzoeken. Het sedimentaire archief van Lake Huelde bevat 17 verschillende detritische lagen verspreid over een periode van 5500 jaren. Deze lagen worden geïnterpreteerd als tsunamiafzettingen met variërende graad van betrouwbaarheid. Dankzij het ongewoon hoog aantal tsunamiafzettingen in een enkel sedimentair archief is het mogelijk om het terugkeerpatroon ervan te analyseren. Terugkeerfrequenties en het terugkeerpatroon vormen een cruciaal onderdeel van tsunamigevaarbeoordelingen. In probabilistische tsunamigevaarbeoordelingen is de terugkeer van tsunami's

meestal gemodelleerd met een Poisson-verdeling, die, zoals we laten zien, niet per se het gevaar op correcte wijze weergeeft. De resultaten van ^{137}Cs- en ^{210}Pb-dateringen, infrarood gestimuleerde luminescentie (IRSL) datering en koolstofdatering worden gebruikt als input voor Bayesiaanse ouderdom-diepte modelleringen. De resulterende ouderdom-diepte relatie wordt dan gebruikt om de ouderdom van tsunamiafzettingen in te schatten. De afgeleide gemiddelde terugkeerperiode van ~325 jaren komt in grote lijnen overeen met de resultaten van ander regionale paleoseismisch en paleotsunami onderzoek. Echter, ons sedimentaire archief toont aan dat er een grote tijdelijke variabiliteit tussen tsunami's is en dat deze variabiliteit in het terugkeerpatroon een bimodale kansverdelingsfunctie heeft met pieken op ~115 en ~490 jaren. De gemiddelde terugkeerperiode valt samen met de laagste waarschijnlijkheid in het terugkeerpatroon. Dit laat ons toe te concluderen dat het gevoel van veiligheid in kustgemeenschappen in zuid-centraal Chili, 55 jaren na de laatste grote tsunami, misleidend kan zijn. Een tsunamigene aardbeving in de nabije toekomst zou de grenzen van de gepresenteerde datareeksen niet overschrijden.

De sedimentaire geschiedenis van paleotsunami's in Lake Cucao is complexer dan dat van Lake Huelde, toch bevat dit sedimentaire archief ook waardevolle paleotsunami-informatie. Het meerbekken werd overspoeld gedurende de postglaciale zeespiegelstijging en heeft waschijnlijk sindsdien tsunamioverstromingen geregistreerd in zijn sedimentaire archief. Een koolstofdatering uit een sedimentkern en seismische profielen waarop interne akoestische reflecties convergeren naar het getijdekanaal, geven aan dat getijdestromingen actief waren, ten minste sporadisch, gedurende de voorbije 3700 jaren. Geringe verticale verplaatsing in de afgelopen 3700 jaren leidde ertoe dat Lake Cucao tsunamiafzettingen kon registreren in zijn sedimentaire archief. In totaal worden 15 detritische lagen geïnterpreteerd als tsunamiafzettingen, en dit met een variërende graad van betrouwbaarheid. De graad van betrouwbaarheid is afhankelijk van vijf criteria; er zijn plaatsspecifieke criteria, b.v. i) hoge magnetische susceptibiliteit van het sedimen, wat wijst op een eerder detritische samenstelling in tegenstelling tot de organisch-rijke gyttja, ii) kern-tot-kern correlatie en iii) correlatie van akoestische reflecties met het sedimentaire archief (de laatste twee kunnen gecorreleerd worden met detritische lagen in de stratigrafie), en er zijn algemene criteria, b.v. iv) aanwezigheid van kleiklasten (mud rip-up clasts) die duiden op een periode van extreme stroming in een anders kalme omgeving en v) de correlatie met bekende paleotsunami's in zuid-centraal Chili aan de hand van de afgeleide ouderdommen. Het sedimentaire archief van het naburige Lake Huelde, bevat 14 of 15 tsunamiafzettingen in hetzelfde tijdsinterval als Lake Cucao, wat erop wijst dat beide meren een gelijkaardige gevoeligheid hebben voor wat betreft het registreren van tsunami-overstromingen. Dit onderzoek levert een nieuwe, en lange tijdsreeks op van paleotsunamiafzettingen aan kustlijn, waar extreme tsunami's relatief vaak voorkomen en waar lange sedimentaire archieven met paleotsunami's nog steeds schaars zijn. Vele belangrijke sedimentaire structuren werden bovendien in beeld gebracht met behulp van side scan sonar data en seismische profielen. Dit toont aanhoe onmisbaar akoestische beeldvorming is in het begrijpen van het lacustriene afzettingsmilieu, en vooral in meren die zo dynamisch zijn als Lake Cucao. Beeldvorming van tsunamiafzettingen in kustmeren met side scan sonars en seismische profielen kan nu toegevoegd worden aan

de groeiende lijst van onderzoeksinstrumenten, die voor het observeren, beschrijven en het herkennen van tsunamiafzettingen nuttig kunnen zijn.
Het aantal data verzameld over de talrijke tsunamiafzettingen in beide meren,laat toe om de tsunamiafzettingen te rangschikken op basis van meerdere criteria, die iets kunnen vertellen over de grootte van de tsunami. Deze criteria zijn i) de maximale magnetische susceptibiliteit, ii) de gemiddelde magnetische susceptibiliteit, iii) de traceerbaarheid (laterale uitbreiding), iv) de gemiddelde dikte van de tsunamiafzetting en v) het percentage aan kleiklasten (mud rip-up clast). De integratie van de sedimentaire archieven uit de twee kustmeren maakt duidelijk dat de AD 1960 tsunami een van de belangrijkste sedimentaire gebeurtenissen was in de voorbije ~4000 jaren. Twee oudere tsunamiafzettingen met vergelijkbare kenmerken als de AD 1960 tsunami zijn voorzichtig gecorreleerd over beide meren. De geassocieerde tsunami's vonden ~3800 en ~3950 jaren geleden plaats. De relatieve rangschikking van de tsunami's geldt alleen voor het sedimentaire effect in beide kustmeren, en kan dus niet direct vertaald worden naar relatieve tsunami-omvang, want veranderingen in de omgeving van de meren worden niet in rekening gebracht in deze analyse. Bijvoorbeeld, landschapsevolutie, horizontale en verticale verplaatsing van de kustlijn, bepalen hoe en waar een bepaalde omgeving een tsunami-overstroming registreert Modellen die de tsunami-grootte kwantificeren met absolute waarden, hebben deze informatie nodig. Deze modellen kunnen fysisch of numeriek zijn. Fysische modellen van tsunami's richten zich op door aardverschuivingen veroorzaakte tsunami's. Onder de numerische modellen zijn er modellen die 'vooruit modelleren' (de zogenaamde forward models), en modellen die 'achteruit modelleren' (de zogenaamde inverse models). *Forward models* zijn zeer complexe dynamische modellen en kunnen alle aspecten van de tsunami's modelleren, van breuk-slip-simulatie, tsunami-veroorzakende verticale zeebodemvervorming, tsunami-verspreiding en -overstroming, en uiteindelijk erosie en afzetting van kustsedimenten. Inverse models trachten tsunami-parameters (bv. stromingsdiepte) af te leiden uit de kenmerken van tsunamiafzettingen. Geen van de bestaande *inverse tsunami models* zijn echter toepasbaar op tsunamiafzettingen in kustmeren. Bovendien zijn de veranderingen in het milieu in het gebied rond Lake Cucao en Lake Huelde niet bekend. Belangrijke veranderingen in het milieu zijn b.v. veranderingen van de relatieve zeespiegel, vegetatie-veranderingen, horizontale verschuivingen van de kustlijn, enz. Verder onderzoek naar de omgevingsgeschiedenis en het gebruik van numerische *forward models* zouden kwantitatief paleotsunami-onderzoek in de toekomst kunnen vergemakkelijken.

Acknowledgements

A doctoral thesis does not appear from thin air. It is an almost geologically slow process. During the doctorate, the list of contributors becomes steadily longer. I would like to stress that there are more people than I mention here, who have contributed directly or indirectly, knowingly or unknowingly to this thesis.

On this long list of people, who have my gratitude, Dr. Jasper Moernaut is chronologically the first. The project was his inception and he and Marc wrote the project. It was Jasper who taught me how to do fieldwork on lakes, during a 3-months stay in Chile over the 2011/12 southern hemisphere fieldwork season. Jasper accepts that everybody can have bad days in the field. As a person with a tendency towards grumpiness, I welcome this trait tremendously. It is a pity that his support throughout the years had to be as remote as it was.

The second person I would like to thank explicitly is my promoter Prof. Dr. Marc De Batist. Marc enabled me to go to my study area in Chile, to fieldwork in Alaska and conferences and workshops in Austria, France, Germany, Switzerland, Japan and the USA. I am very aware that this goes beyond the usual scope of a PhD students' professional travel plans and I am grateful for the opportunities he has given me.

An important influence to this thesis, though not officially involved, is Dr. Maarten Van Daele. Beginning a PhD in a country that, for another 2 years, would have no other tsunami specialist was a daunting and sometimes lonely experience. Given the lack of another tsunami specialist, I could not have asked for a better office mate than Maarten to bounce ideas back and forth with. I thank him for all the ideas he had, some of which parade as my own in this thesis. Nobody will ever know that they are his. My deepest gratitude is his poor payment.

I would like to acknowledge those, who had direct influence on this thesis by going on fieldwork with me, giving me advice for methods and/or constructively criticising parts of this thesis. Chief among those is queen of the office, Nore Praet, and king of all lab-related questions, Prof. Dr. Sebastien Betrand. However, thanks are due to many more, including Evelien Boes, Marco Cisternas, Stanislas Delivet, Ed Garrett, Katrien Heirman, Ferdinand Messens, Mario Pino, Koen De Rycker, Sabine Schmidt, Roberto Urrutia, Dimitri Vandenberghe, Willem Vandoorne, Flor Vermassen, Gauvain Wiemer and all unmentioned members of the RCMG.

I thank my friends and family for their never-ending support. They are the reason I remain reasonably sane.

Contents

List of Figures

List of Tables

"...la nature a toujours été en eux plus forte que l'éducation."
"...nature always had more power than education."

AD 1739, Voltaire, in *La vie de Molière*

1 Introduction

1.1 Recent catastrophic tsunamis

The Indian Ocean Tsunami on the 26th of December in 2004 was the first giant tsunami to be broadcasted worldwide in almost real time. For many people – me included – it was the first time to see footage of a tsunami wave hitting a coast. While people around the world watched the catastrophe unfold, almost 230,000 people at coastlines around the Indian Ocean lost their life. The AD 2004 Indian Ocean Tsunami painfully highlighted how unaware coastal communities were about tsunamis as geohazards at the time and how little was known by the scientific community. Since then, scientists have increased their efforts dramatically to understand all aspects of this multidisciplinary research topic (Fig. 1.1). Among other sciences this includes fluid and wave dynamics for the generation and propagation of tsunami waves, geosciences for the physical damage to coastal environments, ecology to assess the damage to the biosphere, civil engineering to assess physical damage to human built structures, social sciences to describe the impact tsunamis have on the mental health of individuals and societies, history to learn more about past events and many more.

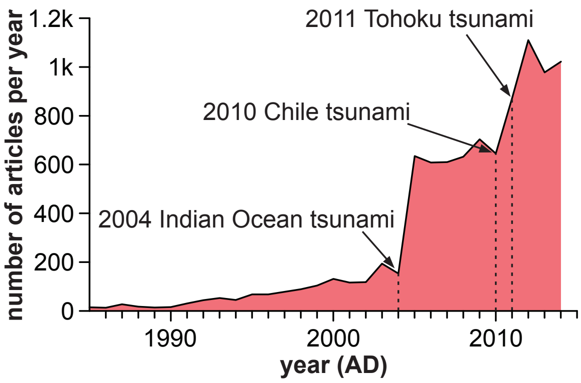

Figure 1.1: Number of "tsunami"-related publications over time according to web of science.

Tsunamis are water waves with long wavelengths generated by sudden displacement of large volumes of water. Earthquakes, landslides, volcano eruptions and meteorite impacts are the four most common causes for tsunamis. This thesis concentrates on earthquake-induced tsunamis, which are generated by seafloor deformation. Earthquake triggered tsunamis amount to ~76 % of all recorded tsunamis since AD 1915 according to the Global Historical Tsunami Database of the National Oceanic and Atmospheric Administration's (NOAA's) National Centers for Environmental Information (NCEI) of the USA.

In the 11 years since the AD 2004 Indian Ocean Tsunami NOAA registered 133 tsunamis. Eleven of the 133 tsunamis killed people and almost all of them caused infrastructural damage. Only two of the 11 deadly tsunamis were responsible for more than 99 % of the fatalities (Tab. 1.1). It is the few giant tsunamis which cause the most damage and kill the most people (Fig. 1.2).

Table 1.1: List of all deadly tsunamis since the 2004 Indian Ocean Tsunami with date, magnitude of the associated earthquake, maximum recorded run-up height and number of fatalities according to NOAA's NCEI Global Historical Tsunami Database.

date (dd.mm.yyyy)	magnitude (M_W)	location	max. run-up height (m)	fatalities
26.12.2004	9.1	Indian Ocean, northern Sumatra, Indonesia	50.90	227899
28.03.2005	8.7	Nias, northern Sumtra, Indonesia	4.20	10
17.07.2006	7.7	western Java, Indonesia	20.90	802
01.04.2007	8.1	Solomon Islands	12.10	52
15.08.2007	8.0	southern Peru	10.05	3
29.09.2009	8.1	Samoa	22.35	192
12.01.2010	7.0	Haiti	3.00	7
27.02.2010	8.8	Maule, central Chile	29.00	156
25.10.2010	7.8	Mentawai, central Sumatra, Indonesia	16.90	431
11.03.2011	9.0	Tōhoku, northern Honshu, Japan	38.90	18482
28.10.2012	7.7	Haida Gwaii,British Columbia, Canada	12.98	1
06.02.2013	7.9	Solomon Islands	n/a	10

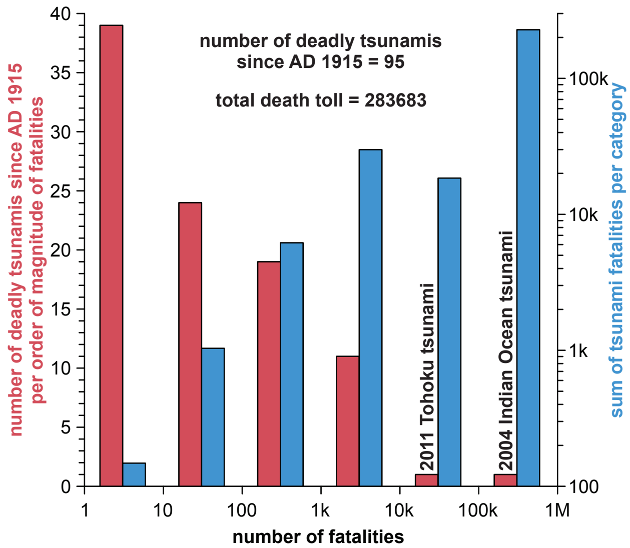

Figure 1.2: Tsunamis with a low number of fatalities are more frequent than tsunamis with a high number of fatalities (red). However, it is the infrequent tsunamis with many fatalities, which cause the most fatalities (blue). Data source is the Global Historical Tsunami Database of the NCEI of the NOAA of the USA.

1.2 Why research tsunamis by geological means

With 133 tsunamis since the AD 2004 Indian Ocean Tsunami, tsunamis cannot be considered infrequent events from a geological point of view. However, catastrophic tsunamis with vast infrastructural damage and numerous fatalities occur less often. At any given place on a tsunami prone, i.e. subduction zone, coastline such catastrophic tsunamis occur with recurrence times of up to millennia. This is too long in most areas to have chronicled more than two tsunamis. The low number of historically known catastrophic tsunamis highlights the necessity to research tsunamis in the sedimentary record. While written history is limited, e.g. to the last ~500 yrs in Chile or ~1300 in Japan, geological archives, e.g. lake sediment sequences, are capable of recording many thousands of years.

1.3 Research questions

This thesis addresses four main research questions surrounding the topic of paleotsunamis, i.e. tsunamis of the past, and in particular south central Chile's tsunami history.

Are Chilean coastal lakes suited for tsunami research?

Prior to this thesis, the only lake in Chile known to contain tsunami deposits was Lake Budi (73.3° W, 38.9° S). Complex patterns of erosion and deposition in the relatively large and shallow Lake Budi caused its sedimentary record to be incomplete. The youngest tsunami deposit in Lake Budi is ~1.5 ka old (Wallner, 2008). However, the findings of Lake Budi triggered more interest in coastal lakes of Chile. The quality of the tsunami record of two coastal lakes south of Lake Budi is discussed in chapter 3, while the maintained ability to record tsunamis over long periods of time in the same lakes are discussed in chapters 4 and 5.

Can particular tsunami deposits in coastal lakes in Chile be assigned to known tsunami inundation from documented history?

To assign a tsunami deposit to a particular tsunami, the deposit needs to express the features of a tsunami deposit, other causative processes need to be excluded and the deposit needs to be dated reasonably well to link the deposit to a known tsunami in history. This is addressed for the most recent tsunami in AD 1960 on the south central Chilean coast in chapter 3. Two older tsunamis from known history, i.e. in AD 1837 and AD 1575, are addressed in chapter 4.

How often and with which recurrence pattern do large-scale tsunamis occur on the south central Chilean coast?

To better protect coastal communities and coastal infrastructure from tsunamis it is essential to know how frequent tsunamis occur on tsunami prone coastlines. Tsunamis do not necessarily recur regularly. This issue is addressed in chapter 4, in which the average recurrence time and the recurrence pattern of tsunamis are discussed on the basis of a 5500 yrs long and continuous sedimentary record with 17 recorded tsunami inundations.

Can tsunami size be inferred from tsunami deposits in coastal lakes?

To a complete tsunami risk assessment the recurrence timing is only half of the necessary information. The other half is information on the size of the tsunami that is to be expected. This is more difficult to tackle with geological tools, because of the problem of equifinality, i.e. that a range of causative processes can produce identical sedimentary results. An attempt to evaluate the relative size of the tsunamis in the lakes is discussed in chapter 6.

Can the growing toolkit for tsunami research be expanded with the tools used in this thesis?

Over time, researchers have developed a geoscientific toolkit to investigate tsunami deposits. This toolkit is exceptionally multidisciplinary due to the complex nature of tsunamis, their deposits and the coastal environment in which they occur. This toolkit is ever growing and repeatedly refined (Chagué-Goff et al., 2011). Most tsunami deposits are investigated in coastal lowlands in form of trenches and with direct measurements on the tsunami deposit. Coastal lakes do not offer the same direct access to tsunami deposits and only small samples in form of sediment cores can be retrieved. However, coastal lakes offer superior depositional records and also offer the opportunity to use a suite of acoustic imagery tools. The indirect measurements on tsunami deposits are new. Their use and potential are discussed in the chapters, where this thesis makes use of them (side scan sonar imagery in chapter 3 and 5; and sub-bottom profiles in chapter 5).

1.4 Principles of tsunami research

Ultimately, all tsunami research serves the purpose to understand the hazard emanating from tsunamis. To understand the hazard of tsunamis is to understand the generation, propagation and inundation of tsunamis. However, before addressing these aspects a few basic parameters need to be established (Fig. 1.3).

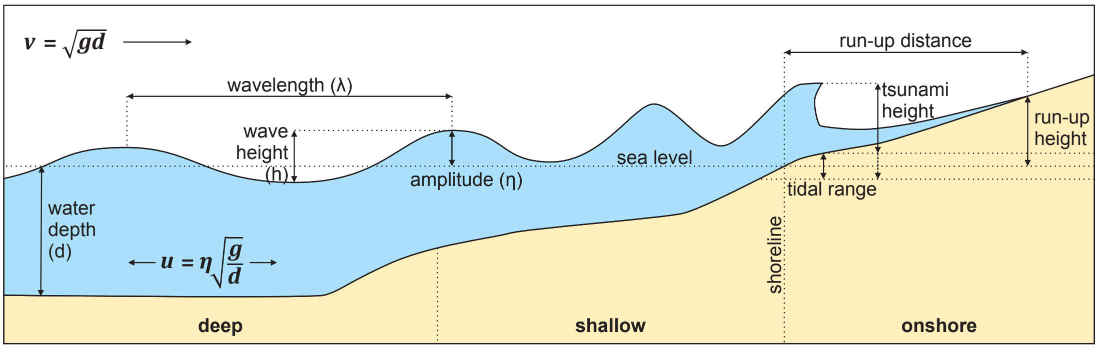

Figure 1.3: Schematic illustration of parameters and formulas describing tsunamis (modified after Sugawara et al., 2008; Brill, 2012).

The **wavelength** (λ) is the distance from one wave crest to the next. The vertical distance between a crest and the adjacent trough is the **wave height** (h). The wave height should neither be confused with the **amplitude** (η_0), which is the vertical distance from the still-water level to the crest, nor with the **tsunami height**, which is the highest elevation of water onshore. The **run-up distance** and **run-up height** are the horizontal and vertical limits reached by the tsunami inundation.

1.4.1 Tsunami generation

As mentioned above, earthquakes are the most common (76 %) tsunamigenic process. Landslides, submarine volcano eruptions and meteorite impacts make up for most of the remaining causes. It is co-seismic sea floor deformation, not seismic waves, which causes the water body to respond with tsunami generation. The vertical component of the co-seismic deformation is the most efficient contributor to tsunami generation. Megathrust earthquakes, i.e. earthquakes on interplate thrust faults between a subducting and an overriding tectonic plate, produce a large amount of far spread vertical co-seismic deformation, due to the convergent motion of the tectonic plates and the high amount of slip during the largest of these earthquakes. Among the subduction zone earthquakes, there are earthquakes, which are particularly efficient in translating co-seismic slip into vertical co-seismic deformation and trigger unexpectedly large tsunamis. These earthquakes are called tsunami earthquakes (Kanamori, 1972). These are earthquakes, typically in a subduction zone setting, which rupture the shallowest portion of a megathrust fault or a splay fault. In contrast, strike slip earthquakes, in which the plate motion and deformation are predominantly horizontal, are often not tsunamigenic even with a large amount of slip, e.g. the 11th April 2012 Sumatra earthquake (M_W 8.6). However, horizontal motion can be an important contributor to tsunami generation in presence of steep slopes (Tanioka and Satake, 1996).

Submarine landslide induced tsunamis are the second most common tsunami type. In some cases the tsunamigenic processes overlap, e.g. when a strong earthquake causes a landslide. Both processes can contribute to tsunami generation. Often it is obvious which process contributed more to the tsunami generation, e.g. Lituya Bay earthquake, rockslide and rockslide-tsunami in 1958 (Fritz et al., 2009), however, sometimes co-seismic deformation and water displacement by landslides contributes to similar extents, e.g. in the 1999 Izmit Bay tsunami (Tinti et al., 2006). Two purely landslide triggered and notorious tsunamis were the giant submarine slump tsunami on the Norwegian passive continental margin, called the Storegga slide (Bondevik et al., 1997a; Dawson et al., 1988), and the volcanic island flank collapses of the past on the Canary Island flanks (Masson et al., 2002) and the expected Cumbe Vieja flank collapse on La Palma (Ward and Day, 2001).

Volcanic eruptions are a rare triggering mechanism. However, two catastrophic events in human history deserve a mention, when writing about tsunami generation mechanisms. The older event was the eruption of the Thera volcano (Santorini) in ~1500 BC in the Aegean Sea (Minoura et al., 2000). The younger event is the extremely deadly eruption of Krakatau in the Sunda Sea in AD 1883, in which two thirds of the island disappeared into the sea, causing a 37 m high tsunami killing ~36,000 people (Nomanbhoy and Satake, 1995; Sugawara et al., 2008).

Meteorite impact tsunamis are luckily the rarest type. 'Luckily', because it is commonly accepted that an asteroid impact produced the greatest known tsunami in earth's history. The asteroid impacted in the Mexican Gulf at the K/T boundary 65 million years ago, creating the so-called Chicxulub crater. The crater alone is 180 km in diameter. Numerical models reconstructed 200 m tsunami wave height with up to 300 km run-up distance on the North American continent (Matsui et al., 2002; Schulte et al., 2010).

1.4.2 Tsunami propagation

Once triggered, tsunamis propagate through the ocean. Tsunami waves have a much greater wavelength (λ), typically tens to hundreds of kilometres, than the water depth (d), in which they travel. In the deep ocean their wave height is commonly tens of centimetres to a few metres. They are called "long-waves" and their behaviour is governed by the long wave equations. The consequence of these equations is that a tsunami wave's loss of energy rate is very low, which explains why tsunamis can be devastating after propagating across thousands of kilometres of deep ocean, as has happened in AD 1960, when the tsunami of the Great Chilean Earthquake inundated the Japanese coast (Satake and Atwater, 2007) or when in AD 2004 the Indian Ocean Tsunami inundated the Somali coast (Fritz and Borrero, 2006). Their propagation velocity is described by

$$v = \sqrt{gd} \tag{1.1}$$

Where v is the velocity of the wave propagating, g is earth's gravity acceleration (~9.81 m s^{-2}) and d is the water depth. Since gravity acceleration is more or less constant on earth, the water depth controls the speed at which tsunamis propagate. For example, a tsunami propagates at a speed of ~800 km h^{-1} in a 5000 m deep ocean basin. The actual flow of water produced by a passing tsunami wave is described by

$$u = \eta\sqrt{\frac{g}{d}} \tag{1.2}$$

Where u is the current velocity and η is the amplitude or the elevation above still-water level. Letters g and d are the earth's gravity acceleration and water depth, respectively, as before. For example, the tsunami passes through 5000 m water depth with an amplitude (η) of 1 m. The resulting current velocity would be merely ~4.4 cm s^{-1}, when the crest of the tsunami wave passes through.

When tsunamis approach the coast the shallower water depth will slow the tsunami wave down. Refraction of the wave energy causes the wave front to focus on convex coastlines, e.g. capes. This refraction of energy towards convex coastlines should not be mistaken to contradict run-up amplification of tsunamis in v-shaped bays, which can amplify tsunami heights by 4–5 times (Sugawara et al., 2008).

The energy that was spread over much larger wavelengths in deep ocean waters concentrates into the shorter wavelengths in shallow water. The resulting increase in wave height is described by

$$hd^{1/4} = h_0 {d_0}^{1/4} \tag{1.3}$$

Where h and h_0 are wave heights corresponding to deep (d) and shallow (d_0) water depth, respectively. The tsunami will stop to behave according to equation 1.1, when shallower water is reached and it begins to interact with the sea floor. At this point, the long wave character of the tsunami wave is lost and the tsunami behaves according to the shallow-water long-wave theory – a set of equations, which are widely used in numerical modelling of tsunami propagation.

1.4.3 Tsunami inundation

The tsunami inundation to near-shore and onshore areas is the destructive episode of a tsunami. In contrast, tsunamis are often not recognised offshore despite their high propagation velocity (v), because of their long wavelengths (λ) and low wave height (h). The tsunami wave either hits the shoreline with a trough first, as is more common for near-field tsunamis, or with a crest first, as is more common for far-field tsunamis. Whether a trough or a crest arrives first is controlled by the co-seismic seafloor deformation pattern, which triggers the tsunami, and the relative position of the shoreline to the deformation area.

As the water depth decreases and eventually becomes equal to increasing tsunami height onshore the current velocity increases dramatically (equation 2). The surging tsunami front and the more channelized back wash onshore with flow depth of 9 m were video taped during the 2011 Tōhoku tsunami and later videometrically measured to flow at 40 km h^{-1} (Fritz et al., 2012). The flow speed profile through the water column of tsunamis in onshore and near-shore areas shows little variation, i.e. laminar flow. The intense flow regime of inundating tsunamis produces high tractive forces at the ground-water-interface. The tractive force of the water interacts with the ground in form of erosion. Conversely, the tractive force also affects the water flow, creating a turbulent boundary layer at the base, in which the flow speed profile has a steep gradient. The further the tsunami inundates and the lower the flow depth the more turbulent the tsunami becomes.

1.4.4 Tsunami deposits – state of the art

The deposition of sediment by tsunamis was described in the early 1960s after the tsunami of the Great Chilean Earthquake in coastal lowlands (Wright and Mella, 1963). The recognition of modern tsunami deposits slowly led to paleotsunami research with purely geological means in the late 1980's when, for example, Atwater (1987) studied a sequence of tsunami deposits and subsidence events in Washington, USA, and realised that subduction zone earthquakes and tsunamis had hit the Cascadia coastline repeatedly. Simultaneously, Dawson et al. (1988) described evidence for tsunami inundation on the Scottish east coast and linked it to the giant Storegga slumps on Norway's passive continental margin. Since then, research has continuously improved the understanding of tsunami sediment transport and deposition of tsunami sediment.

A tsunami can only transport sediment that is available for entrainment along its path of inundation. In most cases this means sub-littoral sands, beach sand and dune sands, which is why tsunami deposits are often described as sand sheets in coastal depositional records. However, tsunami deposits can contain mud (i.e. clay and silt) (e.g. Chagué-Goff et al., 2012) or up to boulders (e.g. Paris et al., 2009) (Fig. 1.4). Depending on particle size, density and shape of the particles, as well as on flow speed, tsunamis exhibit bed load and suspension load as the two principally different modes of sediment transport. With the exception of boulders, large-scale tsunamis transport most of their sediment in suspension.

Tsunami deposits are generally recognised as detrital layers representing high flow energy in

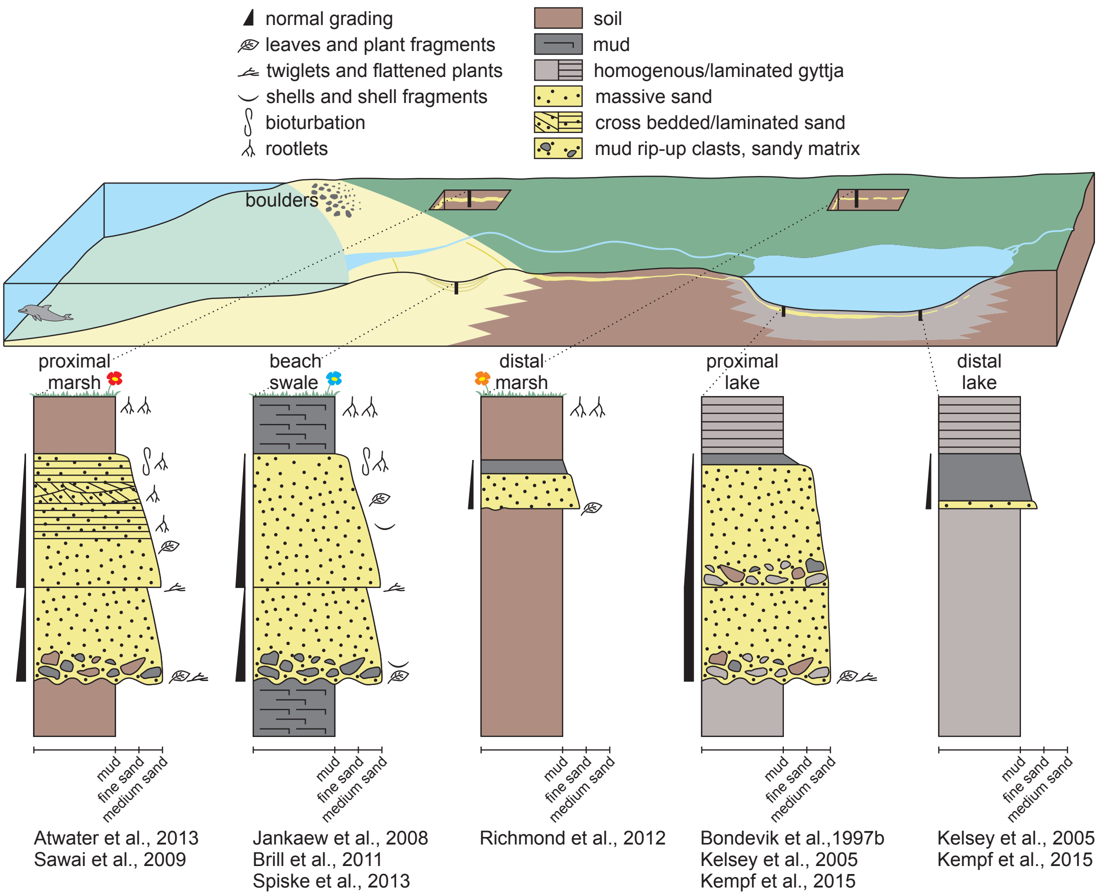

Figure 1.4: Typical sedimentological logs of tsunami deposits in a beach swale (Brill et al., 2011; Jankaew et al., 2008; Spiske et al., 2013), a proximal marsh (Atwater et al., 2013; Sawai et al., 2009), a distal marsh (Richmond et al., 2012), a proximal coastal lake (Bondevik et al., 1997b; Kelsey et al., 2005; Kempf et al., 2015) and a distal coastal lake environment (Kelsey et al., 2005; Kempf et al., 2015).

an otherwise lower energy environment, e.g. a sandy layer within a peaty sequence. However, the differentiation between tsunami and storm surge deposits in coastal lowlands can be difficult to impossible, when one or the other process cannot be excluded on the basis of the investigated environment (e.g. Kortekaas and Dawson, 2007; Morton et al., 2007; Phantuwongraj and Choowong, 2011; Ramírez-Herrera et al., 2012). Many attempts to find the uniting proxy, which will allow differentiation between tsunami deposits and storm surge deposits, resulted in the realisation, that each depositional system needs to be investigated with a multidisciplinary approach to correctly interpret deposits of large wave events (e.g. Switzer and Jones, 2008). Tsunamis typically produce quasi-continuous detrital layers reaching several hundred meters to a few kilometres inland. Tsunami deposit thickness is strongly controlled by topography and small-scale morphology and varies between few millimetres to several decimetres. The overall trends of tsunami deposits are landward thinning and landward fining (Gelfenbaum and Jaffe, 2003; Goto et al., 2014, 2012; Minoura et al., 1997; Nanayama et al., 2000). The two trends do not necessarily occur simultaneously and there are exceptions to both. Fining upwards in form of suspension grading suggest that the majority of tsunami sediment is deposited gradually out of suspension (Gelfenbaum and Jaffe, 2003; Shi et al., 1995).

The extreme current velocities during run-up reached by inundating tsunamis (Fritz et al., 2012) exceed the threshold of erosion for nearly all particle sizes. Which is why the lower contact of tsunami deposits is typically sharp and erosional (Benson et al., 1997). The strong erosion potential can cause bulk erosion of soil and other fine-grained cohesive sediments, e.g. soil or silty/clayey lake sediment, and produce mud rip-up clasts in the tsunami deposit (Atwater et al., 2013; Bondevik et al., 1997b; Kempf et al., 2015). Eventually, the run-up ceases and the inundation comes to a halt. The acquired potential energy begins to convert into kinetic energy again and forms the backwash. The backwash is strongly topographically controlled and not always directly opposite of the run-up direction. Usually the backwash is more channelized with seaward-directed scours behind obstacles in the thalweg, e.g. boulders. Strong erosion of soil and of tsunami run-up deposit occurs within areas of channelized backwash. Elsewhere, the backwash erosion can be comparatively weak (Sato et al., 1995; Yamada et al., 2014), however, there are examples, in which the backwash remobilized up to 90 % of the initially deposited sediment by the tsunami run-up (Bahlburg and Spiske, 2012). Backwash remobilized deposits often occur in form of fans with a point source, which are triangular in map view. Stacked sequences of opposing flow direction of tsunami run-up and backwash can be distinguished in some cases (Nanayama et al., 2000). In the marine settings, tsunami backwash can trigger turbidity currents. These turbidity currents have the potential to reach deep ocean basins (Arai et al., 2013; Ikehara et al., 2014).

Macro- and microfossils play a key role in determining the partially marine origin of tsunami sediment. Precise provenance studies can quantify the marine, brackish and freshwater origin of tsunami sediment (Pilarczyk et al., 2014). In coastal lowland environments it can be the microfossil assemblage, e.g. diatoms, in the under- and overlying sediments that gives evidence for co-seismic uplift or subsidence synchronous with the tsunami deposit. The vertical coastal deformation indicates seismic triggering of the tsunami and the near-field origin, i.e. not from a distant source (Dura et al., 2015; Garrett et al., 2015, 2013; Kelsey et al., 2015; Shennan et al., 2014).

Tsunami deposits in coastal lakes and lagoons are not studied as well as their coastal lowland equivalent, because of the restricted access to the deposit and because of fewer suitable study sites. However, coastal lakes and lagoons typically boast more accommodation space and a higher preservation potential than coastal lowlands (Sugawara et al., 2008). As in coastal lowlands, tsunami deposits in coastal lakes and lagoons are recognised by coarse detrital layers representing high energy deposition with under- and overlying low energy, fine-grained lake sediment. Tsunamis can erode unconsolidated lake sediment (Shinozaki et al., 2015). The eroded mud either forms mud rip-up clasts (Bondevik et al., 1997b; Kempf et al., 2015) or goes into suspension. The suspended, fine-grained lake sediment settles last in the mostly coarse grained sediment suspension and forms a mud cap. The coarse sediment entrained in the near coast environment, e.g. beach sand or dune sand, settles with and after the mud clasts and before the mud cap. Accordingly, tsunami deposits in coastal lakes consist of upwards fining sequences (or subsets thereof) of mud rip-up clasts in a sandy matrix, massive or upwards fining sand and mud caps with potentially high organic content (Bondevik et al., 1997b; Kelsey et al., 2005). The sand volume within the deposit may exhibit landward thinning. However, the muddy fraction usually drapes the lake floor with concentrations towards bathymetrical lows (Kelsey et al., 2005; Kempf et al., 2015). If the inundated area is usually a freshwater environment, then the intrusion of saline seawater changes the soil pore water and lake water chemistry. Increased concentrations of seawater markers (Cl, Br, S) can be measured in organic-rich sediment in freshwater soils (Chagué-Goff et al., 2015, 2012). The change in lake water chemistry can change the sedimentary environment to produce annual layers, i.e. varves, in the post-tsunami sediment (Kelsey et al., 2005). Similar and other characteristics of coastal lake tsunami deposits are described and discussed in detail on samples in chapters 3–5.

1.5 Tectonic Setting

This thesis focuses on two coastal lakes, Lake Cucao (074.09° W, 42.36° S) and Lake Huelde (074.11° W, 42.60° S), and their surroundings. The lakes are located on the west coast of Isla de Chiloé, the northernmost of the Patagonian islands along the south central Chilean coast. South America has an active continental margin off its entire western coast, where the oceanic Nazca Plate is being subducted underneath the overriding South America Plate in the Peru-Chile Subduction Zone. The subduction slabs from Ecuador to southern Chile enter the mantle at varying angles. Beneath northern and central Peru and beneath central Chile (27–33° S) the subducting plate moves along the base of the overriding South America Plate for a few 100s of kilometres before being pulled into the mantle at relatively flat angles (extremes of 10–15°), while the subduction underneath Ecuador, southern Peru-northern Chile and underneath south central and southern Chile (>33° S) enters the mantle immediately and is relatively steep (25–30°) (Barazangi and Isacks, 1976). The Nazca Plate and the South America Plate converge at a rate of 66–74 mm yr^{-1} (Angermann et al., 1999; DeMets et al., 2010). Chile's seismicity can be divided into three domains (Barrientos, 2007).

i There are large earthquakes of shallow and intermediate depth (0–70 km) on the megathrust fault, typically with rupture zones underneath the coastline. Examples of such events are the recent tsunamigenic AD 2010 Maule Earthquake (M_W 8.8) (Moreno et al., 2010) and AD 2014 Iquique Earthquake (M_W 8.1) (Lay et al., 2014). The strongest earthquake since the beginning of instrumental recording, the AD 1960 Great Chilean Earthquake (M_W 9.5) (Cifuentes, 1989), provides another example of such an earthquake. These earthquakes cause deformation of the overriding plate, which is expressed on the surface by trench-parallel zones of down- and upwarp of a few centimetres up to a few metres in extreme cases (Plafker and Savage, 1970).

ii At intermediate depth (70–120 km), large earthquakes of tensional or compressional nature occur within the subducted portion of the Nazca Plate, for example the AD 2005 Tarapaca Earthquake (M_W 7.7) (Peyrat et al., 2006).

iii On the overriding South America Plate, very shallow and shallow earthquakes (typically 0–20 km, up to 60 km) occur typically with a strike-slip or normal focal mechanism. The magnitude of these earthquakes is often lower than the earthquakes in the other two domains. However, their seismic intensities and the associated damage are often greater, due to the shallow focal depth. Examples of such earthquakes are the AD 2007 Aysén Earthquakes (M_W 6.1 and 6.2) on the Liquiñe-Ofqui Fault Zone (LOFZ) (Legrand et al., 2011) and the earthquake with the highest death toll in Chilean history (28.000 deaths), the AD 1939 Chillán Earthquake (M_W ~8.3) (Beck et al., 1998; Lomnitz, 2004).

Isla de Chiloé is part of the Chiloé fore-arc sliver. Due to the 13° obliqueness of the subduction direction, the Chiloé fore-arc sliver is pushed northward, relative to a stable South America. The eastern boundary of the Chiloé fore-arc sliver is the above mentioned Liquiñe-Ofqui Fault Zone, an active dextral strike-slip fault system, which causes shallow earthquakes with high shaking intensities (Hernandez-Moreno et al., 2016). The Peru-Chile Subduction Zone causes earthquakes on the tectonic plate interface. The rupture zones of the historical megathrust earthquakes delineate seismic segments (Lomnitz, 1970, 2004). The cause of this segmentation is not fully understood. Proposed reasons include subduction of bathymetric highs, trench sediment thickness, thickened crust through trench-parallel collision and mass redistribution through large-scale landslides on the continental slope (Bilek, 2010; Geersen et al., 2013; Melnick et al., 2009; Sparkes et al., 2010). The study area is located on the Valdivia Segment. The southern boundary of the Valdivia Segment is probably determined by the subduction of an active mid-ocean spreading ridge between the Nazca Plate and the Antarctic Plate (i.e. a tectonic plate triple junction) or by a fracture zone (Barrientos and Ward, 1990). The northern boundary is caused by the subduction of a positive relief of the Nazca Plate, the northward termination of the Chiloé fore-arc sliver and/or the buoyancy effects of the Southern Giant Slope Failure, a large-scale landslide on the Chilean continental slope at ~38.5° S. The locking state of plates at the interplate surface plays a key role in the build up and subsequent release of seismic energy. The locking state of the Concepción and Valdivia Segment were found to be heterogeneous in both along-strike and along-dip directions. During the decade preceding the 2010 Maule Earthquake that part of the megathrust was in a fully locked state, while the Valdivia Segment exhibited more creep, except for the areas of the highest amounts of co-seismic slip during the AD 1960 Great Chilean Earthquake (Moreno et al., 2011).

1.6 Thesis outline

This thesis follows the concept of a cumulative thesis. Most chapters are intended for publication or have been submitted to or published in a scientific journal.

- **Chapter 2** describes the methods used to produce the data, which are presented in this thesis. Some methods are described in more detail in the following chapters, where the methods were used extensively.
- **Chapter 3** introduces the two coastal lakes, Lake Cucao and Lake Huelde, which are subject to this thesis. The general sedimentary environment of the lakes and their surrounding and most recent sedimentary history of the two lakes are described and discussed

here, especially in regard of the inundation of the AD 1960 Chilean tsunami into both lakes.

- **Chapter 4** discusses the remarkable continuous and long sedimentary record of Lake Huelde, which shows evidence of 17 tsunami inundations into the lake in the last ~5500 yrs. Recurrence times and their variability are the central topic in this chapter, as it has important implications for tsunami hazard assessment.
- **Chapter 5** presents the long sedimentary record of Lake Cucao, which provides evidence of potentially 15 tsunami inundations in the past ~3700 yrs. Indications for a stable vertical shoreline displacement history in the last ~3700 yrs imply that Lake Cucao and Lake Huelde (due to their proximity to each other) were stable recorders of tsunami inundations for a long time.
- **Chapter 6** reviews the published efforts to move paleotsunami research from a qualitative to a quantitative science. The chapter discusses numerical forward models and inverse models as well as physical models. It explains in detail, why the numerical models could not be applied to the data presented here.
- **Chapter 7** summarizes the conclusions of the previous chapters and gives an outlook to research, which may follow this thesis. It is the logic consequence of chapter 6 and thus presents potential next steps in tsunami research and more particularly next steps for this study area.

References

Arai, K., Naruse, H., Miura, R., Kawamura, K., Hino, R., Ito, Y., Inazu, D., Yokokawa, M., Izumi, N., Murayama, M., Kasaya, T., 2013. Tsunami-generated turbidity current of the 2011 Tōhoku-Oki earthquake. Geology 41, 1195–1198.

Angermann, D., Klotz, J., Reigber, C., 1999. Space-geodetic estimation of the nazca-south america euler vector. Earth Planetary Science Letters 171, 329–334.

Atwater, B.F., 1987. Evidence for great holocene earthquakes along the outer coast of Washington State. Science 236, 942–944.

Atwater, B.F., Cisternas, M., Yulianto, E., Prendergast, A.L., Jankaew, K., Eipert, A.A., Ignatius, W., Fernando, S., Tejakusuma, I., 2013. The 1960 tsunami on beach-ridge plains near Maullín, Chile: Landward descent, renewed breaches, aggraded fans, multiple predecessors. Andean Geology 40, 393–418.

Bahlburg, H., Spiske, M., 2012. Sedimentology of tsunami inflow and backflow deposits: key differences revealed in a modern example. Sedimentology 59, 1063–1086.

Barazangi, M., Isacks, B.L., 1976. Spatial distribution of earthquakes and subduction of the Nazca plate beneath South America. Geology 4, 686–692.

Barrientos, S.E., 2007. Geology of Chile - Earthquakes in Chile, in: The Geology of Chile. The Geological Society, pp. 263–287.

Barrientos, S.E., Ward, S.N., 1990. The 1960 Chile earthquake: inversion for slip distribution from surface deformation. Geophysics Journal International 103, 589–598.

Beck, S., Barrientos, S., Kausel, E., Reyes, M., 1998. Source characteristics of historic earthquakes along the central Chile subduction zone. Journal South American Earth Sciences 11, 115–129.

Benson, B.E., Grimm, K.A., Clague, J.J., 1997. Tsunami Deposits beneath Tidal Marshes on Northwestern Vancouver Island, British Columbia. Quaternary Research 48, 192–204.

Bilek, S.L., 2010. Invited review paper: Seismicity along the South American subduction zone: Review of large earthquakes, tsunamis, and subduction zone complexity. Tectonophysics 495, 2–14.

Bondevik, S., Inge Svendsen, J., Mangerud, J., 1997a. Tsunami sedimentary facies deposited by the Storegga tsunami in shallow marine basins and coastal lakes, western Norway. Sedimentology 44, 1115–1131.

Bondevik, S., Svendsen, J.I., Johnsen, G., Mangerud, J., Kaland, P.E., 1997b. The Storegga tsunami along the Norwegian coast , its age and runup. Boreas 26, 29–53.

Brill, D., 2012. The tsunami history of southwest Thailand – Recurrence , magnitude and impact of palaeo- tsunamis inferred from onshore deposits. University of Cologne, Germany.

Brill, D., Brückner, H., Jankaew, K., Kelletat, D., Scheffers, a., Scheffers, S., 2011. Potential predecessors of the 2004 Indian Ocean Tsunami — Sedimentary evidence of extreme wave events at Ban Bang Sak, SW Thailand. Sedimentary Geology 239, 146–161.

Chagué-Goff, C., Andrew, A., Szczuciński, W., Goff, J., Nishimura, Y., 2012. Geochemical signatures up to the maximum inundation of the 2011 Tōhoku-oki tsunami — Implications for the 869 AD Jogan and other palaeotsunamis. Sedimentary Geology 282, 65–77.

Chagué-Goff, C., Goff, J., Wong, H.K.Y., Cisternas, M., 2015. Insights from geochemistry and diatoms to characterise a tsunami's deposit and maximum inundation limit. Marine Geology 359, 22–34.

Chagué-Goff, C., Schneider, J.-L., Goff, J.R., Dominey-Howes, D., Strotz, L., 2011. Expanding the proxy toolkit to help identify past events — Lessons from the 2004 Indian Ocean Tsunami and the 2009 South Pacific Tsunami. Earth-Science Reviews 107, 107–122.

Cifuentes, I.L., 1989. The 1960 Chilean Earthquakes. Journal of Geophysical Research 94, 665–680.

DeMets, C., Gordon, R.G., Argus, D.F., 2010. Geologically current plate motions. Geophysics Journal International. 181, 1–80.

Dawson, A., Long, D., Smith, D., 1988. The Storegga Slides: Evidence from eastern Scotland for a possible tsunami. Marine Geology 82, 271–276.

Dura, T., Cisternas, M., Horton, B.P., Ely, L.L., Nelson, A.R., Wesson, R.L., Pilarczyk, J.E., 2015. Coastal evidence for Holocene subduction-zone earthquakes and tsunamis in central Chile. Quaternary Science Reviews 113, 93–111.

Fritz, H.M., Borrero, J.C., 2006. Somalia Field Survey after the December 2004 Indian Ocean Tsunami. Earthquake Spectra 22, 219–233.

Fritz, H.M., Mohammed, F., Yoo, J., 2009. Lituya Bay Landslide Impact Generated Mega-Tsunami 50(th) Anniversary. Pure and Applied Geophysics 166, 153–175.

Fritz, H.M., Phillips, D.A., Okayasu, A., Shimozono, T., Liu, H., Mohammed, F., Skanavis, V., Synolakis, C.E., Takahashi, T., 2012. The 2011 Japan tsunami current velocity measurements from survivor videos at Kesennuma Bay using LiDAR. Geophysical Research Letters 39, 6.

Garrett, E., Shennan, I., Watcham, E.E.P., Woodroffe, S.S.A., 2013. Reconstructing paleoseismic deformation, 1: modern analogues from the 1960 and 2010 Chilean great earthquakes. Quaternary Science Reviews 75, 11–21.

Garrett, E., Shennan, I., Woodroffe, S.A.A., Cisternas, M., Hocking, E.P.P., Gulliver, P., 2015. Reconstructing paleoseismic deformation, 2: 1000 years of great earthquakes at Chucalén, south central Chile. Quaternary Science Reviews 113, 112–122.

Geersen, J., Völker, D., Behrmann, J.H., Kläschen, D., Weinrebe, W., Krastel, S., Reichert, C., 2013. Seismic rupture during the 1960 Great Chile and the 2010 Maule earthquakes limited by a giant Pleistocene submarine slope failure. Terra Nova 25, 472–477.

Gelfenbaum, G., Jaffe, B., 2003. Erosion and Sedimentation from the 17 July, 1998 Papua New Guinea Tsunami. Pure and Applied Geophysics Appl. Geophys. 160, 1969–1999.

Goto, K., Hashimoto, K., Sugawara, D., Yanagisawa, H., Abe, T., 2014. Spatial thickness variability of the 2011 Tōhoku-oki tsunami deposits along the coastline of Sendai Bay. Marine Geology 358, 38–48.

Goto, K., Takahashi, J., Fujino, S., 2012. Variations in the 2004 Indian Ocean tsunami deposits thickness and their preservation potential, southwestern Thailand. Earth, Planets and Space 64, 923–930.

Hernandez-Moreno, C., Speranza, F., Di Chiara, A., 2016. Paleomagnetic rotation pattern of the southern Chile fore-arc sliver (38°S–42°S): A new tool to evaluate plate locking along subduction zones. Journal of Geophysical Research: Solid Earth 121, 469–490.

Ikehara, K., Irino, T., Usami, K., Jenkins, R., Omura, A., Ashi, J., 2014. Possible submarine tsunami deposits on the outer shelf of Sendai Bay, Japan resulting from the 2011 earthquake and tsunami off the Pacific coast of Tōhoku. Marine Geology 358, 120–127.

Jankaew, K., Atwater, B.F., Sawai, Y., Choowong, M., Charoentitirat, T., Martin, M.E., Prendergast, A., 2008. Medieval forewarning of the 2004 Indian Ocean tsunami in Thailand. Nature 455, 1228–1231.

Kanamori, H., 1972. Mechanism of tsunami earthquakes. Physics of the Earth and Planetary Interiors 6, 346–359.

Kelsey, H.M., Engelhart, S.E., Pilarczyk, J.E., Horton, B.P., Rubin, C.M., Daryono, M.R., Ismail, N., Hawkes, A.D., Bernhardt, C.E., Cahill, N., 2015. Accommodation space, relative sea-level, and the archiving of paleo-earthquakes along subduction zones. Geology 43, 675–678.

Kelsey, H.M., Nelson, A.R., Hemphill-Haley, E., Witter, R.C., 2005. Tsunami history of an Oregon coastal lake reveals a 4600 yr record of great earthquakes on the Cascadia subduction zone. Geological Society of America Bulletin 117, 1009–1032.

Kempf, P., Moernaut, J., Van Daele, M., Vermassen, F., Vandoorne, W., Pino, M., Urrutía, R., Garrett, E., De Batist, M., 2015. The sedimentary record of the tsunami caused by the 1960 Great Chilean Earthquake in two coastal lakes on Chiloé Island, Chile. Sediment. Geol. 328, 73–86.

Kortekaas, S., Dawson, A., 2007. Distinguishing tsunami and storm deposits: An example from Martinhal, SW Portugal. Sedimentary Geology 200, 208–221.

Lay, T., Yue, H., Brodsky, E.E., An, C., 2014. The 1 April 2014 Iquique, Chile, Mw 8.1 earthquake rupture sequence. Geophysical Research Letters 41, 3818–3825.

Legrand, D., Barrientos, S., Bataille, K., Cembrano, J., Pavez, A., 2011. The fluid-driven tectonic swarm of Aysen Fjord, Chile (2007) associated with two earthquakes (Mw=6.1 and Mw=6.2) within the Liquiñe-Ofqui Fault Zone. Cont. Shelf Research 31, 154–161.

Lomnitz, C., 2004. Major Earthquakes of Chile: A Historical Survey, 1535-1960. Seismological Research Letters 75, 368–378.

Lomnitz, C., 1970. Major Earthquakes and Tsunamis in Chile during the period 1535 to 1955. Geologische Rundschau 59, 938–960.

Masson, D.G., Watts, A.B., Gee, M.J.R., Urgeles, R., Mitchell, N.C., Le Bas, T.P., Canals, M., 2002. Slope failures on the flanks of the western Canary Islands. Earth-Science Reviews 57, 1–35.

Matsui, T., Imamura, F., Tajika, E., Nakano, Y., Fujisawa, Y., 2002. Generation and propagation of a tsunami from the Cretaceous-Tertiary impact event. Geological Society of America Special Papers 356 , 69–77.

Minoura, K., Imamura, F., Kuran, U., Nakamura, T., Papadopoulos, G.A., Takahashi, T., Yalciner, A.C., 2000. Discovery of Minoan tsunami deposits. Geology 28, 59–62.

Minoura, K., Imamura, F., Takahashi, T., Shuto, N., 1997. Sequence of sedimentation processes caused by the 1992 Flores tsunami: Evidence from Babi Island. Geology 25, 523–526.

Melnick, D., Bookhagen, B., Strecker, M.R., Echtler, H.P., 2009. Segmentation of megathrust rupture zones from fore-arc deformation patterns over hundreds to millions of years, Arauco peninsula, Chile. Journal of Geophysical Research: Solid Earth 114.

Moreno, M., Melnick, D., Rosenau, M., Bolte, J., Klotz, J., Echtler, H., Baez, J., Bataille, K., Chen, J., Bevis, M., Hase, H., Oncken, O., 2011. Heterogeneous plate locking in the South–Central Chile subduction zone: Building up the next great earthquake. Earth Planetary Science Letters 305, 413–424.

Moreno, M., Rosenau, M., Oncken, O., 2010. 2010 Maule earthquake slip correlates with pre-seismic locking of Andean subduction zone. Nature 467, 198–202.

Morton, R.A., Gelfenbaum, G., Jaffe, B.E., 2007. Physical criteria for distinguishing sandy tsunami and storm deposits using modern examples. Sedimentary Geology 200, 184–207.

Nanayama, F., Shigeno, K., Satake, K., Shimokawa, K., Koitabashi, S., Miyasaka, S., Ishii, M., 2000. Sedimentary differences between the 1993 Hokkaido-nansei-oki tsunami and the 1959 Miyakojima typhoon at Taisei, southwestern Hokkaido, northern Japan. Sedimentary Geology 135, 255–264.

Nomanbhoy, N., Satake, K., 1995. Generation mechanism of tsunamis from the 1883 Krakatau Eruption. Geophysical Research Letters 22, 509–512.

Paris, R., Wassmer, P., Sartohadi, J., Lavigne, F., Barthomeuf, B., Desgages, E., Grancher, D., Baumert, P., Vautier, F., Brunstein, D., Gomez, C., 2009. Tsunamis as geomorphic crises: Lessons from the December 26, 2004 tsunami in Lhok Nga, West Banda Aceh (Sumatra, Indonesia). Geomorphology 104, 59–72.

Peyrat, S., Campos, J., de Chabalier, J.B., Perez, A., Bonvalot, S., Bouin, M.-P., Legrand, D., Nercessian, A., Charade, O., Patau, G., Clévédé, E., Kausel, E., Bernard, P., Vilotte, J.-P., 2006. Tarapacá intermediate-depth earthquake (Mw 7.7, 2005, northern Chile): A slab-pull event with horizontal fault plane constrained from seismologic and geodetic observations. Geophysical Research Letters 33.

Phantuwongraj, S., Choowong, M., 2011. Tsunamis versus storm deposits from Thailand. Natural Hazards 63, 31–50.

Pilarczyk, J.E., Dura, T., Horton, B.P., Engelhart, S.E., Kemp, A.C., Sawai, Y., 2014. Microfossils from coastal environments as indicators of paleo-earthquakes, tsunamis and storms. Palaeogeography Palaeoclimatology Palaeoecology 413, 144–157.

Plafker, G., Savage, J.C., 1970. Mechanism of the Chilean Earthquakes of May 21 and 22, 1960. Geological Society of America Bulletin 81, 1001–1030.

Ramírez-Herrera, M.-T., Lagos, M., Hutchinson, I., Kostoglodov, V., Machain, M.L., Caballero, M., Goguitchaichvili, A., Aguilar, B., Chagué-Goff, C., Goff, J., Ruiz-Fernández, A.-C., Ortiz, M., Nava, H., Bautista, F., Lopez, G.I., Quintana, P., 2012. Extreme wave deposits on the Pacific coast of Mexico: Tsunamis or storms? — A multi-proxy approach. Geomorphology 139–140, 360–371.

Richmond, B., Szczuciński, W., Chagué-Goff, C., Goto, K., Sugawara, D., Witter, R., Tappin, D.R., Jaffe, B., Fujino, S., Nishimura, Y., Goff, J., 2012. Erosion, deposition and landscape change on the Sendai coastal plain, Japan, resulting from the March 11, 2011 Tōhoku-oki tsunami. Sedimentary Geology 282, 27–39.

Satake, K., Atwater, B.F., 2007. Long-Term Perspectives on Giant Earthquakes and Tsunamis at Subduction Zones. Annual Review of Earth and Planetary Sciences 35, 349–374.

Sato, H., Shimamoto, T., Tsutsumi, A., Kawamoto, E., 1995. Onshore tsunami deposits caused by the 1993 Southwest Hokkaido and 1983 Japan Sea earthquakes. Pure and Applied Geophysics 144, 693–717.

Sawai, Y., Kamataki, T., Shishikura, M., Nasu, H., Okamura, Y., Satake, K., Thomson, K.H., Matsumoto, D., Fujii, Y., Komatsubara, J., Aung, T.T., 2009. Aperiodic recurrence of geologically recorded tsunamis during the past 5500 yrs in eastern Hokkaido, Japan. Journal of Geophysical Research: Solid Earth 114, B01319.

Schulte, P., Alegret, L., Arenillas, I., Arz, J.A., Barton, P.J., Bown, P.R., Bralower, T.J., Christeson, G.L., Claeys, P., Cockell, C.S., Collins, G.S., Deutsch, A., Goldin, T.J., Goto, K., Grajales-Nishimura, J.M., Grieve, R.A.F., Gulick, S.P.S., Johnson, K.R., Kiessling, W., Koeberl, C., Kring, D.A., MacLeod, K.G., Matsui, T., Melosh, J., Montanari, A., Morgan, J. V, Neal, C.R., Nichols, D.J., Norris, R.D., Pierazzo, E., Ravizza, G., Rebolledo-Vieyra, M., Reimold, W.U., Robin, E., Salge, T., Speijer, R.P., Sweet, A.R., Urrutia-Fucugauchi, J., Vajda, V., Whalen, M.T., Willumsen, P.S., 2010. The Chicxulub Asteroid Impact and Mass Extinction at the Cretaceous-Paleogene Boundary. Science 327, 1214–1218.

Shennan, I., Barlow, N., Carver, G., Davies, F., Garrett, E., Hocking, E., 2014. Great tsunamigenic earthquakes during the past 1000 yr on the Alaska megathrust. Geology 42, 687–690.

Shi, S., Dawson, A.G., Smith, D.E., 1995. Coastal sedimentation associated with the December 12th, 1992 tsunami in Flores, Indonesia. Pure and Applied Geophysics 144, 525–536.

Shinozaki, T., Goto, K., Fujino, S., Sugawara, D., Chiba, T., 2015. Erosion of a paleo-tsunami record by the 2011 Tōhoku-oki tsunami along the southern Sendai Plain. Marine Geology 369, 127–136.

Sparkes, R., Tilmann, F., Hovius, N., Hillier, J., 2010. Subducted seafloor relief stops rupture in South American great earthquakes: Implications for rupture behaviour in the 2010 Maule, Chile earthquake. Earth Planetary Science Letters 298, 89–94.

Spiske, M., Piepenbreier, J., Benavente, C., Bahlburg, H., 2013. Preservation potential of tsunami deposits on arid siliciclastic coasts. Earth-Science Reviews 126, 58–73.

Sugawara, D., Minoura, K., Imamura, F., 2008. Chapter 3 - Tsunamis and Tsunami Sedimentology, in: Minoura, T., Shiki, Y., Tsuji, T., Yamazaki, K. (Eds.), Elsevier, Amsterdam, pp. 9–49.

Switzer, A.D., Jones, B.G., 2008. Large-scale washover sedimentation in a freshwater lagoon from the southeast Australian coast: sea-level change, tsunami or exceptionally large storm? The Holocene 18, 787–803.

Tanioka, Y., Satake, K., 1996. Tsunami generation by horizontal displacement of ocean bottom. Geophysical Research Letters 23, 861–864.

Tinti, S., Armigliato, A., Manucci, A., Pagnoni, G., Zaniboni, F., Yalçiner, A.C., Altinok, Y., 2006. The generating mechanisms of the August 17, 1999 İzmit bay (Turkey) tsunami: Regional (tectonic) and local (mass instabilities) causes. Marine Geology 225, 311–330.

Wallner, J., 2008. Holozäne Landschaftsentwicklung am Lago Budi, Chile (38,9°S) - Paläolimnologisch paläoseismische Untersuchungen an Lagunensedimenten. Friedrich Schiller University of Jena, Germany.

Ward, S.N., Day, S., 2001. Cumbre Vieja Volcano—Potential collapse and tsunami at La Palma, Canary Islands. Geophysical Research Letters 28, 3397–3400.

Wright, C., Mella, A., 1963. Modifications to the soil pattern of South-Central Chile resulting from seismic and associated phenomenona during the period May to August 1960. Bulletin of the Seismological Society of America 53, 1367–1402.

Yamada, M., Fujino, S., Goto, K., 2014. Deposition of sediments of diverse sizes by the 2011 Tōhoku-oki tsunami at Miyako City, Japan. Marine Geology 358, 67–78.

"We are stuck with technology, when what we really want is just stuff that works."

AD 2002, Douglas Adams in *The Salmon of Doubt*

2 Methods

2.1 Acoustic imagery

2.1.1 High-resolution sub-bottom profiling

High-resolution sub-bottom profiles are used to image the sedimentary geometry of a basin infill in the targeted lakes. They are acquired using an acoustic source and recorder. In this thesis all sub-bottom profiles were recorded with a Geopulse Pinger, which runs on a source frequency of 3.5 kHz. In a pinger, the acoustic source is also the recorder. A piezo-element, called the transducer, is caused to vibrate by an electric pulse, which produces an acoustic signal (reverse piezo-electric effect). As soon as the acoustic signal is sent out, the same piezo-element transforms the acoustic echo into an electrical signal (piezo-electric effect).

The recorded electrical signal is the product of the acoustic pulse travelling through the water column and through the sediment, where it is reflected at interfaces with high acoustic impedance contrasts, e.g. at the lake floor surface. The recorded data file contains multiple shot points and a navigation file, which allows geo-referencing of the acquired data. The vertical resolution of sub-bottom profiles depends on the wavelength of the acoustic pulse. The Geopulse Pinger's vertical resolution is between 10 and 20 cm. The sub-bottom profiles were processed (bandpass filtering) and interpreted with the IHS Kingdom Suite v8.8 software. The unit of the y-axis on sub-bottom profiles is two-way-travel-time, which is the time it takes for the acoustic signal to propagate through water column and sediment, be reflected at an interface and propagate back to the pinger (Fig. 2.1).

In this study, the Pinger was mounted on an inflatable cata-raft, which was attached to the side (rather than towed) of RV Percilia (the research boat of Centro EULA at the Universidad de Concepción) to avoid air bubbles at the transducer. All existing profile lines from the two coastal lakes, presented in this thesis, are shown in figure 2.2.

2.1.2 Side scan sonar

Side scan sonar maps are used to get detailed spatial information about lake- or seafloor morphology and acoustic reflectivity (a function of sediment hardness and roughness). Side scan sonars send an acoustic swath to both sides and record the reflected acoustic signal. A transducer on each side of the side scan sonar is the source and recorder of the acoustic signal. In this study all side scan sonar data was acquired with a Klein System 3000, which utilises frequencies of 100 kHz and 500 kHz. At swath widths of 50 m the horizontal resolution is 8–40 cm depending on the swath angle.

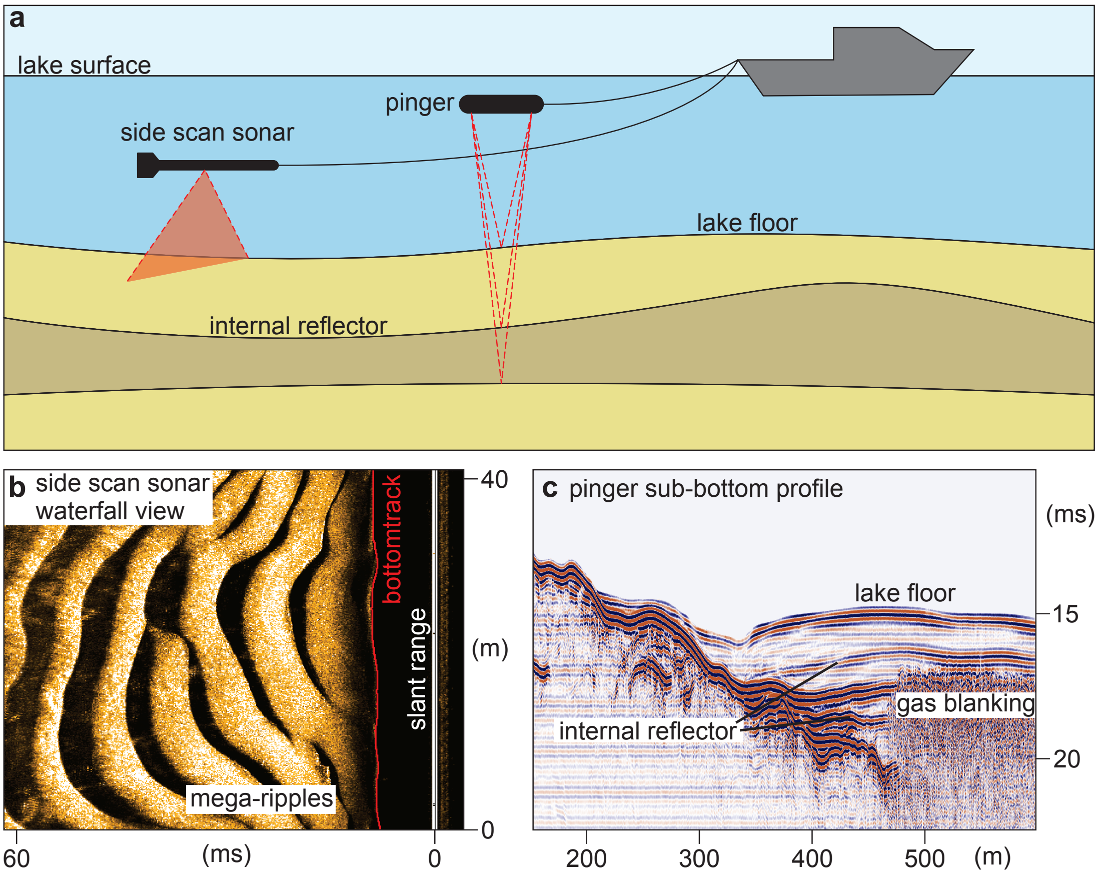

Figure 2.1: a) Schematic explanation of the principles of side scan sonars and pinger sub-bottom profilers; b) image of side scan sonar data; c) image of a sub-bottom profile.

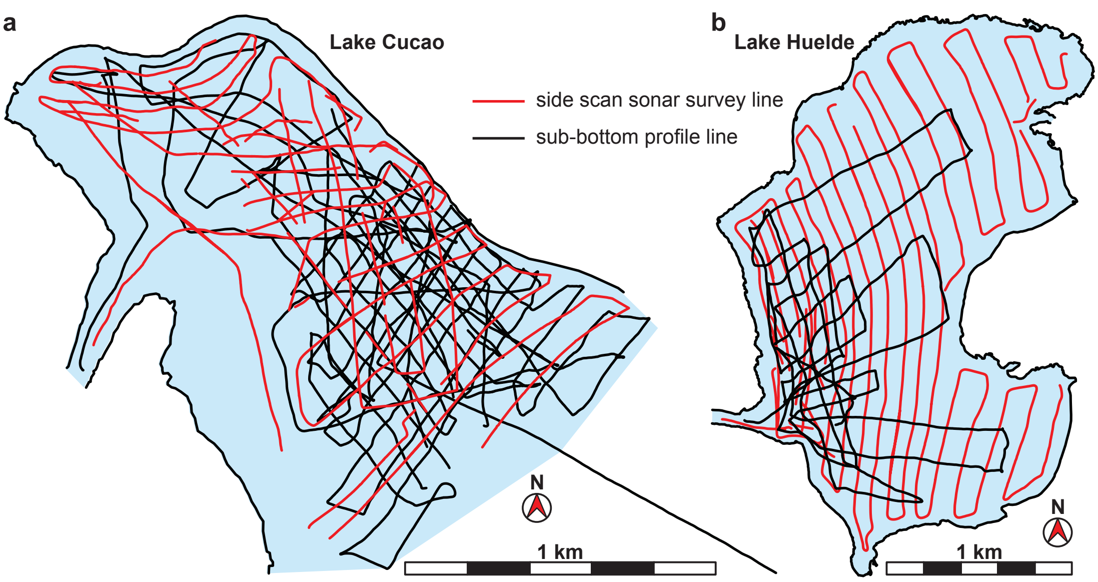

Figure 2.2: Acoustic imagery survey lines on a) Lake Cucao and b) Lake Huelde indicated in black for sub-bottom profile lines and red for side scan sonar lines.

The positioning was recorded with a Garmin GPS antenna with a ~3 m horizontal error. The raw data is arranged in a so-called waterfall view, in which acoustic reflectivity is plotted in x-direction and each shot point adds another line in y-direction (Fig. 2.1b). The data was recorded using SonarPro v9 software. The waterfall view can be transformed into a geo-referenced mosaic using the GPS information. Navigation smoothening, slant range correction, beam angle correction and mosaic selection were performed using SonarWizMap v4.

For all side scan sonar data presented in this thesis the Klein System 3000 was towed at short range from the side of RV Percilia to avoid turbulence and air bubbles produced by the motor around the transducers of the side scan sonar. The navigation lines of all side scan sonar data from Lake Cucao and Lake Huelde are displayed in figure 2.2.

2.2 Coring

Subaerial sediment samples were collected with a shovel and sampling tubes. Sediment cores from lakes are the basis of most results and provide all physical material for sediment analysis in this thesis. Coring was performed from a UWITEC platform, which provides the mobility and the equipment needed for coring on lakes. All sample sites and core sites are compiled in figure 2.3.

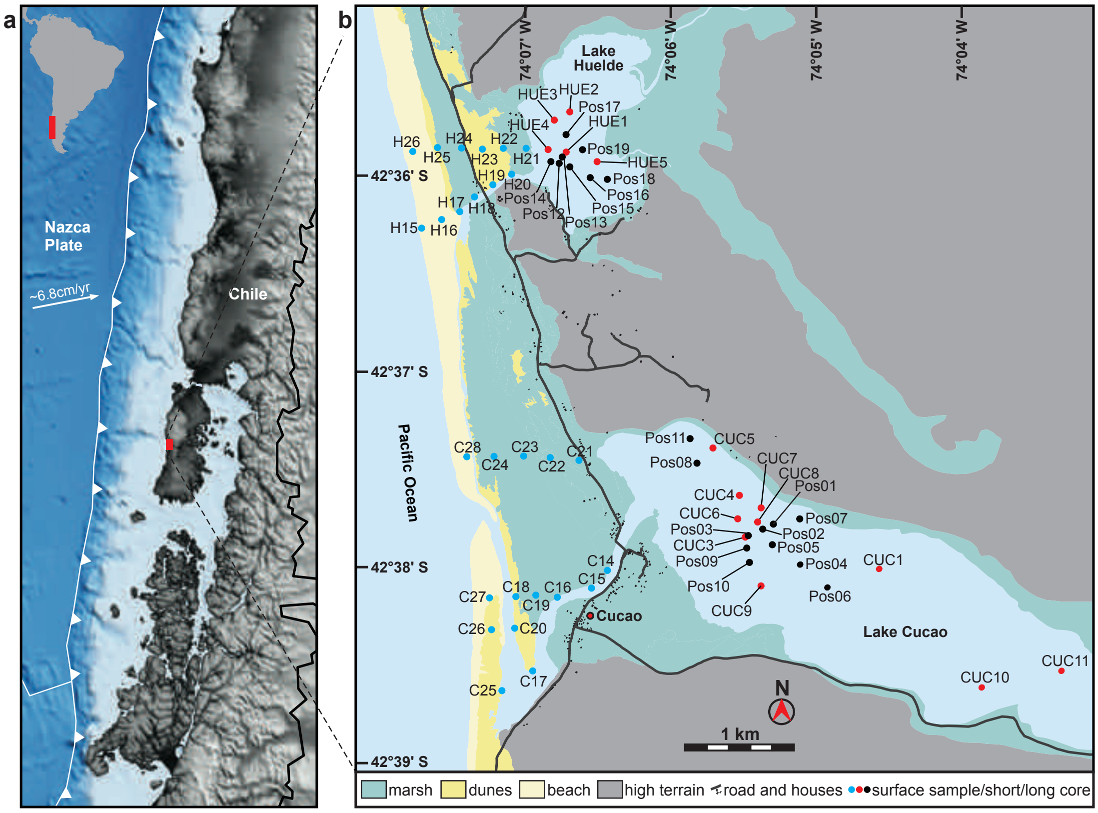

Figure 2.3: a) overview of the Pacific coast of southern South America and b) a map of all sediment samples from the study area of this thesis.

2.2.1 Gravity coring

Short gravity cores were taken with a 6.0 cm inner diameter gravity corer (Swiss corer) of Universidad Austral de Chile, Valdivia. For coring, an empty PVC liner is placed in the corer. Metal weights are added depending on how stiff the target sediment is anticipated to be and on how deep the corer needs to penetrate. The corer is then lowered on a Kevlar cable from the platform until it sinks into the sediment. When the corer is retrieved, it closes a rubber valve at the top, which provides suction in order to keep the cored sediment from falling out of the PVC liner. When the filled PVC liner is put on the platform, it is cut to the appropriate length and sealed off with caps and tape. The short gravity corer is used to retrieve undisturbed samples of the uppermost ~1 m of sediment in lakes.

2.2.2 Piston hammer coring

Piston hammer cores were taken with a UWITEC 3 m long piston corer. In piston hammer coring a piston is placed at the lower end of a 6.0 cm inner diameter PVC liner inside a hollow metal cylinder (the corer). The piston can be triggered at any given depth, after which it does not move anymore. From this moment on, the corer cylinder is hammered into the sediment, filling the PVC liner with sediment. Hammering means repeatedly raising a 40 kg lead weight and letting it fall onto the corer in order to drive the corer cylinder further into the sediment (Fig. 2.4). Piston hammer coring can disturb the sediment, which is why for each piston hammer coring location a gravity core was taken to sample the soft upper ~1 m of sediment. To reach deeper sediment the piston is triggered at a depth within the sediment. The retrieved 3 m pieces ideally overlap each other in depth by 1 m, creating a composite core. Thus, the strategy was to core from 0–3 m sub surface, from 2–5 m, from 4–7 m and so on. The longest composite cores in this thesis are ~9 m long, which is owed to the shallow water depth of the sampled lakes rather than the coring system's limitation.

2.3 Sediment analysis

All cores were shipped from Concepción, Chile, to Ghent University. Core analysis evolved during this doctorate, because the core lab facilities improved tremendously at the Renard Centre of Marine Geology (RCMG). Some of the following methods were applied to all 140 m of retrieved cores. However, analysis efforts were focused on scientifically interesting core sections. Microfossils are not discussed in this thesis. Diatoms were found within tsunami deposits, but were not analysed further. Foraminifera and dinoflagellates, which could give evidence for marine incursions, were absent in tsunami deposits.

2.3.1 Split core image acquisition

Split core images are an invaluable tool to archive the fresh split core surface before the sediment changes colour due to oxidisation. Analysis of sedimentary structures and correlation of cores can also rely strongly on high quality split core images.

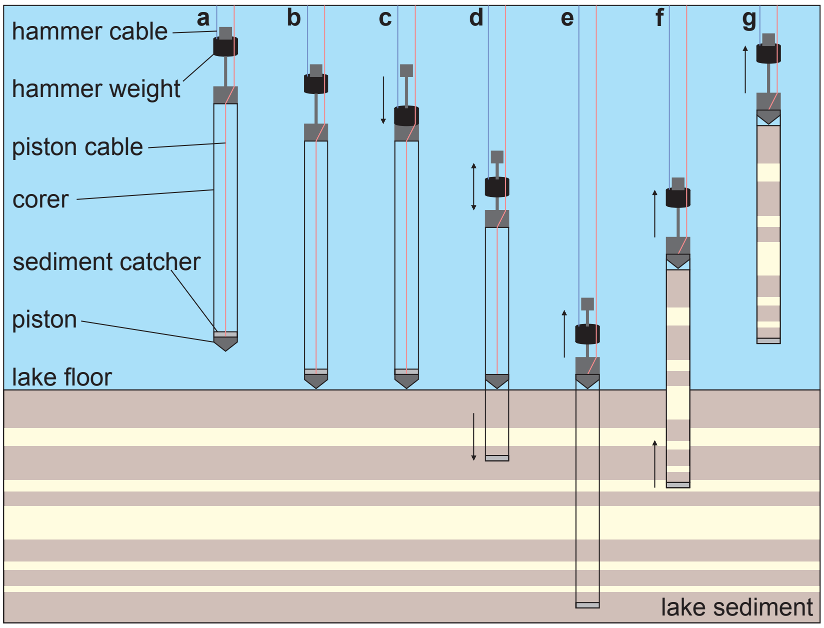

Figure 2.4: The processes during hammer piston coring; a) lowering the corer on the hammer cable, b) fixing the piston cable, which fixes the piston in place, c) lowering the hammer weight with the hammer cable, which triggers the piston, d) hammering, which means repeatedly raising the hammer weight and letting it fall onto the corer until, e) the corer is filled completely with sediment, f) raising the corer with the hammer cable, g) the sediment catcher hold the sediment in the corer, when the corer is retrieved from the lake floor.

2.3.1.1 Split core photo lab

In the beginning of this thesis, split core images were taken in a photo lab that consists of a Canon EOS 450D DSLR camera mounted above a homogenously lit black wooden box. A detailed description of this set-up can be found in Van Daele (2013). Multiple single images covering ~15 cm each were digitally stitched together to form the entire core image. For this step, Autostitch, an automatic digital image stitching tool, was used (Brown and Lowe, 2007), to ensure quick and reliable core image stitching. The resulting split core image had a resolution of 330 dpi (130 pixels cm^{-1}).

2.3.1.2 Split core line scans

Later, split core images were acquired using the Geotek Ltd. Geoscan IV Linescan Imaging system, which is operational in the RCMG lab since 2013. For image acquisition a cleaned split core is placed on a rail with a mechanical core pusher (Fig. 2.5). The Geoscan IV line scan camera is mounted above the rail and a light source of two arrays of super-bright white LEDs. The camera is equipped with three CCD sensors, one for red, green and blue each, and with a Nikon lens mount. The lens, an EX Sigma 105 mm F2.8 DG MACRO, is equipped with a polarisation filter. An additional polarisation filter is present between the light source and the split core surface. This set-up filters unwanted direct light reflection effects and makes the image's lighting more ambient.

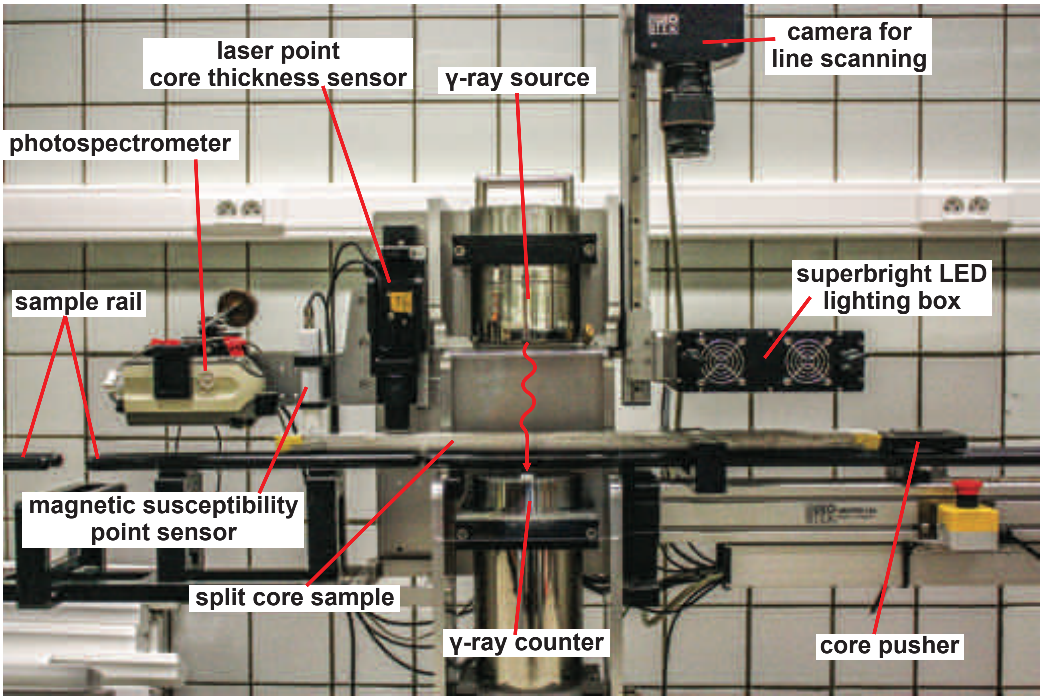

Figure 2.5: Photograph of the multisensor core logger (MSCL) with explanatory annotations.

For image acquisition, single lines of image data are collected in down-core direction, while the core pusher slowly and steadily pushes the core through the camera frame. In terms of geometry, line scan images are superior to area photographs, because line scans do not suffer from uneven lighting, spherical distortion or stitching effects.
The image resolution can be adapted separately for down-core and cross-core direction. However, both directions were kept at identical resolutions to not stretch or squash the core image. The image resolution is 510 dpi (200 pixels cm^{-1}) and the output is in 48-bit RGB TIF format. An XML-file is created together with the image with the image's metadata, e.g. the core length, used aperture etc. A digital ruler can be added after image acquisition making use of the image and the XML-file.

2.3.2 Magnetic susceptibility (MS)

Magnetic susceptibility (MS) is the response of a material to a change in the magnetic field. If the material strengthens the change in magnetic field strength, MS is positive. If the material weakens the magnetic field, MS is negative. In natural sediments MS is usually 0 or positive. In the sediments discussed in this thesis ferrimagnetic iron oxides (hematite and magnetite) are responsible for most of the MS responses.
MS measurements rely on the same rail and core pusher system of the Geotek Ltd. Multi Sensor Core Logger (MSCL) as the line scan (as well as the γ-ray attenuation density, see chapter 2.4.3). In contrast to line scanning, the core pusher pushes the core in incremental steps, instead of continuous slow pushing (Fig. 2.5).

MS is measured directly on the split core surface with a Bartington point sensor (MS2E). The window of sensitivity of the MS probe is 3.8 mm in down-core direction and 10.5 mm in cross-core direction. The depth of response is ~50 % of the signal from 1 mm and ~10 % at 3.5 mm. MS was measured in 2 mm increments in down-core direction.

2.3.3 γ-ray attenuation density

The γ-ray attenuation densometer is also mounted on the rail and core pusher system of the MSCL and is used to estimate the density of core material non-destructively. A radioactive ^{137}Cs source in a thick lead mantle emits a 0.5 cm beam of γ-radiation at 0.662 MeV through the core. At that energy level of γ-radiation, the primary γ-ray absorption mechanism is through Compton scattering, which causes a partial energy loss of the photons (increase in wavelength), when they hit an electron. On the other side of the core a γ-radiation sensor records the amount of unchanged photons, i.e. at 0.662 MeV, travelling through the core (Fig. 2.5).
Essentially the number of electrons between the γ-radiation source and sensor determines each measurement's outcome. In order to estimate density the core thickness is measured alongside the γ-ray attenuation. Electron density is closely related to volumetric density. With the help of a calibration piece, with steps of known thickness and density, the γ-ray attenuation measurements and the core thickness are used to estimate the γ-attenuation density for each measurement (every 2 mm).

2.3.4 Laser granulometry

Grain size measurements were performed using the Malvern Mastersizer 2000 laser granulometer of the Marine Biology group of Ghent University and later the Malvern Mastersizer 3000 of the RCMG. The Malvern Mastersizer measures grain sizes from 0.02 μm to 2 mm. Laser granulometry relies on the principle of laser diffraction; grain size distributions are measured by determining the angular variation in intensity of light scattered as a laser beam passes through a dispersed sediment sample. To cover the range from 0.02 μm to 2 mm two different wavelengths, blue and red, are used. The result is expressed as a volume equivalent sphere diameter. Grain size distribution parameters were calculated according to Folk and Ward (1957) using the GRADISTAT macro (Blott and Pye, 2001) for Microsoft Excel.

2.3.5 Loss on ignition (LOI)

To estimate the organic content, sediment is slowly combusted in a muffle oven. This technique is called loss on ignition (LOI). The weight difference before and after the combustion gives the weight percentage (wt%) of organic content of the total weight before combustion. To deprive the sample of water the samples were freeze-dried. The weight difference after the freeze-drying process determined the weight percentage of the water content in the sediment. The dry samples were placed in a muffle oven for 4 hours at 550 °C, which slowly combusts organic carbon. This temperature is optimised for slow and complete combustion of organic carbon, which is the value of interest in this thesis. Increasing the temperature to 950 °C for another 2 hours would combust carbonate, which would further determine the carbonate content. However, the latter step was not required and also not performed. A detailed description of the method can be found in Heiri et al. (2001). The results are treated as first order estimates, because effects of evaporation of interstitial water in clay and mica minerals and oxidization of mineralogenic sulfur may cause overestimation of the organic content.

2.3.6 Medical CT-scanning

Medical X-ray computerized tomography (CT) scanning is used for external and internal structure analysis in three-dimensional (3D) space (Kak and Slaney, 1988). To create a volume, the cores were placed on the stretcher of a Siemens Somatom Definition Flash medical X-ray CT-scanner of the Ghent University Hospital (UZ Gent). The CT scanner was operated at 100 kV with an effective 100 mAs and a 0.55 pitch. The core is pushed slowly through the scanner, while X-ray source and sensor rotate around the core. The produced helical scan is reconstructed into a DICOM image stack at ~0.15 mm $\times$ ~0.15 mm $\times$ 0.60 mm voxel size. Each DICOM image stack was imported into the VG Studio v2.1 software package, which allows colour scale adjustments and the creation of digital cross-sections through the volume for analysis (Fig. 2.6).

2.3.7 μCT-scanning

A few μCT scans were performed on cores with a μCT-scanner developed at the Ghent University Centre for X-ray Tomography (UGCT) called HECTOR. In contrast to the medical CT scanner described above, the sample rotates during the analysis, while the X-ray source and detector are stationary. The relative position of the sample between the source and the detector then determines the magnification. HECTOR produces a volume of 2000 $\times$ 2000 $\times$ ~1700 voxels and is capable to squeeze these voxels into a volume of about 8 mm^3, with 1 voxel representing 1 μm^3. These high resolutions are not necessary for this thesis. The chosen volume was ~125 cm^3 (i.e. 5 $\times$ 5 $\times$ 5 cm), for which the voxel size is ~1000 μm^3 (i.e. 10 μm $\times$ 10 μm $\times$ 10 μm). The scanner was operated at 130 kV accelerating voltage with a target power of 15 W. Each image was illuminated for 1 s. More details about the μCT-scanner can be found in Masschaele et al. (2013) (Fig. 2.6).

2.3.8 Radionuclide dating

Two methods were used for radionuclide dating. The first method is to locate a peak of ^{137}Cs (half life ~30 yrs) concentration in the sediment, because this corresponds to AD 1965 in southern South America (Quintana, 2011). The peak originates from nuclear bomb testing, beginning in AD 1945 and peaking in the 1960s.

The second method is to measure the concentration of ^{210}Pb (half life ~22.3 yrs) in sediments and comparing it to the abundance of its parent isotope ^{226}Ra. The part of ^{210}Pb content that is unaccounted for by the ^{226}Ra concentration is called the excess ^{210}Pb (or $^{210}Pb_{xs}$) and is the basis of a resulting age estimate.

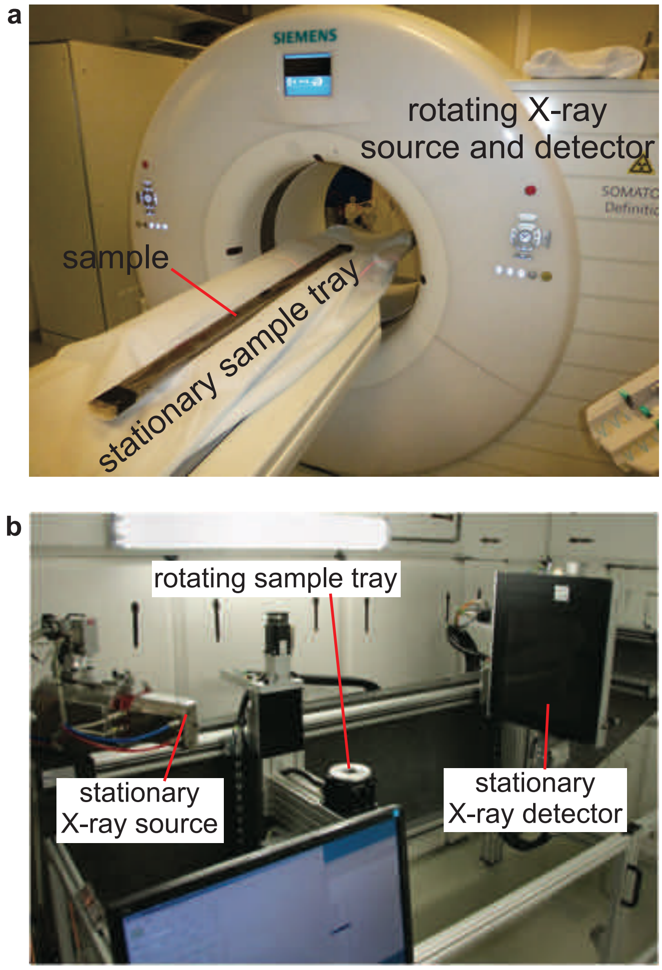

Figure 2.6: There are two principally different CT-scanners; a) medical CT-scanners have a stationary sample tray (the stretcher for the patients), while the X-ray source and detector rotate around the sample (patient); b) HECTOR, a μCT-scanner designed and operated at the Ghent University Centre for X-ray Tomography (UGCT), has a stationary X-ray source and detector, while the sample rotates.

The ^{137}Cs-, ^{210}Pb-, and ^{226}Ra-activities were γ-counted with a low-background, high-efficiency well-type germanium detector (Ge volume of 260 cm^3, low-noise Al and Cu components) equipped with a Cryo-Cycle (CANBERRA) at the University of Bordeaux.

2.3.9 Radiocarbon dating

Radiocarbon dating is a widely used method and for many researchers a field of investigation in itself. I will only scratch the surface with this explanation and direct the reader to the textbooks by Bowman (1990) and Walker (2005) for further information and to the review article by Hua (2009) for an update on recent developments in this method.
The basic principle of radiocarbon dating is the decay of an atomic species (^{14}C) into another (^{14}N) over time. Living plants are in radiocarbon equilibrium with the atmosphere. Once the plant dies, the radiocarbon clock starts ticking, because the carbon exchange is interrupted and

the radiocarbon decays without the constant flux of radiocarbon from the atmosphere. The half-life of radiocarbon is 5730 yrs. When a radiocarbon sample is measured, it is the relative amount of radiocarbon to stable carbon isotopes (^{13}C and ^{12}C) that allows determining the age of the sample.

The level of radiocarbon in the atmosphere changed over time. For example, the method cannot be used in the classic way for samples younger than AD 1950, because nuclear bomb testing changed the atmospheric carbon composition. Earlier man-made changes in radiocarbon concentration in the atmosphere make most samples from the industrialisation ambiguous. However, natural variations occurred as well, which is why radiocarbon measurements need to be calibrated with so-called calibration curves. All radiocarbon dates presented in this thesis were calibrated with the SHCal13 atmospheric southern hemisphere calibration curve (Hogg et al., 2013). The lab result of a radiocarbon date is typically given with the mean in radiocarbon ages and a single standard deviation interval with a normally distributed uncertainty. The result of a calibration is presented as a probability density function (PDF) of the calibrated radiocarbon date and reported in calibrated years before present (cal. yrs BP), where "present" is defined to AD 1950.

2.3.10 Age-depth modelling

Age-depth modelling describes the attempt to assign age information to the entire core, even though direct age information is only available for a few points in depth. There are two different model types. The simpler, classical models use the radiocarbon dates to calibrate direct age information and calculate regressions through the discrete age-depth points. The more complex models use the radiocarbon dates to calibrate direct age information and combine it with additional information to compute an age-depth model using Bayesian statistics.

2.3.10.1 Clam

Clam v2.2 is the latest version of a classical age-depth model algorithm (Blaauw, 2010), which only uses age and depth information as priors and determines the posterior probabilities in a purely algebraic way. The algorithm is based in an R environment, an open source statistical software package. Apart from the age and depth information, model type (linear interpolation, polynomial regression, spline, cubic spline, smooth spline or locally weighted spline) can be chosen, along with the correct calibration curve for the region and type of the radiocarbon sample. With a "slump" function quasi-instantaneously deposited depth intervals, e.g. tsunami deposits, can be removed from the age-depth model, allowing for an easy way to treat the abrupt changes in accumulation rate correctly. The result is an age-depth model that expresses the likelihood of age at any given depth according to the data and defined model parameters. If there are radiocarbon dates outside of the range of possibility after the first model runs, then these dates can be taken out of consideration prior to the next run. Clam is a powerful tool for quick application and easy to understand results.

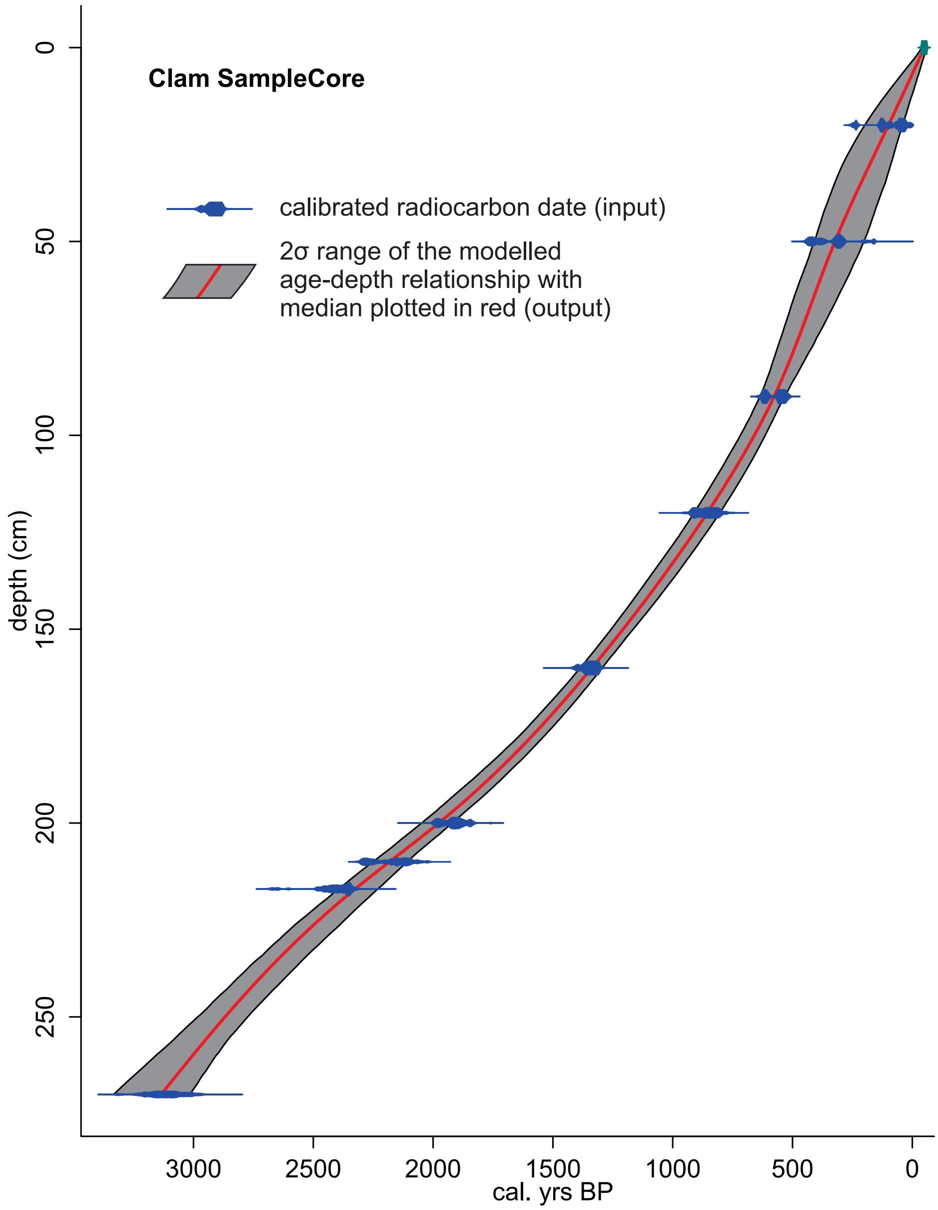

Figure 2.7: Example age-depth model of a made up sample core with the age-depth algorithm Clam.

2.3.10.2 Bacon

Bacon v2.2 is a complex age-depth model algorithm. Like Clam, it runs in an R-environment, however, Bacon does not determine the posterior age-depth model using purely algebraic functions. Instead, Bayesian statistics and an auto-regressive Markov-chain Monte Carlo (MCMC) algorithm are used to produce the age-depth model (Blaauw and Christen, 2011). The input to this Bayesian model are the radiocarbon dates, which are calibrated the same way as in Clam. Additionally, the prior accumulation rate needs to be defined in form of a γ-distribution. The model will adapt this distribution with every MCMC step, however, how much the model can change the accumulation rate from step to step can be defined, too.

The model makes use of all these priors and reports how well the posteriors match with the prior after the model run. If the difference between the priors and the posteriors are large, then the priors should be adjusted and the model should be run again. The extremely flexible R-environment allows diverse visualisation and further statistical analysis of the results (Fig. 2.8).

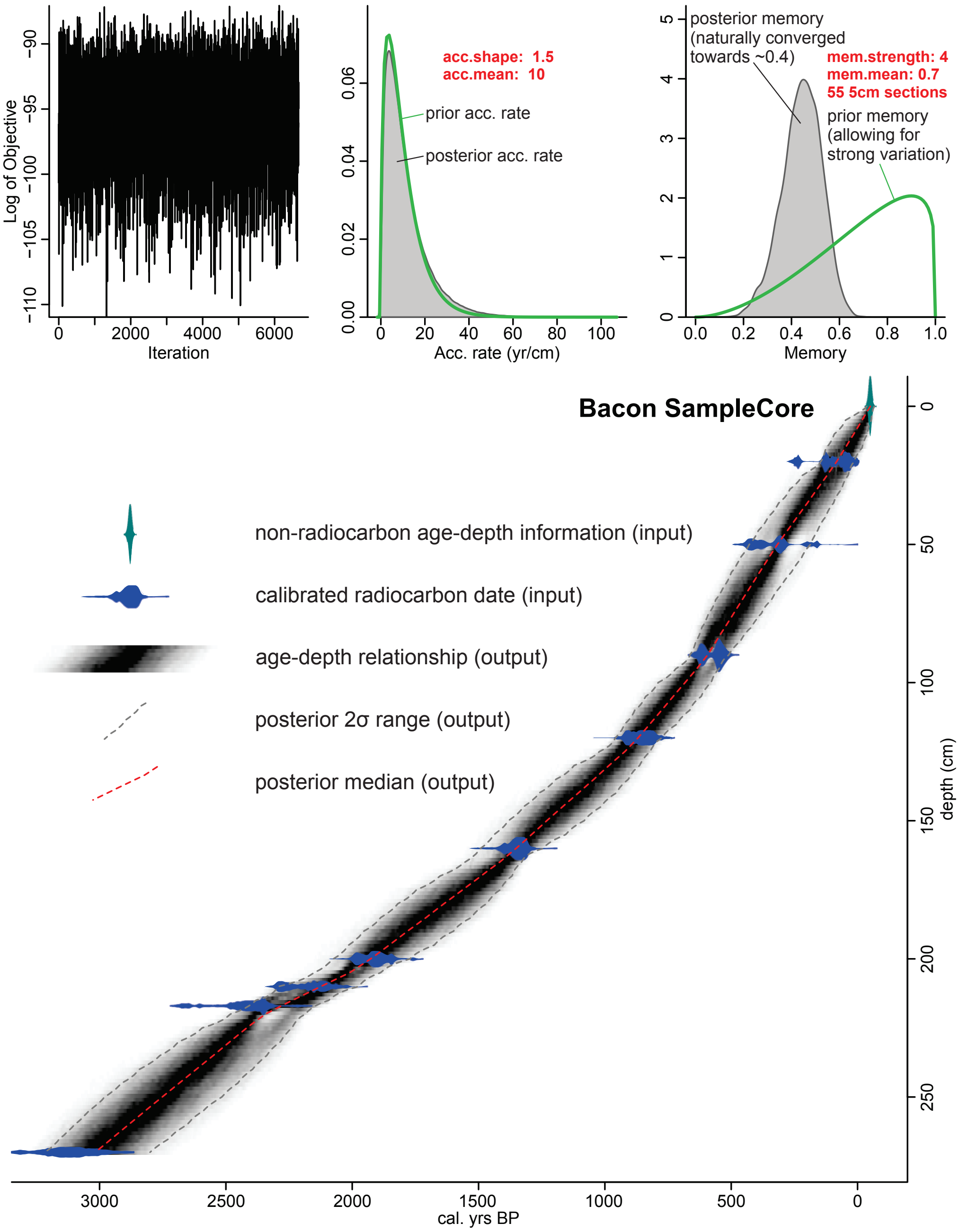

Figure 2.8: Example age-depth model of a made up sample core with the age-depth algorithm Bacon.

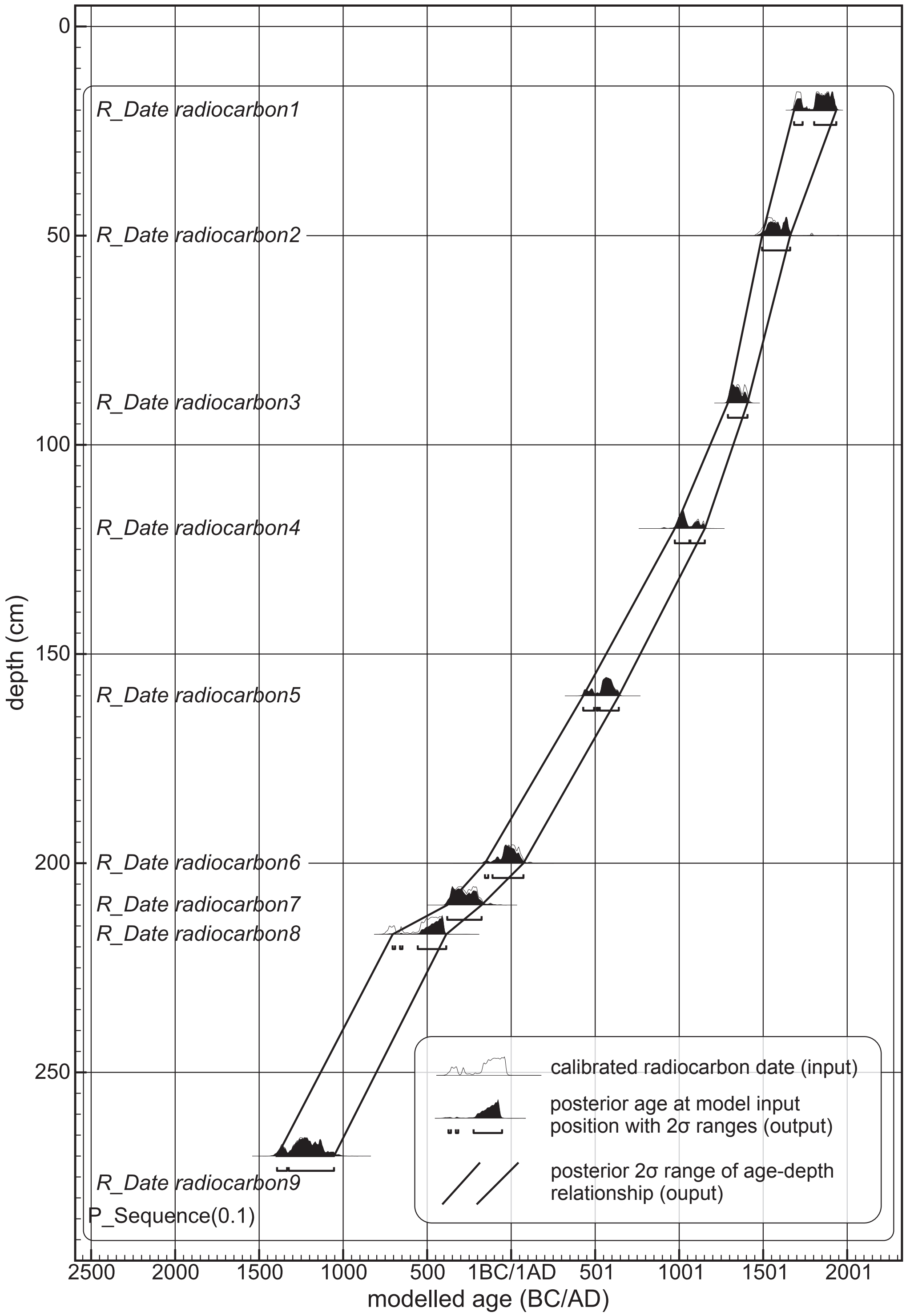

Figure 2.9: Example age-depth model of a made up sample core with the age-depth algorithm OxCal's P_Sequence.

2.3.10.3 OxCal

OxCal v4.2 is run on a server of the Oxford Radiocarbon Accelerator Unit (Bronk Ramsey, 1995, 2009). It offers a variety of age-models. The one used in this thesis is the P_Sequence (Bronk Ramsey, 2008), which is the closest relative in the OxCal algorithm family to the age-depth model of Bacon. It also uses the age and depth information as priors, as well as a parameter for accumulation rate flexibility called the k-value. For age-depth modelling OxCal makes use of Bayesian statistics and MCMC iterations to give posterior age-depth probabilities. Unlike Clam and Bacon, the prior age-depth information and the tuning of the model need to be done in the same dialog box. The post run visualisation and export options in OxCal allow diverse analyses of the model's results (Fig. 2.9).

References

Blaauw, M., 2010. Methods and code for "classical" age-modelling of radiocarbon sequences. Quaternary Geochronology 5, 512–518.

Blaauw, M., Christen, J.A., 2011. Flexible Paleoclimate Age-Depth Models Using an Autoregressive Gamma Process. Bayesian Analysis 6, 457–474.

Blott, S.J., Pye, K., 2001. GRADISTAT: a grain size distribution and statistics package for the analysis of unconsolidated sediments. Earth Surface Processes and Landforms 26, 1237–1248.

Bowman, S., 1990. Interpreting the past: radiocarbon dating. British Museum Publications, London.

Bronk Ramsey, C., 1995. Radiocarbon calibration and analysis of stratigraphy: The OxCal program. Radiocarbon, 37, 425-430.

Bronk Ramsey, C., 2008. Deposition models for chronological records. Quaternary Science Reviews 27, 42–60.

Bronk Ramsey, C., 2009. Bayesian Analysis of Radiocarbon Dates. Radiocarbon, 51, 337-360.

Brown, M., Lowe, D., 2007. Automatic Panoramic Image Stitching using Invariant Features. International Journal of Computer Vision 74, 59–73.

Folk, R.L., Ward, W.C., 1957. Brazos river bar: a study in the significance of grain size parameters. Journal of Sedimentary Petrology 27, 3–26.

Heiri, O., Lotter, A.F., Lemcke, G., 2001. Loss on ignition as a method for estimating organic and carbonate content in sediments : reproducibility and comparability of results. Journal of Paleolimnology 25, 101–110.

Hogg, A.G., Hua, Q., Blackwell, P.G., Niu, M., Buck, C.E., Guilderson, T.P., Heaton, T.J., Palmer, J.G., Reimer, P.J., Reimer, R.W., Turney, C.S.M., Zimmerman, S.R.H.,

2013. SHCal13 Southern Hemisphere Calibration, 0–50,000 Years cal BP. Radiocarbon 55, 1889–1903.

Hua, Q., 2009. Radiocarbon: A chronological tool for the recent past. Quat. Geochronol. 4, 378–390.

Kak, A.C., Slaney, M., 1988. Principles of computerized tomography imaging. IEEE press, New York.

Masschaele, B., Dierick, M., Van Loo, D., Boone, M., Brabant, L., Pauwels, E., Cnudde, V., Van Hoorebeke, L., 2013. Hector: a 240kV micro-CT setup optimized for research, in: Journal of Physics Conference Series. Bristol, UK, p. 4.

Quintana, E., 2011. Environmental impact in Argentina of the nuclear tests, Comprehensive nuclear test-ban treaty, science and technology. Nuclear Regulatory Authority (ARN), Argentina.

Van Daele, M., 2013. Recent history of natural hazards in Chile: imprints of earthquakes and volcanic events in lacustrine and marine sediments. Ghent University, Belgium.

Walker, M., 2005. Quaternary Dating Methods. Wiley.

“Substitute ’damn’ every time you’re inclined to write ’very’;
your editor will delete it and the writing will be just as it should be.”

AD 1935 William Allen White, newspaper editor

3 The AD 1960 tsunami deposit

Modified version published in Sedimentary Geology as:

Kempf, P., Moernaut, J., Van Daele, M., Vermassen, F., Vandoorne, W., Pino, M., Urrutia, R., Schmidt, S., Garrett, E., De Batist, M., 2015. The sedimentary record of the 1960 tsunami in two coastal lakes on Isla de Chiloé, south central Chile. Sedimentary Geology 328, p.73–86.

Abstract: This study describes sediments deposited by the tsunami following the 1960 Great Chilean Earthquake (M_W 9.5) in two coastal lakes, Lakes Cucao and Huelde, on the west coast of Isla de Chiloé, south central Chile (42.6° S). Sub-bottom profiles and side scan sonar mosaics illustrate the sedimentary context of transects of gravity cores. The stratigraphy of both lakes features gyttja sedimentation, interrupted by the abrupt emplacement of a sandy layer with mud rip-up clasts and a mud cap. This sandy layer reflects a sudden change in sedimentary environment, most probably caused by a high-energy inundation. Radionuclide analyses (^{137}Cs and ^{210}Pb) date the inundation deposit to shortly before the mid 1960s. The only known event that matches the sedimentological and chronological criteria is the AD 1960 tsunami. Using grain size analysis and comparisons with samples from modern environments, we demonstrate that the proximal (seaward) part of the deposit consists of a mixture of sand derived from subaerial sources and reworked gyttja lake sediment. In the distal (landward) part of Lake Cucao, the sand component is lost and the deposit consists entirely of remobilised lake sediments. The repetition of tsunami deposit sequences in Lake Huelde suggests a minimum of three inundating waves. Sub-bottom profiles and side scan sonar mosaics reveal tsunami inundation over the barrier and more prominently through the outlet river channel. The dominant role of the river channel as a pathway for sediment transport is also described in core samples by tsunami deposits that fine away from the channel mouth. The identification and description of the deposit left by a known tsunami provide important insights into tsunami sedimentation in coastal lakes and have the potential to help in the search for paleotsunami evidence.

Contributions: The manuscript was written by PK. Fieldwork was conducted by PK, JM, MVD and WV, and facilitated by MP and RU. Discussion of results and interpretation were done by PK, JM, MVD, EG and MDB. FV helped PK to process the side scan sonar data. SS conducted the radionuclide analysis. All other analyses were done by PK.

3.1 Introduction

Investigations into the sedimentary records of tsunamis predominantly focus on subaerial coastal settings, including lowlands, marshes, and swales (e.g., Cisternas et al., 2005; Brill et al., 2011; Bahlburg and Spiske, 2012; Szczuciński et al., 2012a, 2012b; Goto et al., 2014). Particularly along generally subsiding coastlines, these locations have the potential to preserve evidence of multiple tsunamis over hundreds or thousands of years (e.g., Atwater, 1992; Cisternas et al., 2005; Nanayama et al., 2007; Spiske et al., 2013).

Tsunami deposits on coastal lowlands have been the subject of extensive studies and many of their characteristics are well described. They typically consist of coarse-grained sheets extending hundreds of metres to a few kilometres inland (e.g., Dawson et al., 1995; Goto et al., 2014) with similar quasi-simultaneous deposition along vast areas of coast potentially exceeding 100 km (e.g., Goff et al., 2010). Deposits may reach a few tens of centimetres in thickness and often thin in a landward direction (e.g., Goto et al., 2014). Proximal onshore tsunami deposits may consist of grain sizes from mud to boulders (e.g., Dawson et al., 1988; Paris et al., 2009; Chagué-Goff et al., 2012a; Szczuciński et al., 2012a), depending on available source material, and may include rip-up clasts reflecting erosion of underlying sediments (e.g., Goff et al., 2009; Atwater et al., 2013). Tsunami deposits often have an erosional lower contact (e.g., Atwater, 1987; Minoura et al., 1997). Sand and mud particles are principally transported in suspension. Their gravitational settling often results in single or multiple upward fining sequences (Gelfenbaum and Jaffe, 2003). Tsunami backwash is often more channelised than tsunami run-up; seaward-extending scours commonly form behind boulders in the thalweg; relatively little erosion and reworking of the tsunami run-up deposit may occur outside the thalweg during backwash (Yamada et al., 2014).

In contrast to tsunami deposits on coastal lowlands, tsunami deposits in coastal lakes are studied less often, although these settings have two principal advantages: 1) coastal lakes often have excess accommodation space and a higher preservation potential; and 2) continuous sedimentation with relatively stable accumulation rates between tsunami inundations may enable the development of high-resolution age models. However, suitable coastal lakes are rare as the width, height, and geomorphology of the barrier separating the lake from the ocean must be such that only infrequent extreme wave events reach the lake. For example, during a relative sea-level fall, the barrier will become wider and the lake level will become higher, possibly resulting in a coastal lake, which is no longer reached by large wave events. Nevertheless, coastal lakes and lagoons have provided insights into the sedimentary processes associated with tsunami occurrence in several regions, e.g., Norway (Bondevik et al., 1997), Sri Lanka (Jackson et al., 2014), Japan (Minoura et al., 1994; Sawai et al., 2008), and Cascadia (Hutchinson et al., 1997; Kelsey et al., 2005; Witter et al., 2012).

Tsunami deposits in coastal lakes reflect turbulent, high-energy transport and deposition in an otherwise low-energy steady state sedimentary environment (e.g., Kelsey et al., 2005; Sugawara et al., 2008). They are composed of surrounding shallow marine, terrestrial, and lacustrine sediments, e.g., dune sand and organic-rich lacustrine mud. Deposits may contain mud rip-up clasts comprising eroded lake sediments, including peat, gyttja, and silt (e.g., Bondevik et al., 1997). Resuspended lake sediments are trapped within the lake basin and settle slowly to form a mud cap after the coarser fraction is deposited (Minoura et al., 1994).

This paper is the first to describe the deposit left by the AD 1960 tsunami in coastal lakes in Chile. Using a combination of side scan sonar, sub-bottom reflection seismic profiles, and sediment cores, we reconstruct the inundation of two lakes near the village of Cucao on Isla de Chiloé, south central Chile (Fig. 3.1) and characterise the resulting tsunami deposit. This study aims to 1) describe the setting of the lakes and put sediment cores into their sedimentary context using geophysical tools; 2) identify the sedimentary characteristics of the tsunami deposit; and 3) assess the contributions of subaerial and lacustrine sediment sources to the tsunami deposit.

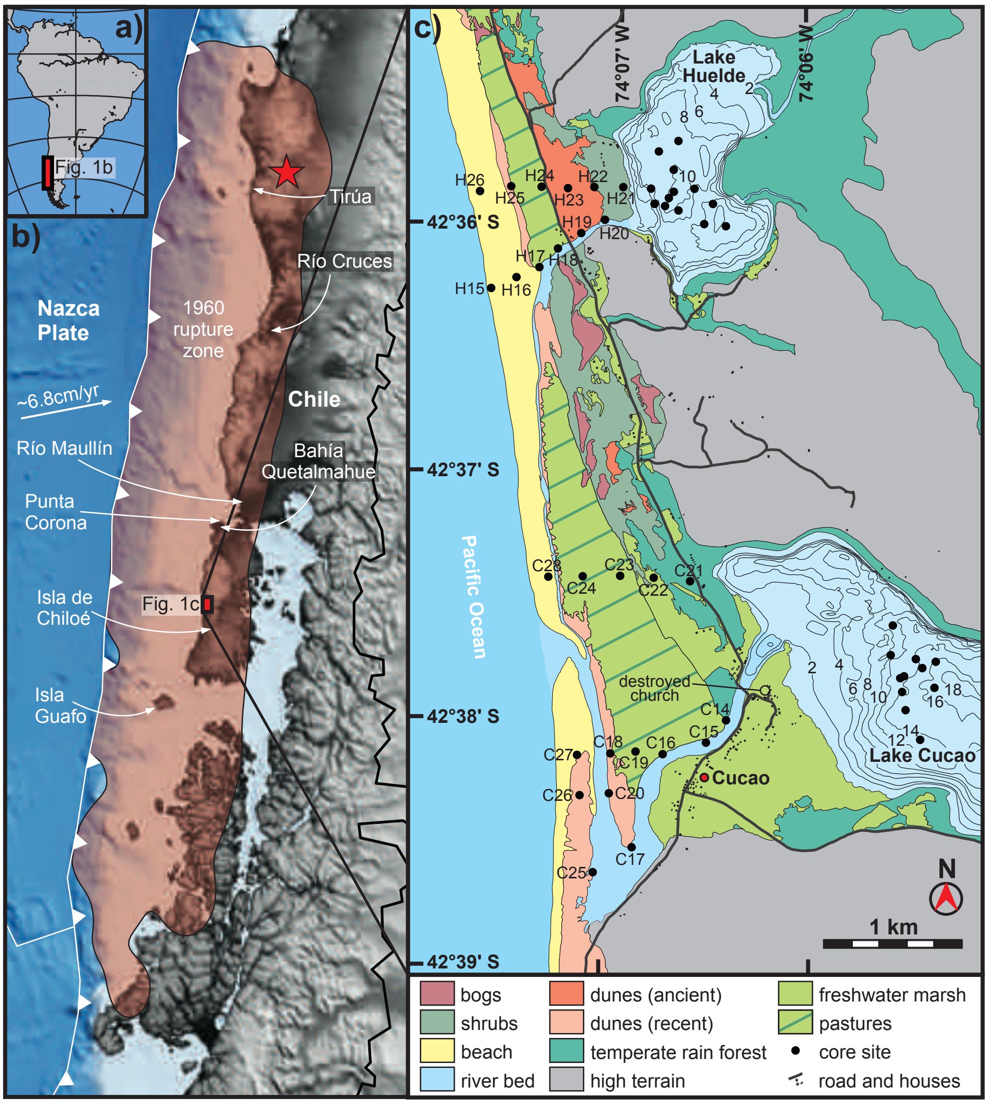

Figure 3.1: a) Overview map of South America; b) the topographic and bathymetric maps of south central Chile are based on ETOPO data (Amante and Eakins, 2009) with the AD 1960 epicentre (star) and rupture zone after Moreno et al. (2009); c) geomorphological units are based on field observations and extended using satellite imagery (Google Earth). The lake bathymetric maps are based on the bottom track of side scan sonar data.

3.2 The AD 1960 earthquake and tsunami

On the 22nd of May 1960, the entire 1000 km long Valdivia segment of the Chilean subduction zone ruptured in the main event of the (M_W 9.5) AD 1960 Great Chilean Earthquake (Cifuentes, 1989). This megathrust earthquake, with its rupture zone mostly offshore (Barrientos and Ward, 1990; Moreno et al., 2009) (Fig. 3.1), generated a tsunami with a maximum reported near-field wave height between 15 and 20 m (Sievers et al., 1963). Damage to coastal infrastructure and

loss of life occurred not only in Chile (Sievers et al., 1963) but also in far-field regions across the Pacific, including Hawaii (Lander and Lockridge, 1989), New Zealand (Chagué-Goff et al., 2000), French Polynesia (Vitousek, 1963), and Japan (Nanayama et al., 2007).
Isla de Chiloé lies in the central part of the 1960 rupture zone (Fig. 3.1). The two closest eyewitness reports of the tsunami are from lighthouses. The chief of the Punta Corona lighthouse, about 90 km north of Cucao, reported a 15–20 m high wave. Officers of the Punta Weather lighthouse on Isla Guafo, about 120 km south of Cucao, measured run-up of 10 m (Sievers et al., 1963). No eyewitness reports were obtained from close to our study locations (Fig. 3.1). Nevertheless, a later sociological study about life in the village of Cucao describes the 1960 tsunami as having damaged 12 and completely destroyed 27 of the 52 buildings that formed the village at the time, including the church, which was located only tens of metres away from the shoreline of Lake Cucao (Weisner, 2003) (Fig. 3.1). An extensive survey, 8 years after the earthquake, reported that co-seismic subsidence in Cucao was about 1 m (Plafker and Savage, 1970).
At least 13 lakes in south central Chile recorded the intense shaking that accompanied the AD 1960 earthquake through a variety of seismically triggered event deposits (Van Daele et al., 2015). Deposits of the tsunami and evidence for co-seismic subsidence are described in coastal lowlands located to the north of our study area, i.e., at Bahía Quetalmahue (41.85°S) on Isla de Chiloé (Garrett et al., 2015), in the Río Maullín estuary (41.60°S) (Cisternas et al., 2005; Atwater et al., 2013), in Río Cruces (39.77°S) (Reinhardt et al., 2010), and at Tirúa (38.34°S) (Garrett et al., 2013; Ely et al., 2014; Nentwig et al., 2015) (Fig. 3.1).

3.3 Geomorphic setting

This study focuses on two lakes on the west coast of Isla de Chiloé: Lake Cucao (074.09° W, 42.63° S) and Lake Huelde (074.11° W, 42.60° S) (Fig. 3.1). Lake Cucao is separated from the ocean by a 1.3 km wide and 5–6 m high barrier; the maximum lake water depth is 21 m. The lake surface is at sea-level and a river channel through the barrier allows exchange of water with the ocean. The marine water inflow during high tide is enough to cause a stable saline bottom-water body throughout the year, despite strong winds and shallow water depth (Villalobos et al., 2003).
A barrier 1.1 km wide and 5–6 m high separates Lake Huelde from the ocean. The lake surface lies at an altitude of ~1 m and the maximum water depth is 11 m. A small stream discharges water to the ocean; the lake is situated above the intertidal zone and there is no interchange of saline water at present.
The bedrock in the area consists of metamorphic rocks of Paleozoic and Triassic age, mostly metapelites, metacherts, and metabasites. This metamorphic basement is covered by sandur sediments from the last glacial period (35–14.1 ka) and its predecessors (SERNAGEOMIN, 2003; Glasser et al., 2008). The geomorphological and landscape units between the ocean and the lakes are beaches, recent and ancient dunes, bogs, riverbeds, freshwater marshes, pastures (protected from wind erosion by man-made 3–5 m high sand ridges), dense shrubs, and temperate rain forest (Fig. 3.1). Forest covers more than 70 % of the catchments of both lakes. The catchment-area-to-lake-area ratios of Lake Cucao and Lake Huelde are 3.1 (Villalobos et al., 2003) and ~75, respectively.

3.4 Methods

3.4.1 Acoustic imaging

In order to get detailed spatial information about the lake floor morphology and acoustic reflectivity (a function of sediment hardness and roughness), we collected side scan sonar data in Lake Huelde and in the western part of Lake Cucao. The data were obtained with a Klein3000 side scan sonar, which utilises frequencies of 100 and 500 kHz and produces a 50 m wide swath. The resulting horizontal resolution is 8–40 cm depending on the beam angle. Positioning was recorded with a Garmin GPS antenna with a 3 m horizontal error. Navigation smoothening, slant range correction, and mosaic selection were performed using SonarWizMap v. 4.We also extracted the bottom track of the side scan sonar data to create bathymetric maps for the lakes using a sound velocity of 1480 m s^{-1}.

High-resolution seismic reflection profiles were acquired in the western part of Lake Cucao and the whole of Lake Huelde, using a Geopulse pinger (frequency ~3.5 kHz). Lake Cucao and Lake Huelde were surveyed with 71 and 31 lines with a total of 25 km and 23 km with a line spacing of 150–200 m and 200 m, respectively, in areas of interest. These seismic data image the stratigraphy of the lacustrine sediment infill at a vertical resolution between 10 and 20 cm. Profiles were processed (bandpass filtering) and interpreted using IHS Kingdom Suite v. 8.8.

3.4.2 Subaerial and lacustrine samples

To identify tsunami deposits and their source sediments and to distinguish tsunami deposits from regular lacustrine sediments, we sampled both the barrier between the lakes and the ocean and the sediments within the lakes and analysed their sedimentological characteristics, specified below.

In 2013, we used 10 cm long plastic tubes (3.0 cm diameter) to collect 27 surface samples from the barrier area of Lake Cucao (C14–C28) and Lake Huelde (H15–H26) (Fig. 3.1). These samples give an overview of the subaerial sediments that would be available for transport during extreme wave events at present. Surface samples were taken from the beach, dune, freshwater marsh, and other subaerial environments that lie between the lakes and the ocean.

Gravity cores were collected from Lake Cucao (cores CUC1–CUC9 and at core sites Pos01–Pos11) and Lake Huelde (cores HUE1–HUE5 and at core sites Pos12–Pos19) in 2011 and 2012 (Fig. 3.2). These cores have a length of up to 1 m and an inner diameter of 6.0 cm. Coring locations were selected based on acoustic imagery data.

3.4.3 Sediment analysis

All subaerial samples were analysed for magnetic susceptibility using a Bartington MS2E point sensor. The mineralogy was determined under a stereoscopic microscope. Because the higher magnetic susceptibility values correlate with coarser and heavier minerals (iron oxides density ~5.2 g cm^{-3}), we subsampled lake gravity cores 3–5 times with a 0.5 cm depth interval around the highest magnetic susceptibility values for grain size analysis. The grain size of subaerial and la-

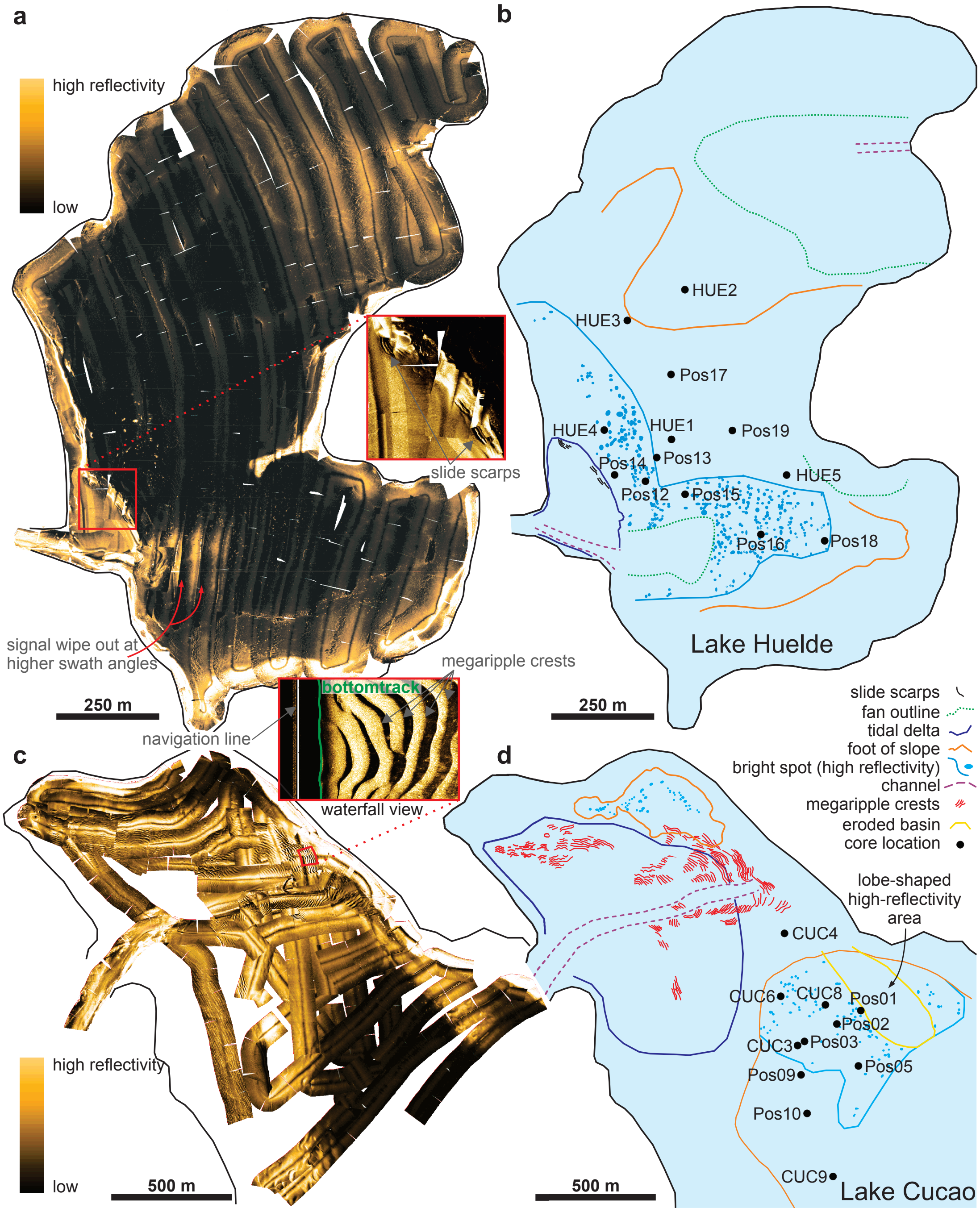

Figure 3.2: Side scan sonar mosaics from a) Lake Huelde and c) Lake Cucao and their respective interpretation maps in b) and d). Megaripples on the shallow plateau in Lake Cucao are aligned concentrically around the channel. Lobate high reflectivity areas adjacent to channel mouths are linked to sandy surfaces caused by tidal current erosion in Lake Cucao and fan-like tsunami sand deposition in Lake Huelde.

custrine samples was measured with laser granulometry using a Malvern Mastersizer 2000 after removing the organic content with hydrogen peroxide. The maximum grain size that can be measured by the Mastersizer 2000 is 2 mm.
The lacustrine gravity cores were analysed with a Geotek multisensory core logger (MSCL) to measure γ-ray attenuation density and magnetic susceptibility (same point sensor as above) at a down-core resolution of 2 mm. A line-scan camera mounted on the MSCL provided high-resolution split-core surface images. A Siemens Flash medical X-ray computed tomography (CT) scanner was used to provide 3D views for five cores (voxel size of $0.15 \times 0.15 \times 0.6$ mm, with the 0.6 mm in down-core direction). Additional classic X-radiography visualised the sedimentary structures in core Pos17, which was also selected for dating. Organic matter was removed and grain size distributions measured with the same methods as for the subaerial surface samples.
To measure water and organic matter content of the lake sediments, twelve samples from lake gravity cores at depths between 1 and 32 cm and a weight of 2–4 g of wet sediment were analysed using loss on ignition after Heiri et al. (2001).
For age control, ^{137}Cs-, ^{210}Pb-, and ^{226}Ra-activities were analysed in core Pos08 and Pos17 with a low-background, high-efficiency well-type germanium detector (Ge volume of 260 cm^3, low-noise Al and Cu components) equipped with a Cryo-Cycle (CANBERRA) (Schmidt et al., 2014) at the University of Bordeaux. In core Pos08 radionuclide activity was measured on 8 samples, in core Pos17 on 17 samples. Activities are expressed in mBq g^{-1} and errors are based on 1 standard deviation. Excess lead ($^{210}Pb_{xs}$) was calculated by subtracting the activity supported by its parent isotope, ^{226}Ra, from the total ^{210}Pb activity in the sediment. We used the constant-flux, constant-sedimentation (CFCS) model (Robbins, 1978) excluding the depth interval of the tsunami deposit, to derive a ^{210}Pb-based age-depth model.

3.5 Results and interpretation

3.5.1 Side scan sonar data

The side scan sonar mosaics from Lake Huelde and from the western part of Lake Cucao (Fig. 3.2) show an acoustic facies of high reflectivity on lake basin slopes and on 2m shallow plateaus adjacent to the lake outflows, suggesting coarse sediments at the surface in these areas (bright yellow colour, Fig. 3.2a, c). Sediments in the central basins below ~13 m water depth in Lake Cucao and ~7 in Lake Huelde present a facies of low reflectivity (dark colour, Fig. 3.2a, c). Low reflectivity corresponds to smooth, fine, and soft sediment surfaces. In both lakes, the transition from high reflectivity on the slopes to low reflectivity in the basins is sharp. The line dividing the two areas generally coincides with the foot of the slope.

3.5.1.1 Side scan sonar map of Lake Cucao

In the west of Lake Cucao at the outlet, a channel of up to 100 m wide and 5 m deep dissects a 0.8 km wide platform. The plateau bears megaripples on an otherwise smooth surface. There are 217 megaripples with an average ripple length of 8 m from crest to crest, approximately 1.5 m high and oriented concentrically around the channel (Fig. 3.2c, d). Their orientation suggests that the megaripples are probably formed by flood currents in shallow water (cf., McCave and Geiser, 1978). As the megaripples still appear fresh and have not been eroded (e.g., by wind induced waves), the plateau can be regarded as an active tidal delta.

In the southeast of the surveyed area, a lobe-shaped area at the channel mouth shows high reflectivity (Fig. 3.2d) and is a bathymetric depression. Due to its position and its erosional character, the lobe-shaped area is most likely an extension of the channel system into the basin.

Around the inferred continuation of the channel, there are numerous 1–6 m wide high-reflectivity features (Fig. 3.2c, d). The distribution of these superficial or near-superficial features is limited to the west of the basin. During the coring campaign, anchors caught grasses and bushes, similar to the contemporary vegetation on the barrier. These accumulations of vegetation possibly caused the high-reflectivity features.

3.5.1.2 Side scan sonar map of Lake Huelde

A 200 m wide plateau with ~2 m water depth at the outlet of Lake Huelde bears no geomorphological features except for a ~50 m wide crosscutting channel in the south linked to the outlet river (Fig. 3.2a, b). Two groups of sub-parallel curved linear features lie at the northeastern edge of the plateau. The linear features are 30–50 m long and 1–3 m wide. The interpretation of these features as rotational landslide scarps is supported by intact rotated sediment blocks on sub-bottom profiles and is discussed further in chapter 3.5.2.

An area of high reflectivity is located at the mouth of the crosscutting channel at the plateau. It is ~250 m long and 150 m wide with the long axis oriented from west to east. The positive morphology of this feature suggests that, unlike the lobate shape in Lake Cucao, this is a depositional feature, i.e., a fan. However, the strong signal wipe-out at higher swath angles suggests that the sedimentary body, which is producing the high-reflectivity in the lower swath angles, is buried underneath a soft, acoustically transparent sediment cover. This means that the side scan sonar may have directly imaged an acoustically harder layer buried beneath the present sediment surface. Numerous 1–7 m wide high reflectivity features occur within the otherwise low-reflectivity basin. Close to the western shore and north of the plateau, these bright spots are less jagged and more rounded (Fig. 3.2).

Elevated reflectivity values are observed in the northeast of Lake Huelde. This area is adjacent to the only noteworthy fluvial input into the lake. Stronger reflectivity is most likely caused by this terrigenous input.

3.5.2 Sub-bottom profiles

The sub-bottom seismic profiles reveal the sedimentary architecture of Lake Cucao and Lake Huelde (Fig. 3.3). On shallow plateaus in the west of both lakes, penetration of the sub-bottom profiler signal was strongly reduced, probably caused by the presence of coarse-grained sediment. In the deeper basins, the acoustic signal is absorbed after short travel in the soft sediment, due to the presence of shallow gas (likely a product of organic matter decomposition). While there is a ~200 m wide acoustic window into basin sediments along the gentle western slope of

Lake Cucao, in Lake Huelde penetration below the first strong reflector is scarce. However, we define three seismic units common to both lakes, which we refer to as units U1a, U1b, and U2.

U1a's upper boundary is a sharp, hummocky unconformity in the basin. The lower boundary is not defined. Internally, U1a is made up of strong, wavy, and continuous reflections, with strongly decreasing amplitude and continuity with depth (Fig. 3.3a, b). U1a is interpreted as sandur sediments, which build the base of both lakes.

U1b is similar to U1a in most aspects, including the abundance of strong continuous reflections and the lack of a defined lower boundary. U1b occurs in shallow water. Unlike U1a, U1b has internal unconformities and its upper boundary is the lake floor (Fig. 3.3). Seismic penetration is rarely more than 3 m sub-surface. Where penetration is higher, strong hummocky and discontinuous reflections are the lowermost visible features. Acoustic ringing effects and the low signal-to-noise ratio prevent characterisation of the deeper parts. In both lakes, U1b includes eroded channels that cross cut the shallow plateaus in the west. There are areas of wavy lake floor in the vicinity of the modern channel in Lake Cucao, caused by the megaripples that are described on the side scan sonar imagery (Fig. 3.3a). U1b is interpreted as reworked sandur sediments and other sediments from the barrier, which build the base in the shallow areas of both lakes.

U2 overlies and onlaps U1a wherever the lower contact of U2 is visible. The most prominent internal signature in U2 consists of a series of strong, infrequent, and sub-parallel reflections in both lakes. Between these strong continuous reflections, U2 consists of very low acoustic amplitudes. The top of U2 is the lake floor, which in Lake Cucao is a strong reflection (Fig. 3.3a, b), and in Lake Huelde is an exceptionally weak reflection (Fig. 3.3c). The uppermost strong reflection in Lake Huelde usually lies between 0.3 and 0.4 m below the lake floor. The same reflector may be responsible for the high reflectivity on low swath angles on side scan sonar data. The reflection is hummocky in the west and transitions gradually to a flat reflection in the east. Within the area of flat reflection the acoustic amplitude decreases eastwards. U2 is interpreted as the sediment infill of both lake basins. This infill mostly consists of almost acoustically transparent lake sediments and of sheets of sediment with high acoustic impedance.

The two groups of sub-parallel curved linear features identified in the Lake Huelde side scan sonar maps can be linked with intact rotated sediment blocks and confined wedge-shaped sedimentary bodies seen in the sub-bottom profiles (Fig. 3.2, 3.3). All of these sedimentary bodies are in direct contact with the uppermost high amplitude reflection of U2. The scarps and rotated blocks in Lake Huelde are therefore interpreted as simultaneously triggered rotational landslides with compressional toes. Such simultaneously triggered slope failures and landslide deposits in lakes are usually attributed to earthquake triggering and to local earthquake intensities of VI or higher (Monecke et al., 2004; Strasser et al., 2013; Moernaut et al., 2014; Van Daele et al., 2015). The run-out of these landslides is minimal (10–40 m) and their volume is insufficient to cause lake-wide sheet-like deposits that would be imaged as high amplitude reflections on sub-bottom profiles.

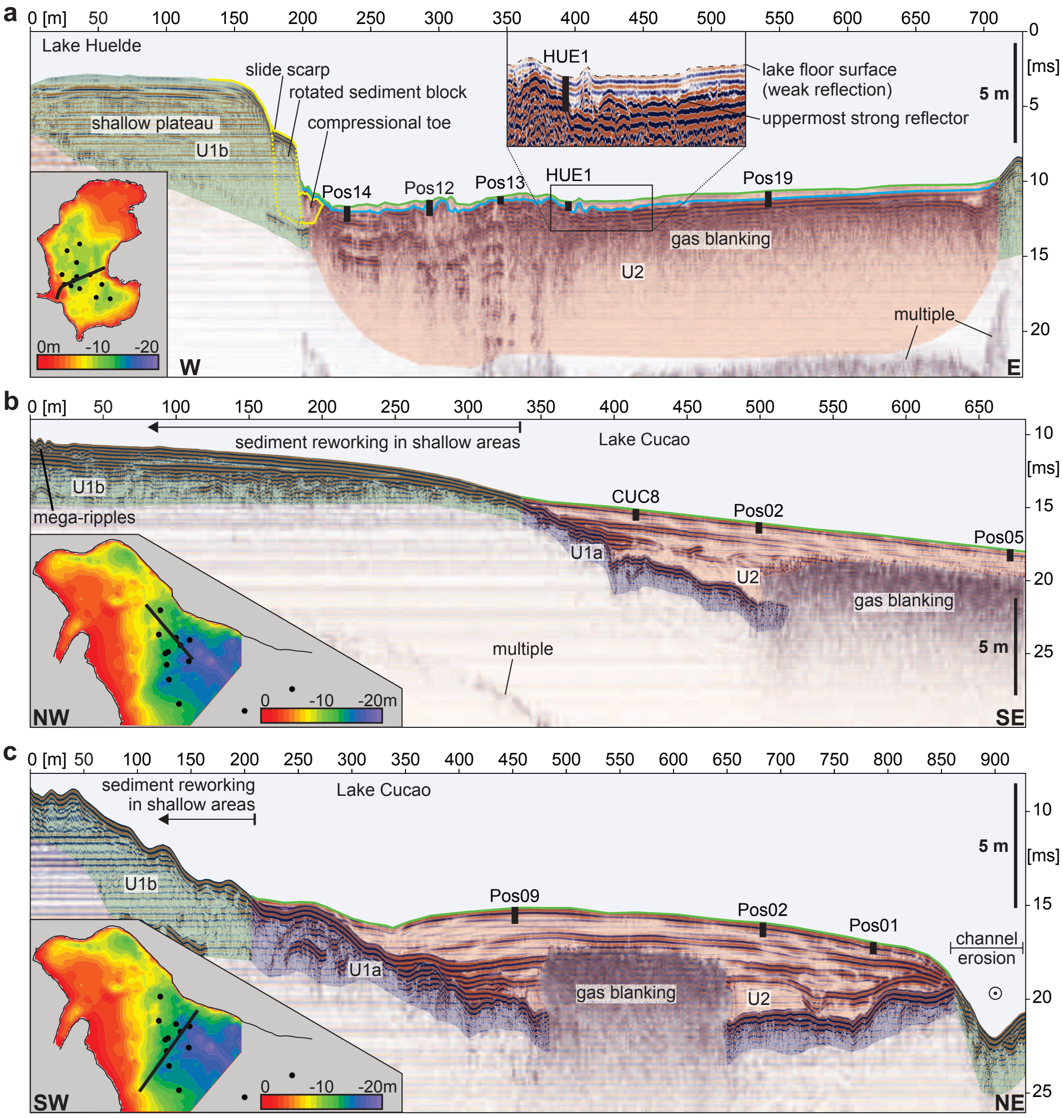

Figure 3.3: Pinger sub-bottom profiles of Lake Huelde in a), and Lake Cucao in b) and c). In all three cases there are areas of non-deposition or reworking of sediment on the shallow plateaus in the west and on the upper slope. Seismic units are visible as coloured semi-transparent overlays (U1a: purple, U1b: green, U2: red). Short cores location and penetration are depicted in thick, black vertical lines. In Lake Huelde, a), the lake floor (green line, dotted line in inset) is a weak reflection in comparison with the surface of the 1960 tsunami deposit (blue line). In Lake Cucao (b and c) the 1960 tsunami surface is too close to the lake floor to be distinguishable (green line).

3.5.3 Stratigraphy and sedimentology

3.5.3.1 Subaerial sediments

All of the subaerial samples from both barriers (Fig. 3.1) consist of well-sorted, fine to medium sand. The modal grain size varies from 224 to 430 μm (ϕ = 2.16–1.22). The sand is made of equal amounts of mineral grains and lithic grains. The minerals are orthoclase, plagioclase, quartz, iron oxides, epidote, hornblende, and rarely zircon. Magnetic susceptibility is generally high at >250 $\times 10^{-5}$ SI (mean 780 $\times 10^{-5}$ SI) with extreme values of 3000 $\times 10^{-5}$ SI.

3.5.3.2 Lacustrine sediments

The sediments retrieved in the 27 gravity cores from Lakes Cucao and Huelde can be subdivided into six main sedimentary facies (Fig. 3.4):

i **Homogeneous gyttja** — Brown to black organic-rich homogeneous mud is the most abundant sediment facies in the lake cores. The sediment contains up to 80 wt% water; of the dry material, up to 40 wt% is organic. The organic matter consists mostly of unidentifiable fragments, fibrous plant fragments (e.g., culms and leaf veins), diatoms, pollen, and seeds. In Lake Cucao, the organic component also includes periostraca of bivalves, possibly *Diplodon chilensis*. The homogeneous mud is easily deformed and has an average γ-attenuation density of 1.3 g cm^{-3}. The grain size distribution is symmetrical and is poorly to very poorly sorted. The mode is 15 μm (ϕ = 6.06) on average, and particle sizes range from clay to medium silt. This lithofacies has a low magnetic susceptibility between 0 and 40×10^{-5} SI.

ii **Laminated gyttja** — Dark brown, organic-rich laminated mud occurs only in Lake Huelde sediments. Where it occurs, it is invariably at the top of the gravity cores. The irregular millimetre to centimetre-scale laminations consist of yellowish grey and black layers within the generally dark brown sediment. The other physical properties and the organic content are identical to those described for the homogeneous gyttja.

iii **Mud rip-up clasts** — Dark brown organic-rich mud clasts of sizes ranging from 0.5 cm to larger than the inner core diameter (6.0 cm) occur within a matrix of sand. The mud clasts, which are composed of gyttja, are angular in shape (Fig. 3.4) and sometimes aligned in horizons. This facies occurs only in Lake Huelde and predominantly in cores closer to the western shore. Because of the gyttja material and the angular shape, they are interpreted as mud rip-up clasts, representing a high-energy flow regime.

iv **Massive sand** — Massive sands in the lake cores are well to moderately well sorted and can contain finely dispersed organic matter. The grain size distribution consists of a narrow symmetrical peak around 205 μm (ϕ = 2.29); however, 6 out of 11 samples have a very low secondary peak of silt-sized grains. Mineral and lithic grains are equally abundant in the sand. The mineral grains have the same composition as the subaerial sands, i.e., orthoclase, plagioclase, quartz, iron oxides, epidote, hornblende, and rarely zircon. Strongly ferrimagnetic iron oxides produce positive peaks in magnetic susceptibility with a mean of 500×10^{-5} SI and up to 1750×10^{-5} SI. Massive sand units often have a sharp and sometimes erosional contact to the underlying homogenous gyttja (facies i). In Lake Huelde, massive sand units often occur in association with a mud cap on top (facies vi) and mud rip-up clasts (facies iii) towards the base. Such sands are transported in a high-energy environment.

v **Organic-rich silt and sand** — The dark brown to black, organic-rich, medium silt to fine sand is sometimes indistinguishable from homogeneous gyttja in colour and consistency; however, differentiation is possible through the higher magnetic susceptibility (>60×10^{-5} SI) and the coarser grain size distribution, with a mode of 25 μm (ϕ = 5.31). Out of 19 samples, 9 are bimodal with a second mode around 182 μm ($\phi = 2.46$). The dominance of these two modes varies strongly with location.

vi **Mud cap** — Mid grey to brownish grey organic-rich silt layers with a transitional or sharp lower contact and a sharp upper contact. The silt layers are between 0.5 and 5.0 cm thick and always occur in association with an underlying massive sand layer. The magnetic susceptibility is low (50×10^{-5} SI). The mud cap shares similarities with the gyttja of facies i and ii in organic content and magnetic susceptibility.

3.5.4 Facies associations

We group the described lithofacies into 2 facies associations (Fig. 3.4), gyttja and tsunami deposit. The main criterion is the energy associated with the deposition of each facies. Gyttja, including lithofacies i and ii, reflects the gradual deposition of fine grained material in a low-energy environment with an organic fraction, including plant fragments, diatoms, pollen and seeds, and little clastic input from the rivers or wind.

The mud rip-up clasts in sandy matrix (facies iii), medium to fine massive sand (facies iv), organic-rich silt and sand (facies v), and mud cap (facies vi) form a high flow energy facies association. Apart from the mud cap, the required flow energy for producing such facies is markedly higher than the low-energy depositional environment associated with gyttja. The erosional contact of massive sand or mud rip-up clasts in a sandy matrix with the underlying gyttja and the mud cap mark the sudden changes from a low- to a high-energy flow regime and back to a low-energy flow regime, respectively. The group of sedimentary facies iii to vi is interpreted as a tsunami deposit facies association (Fig. 3.4, 3.5), because this sudden change to extreme flow energy in this coastal lake environment on the Chilean subduction zone in combination with the described sedimentary facies may be linked to a tsunami.

3.5.5 Core chronology

In Lake Cucao, the inferred tsunami deposit consistently lies only a few centimetres below the lake floor. Because the lake floor reflection on the sub-bottom profiles is strong, we link the sandy and silty material in each of the cores with this strong reflector. $^{210}Pb_{xs}$ and ^{137}Cs profiles cannot be used to precisely constrain the age of the sand layer in core C8. The gyttja above the sand is only 2 cm thick, leaving room for only two samples (Fig. 3.6). However, activity levels of ^{137}Cs in the two samples above the sand are higher than in all samples below, indicating that the sand layer probably predates the mid 1960s. The radionuclide activity in core Pos08 is too low to allow a robust ^{210}Pb age-depth model.

In all Lake Huelde cores, a tsunami deposit lies at 21–41 cm depth below the lake floor. This matches well with the depth of 0.4–0.5 ms two-way travel time (30–37.5 cm) of the uppermost strong seismic reflection. Therefore, the uppermost strong reflector in Lake Huelde is interpreted as the surface of this sandy deposit.

In core Pos17, $^{210}Pb_{xs}$ activities present a rapid decrease from 77 mBq g^{-1} at the core top to below 10 mBq g^{-1} at about 30 cm, as expected due to the radioactive decay of ^{210}Pb (Fig. 3.6). Con-

facies association	lithofacies	lithofacies description	split core surface image	CT-scan
tsunami deposit	vi) mud cap	middle grey to brownish grey silt with a transitional or sharp lower contact and a sharp upper contact, between 0.5 and 5 cm thick		
tsunami deposit	v) organic-rich silt and sand	dark brown to black organic-rich, medium silt to fine sand		
tsunami deposit	iv) massive sand	massive sand with a sharp, often erosional lower contact and either a sharp upper contact to background sediment or a sharp to transitional contact to a mud cap		
tsunami deposit	iii) mud rip-up clasts	dark brown organic rich mud clasts 0.5 to 6 cm in diameter in a matrix of sand, sometimes aligned in layers (only in Lake Huelde)		
gyttja	ii) laminated	dark brown, organic-rich laminated mud (only in Lake Huelde)		
gyttja	i) homogeneous	brown to black organic-rich homogeneous mud		

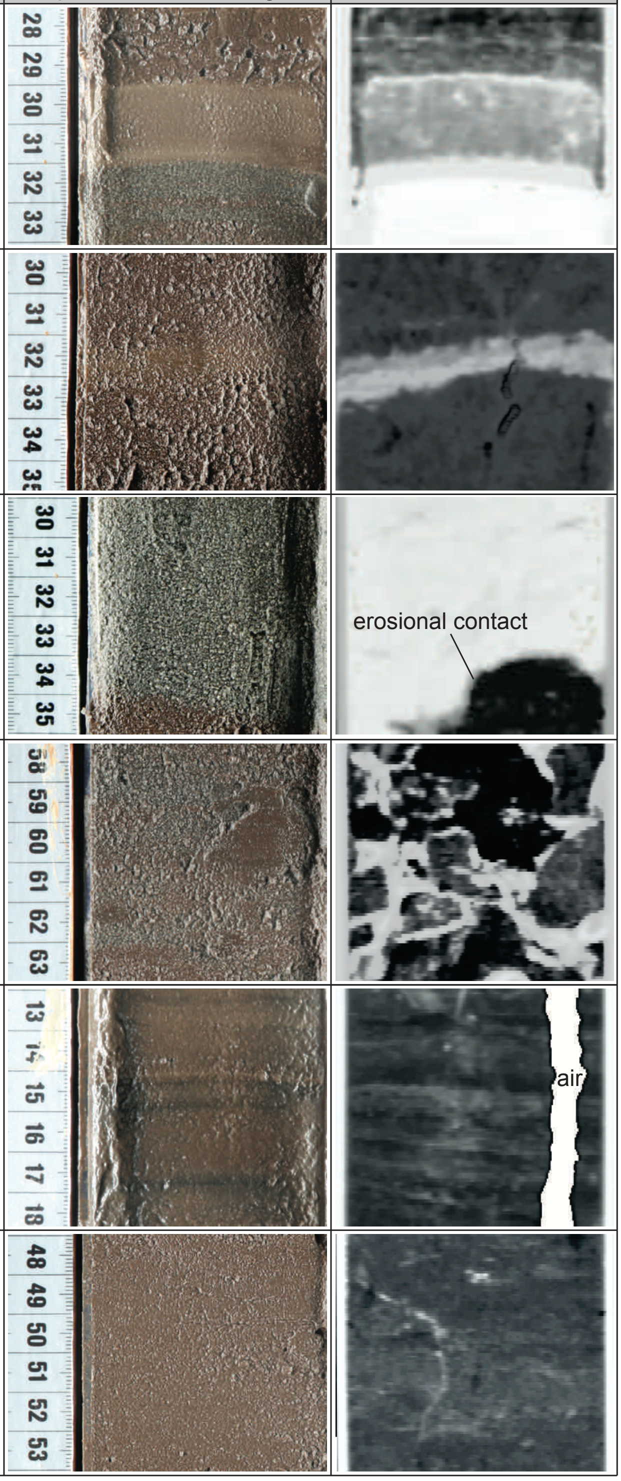

Figure 3.4: Description of the sedimentary facies and facies associations with the split core surface image and a computed tomography (CT) X-radiograph.

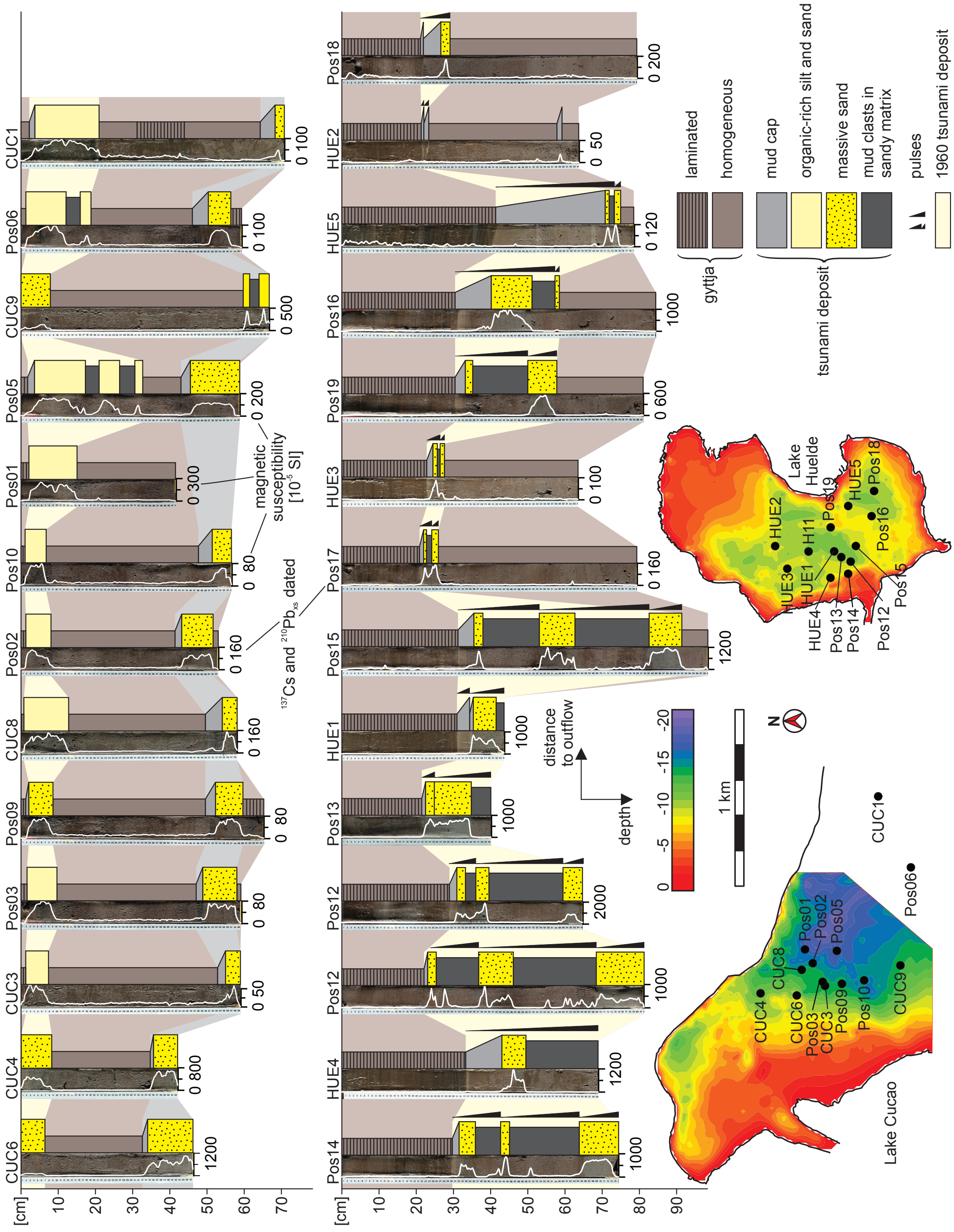

Figure 3.5: Transects of short cores from Lake Cucao (upper row) and Lake Huelde (lower row). The magnetic susceptibility (white line) is plotted on top of the core image – note the difference in scale between each core site. The 1960 tsunami deposit is highlighted in light red. Interpretations of depositional pulses are indicated in black triangles.

sidering the sudden deposition at about 20–25 cm and the low activity of $^{210}Pb_{xs}$ in depth, we applied a constant-flux-constant-sedimentation model only to the upper part of the $^{210}Pb_{xs}$ profile. The mean sediment accumulation rate is 0.39 cm y^{-1}, implying an age of AD 1961 ± 5 at 20 cm depth, i.e. just above the tsunami deposit. The ^{137}Cs profile in core Pos17 presents a peak at a depth between 13 and 17 cm (12 mBq g^{-1}), low values near the top (5 mBq g^{-1}), and negligible activities below the tsunami deposit (≤ 2 mBq g^{-1}).

The ^{137}Cs peak corresponds to the mid 1960s, according to the annually measured atmospheric fallout of ^{137}Cs recorded at Buenos Aires, Argentina (Quintana, 2011), and soil profiles from the vicinity of Puerto Montt, 20 km north of Isla de Chiloé (Schuller et al., 2002). This is in strong agreement with the modelled age from the ^{210}Pb age-depth model. As a result of the radiometric dating, combined with the indication of inundating flow deposition, we interpret that the deposit is the product of the tsunami that followed the AD 1960 Great Chilean Earthquake.

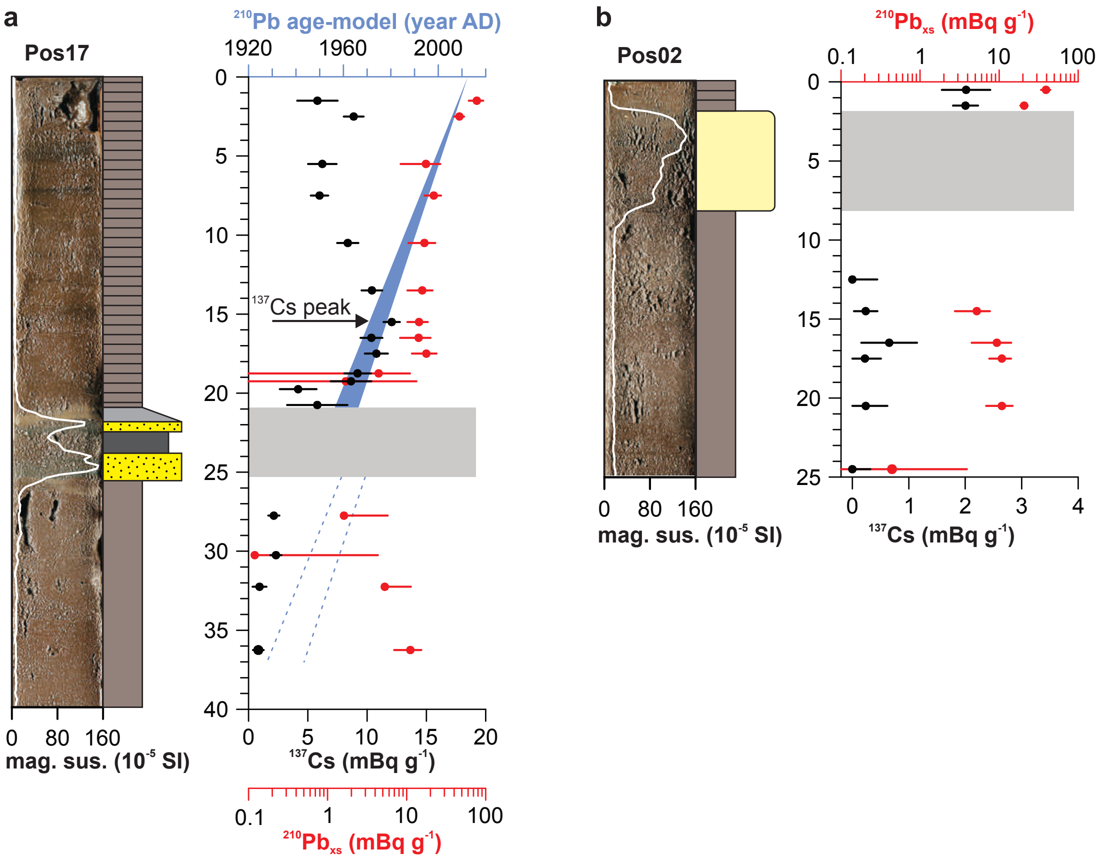

Figure 3.6: Radionuclide analyses on cores Pos17 (a) and Pos02 (b). ^{137}Cs values (black) show the ^{137}Cs peak in Pos17 between 13 and 17 cm depth. The ^{210}Pbxs profiles (red) are the basis for the ^{210}Pb age-depth model (blue). In Pos02 the ^{137}Cs activities are detectable above the tsunami deposit (grey bar) and negligible below, indicating the mid-1960s peak to be above the tsunami deposit.

3.5.6 Spatial trends of the AD 1960 tsunami deposit

In the proximal lake cores, the tsunami deposit is up to 61 cm thick. When, as in five Lake Huelde cores (HUE1, HUE4, Pos12 and Pos14), the base was not retrieved, then the thickness from the top to the core base is taken as a minimum thickness. The tsunami deposit thickness decreases with increasing distance from the ocean; however, there is no thinning trend in areas beyond ~2.5 km distance from the ocean (~1.3 km distance from the outflow) (Fig. 3.7a). The lowest thickness in the cores is 1.7 cm. For the following measurements of magnetic susceptibility and grain size distributions, we used extreme values to represent the strongest signal for the core location, i.e., highest magnetic susceptibility and coarsest grain size distribution.

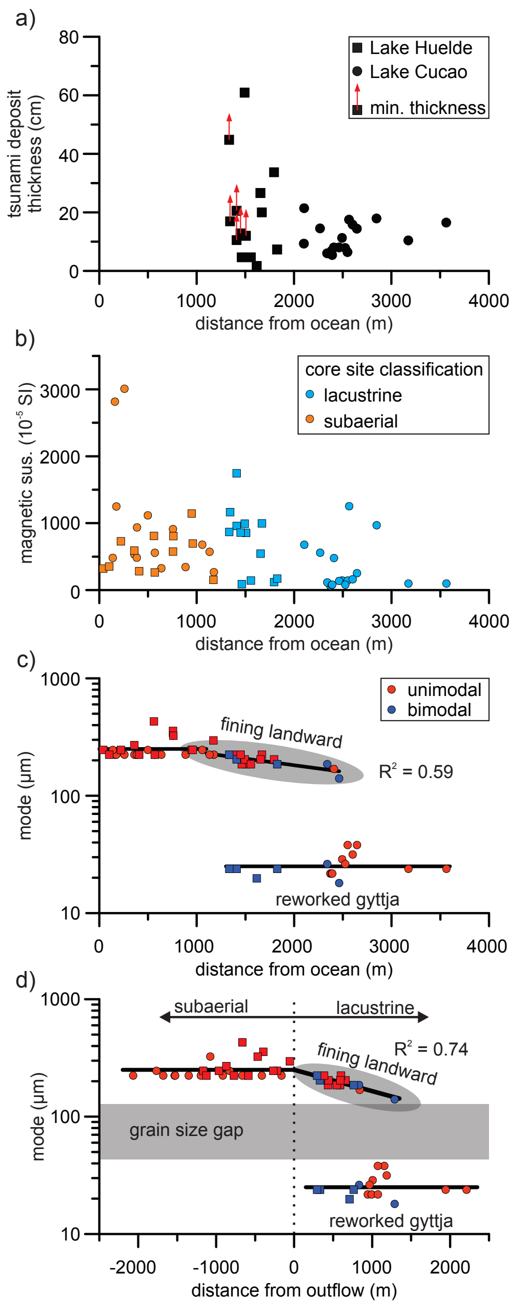

Figure 3.7: Spatial trends of a) tsunami deposit thickness, b) maximum magnetic susceptibility in each core and c) grain size modes plotted against the distance from the ocean. In d) the same modes are plotted over distance from the lake outflow.

Magnetic susceptibility is primarily controlled by the content of ferrimagnetic and heavy iron oxides (hematite and magnetite have a density of 5.2 g cm^{-3}). Secondarily, magnetic susceptibility underlies a grain size effect (Thompson and Morton, 1979), i.e., larger sand grains produce a higher value. Both grain size and density influence the capacity of erosion, transport, and deposition of grains; therefore, higher magnetic susceptibility values may reflect stronger flow during tsunami inundation. Organic content, in the form of larger mud clasts, and finer dispersed organic material in sandy beds attenuates the magnetic susceptibility values. The maximum magnetic susceptibility of the tsunami deposit decreases from an extremely high 1750×10^{-5} SI to 73×10^{-5} SI with increasing distance from the ocean (Fig. 3.7b). The latter is still higher than for gyttja of facies i and ii (40×10^{-5} SI). However, the decreasing trend in magnetic susceptibility is widely dispersed.

Within the complete grain size dataset, there are three groups of grain size distributions (Fig. 3.8), i.e., silt, sand, and bimodal silt and sand. The grain size modes within the tsunami deposit group around a fine (silt) and a coarse (sand) mode. The average fine mode is ~25 μm ($\phi = 5.31$) and does not change with distance from the ocean (Fig. 3.7c, d). This mode is represented in the unimodal, symmetrical silt samples, and in the fine part of the bimodal silt and sand samples. The unimodal silt grain size distributions occur exclusively in organic-rich silt (facies v) and resemble the grain size distribution of gyttja (facies i and ii). The average coarse mode is 194 μm ($\phi = 2.36$) and decreases with increasing distance from ocean. The exponential fit curve of this negative correlation has an R^2-value of 0.59 (Fig. 3.7c). The R^2-value increases to 0.74, when the grain size modes are plotted against the distance from outflow (Fig. 3.7d), which is the distance of each sample from an arbitrary point at the lakes' outflow. The coarse mode is represented in unimodal, symmetrical sand samples and in the coarse part of the bimodal silt and sand samples. The unimodal sand grain size distributions describe the grain size of massive sand (facies iv) and organic-rich sand (facies v) and resemble the grain size distribution of subaerial samples. The most distal sample with a coarse mode (core CUC9) is located at ~1.3 km distance from outflow; beyond that distance the tsunami deposit consists only of silt (Fig. 3.7d).

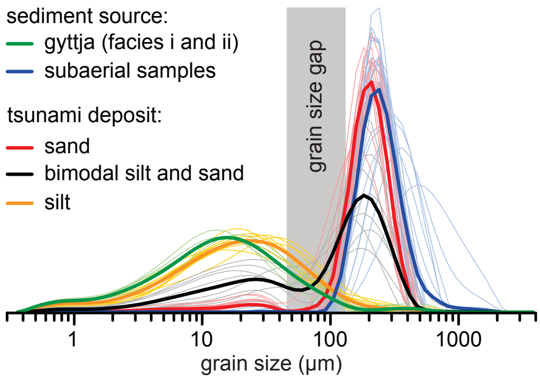

Figure 3.8: Averaged grain size distribution curves (thick lines) of the single samples (thin lines) describe two source sediments of subaerial sand (blue) and gyttja (green), as well as the three different grains size compositions from the tsunami deposit (red, black and yellow). The graph shows the transition of the grain size distributions of the tsunami deposit from a subaerial sand controlled composition (red) to a gyttja controlled composition (yellow).

3.6 Discussion

The two lakes share many similarities, yet the post-1960 sedimentation rate is drastically different. Lake Cucao has a low sedimentation rate of 0.4 mm yr^{-1}, while Lake Huelde has a high sedimentation rate of ~5.9 mm yr^{-1}. Due to their different catchment-area-to-lake-area ratios (Lake Cucao: 3.1; Lake Huelde: ~75), Lake Huelde can be expected to have a ~7 times higher sedimentation rate than Lake Cucao (Van Daele et al., 2015). In addition, tidal currents may have inhibited sedimentation or even eroded gyttja in the western parts of Lake Cucao, especially after the AD 1960 earthquake, which resulted in ~1 m of co-seismic subsidence in the study area (Plafker and Savage, 1970).

3.6.1 Sediment source and distribution in the lakes

The unimodal silt and unimodal sand distributions in the tsunami deposit resemble the grain size distributions of gyttja and subaerial sand, respectively, so closely (Fig. 3.8d) that the latter two are interpreted to be reworked and transported by the tsunami. Moreover, the mineralogical similarity between subaerial and tsunami sand supports this interpretation. Both the gyttja and subaerial sand can be seen as end-member sources to the bimodal silt and sand in the tsunami deposit. The prominence of the fine and the coarse mode describes the relative contribution of either source.

The area of the landward thinning trend and the occurrence of sand in the tsunami deposit overlap (Fig. 3.7a, c); they are both limited to ~2.5 km distance from ocean, i.e., ~1.3 km distance from outflow. The distal tsunami deposit, i.e., beyond ~1.3 km distance from outflow, does not follow this landward thinning and fining, because the distal tsunami deposit drapes the basin with the thickest accumulations in the deepest areas (e.g., in cores CUC1, Pos06, HUE2, and Pos18). This matches the observations from Bradley Lake, Cascadia, in which sandy "disturbance event" deposits exhibit landward thinning, while thinner, muddy "disturbance event" deposits drape the lake basin, with thicker deposits in the deeper parts (Kelsey et al., 2005). The reason for the lack of thinning in the solely gyttja-derived tsunami deposit may be the slow settling velocity of the grains and the relatively high-energy, turbulent currents mixing the lakes during the tsunami. When the grains cannot settle fast enough, then thinning cannot develop before the entire lake is evenly mixed. This is especially true for small lakes, e.g., Lake Huelde and Bradley Lake, Cascadia.

This subdivides the lake cores into three zones; 1) a proximal zone, where the tsunami deposit mostly consists of reworked subaerial sands; 2) an intermediate zone, where the tsunami deposit consists of a mixture of both reworked gyttja and reworked subaerial sands, and 3) a distal zone, where no subaerial sand occurs and the tsunami deposit consists entirely of reworked gyttja (Fig. 3.9).

The sand deposition limit within the lake may provide a site-specific relative measure of tsunami size, applicable to paleotsunami deposits in the same sedimentary record. However, at the moment, this hypothesis lacks the data for testing. Studies using the sand deposition limits to reconstruct tsunami size onshore are prone to strong site-dependent variations, e.g., coastal geo-

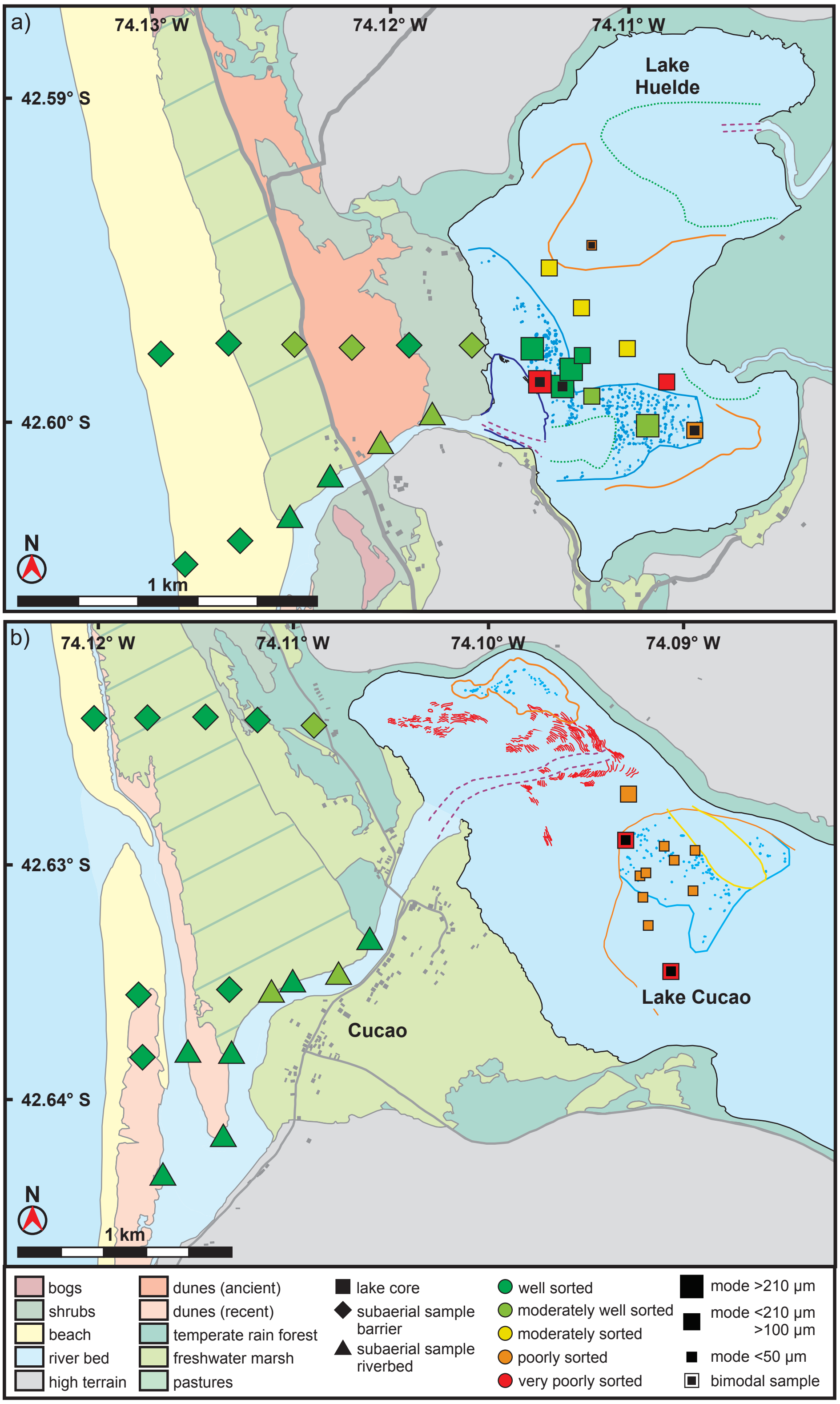

Figure 3.9: Maps of both lakes describing the type of sample coded in shape, the sedimentary sorting in colour, and the grain size modes in size of the symbol. Note the coarse grained proximal samples in Lake Huelde around the shallow plateau in the west, and the long distance between subaerial samples and the fine grained basin samples in Lake Cucao caused by the tidal delta.

morphology (Gelfenbaum and Jaffe, 2003; Furusato and Tanaka, 2014; Chagué-Goff et al., 2015), which should also be expected in a coastal lake environment.

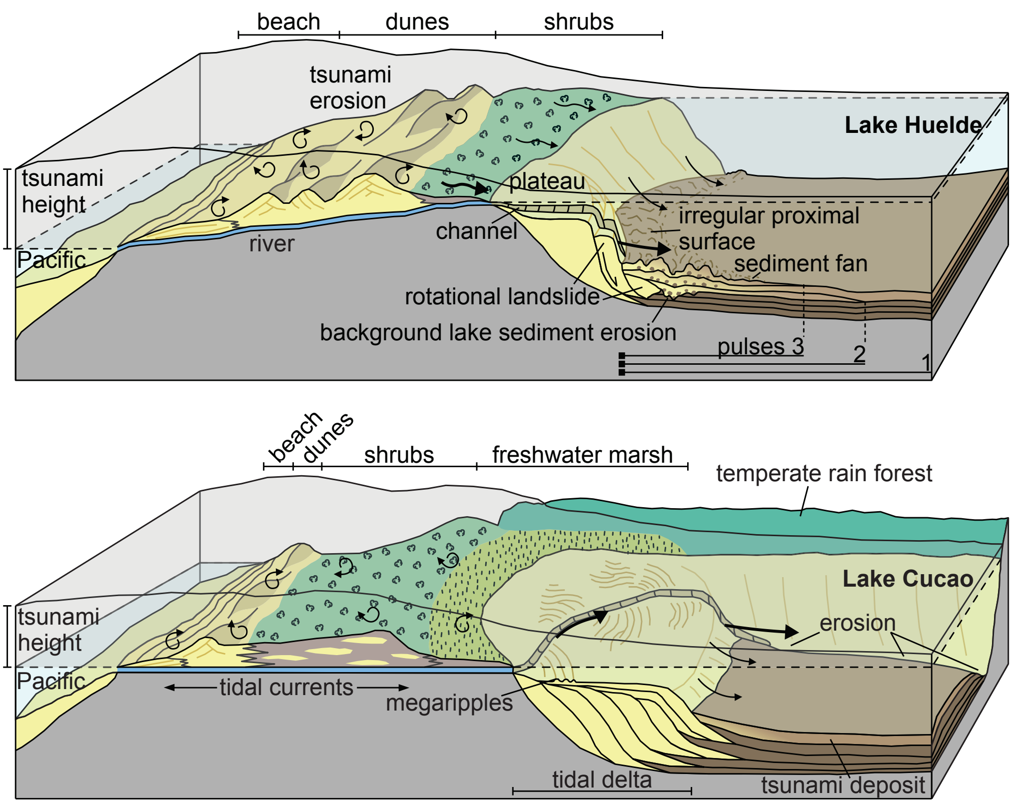

Figure 3.10: Conceptual sketches of both Lake Huelde (above) and Lake Cucao (below) during tsunami inundation.

3.6.2 Role of the incised channels

Lake Cucao and Lake Huelde have shallow plateaus that are 0.8 km and 0.2 km wide, respectively, around their outlets, increasing the distance for tsunamis to travel from the ocean to reach the lacustrine depocentre. In Lake Cucao, this plateau is described as a tidal delta due to the water inflow from the ocean at high tide (Villalobos et al., 2003). The size of the tidal delta in Lake Cucao and the megaripples on its surface indicate considerable inflow and sediment transport (Fig. 3.2c, d). The tidal currents in the channel are strong enough to erode lake sediments at the basin end of the channel (Fig. 3.3, 3.10). The small plateau in Lake Huelde can be tentatively interpreted as a tidal delta, although an inflow at high tides is presently missing. Net uplift in the late Holocene (cf., Atwater et al., 1992) may have caused Lake Huelde to rise out of the intertidal zone.

Reports of destruction (Weisner, 2003) and the distribution of bright spots on side scan sonar maps near the western shores of the lakes (Fig. 3.2) point towards overspilling of the barriers in front of both lakes during the AD 1960 tsunami. In Lake Huelde, the high-reflectivity fan off the channel mouth highlights the channel as a point source of sandy tsunami sediment (Fig. 3.2a, b). The shape of the fan and the bright spots beyond the fan far into the lake basin provide an

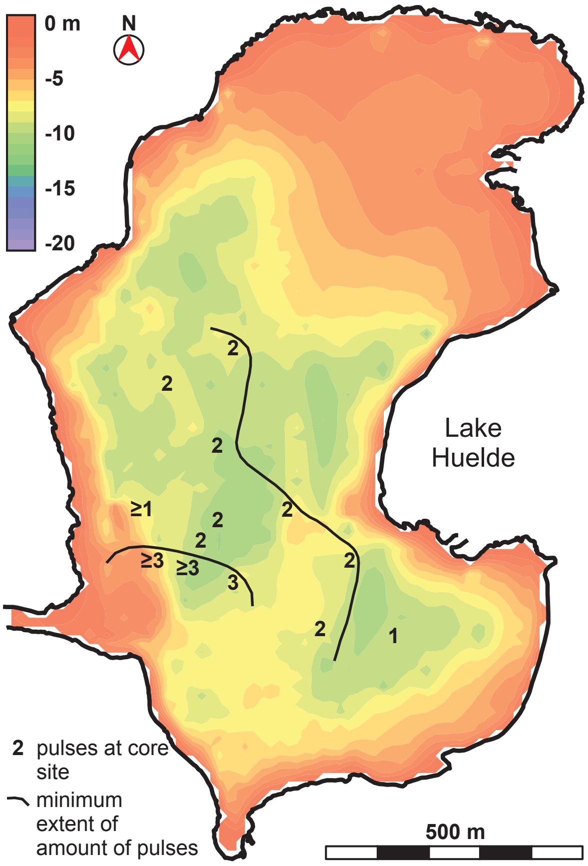

Figure 3.11: Mapped number of tsunami pulses per core in Lake Huelde forming distinct areas of equal number of pulses.

insight into inundation dynamics. This point source behaviour of tsunami sediment is also revealed in grain size data, where the exponential fit curve for grain size modes has a markedly higher R^2-value, when plotted over distance from the outflow ($R^2 = 0.74$) rather than distance from the ocean ($R^2 = 0.59$) (Fig. 3.7). Accordingly, the coarse tsunami sediment in the lake is distributed on and near the fan (Fig. 3.9). Despite the tsunami overspilling the barrier, the channels crossing the tidal deltas act as the main pathways for efficient sediment transport into and within the proximal part of the lakes.

3.7 Reconstruction of tsunami inundation characteristics

In the distal cores of Lake Huelde, it becomes increasingly difficult with decreasing tsunami deposit grain size to infer multiple pulses. Sometimes, X-radiography or X-ray computed tomography resolves this problem. Due to the wide barrier between the Pacific and Lake Cucao (1.3 km) and the large tidal delta (0.8 km) in the lake, all cores from Lake Cucao are very distal and multiple pulses cannot be recognised. In Lake Huelde, the distribution of the number of pulses delineates distinct areas with up to three pulses close to the outlet and only one pulse in the east (Fig. 3.5, 3.11). The number of large-scale pulses, like the ones described in Lake Huelde tsunami

deposits, can be linked with the number of waves of the tsunami (Chagué-Goff et al., 2012b; Goff et al., 2012). The number of large waves during the tsunami was not reported at the study area; however, our data are in agreement with eyewitness reports of four and two or more large waves from Isla Guafo and Punta Corona, respectively (Sievers et al., 1963). The presence of multiple pulses in Lake Huelde and the lack thereof in Lake Cucao demonstrates the strong variability within tsunami deposits and the control exerted by coastal and lacustrine morphology on the deposit characteristics. Taking a single core from a lake would likely lead to an underrepresentation of pulses and possibly to an underrepresentation of tsunami deposits, when coring for longer paleotsunami records.
The landward flow energy loss in tsunami deposition is described in this and other studies by landward thinning and landward fining of the tsunami deposit (Gelfenbaum and Jaffe, 2003; Witter et al., 2003; Goto et al., 2014). In this study, the transition from a hummocky to a flat seismic reflection of the tsunami deposit in Lake Huelde (Fig. 3.3a) may be a new indication for landward energy flow loss by the means of a geophysical acoustic method. The erosion and deposition of mud rip-up clasts may explain the hummocky shape of the seismic reflection in the most proximal areas of the Lake Huelde basin. The transition from hummocky to flat reflection possibly also reflects the decreasing turbulence of the inundating flow. Alternatively, the hummocky shape of the seismic reflection may be caused by sediment loading, in which case the hummocky reflection would occur where the tsunami deposit is thickest.

3.8 Conclusions

Sub-bottom profiles and side scan sonar mosaics as well as sediment cores were analysed for radionuclides (dating), magnetic susceptibility, γ-ray attenuation density, and grain size. The data describe a tsunami deposit of the AD 1960 Great Chilean Earthquake in two coastal lakes on Isla de Chiloé in south central Chile.
The mode of the grain size distribution was used to distinguish between subaerial and lacustrine sediment sources of the 1960 tsunami deposit within the lakes. In the proximal area, the subaerial component dominates. After 100–200 m of in-lake transport, lacustrine sediment is part of the tsunami deposit. The maximum in-lake transport distance of the subaerial component is 1.3 km. Beyond that distance, the tsunami deposit entirely consists of reworked lacustrine gyttja. From Lake Huelde cores it is possible to map and infer a minimum of three lake-inundating waves during the AD 1960 tsunami, which is in agreement with eyewitness reports north and south of the study area.
Side scan sonar data revealed that the AD 1960 tsunami inundated both lakes over the barrier and through the river channel. A sediment fan at the outflow in Lake Huelde reaches far across the lake and highlights the dominant role of existing tidal delta channels as a pathway for sediment transport by the tsunami, despite the overspill of the barrier. By plotting grain size modes against distance from ocean and against distance from outflow, the dominating role of the river channel can be described, without the use of acoustic geophysical data.
Lake Cucao and Lake Huelde present two different settings for recording tsunami inundation despite their shared beach system and similar barrier topography. In Lake Cucao, the proximal

record is lost due to constant reworking on the shallow tidal delta by tidal currents. Valuable paleotsunami information can be retrieved from the distal record. In Lake Huelde, both the proximal and distal records are preserved. This study demonstrates that it is paramount to understand the depositional environment of coastal lakes and the tsunami deposit characteristics in its spatial variability before the record becomes meaningful.

Ackowledgements

PK acknowledges financial support by the Special Research Fund of Ghent University (BOF), JM from the Swiss National Science Foundation (SNF) grant 133481 and the Chilean Fondecyt projects nr. 1150346 and 1150321, and MVD from the Research Foundation Flanders (FWO travel grant K201512N). We thank Koen De Rycker and Gauvain Wiemer for fieldwork support, Dr. Claire Schepens and Dr. Eric Achten for CT scanner support, Magda Vincx for access to the Malvern 2000 and Alan Nelson, Evelien Boes, Michaela Spiske, Jasper Knight, and two anonymous reviewers for constructive criticism on the manuscript.

References

Amante, C., Eakins, B.W., 2009. ETOPO1 1 Arc-Minute Global Relief Model: Procedures, Data Sources and Analysis. NOAA Technical Memorandom NESDIS NGDC-24. National Geophysical Data Center, NOAA.

Atwater, B.F., 1987. Evidence for great Holocene earthquakes along the outer coast of Washington State. Science 236, 942–944.

Atwater, B.F., 1992. Geologic evidence for earthquakes during the past 2000 years along the Copalis River, southern coastal Washington. Journal of Geophysical Research: Solid Earth 97, 1901–1919.

Atwater, B.F., Núñez, H.J., Vita-Finzi, C., 1992. Net Late Holocene emergence despite earthquake-induced submergence, south-central Chile. Quaternary International 15/16, 77–85.

Atwater, B.F., Cisternas, M., Yulianto, E., Prendergast, A.L., Jankaew, K., Eipert, A.A., Ignatius, W., Fernando, S., Tejakusuma, I., 2013. The 1960 tsunami on beach-ridge plains near Maullín, Chile: landward descent, renewed breaches, aggraded fans, multiple predecessors. Andean Geology 40, 393–418.

Bahlburg, H., Spiske, M., 2012. Sedimentology of tsunami inflow and backflow deposits: key differences revealed in a modern example. Sedimentology 59, 1063–1086.

Barrientos, S.E., Ward, S.N., 1990. The 1960 Chile earthquake: inversion for slip distribution from surface deformation. Geophysical Journal International 103, 589–598.

Bondevik, S., Svendsen, J.I., Mangerud, J., 1997. Tsunami sedimentary facies deposited by the Storegga tsunami in shallow marine basins and coastal lakes,western Norway. Sedimentology 44, 1115–1131.

Brill, D., Brückner, H., Jankaew, K., Kelletat, D., Scheffers, A., Scheffers, S., 2011. Potential predecessors of the 2004 Indian Ocean Tsunami—sedimentary evidence of extreme wave events at Ban Bang Sak, SW Thailand. Sedimentary Geology 239, 146–161.

Chagué-Goff, C., Nichol, S., Jenkinson, A., Heijnis, H., 2000. Signatures of natural catastrophic events and anthropogenic impact in an estuarine environment, New Zealand. Marine Geology 167, 285–301.

Chagué-Goff, C., Andrew, A., Szczuciński, W., Goff, J., Nishimura, Y., 2012a. Geochemical signatures up to the maximum inundation of the 2011 Tōhoku-oki tsunami—implications for the 869 AD Jogan and other palaeotsunamis. Sedimentary Geology 282, 65–77.

Chagué-Goff, C., Goff, J., Nichol, S.L., Dudley, W., Zawadzki, A., Bennett, J.W., Mooney, S.D., Fierro, D., Heijnis, H., Dominey-Howes, D., Courtney, C., 2012b. Multi-proxy evidence for trans-Pacific tsunamis in the Hawai'ian Islands. Marine Geology 299–302, 77–89.

Chagué-Goff, C., Goff, J., Wong, H.K.Y., Cisternas, M., 2015. Insights from geochemistry and diatoms to characterise a tsunami's deposit and maximum inundation limit. Marine Geology 359, 22–34.

Cifuentes, I.L., 1989. The 1960 Chilean Earthquakes. Journal of Geophysical Research 94, 665–680.

Cisternas, M., Atwater, B.F., Torrejón, F., Sawai, Y., Machuca, G., Lagos, M., Eipert, A., Youlton, C., Salgado, I., Kamataki, T., Shishikura, M., Rajendran, C.P., Malik, J.K., Rizal, Y., Husni, M., 2005. Predecessors of the giant 1960 Chile earthquake. Nature 437, 404–407.

Dawson, A., Long, D., Smith, D., 1988. The Storegga Slides: evidence from eastern Scotland for a possible tsunami. Marine Geology 82, 271–276.

Dawson, G., Smith, D.E., Shi, S., Dawson, A., Smith, D.E., 1995. Coastal sedimentation associated with the December 12th, 1992 tsunami in Flores, Indonesia. Pure and Applied Geophysics 144, 525–536.

Ely, L.L., Cisternas, M., Wesson, R.L., Dura, T., 2014. Five centuries of tsunamis and landlevel changes in the overlapping rupture area of the 1960 and 2010 Chilean earthquakes. Geology 42, 995–998.

Furusato, E., Tanaka, N., 2014. Maximum sand sedimentation distance after backwash current of tsunami—simple inverse model and laboratory experiments. Marine Geology 353, 128–139.

Garrett, E., Shennan, I., Watcham, E.E.P., Woodroffe, S.S.A., 2013. Reconstructing paleoseismic deformation, 1: modern analogues from the 1960 and 2010 Chilean great earthquakes. Quaternary Science Reviews 75, 11–21.

Garrett, E., Shennan, I., Woodroffe, S.A.A., Cisternas, M., Hocking, E.P.P., Gulliver, P., 2015. Reconstructing paleoseismic deformation, 2: 1000 years of great earthquakes at Chucalén, south central Chile. Quaternary Science Reviews 113, 112–122.

Gelfenbaum, G., Jaffe, B., 2003. Erosion and sedimentation from the 17 July, 1998 Papua New Guinea tsunami. Pure and Applied Geophysics 160, 1969–1999.

Glasser, N.F., Jansson, K.N., Harrison, S., Kleman, J., 2008. The glacial geomorphology and Pleistocene history of South America between 38°S and 56°S. Quaternary Science Reviews 27, 365–390.

Goff, J.R., Lane, E., Arnold, J., 2009. The tsunami geomorphology of coastal dunes. Natural Hazards and Earth System Science 3, 847–854.

Goff, J., Pearce, S., Nichol, S.L., Chagué-Goff, C., Horrocks, M., Strotz, L., 2010. Multi-proxy records of regionally-sourced tsunamis, New Zealand. Geomorphology 118, 369–382.

Goff, J., Chagué-Goff, C., Nichol, S., Jaffe, B., Dominey-Howes, D., 2012. Progress in palaeotsunami research. Sedimentary Geology 243–244, 70–88.

Goto, K., Hashimoto, K., Sugawara, D., Yanagisawa, H., Abe, T., 2014. Spatial thickness variability of the 2011 Tōhoku-oki tsunami deposits along the coastline of Sendai Bay. Marine Geology 358, 38–48.

Heiri, O., Lotter, A.F., Lemcke, G., 2001. Loss on ignition as a method for estimating organic and carbonate content in sediments: reproducibility and comparability of results. Journal of Paleolimnology 25, 101–110.

Hutchinson, I., Clague, J.J., Mathewes, R.W., 1997. Reconstructing the tsunami record on an emerging coast: A case Study of Kanim Lake, Vancouver Island, British Columbia, Canada. Journal of Coastal Research 13, 545–553.

Jackson, K.L., Eberli, G.P., Amelung, F., McFadden, M.A., Moore, A.L., Rankey, E.C., Jayasena, H.A.H., 2014. Holocene Indian Ocean tsunami history in Sri Lanka. Geology 42, 859–862.

Kelsey, H.M., Nelson, A.R., Hemphill-Haley, E., Witter, R.C., 2005. Tsunami history of an Oregon coastal lake reveals a 4600 yr record of great earthquakes on the Cascadia subduction zone. Geological Society of America Bulletin 117, 1009–1032.

Lander, J.F., Lockridge, P., 1989. United States Tsunamis 1690–1988 (including United States possession). National Geophysical Data Center, Boulder, Colorado, pp. 41–42 (publication, v).

McCave, I.N., Geiser, A.C., 1978. Megaripples, ridges and runnels on intertidal flats of the Wash, England. Sedimentology 26, 353–369.

Minoura, K., Nakaya, S., Uchida, M., 1994. Tsunami deposits in a lacustrine sequence of the Sanriku coast, northeast Japan. Sedimentary Geology 89, 25–31.

Minoura, K., Imamura, F., Takahashi, T., Shuto, N., 1997. Sequence of sedimentation processes caused by the 1992 Flores tsunami: evidence from Babi Island. Geology 25, 523–526.

Moernaut, J., Van Daele, M., Heirman, K., Fontijn, K., Strasser, M., Pino, M., Urrutia, R., De Batist, M., 2014. Lacustrine turbidites as a tool for quantitative earthquake reconstruction: new evidence for a variable rupture mode in south central Chile. Journal of Geophysical Research: Solid Earth 119, 1607–1633.

Monecke, K., Anselmetti, F.S., Becker, A., Sturm, M., Giardini, D., 2004. The record of historic earthquakes in lake sediments of Central Switzerland. Tectonophysics 394, 21–40.

Moreno, M.S., Bolte, J., Klotz, J.,Melnick, D., 2009. Impact ofmegathrust geometry on inversion of coseismic slip from geodetic data: application to the 1960 Chile earthquake. Geophysical Research Letters 36, L16310.

Nanayama, F., Furukawa, R., Shigeno, K., Makino, A., Soeda, Y., Igarashi, Y., 2007. Nine unusually large tsunami deposits from the past 4000 years at Kiritappu marsh along the southern Kuril Trench. Sedimentary Geology 200, 275–294.

Nentwig, V., Tsukamoto, S., Frechen, M., Bahlburg, H., 2015. Reconstructing the tsunami record in Tirúa, Central Chile beyond the historical record with quartz-based SAROSL. Quaternary Geochronology 30, 299–305.

Paris, R., Wassmer, P., Sartohadi, J., Lavigne, F., Barthomeuf, B., Desgages, E., Grancher, D., Baumert, P., Vautier, F., Brunstein, D., Gomez, C., 2009. Tsunamis as geomorphic crises: lessons from the December 26, 2004 tsunami in Lhok Nga, West Banda Aceh (Sumatra, Indonesia). Geomorphology 104, 59–72.

Plafker, G., Savage, J.C., 1970. Mechanism of the Chilean Earthquakes of May 21 and 22, 1960. Geological Society of America Bulletin 81, 1001–1030.

Quintana, E., 2011. Environmental impact in Argentina of the nuclear tests, comprehensive nuclear test-ban treaty, science and technology. Nuclear Regulatory Authority (ARN), Argentina.

Reinhardt, E.G., Nairn, R.B., Lopez, G., 2010. Recovery estimates for the Río Cruces after the May 1960 Chilean earthquake. Marine Geology 269, 18–33. Robbins, J., 1978. Geochemical and geophysical applications of radioactive lead isotopes. In: Nriago, J. (Ed.), Biogeochemistry of Lead. Elsevier, Amsterdam, pp. 285–393.

Robbins, J.A., 1978. Geochemical and geophysical applications of radioactive lead. In: J.O. Nriagu (ed.), Biogeochemistry of Lead in the Environment. Elsevier Scientific, Amsterdam, 285-393.

Sawai, Y., Fujii, Y., Fujiwara, O., Kamataki, T., Komatsubara, J., Okamura, Y., Satake, K., Shishikura, M., 2008. Marine incursions of the past 1500 years and evidence of tsunamis at Suijin-numa, a coastal lake facing the Japan Trench. The Holocene 18, 517–528.

Schmidt, S., Howa, H., Diallo, A., Martín, J., Cremer, M., Duros, P., Fontanier, C., Deflandre, B., Metzger, E., Mulder, T., 2014. Recent sediment transport and deposition in the Cap-Ferret Canyon, South-East margin of Bay of Biscay. Deep Sea Research Part II: Topical Studies in Oceanography 104, 134–144.

Schuller, P., Voigt, G., Handl, J., Ellies, A., Oliva, L., 2002. Global weapons' fallout 137Cs in soils and transfer to vegetation in south–central Chile. Journal of Environmental Radioactivity 62, 181–193.

SERNAGEOMIN, 2003. Mapa Geologico de Chile: Version Digital. Gobierno de Chile, Santiago de Chile.

Sievers, H., Villegas, G.C., Barros, G., 1963. The seismic sea wave of 22May 1960 along the Chilean coast. Bulletin of the Seismological Society of America 53, 1125–1190.

Spiske, M., Piepenbreier, J., Benavente, C., Bahlburg, H., 2013. Preservation potential of tsunami deposits on arid siliciclastic coasts. Earth-Science Reviews 126, 58–73.

Strasser, M., Monecke, K., Schnellmann, M., Anselmetti, F.S., 2013. Lake sediments as natural seismographs: a compiled record of Late Quaternary earthquakes in Central Switzerland and its implication for Alpine deformation. Sedimentology 60, 319–341.

Sugawara, D., Minoura, K., Imamura, F., 2008. Chapter 3 – Tsunamis and tsunami sedimentology. In: Minoura, T., Shiki, Y., Tsuji, T., Yamazaki, K. (Eds.), Tsunamiites – Features and Implications. Elsevier, Amsterdam, pp. 9–49.

Szczuciński, W., Kokociński, M., Rzeszewski, M., Chagué-Goff, C., Cachão, M., Goto, K., Sugawara, D., 2012a. Sediment sources and sedimentation processes of 2011 Tōhoku-oki tsunami deposits on the Sendai Plain, Japan—insights from diatoms, nannoliths and grain size distribution. Sedimentary Geology 282, 40–56.

Szczuciński, W., Rachlewicz, G., Chaimanee, N., Saisuttichai, D., Tepsuwan, T., Lorenc, S., 2012b. 26 December 2004 tsunami deposits left in areas of various tsunami run-up in coastal zone of Thailand. Earth, Planets and Space 64, 843–858.

Thompson, R., Morton, D.J., 1979. Magnetic susceptibility and particle-size distribution in recent sediments of the Loch Lomond Drainage Basin, Scotland. Journal of Sedimentary Petrology 49, 801–812.

Van Daele, M., Moernaut, J., Doom, L., Boes, E., Fontijn, K., Heirman, K., Vandoorne, W., Hebbeln, D., Pino, M., Urrutia, R., Brümmer, R., De Batist, M., 2015. A comparison of the sedimentary records of the 1960 and 2010 great Chilean earthquakes in 17 lakes: implications for quantitative lacustrine palaeoseismology. Sedimentology 62 (5), 1466–1496.

Villalobos, L., Parra, O., Grandjean, M., Jaque, E., Woelfl, S., Campos, H., 2003. A study of the river basins and limnology of five humic lakes on Chiloé Island. Revista Chilena de Historia Natural 76, 563–590.

Vitousek, M.J., 1963. The tsunami of 22 May 1960 in French Polynesia. Bulletin of the Seismological Society of America 53, 1229–1236.

Weisner, L., 2003. Cucao - Tierra de Soledades. 1st ed. RIL Editores, Santiago de Chile.

Witter, R.C., Kelsey, H.M., Hemphill-Haley, E., 2003. Great Cascadia earthquakes and tsunamis of the past 6700 years, Coquille River estuary, southern coastal Oregon. Geological Society of America Bulletin 115, 1289–1306.

Witter, R.C., Zhang, Y., Wang, K., Goldfinger, C., Priest, G.R., Allan, J.C., 2012. Co-seismic slip on the southern Cascadia megathrust implied by tsunami deposits in an Oregon lake and earthquake-triggered marine turbidites. Journal of Geophysical Research 117, B10303.

Yamada, M., Fujino, S., Goto, K., 2014. Deposition of sediments of diverse sizes by the 2011 Tōhoku-oki tsunami at Miyako City, Japan. Marine Geology 358, 67–78.

"Je n'ai fait celle-ci plus longue que parce que je n'ai pas eu le loisir de la faire plus courte."
"I have made this [letter] rather long, because I have not had the time to make it shorter."

AD 1656, Blaise Pascal in *Lettres provinciales* (letter XVI)

4 Bimodal recurrence pattern of tsunamis

A modified version of this chapter will be submitted for publication as:

Bimodal recurrence pattern of tsunamis in south central Chile

Kempf, P., Moernaut, J., Van Daele, M., Vandoorne, W., Messens, F., Vandenberghe, D., Pino, M., Urrutia, R., De Batist, M.

Abstract: Tsunamis are among the greatest geohazards to coastal communities, especially for coastlines on subduction zones, where large megathrust earthquakes can occur relatively frequently. For tsunami hazard assessments, recurrence time and pattern of tsunamigenic earthquakes are commonly modelled with a Poisson distribution, which, as we demonstrate, does not necessarily represent tsunami recurrence correctly. Limited continuity and number of tsunami deposits in most sedimentary archives hampers reliable recurrence pattern analyses. Here we present a new 5500 yrs long and continuous record with 17 detrital layers from Lake Huelde, a coastal lake on Isla de Chiloé, in south central Chile – the area of the giant AD 1960 earthquake (M_W 9.5) and tsunami. The detrital layers are interpreted as tsunami deposits with varying levels of confidence. Results of Cs- and Pb-dating, infrared stimulated luminescence (IRSL) dating and radiocarbon dating are used as input for Bayesian age-depth modelling. The inferred mean recurrence time of ~325 yrs broadly agrees with the existing regional paleoseismic and paleotsunami records. However, our record reveals a large temporal variability between tsunami events, which forms a bimodal pattern with peaks at ~115 and ~490 yrs. As the mean recurrence time coincides with the lowest probability, we conclude that the sense of safety in coastal communities in south central Chile, 55 yrs after the last catastrophe, may be deceiving. A tsunamigenic earthquake in the near future would not redefine the extremes of the presented record.

Contributions: The manuscript was written by PK. Fieldwork was conducted by PK, JM, MVD and WV, and facilitated by MP and RU. Discussion of results and interpretation were done by PK, JM, MVD and MDB. FM, DV and PK conducted the IRSL analysis. All other analyses were done by PK.

4.1 Introduction

Modern tsunami risk mitigation plans are based on the results of probabilistic tsunami hazard assessments (PTHAs), in which tsunami source parameters are defined and a recurrence probability model is applied to the source (Geist and Lynett, 2014). So far, tsunami sources, in the case of seismic triggering, have been modelled to recur independently from previous earthquakes, most commonly with a Poisson distribution, around a paleoseismologically established mean recurrence time. It has been recognized, however, that tsunami generation may have a more complex recurrence pattern, because different earthquake types and magnitudes can trigger tsunamis. Paleotsunami data are used to refine models, but PTHAs with paleotsunami data with a complex recurrence pattern as input do not exist. General lack of knowledge of tsunamigenic earthquakes from historical records and unaccounted variability in recurrence times can lead to costly overprotection of coastal areas or to an insufficiently prepared population exposed to a great hazard. Extreme examples are the unexpectedly catastrophic AD 2004 Indian Ocean earthquake and tsunami in Sumatra and the AD 2011 Tōhoku earthquake and tsunami in northern Japan.

A high magnitude earthquake record (e.g. $M_W \geq 9$) must include 5 or more events to determine the mean recurrence time with reasonably low uncertainty. However, under the assumption of temporal independence (Poisson distribution) ~20 or more events in a record are necessary to reliably assess the variability in recurrence times (McCaffrey, 2008). Given the often multi-centennial recurrence times of tsunamigenic earthquakes, regional historical records rarely include more than 5 events (Ando, 1975; Lomnitz, 2004, 1970). With few exceptions, like the records from the Cascadia subduction zone (Goldfinger et al., 2012; Kelsey et al., 2005) or the Hikurangi subduction zone (Gomez et al., 2015; Pouderoux et al., 2014, 2012), most subduction zone paleoseismic and paleotsunami records are also too short or lack continuity to determine the recurrence time variability. Rapid stress recovery after giant earthquakes indicates virtually time-independent earthquake occurrence on some subduction zones (Tormann et al., 2015). At the same time, subduction zones with wide seismogenic zones may rupture time-dependently in supercycles (Goldfinger et al., 2013; Herrendorfer et al., 2015). The efficiency of translating elastically stored seismic moment to tsunami energy is dependent on the amount, rate and direction of co-seismic seafloor deformation. Therefore, complex slip distributions (Kaneko et al., 2010), changing rupture depths (Ely et al., 2014; Lay et al., 2012), shallow tsunami earthquakes (Satake et al., 2013) and incomplete segment ruptures (Satake and Atwater, 2007) add variability to the recurrence pattern of large-scale tsunamis.

4.2 Setting

Lake Huelde (74.11° E, 42.59° S) is a small (1.49 km²) coastal lake on the west coast of Isla de Chiloé, south central Chile (Fig. 4.1), and an ideal recorder of tsunami inundation (Kempf et al., 2015). Tsunamis need to inundate 1.1 km eastward to reach the lake. Beach and dunes provide loose sediment for entrainment and subsequent deposition in the lake. The lake level is at ~1 m altitude. A small stream enters the lake from the northeast and Lake Huelde discharges water in the southwest to the ocean at all times. This means that Lake Huelde is currently a freshwater lake without a saline bottom water body. The deepest part of Lake Huelde is 11 m deep, which makes the deepest part ~10 m below current sea-level. The lake basin is surrounded by glacifluvial terraces at ~45 m altitude. The sill, which separates Lake Huelde from the Pacific Ocean, consists of aeolian sediments.

The historical record in south central Chile reports strong earthquakes in AD 1960, AD 1837, AD 1737 and AD 1575 (Cisternas et al., 2005; Lomnitz, 2004, 1970), for which only the AD 1737 event has neither written nor geological evidence of a tsunami. Multiple studies extend the sedimentary record by two large-scale earthquakes and tsunamis in AD 1319 ± 9 and AD 1127 ± 44 (Cisternas et al., 2005; Moernaut et al., 2014; Garrett et al., 2015). A record from Maullín (Fig. 4.1)

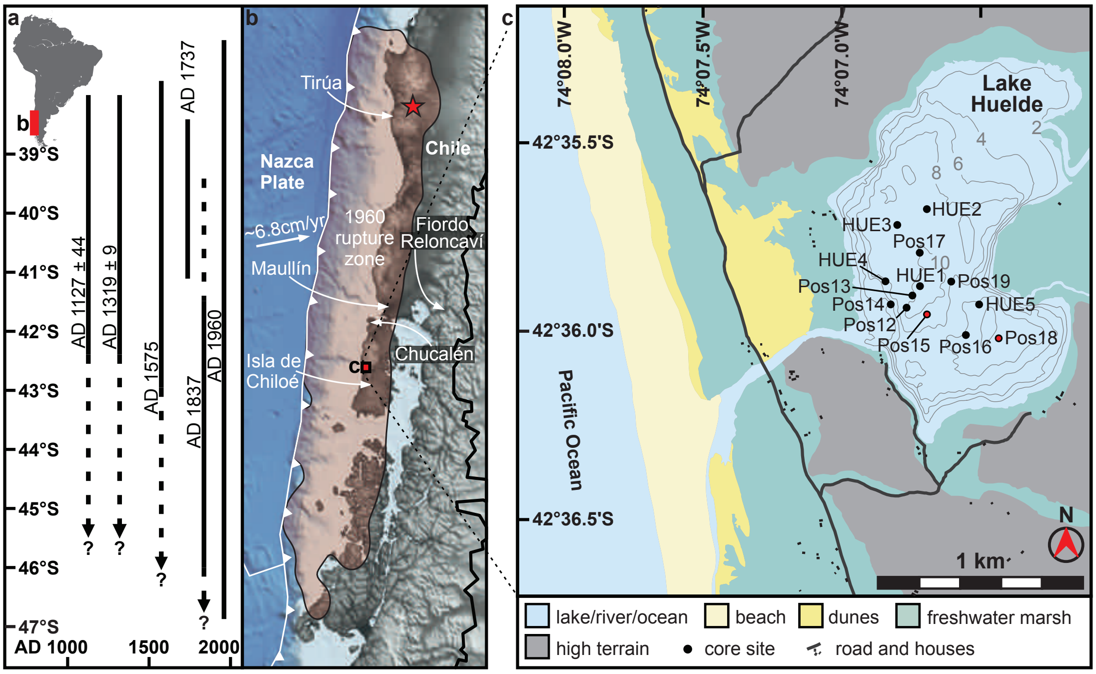

Figure 4.1: a) Overview map of the study area with rupture lengths of past megathrust earthquakes. b) The AD 1960 earthquake rupture zone (>1 m slip contour) is represented by a red semi-transparent overlay (Moreno et al., 2009) and the epicenter as a red star. The digital elevation model is an ETOPO1 dataset (Amante and Eakins, 2009). c) Physiographic map of the study area with core locations (black dots) from Lake Huelde. The cores used for the master core are highlighted (red dots).

of co-seismic subsidence and tsunami deposits introduces four otherwise unknown events from AD 1 to AD 1127 and infers a mean recurrence time of ~285 yrs (Cisternas et al., 2005). The short time (55 yrs) since the last great earthquake and tsunami would suggest relative safety to local infrastructure and people for now. However, this assuring implication may be flawed. We argue that the growing evidence of temporal and spatial variability in tsunami recurrence commands consideration of complex recurrence patterns in tsunami hazard assessments. We underpin our argument with a long and continuous paleotsunami record from south central Chile, which gives evidence for a bimodal recurrence pattern of large-scale tsunamis.

4.3 Methods

4.3.1 Acousting imaging

Cores of lake sediments only become meaningful in their sedimentary context. To understand this context we surveyed Lake Huelde with a Geopulse Pinger sub-bottom profiler and a Klein 3000 side scan sonar. The sub-bottom profiles have a vertical resolution between 10 and 20 cm. Biogenic gas in the sediment often prevents acoustic penetration, but acoustic windows allow imaging of numerous buried high amplitude reflectors.
The side scan sonar map is obtained at frequencies of 100 and 500 kHz with a 50 m wide swath covering the entire lake. The resulting horizontal resolution is 8 to 40 cm, depending on the

swath angle. Navigation line smoothening, slant range correction, mosaic selection and bottom track extraction for a bathymetric map are performed with the software SonarWizMap 4. Sub-bottom profiles and the side scan sonar map are published in Kempf et al. (2015).

4.3.2 Sediment analysis

Sediment cores recovered up to 9 m of lake sediment. Every coring site consists of a Swiss gravity core at the top for an undisturbed sediment sample of the soft lake floor. Long cores are achieved by overlapping 3-m-long UWITEC piston hammer cores. The inner core diameter of both gravity and piston hammer cores is 6.0 cm.

All cores were analysed with a Geotek multi sensor core logger (MSCL) measuring γ-ray attenuation density and magnetic susceptibility. Split core surface images were taken with a line scan camera mounted on the MSCL. Several cores were CT-scanned with a Siemens Flash medical CT-Scanner with a voxel size of 0.15 mm $\times$ 0.15 mm $\times$ 0.6 mm (xyz). The results of these analyses facilitated sediment description, correlation and interpretation, which are visualised in the core logs.

4.3.3 Age-depth modelling

We applied the age-depth information to two age-depth model algorithms to avoid algorithm-specific artifacts. One of two age-depth models presented here is calculated with an R-based algorithm called Bacon (Blaauw and Christen, 2011). Bacon uses Bayesian statistics to reconstruct the accumulation history by combining radiocarbon dates, infrared stimulated lumniscence (IRSL) dating, the ^{137}Cs peak and ^{210}Pb dating, with prior information, e.g. accumulation rate and the variability thereof. The IRSL dating was performed at Ghent University directly on tsunami sands. Radiocarbon samples were analysed at the ^{14}Chrono Centre for Climate, the Environment, and Chronology at Queen's University, Belfast. The ^{14}C-ages were calibrated with the latest Southern Hemisphere atmospheric calibration curve, SHCal13 (Hogg et al., 2013).

Bacon divides the core into 100–200 sections and through Markov Chain Monte Carlo (MCMC) iterations estimates the accumulation rate for each section. Combined with the age-depth information these accumulation rates then form the age-depth model. Intervals of extremely high accumulation rates, e.g. tsunami deposits, can be treated as instantaneously deposited layers.

A time interval of non-deposition or erosion can be inserted into the model as a hiatus. The age-depth model quantifies the modelled hiatus with a probability density function (PDF). The model allows extraction of age PDFs for each tsunami deposit. This way the probabilistic character of radiocarbon dates and age-depth modelling is not lost in the process. The PDFs of two tsunami deposit ages can be subtracted; the result is a PDF for the recurrence time between the two tsunamis. The average of all recurrence time PDFs displays the overall probability density of recurrence time for tsunami deposition in Lake Huelde. The Bacon age-depth model is used for the regional correlation of tsunami deposits.

The other age depth model was calculated using a P_Sequence in OxCal v.4.2 (Ramsey, 2008) with a k-variable of 0.3 (Bronk Ramsey and Lee, 2013). The tsunami deposits were removed from the master core log for age depth modelling purposes. The age depth model is then computed in similar fashion to the Bacon algorithm using Bayesian statistics and MCMC iterations. The tsunami ages and recurrence time PDFs were calculated within OxCal making use of the Difference()-function. For the overall recurrence pattern the recurrence time PDFs had to be exported as tables with 5-year bin sizes.

The age-depth model output of both algorithms agree with each other to a large extent. Model-specific artifacts, if they exist in the presented age-depth relationships, are therefore considered negligible.

4.4 Results and discussion

4.4.1 Lake Huelde sediment

Lake Huelde's sediment is mostly dark brown gyttja. The gyttja consists of silt and a wide range of particles of organic matter, e.g. seeds, pollen, diatoms, multicellular algae, leaves and other plant fragments. The gyttja is mostly homogenous, however, some intervals are finely (1–2 mm) laminated. These finely laminated intervals share similarities with varves from other lakes in south central Chile (cf. Boës and Fagel, 2007; Fagel et al., 2007). Furthermore, the finely laminated intervals almost always have a detrital layer (which are described below) at their basal contact. Towards the top, the laminae gradually transition into homogenous gyttja. The laminae consist of dark brown and yellowish grey layer couplets. Similar couplets in a coastal lake in Cascadia were interpreted as annual layers, i.e. varves (Kelsey et al., 2005). The gyttja's magnetic susceptibility is low with values usually between 0 and 30×10^{-5} SI. In few cases the magnetic susceptibility is as high as 50×10^{-5} SI. The gyttja makes up ~85 % of the retrieved sedimentary record of Lake Huelde.

Sporadically, the gyttja-dominated stratigraphy incorporates thin (0.1–0.5 cm) grey layers (Fig. 4.2). The thin layers lack the organic content of the gyttja. Silty, transparent and amorphous shards (glass) make up almost the entire mineral content. The thin grey layers occur either as singular layers or in groups of two or three. Their distribution within the stratigraphy concentrates on the lower half of the sedimentary record. The thin grey layers often form a distinct pattern, which appears to be identical in the entire lake basin. Their basin-wide distribution makes them a useful tool for core-to-core correlation (Fig. 4.2). Their relative abundance in the sedimentary record of Lake Huelde is below 1 % of the entire stratigraphy. Because of the amorphous mineral content and the fine grain size, we interpret these thin grey layers as tephras, i.e. volcanic ash. The ash layers are similar to the distal lake record of an ash layer in Lake Puyehue, which was produced by the AD 2011 Cordon-Caulle eruption in central Chile (Bertrand et al., 2014).

Detrital layers interrupt the gyttja-dominated sediment frequently. We label the detrital layers with the prefix "h" for "Huelde" followed by a capital letter running in alphabetical order down the stratigraphic order. The detrital layers contain three sediment facies: i) mud rip-up clasts in sandy matrix, ii) massive sand and iii) mud caps. All three facies together comprise a full sequence from bottom to top, i.e. mud rip-up clasts under massive sand under mud caps. There are 17 separate detrital layers in the Lake Huelde sedimentary record, which can consist of multiple sequences of the described facies above or subsets thereof.

The uppermost detrital layer was interpreted as the AD 1960 tsunami deposit in chapter 3, where these facies where described in detail (Fig. 3.4 on page 49). The detrital layers vary strongly in their lateral extent, thickness, maximum and average magnetic susceptibility from core to core and from detrital layer to detrital layer. Respectively, detrital layers can be recovered in only one core or many cores from the entire lake basin. They can be between 0.5 and 130 cm thick and their maximum magnetic susceptibility ranges from 92–3791 $\times 10^{-5}$ SI. Some of the thicker and sandier detrital layers were suitable for luminescence dating.

4.4.2 Core chronology

To date the detrital layers we calculate age-depth models in Bacon (Blaauw and Christen, 2011) and OxCal (Ramsey, 2008) (Figs. 4.3, 4.4). The age-depth models of the master core draw information from four independent dating techniques: 1) the mid-1960s are identified using the nuclear bomb-testing peak in a ^{137}Cs profile (Kempf et al., 2015); 2) an accumulation rate model based on excess ^{210}Pb activity puts the top of the uppermost detrital layer in the age range of AD 1961 ± 5, thus dating the AD 1960 tsunami deposit (Kempf et al., 2015); 3) feldspars from the basal sand unit in the uppermost superimposed detrital layers were dated to AD 1839 ± 20 using IRSL-dating, giving evidence of the historically reported AD 1837 tsunami in the Lake Huelde record (Messens, 2014) and 4) 23 radiocarbon dates (Tab. 4.1) of terrestrial plant fragments from gyttja provide data coverage for the record in depths greater than ~1 m. The base of the master core dates to 5515 ± 140 cal. yrs BP.

Four varved intervals of gyttja above detrital layers hI, hJ, hK and hM are varve-counted. The accumulation rate produced by the Bacon age-depth model can be compared with the varve-counted accumulation rate at the same depth as an independent control. Pairs of modelled and varve-counted accumulation rates above detrital layers hI (modelled: 3.06 mm yr^{-1}; varve-counted: 3.10 mm yr^{-1}), hJ (modelled: 2.47 mm yr^{-1}; varve-counted: 3.28 mm yr^{-1}), hK (modelled: 1.73 mm yr^{-1}; varve-counted: 2.00 mm yr^{-1}) and hM (modelled: 1.52 mm yr^{-1}; varve-counted: 1.62 mm yr^{-1}) show identical variation. This indicates that the accumulation rate variations in the age-depth model are real and do not stem from unsuited radiocarbon samples.

4.4.3 Criteria for tsunami deposit interpretation

We hypothesize that all described detrital layers are tsunami deposits, because they share sedimentary characteristics with the uppermost detrital layer, which was identified as the AD 1960 tsunami deposit (Kempf et al., 2015). To support the tsunami deposit interpretation we discuss the following criteria. They are not stand-alone criteria, however, together these criteria make a good case for tsunami deposition and can be used to exclude other causative processes, if fulfilled.

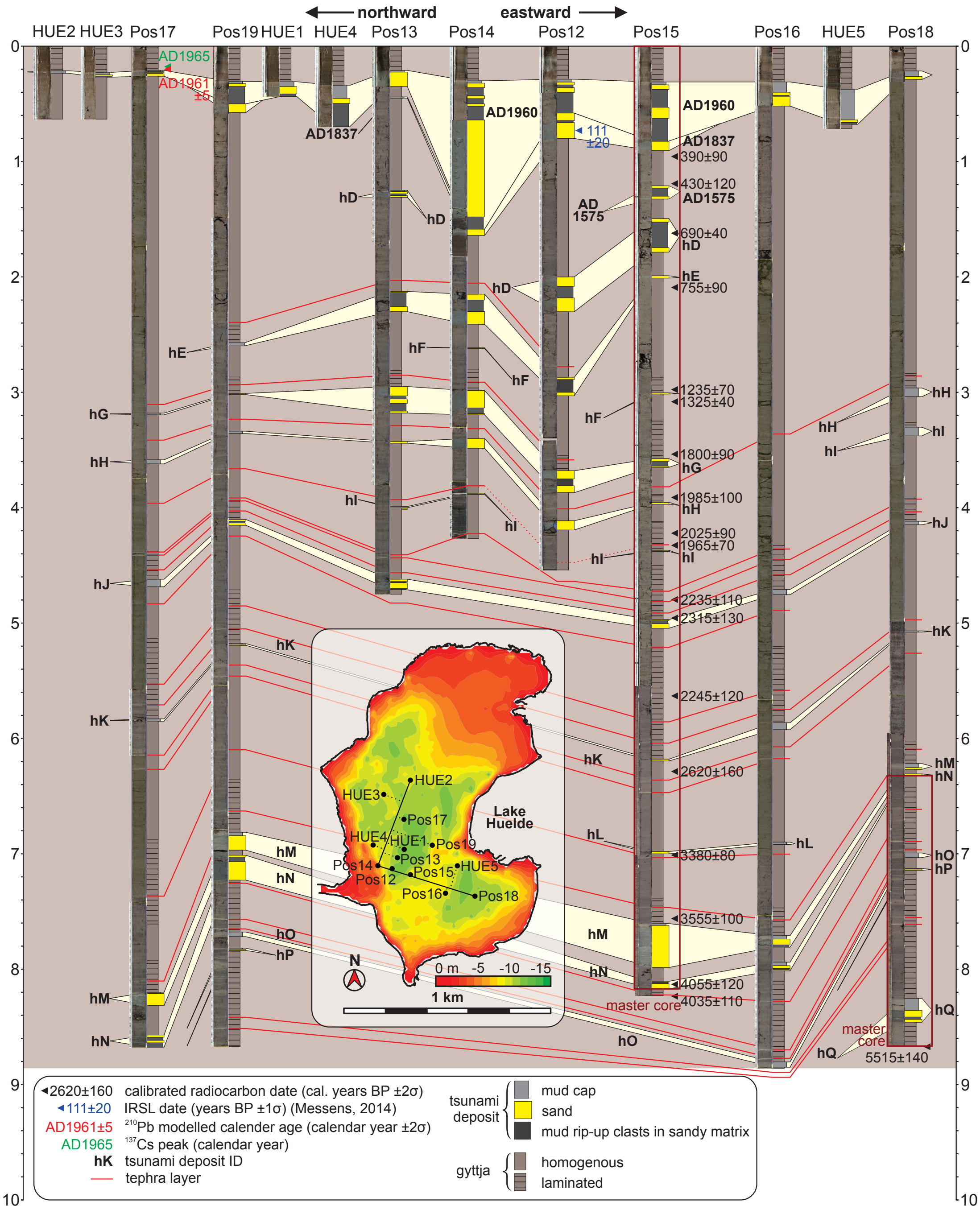

Figure 4.2: Core correlation with indication for master core sections (red rectangles on cores Pos15 and Pos18), age information, and correlated tsunami deposits. The core-to-core correlation is based on thin, grey tephra layers, CT-scans and magnetic susceptibility logs. ^{14}C-ages that were rejected by the age depth model in figure 4.3 are not annotated.

Table 4.1: Radiocarbon data for fossil plant fragments from the master core in Lake Huelde. The samples were analysed at the ^{14}Chrono Centre for Climate, the Environment, and Chronology, Queen's University, Belfast, Northern Ireland.

lab ID	depth (cm)	material	^{14}C age ± 1σ (^{14}C yrs)	δ^{13}C (‰)	calibrated 2σ ranges (cal. yrs BP)	relative probability (%)
UBA-23494	95	plant fragments	317±31	-29.0	300-470	95.4
UBA-23326	123.5	plant fragments	369±36	-28.7	315-415	44.3
					420-505	51.1
UBA-21474	143	wood	1214±34	-27.5	980-1178	95.4
UBA-23495	161.5	plant fragments	760±31	-27.9	665-735	95.4
UBA-23327	208.5	plant fragments	848±31	-25.6	685-800	90.5
					870-900	4.9
UBA-23802	249.5	plant fragments	1694±30	-27.7	1433-1441	0.9
					1457-1462	0.5
					1468-1613	90.0
					1663-1695	4.1
UBA-23328	301	plant fragments	1289±29	-29.8	1180-1290	95.4
UBA-23803	311.5	plant fragments	1423±32	-26.7	1290-1375	95.4
UBA-23804	359	plant fragments	1863±29	-27.0	1720-1875	95.4
UBA-23329	398.5	single leaf	2032±32	-21.8	1895-2065	90.8
					2080-2110	4.6
UBA-23500	429.5	plant fragments	2056±30	-27.5	1945-2120	95.4
UBA-23330	435	plant fragments	2015±27	-32.4	1890-2010	91.1
					2015-2040	4.3
UBA-23805	479	plant fragments	2201±31	-26.5	2130-2320	95.4
UBA-21475	495	plant fragments	2292±43	-20.9	2150-2275	41.4
					2290-2360	54.0
UBA-23331	562.5	plant fragments	2266±34	-24.3	2155-2265	53.3
					2295-2350	42.1
UBA-23502	583	plant fragments	6628±42	-29.3	7429-7566	95.4
UBA-23332	621	wood	3029±39	-25.5	3004-3259	88.2
					3291-3334	7.2
UBA-23843	628	plant fragments	2533±35	-27.4	2490-2645	58.9
					2655-2670	1.0
					2675-2750	35.6
UBA-23333	700.5	plant fragments	3155±31	-29.9	3265-3290	5.4
					3330-3450	90.0
UBA-23504	755.5	plant fragments	3325±34	-33.1	3460-3640	95.4
UBA-23334	812.5	plant fragments	3718±38	-26.2	3925-3945	1.6
					3965-4160	92.3
					4205-4225	1.5
UBA-21477	829	single culm	3692±35	-27.5	3920-4105	87.8
					4110-4150	7.6
UBA-21473	1056.5	single culm	4757±36	-31.2	5330-5380	12.8
					5455-5590	82.6

Table 4.2: Tsunami deposit data and age information. Reported ages are extracted from the Bacon age-depth model (Fig. 4.3).

tsunami deposit ID	2σ range of modelled age (cal. yrs BP)	median (cal. yrs BP)	reported as (AD or cal. yrs BP)	age information source
AD 1960	-12 - -6	-10	AD 1960	Cisternas et al., 2005; Lomnitz, 1970, 2004
AD 1837	101 - 121	111	AD 1837	Cisternas et al., 2005; Lomnitz, 1970, 2004
AD 1575	303 - 483	397	AD 1575	Cisternas et al., 2005; Lomnitz, 1970, 2004
hD	553 - 670	593	AD 1355 ± 60/AD 1319 ± 9	this study/Moernaut et al., 2014
hE	655 - 764	704	AD 1245 ± 55/AD 1127 ± 44	this study/Moernaut et al., 2014
hF	1185 1291	1253	1250 ± 50 cal. yrs BP	this study
hG	1604 - 1786	1693	1690 ± 90 cal. yrs BP	this study
hH	1761 - 1926	1856	1860 ± 80 cal. yrs BP	this study
hI	1903 - 2006	1962	1960 ± 50 cal. yrs BP	this study
hJ	2128 - 2302	2200	2200 ± 90 cal. yrs BP	this study
hK	2563 - 2821	2672	2670 ± 130 cal. yrs BP	this study
hL	3182 - 3407	3299	3300 ± 110 cal. yrs BP	this study
hM	3590 - 3897	3742	3740 ± 150 cal. yrs BP	this study
hN	3729 - 4011	3889	3890 ± 140 cal. yrs BP	this study
hO	4156 - 4535	4342	4340 ± 190 cal. yrs BP	this study
hP	4209 - 4603	4403	4400 ± 200 cal. yrs BP	this study
hQ	4962 - 5360	5162	5160 ± 200 cal. yrs BP	this study

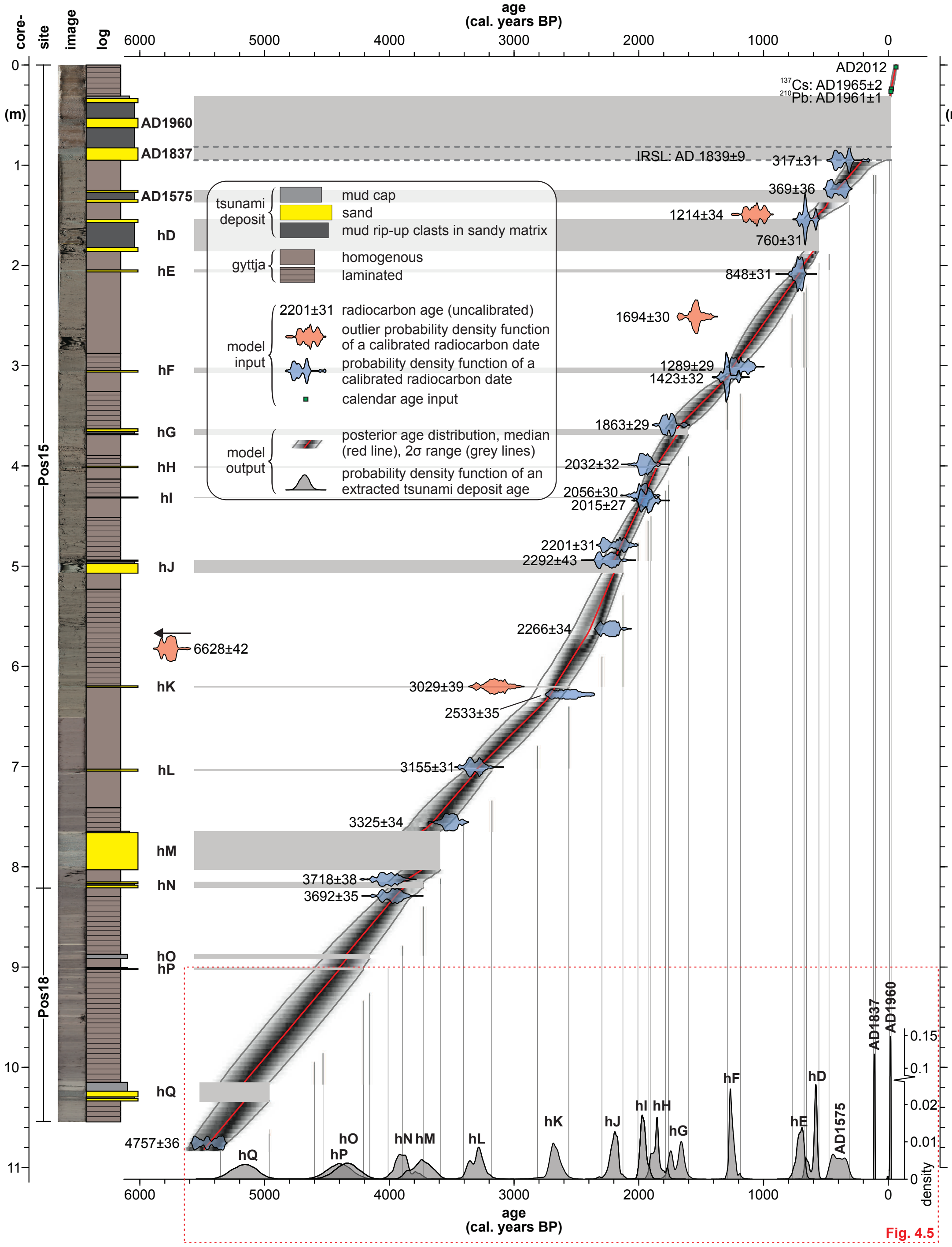

Figure 4.3: Bacon-based age-depth model of Lake Huelde's master core. The core sites, images and log on the left together with the age information (mostly radiocarbon dates) give input to the age-depth model algorithm. Tsunami deposits (horizontal grey bars) are considered instantaneous deposits.

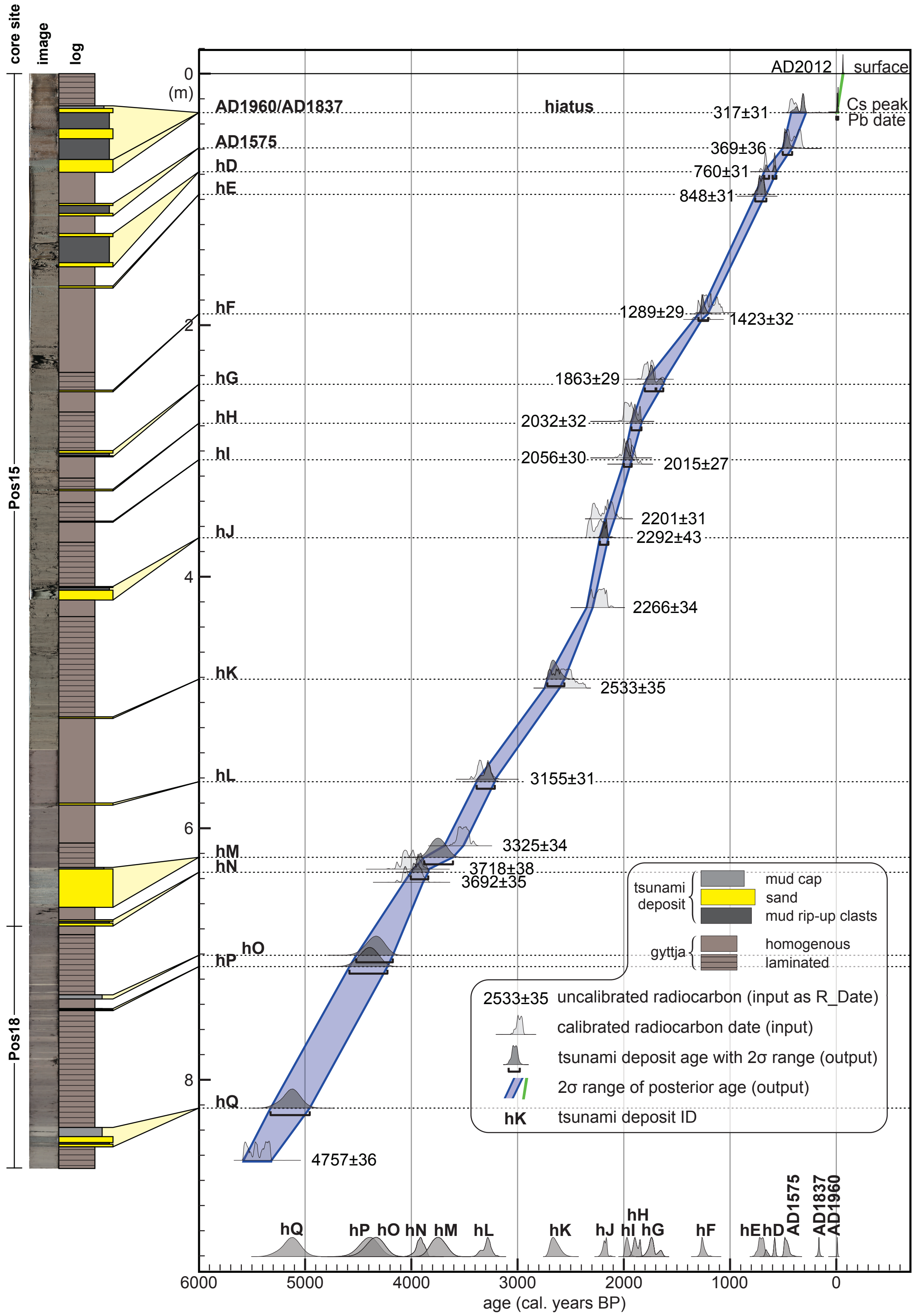

Figure 4.4: OxCal's P_Sequence-based age-depth model of Lake Huelde's master core. The core sites, images and log on the left, together with the age information (mostly radiocarbon dates; R_Dates) give input to the P_Sequence algorithm. The depth is corrected by removing the instantaneous tsunami deposits from the core log. The tsunami deposit age is extracted, where the deposit was removed from the model.

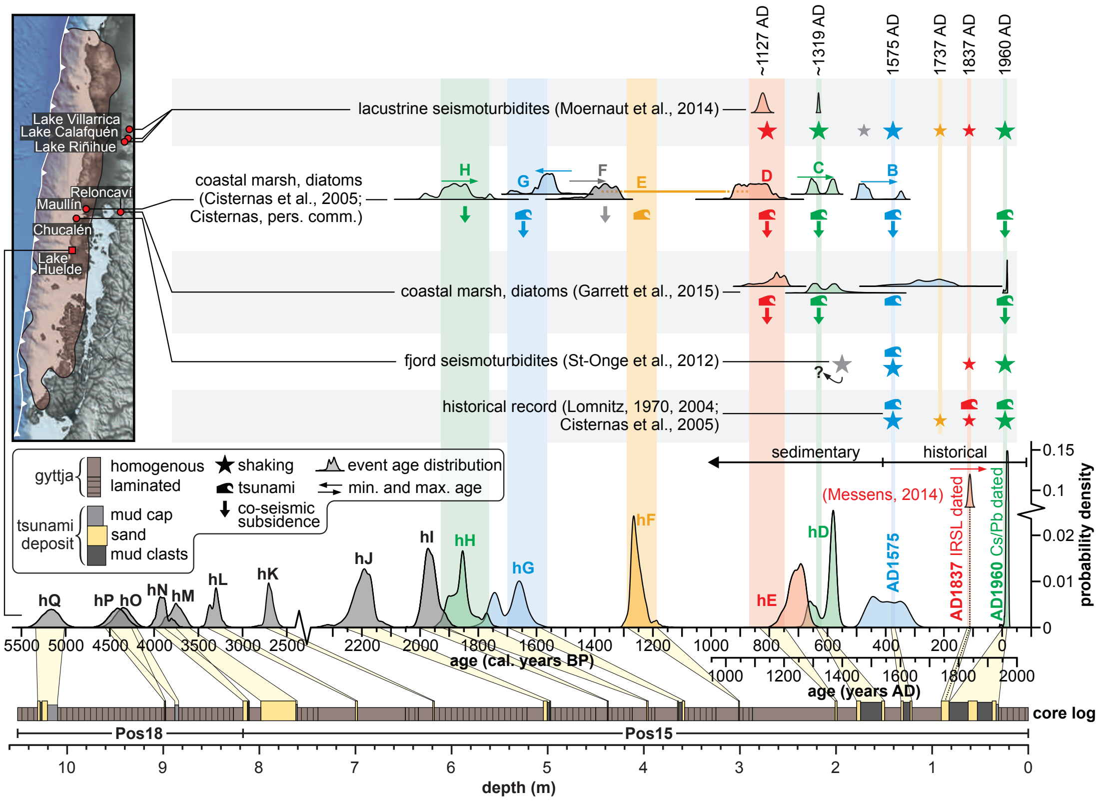

Figure 4.5: Comparison between dates for tsunami deposits from Lake Huelde (grey and colored probability density functions) and known historical and prehistoric records of shaking (stars), co-seismic subsidence (downward arrows) and tsunami deposition (waves).

i **high magnetic susceptibility** – The mineral content in the sediment cores controls the magnetic susceptibility. The sedimentary surrounding of Lake Huelde consists of glacifluvial terraces in the north, east and south (Glasser et al., 2008). The glacifluvial terraces contain glacially eroded metamorphic rocks of the Paleozoic and Triassic Cordillera de Pirulil (a part of Chile's Coastal Cordillera) to the east of the study area (SERNAGEOMIN, 2003). Dunes and beaches dominate the sediment to the west of the lake (Kempf et al., 2015). All source sediments have high magnetic susceptibilities, while the lacustrine sediment, i.e. gyttja, has a low magnetic susceptibility. High magnetic susceptibility in lake sediment therefore means that there is an increased input from outside of the lake. This is a site-specific criterion for recognizing deposit with sediment sources outside Lake Huelde. This criterion cannot be translated to other study areas without prior investigation of the study area.

ii **traceability in the sedimentary record** – Tsunamis are typically large-scale inundations, which interrupt the normal lake sediment accumulation. Tsunami deposits on land are often described as quasi-continuous deposits, which wedge out towards their maximum lateral extent with a high degree of variability in thickness (e.g. Goto et al., 2014). In lakes tsunamis erode the typically muddy lacustrine sediment and deposit reworked muddy sediment beyond the lateral extent of sand deposition (Kelsey et al., 2005; Kempf et al., 2015). Therefore tsunamis should be traceable throughout large parts of the Lake Huelde. Therefore, we consider representation in most parts of the lake basin indicative of tsunami origin.

iii **mud rip-up clasts** – Momentarily extreme flow conditions in otherwise low flow energy environments have the potential to erode fine-grained and cohesive sediment in bulk pieces. These pieces are called mud rip-up clasts and tsunamis belong to the short list of their causative processes (e.g. Bondevik et al., 1997; Peters et al., 2007) together with a range of mass transport processes (e.g. Lee et al., 2013) and storm surges (e.g. Phantuwongraj et al., 2013). Large-scale mass transport processes can be excluded, because of the lack of long or steep slopes in the comparatively small and shallow Lake Huelde.

iv **age-correlation** – The AD 1960 tsunami deposit in Lake Huelde was identified through precise dating (Kempf et al., 2015). Megathrust earthquake-induced tsunamis usually hit coastlines of a 100 km or more (e.g. Fritz et al., 2011; Mori et al., 2011). Similarly, if older detrital layers in Lake Huelde coincide chronologically with regionally known tsunami deposits, then a correlation across study areas seems likely. This criterion can only be applied to detrital layers of an equal or younger age than the oldest regionally known tsunami deposits. For south central Chile, tsunami deposits are known for the last ~2000 yrs (Cisternas et al., 2005).

The criteria above are also indicative of storm surge deposits. Generally, the differentiation between storm surge and tsunami deposits is a difficult issue at most subduction zone coastlines. There is little data about storm surges or the deposits thereof in Chile. The few sites that have been studied, however, are confined to beaches under persistent stormy conditions (May et al., 2013). At our study site, we bypass this differentiation problem, because tropical cyclones, which could have the potential to produce a deposit more than 1 km inland, do not occur on the western South American coast – not even under more favorable El Niño conditions (Fedorov et al., 2010). Fulfilling the criteria is therefore treated as indicative for tsunami origin only. Confidence in the tsunami interpretation depends on the degree to which the criteria are fulfilled (Tab. 4.3).

Eventually, we interpret all detrital layers to be tsunami deposits. However, 3 of the 17 detrital layers (hF, hL and hO) only fulfill one or none of the defined criteria. These 3 deposits are represented in only 3 cores or less. With the variability of tsunami deposits in mind, this interpretation is speculative. However, by analogy to the other detrital layers the tsunami interpretation is most plausible, especially considering the absence of competing plausible explanations. We interpret 4 detrital layers as tsunami deposits with medium level confidence (AD 1575, hI, hK and hP). They fulfill at least two of the four or three applicable criteria. Leaving 10 detrital layers (AD 1960, AD 1837, hD, hE, hG, hH, hJ, hM, hN and hQ), which we interpret as tsunami deposits with a high level of confidence. All 10 detrital layers fulfill at least three criteria (Tab. 4.3).

Table 4.3: Summary of confidence levels for the interpretation of tsunami deposits for each detrital layer in Lake Huelde, with maximum magnetic susceptibility, traceability of the detrital layers throughout the sedimentary record, correlation to acoustic reflections, content of mud rip-up clasts, age-correlation to a known tsunami. Characteristics written in green contribute to confidence, red denotes doubt and black stands for neutral or inconclusive characteristics.

detrital layer ID	max. magnetic susceptibility $\times 10^{-5}$ SI	traceability in the sedimentary record in cores / total cores	mud rip-up clasts	age-correlated to other tsunami deposits	confidence level
AD 1960	1794	13/13	yes	AD 1960	high
AD 1837	1585	5/8?	yes	AD 1837	high
AD 1575	763	1/8 (very low)	yes	AD 1575	medium
hD	865	3/8	yes	event C (Cisternas et al., 2005; Garrett et al., 2015)	high
hE	816	5/8	yes	event D (Cisternas et al., 2005; Garrett et al., 2015)	high
hF	92 (very low)	2/8	not observed	event E (Cisternas et al., 2005)	low
hG	1367	6/8	yes	event G (Cisternas et al., 2005)	high
hH	773	7/8	not observed	event H (Cisternas et al., 2005)	high
hI	310	4/7	not observed	preceeds all other regional records	medium
hJ	1030	6/6	yes	preceeds all other regional records	high
hK	162	5/5	yes	preceeds all other regional records	medium
hL	172	2/5	not observed	preceeds all other regional records	low
hM	2480	5/5	yes	preceeds all other regional records	high
hN	3791	5/5	yes	preceeds all other regional records	high
hO	200	3/3	not observed	preceeds all other regional records	low
hP	132	2/2	yes	preceeds all other regional records	medium
hQ	877	1/1	yes	preceeds all other regional records	high

4.5 Regional historical and paleoseismic records

In AD 1960, the Great Chilean Earthquake (M_W 9.5) with its rupture zone mostly offshore (Moreno et al., 2009), triggered a tsunami with up to 20 m wave height along the coast (Sievers et al., 1963). The tsunami caused vast damage and casualties in both near-field and far-field areas (Lander and Lockridge, 1989). Reciprocally, it remains unclear whether similar far-field sources can produce large tsunamis on the Chilean coast. Tsunami deposits of the AD 1960 event are described along the central and northern part of the rupture zone (Fig. 4.1), including on Isla de Chiloé (Atwater et al., 2013; Cisternas et al., 2005; Ely et al., 2014; Garrett et al., 2013). Lake Huelde was inundated by the AD 1960 tsunami through the outlet river channel and by barrier overspill (Kempf et al., 2015).

The historical sedimentary records describe an earthquake in AD 1837 with a speculated rupture zone in the southern half of the 1960 rupture zone (Cisternas et al., 2005; Garrett et al., 2015; Lomnitz, 2004, 1970; Moernaut et al., 2014). The subsequent tsunami damaged buildings on Isla de Chiloé and in far-field regions, e.g. in Hawaii and Japan (Cisternas et al., 2005; Lander and Lockridge, 1989; Lomnitz, 2004, 1970). IRSL dating of the basal sand of the uppermost package of tsunami deposits at core site Pos12 (Figs. 4.1, 4.2, 4.5) produced an age of AD 1839 ± 20. This suggests that the AD 1837 tsunami reached and deposited sand in Lake Huelde and that the 1960 tsunami eroded the post-1837 sediment at core site Pos12 (and in all other cores, except in core Pos13), where the sand was IRSL-dated (Fig. 4.2).

The AD 1575 earthquake and tsunami are known from the historical record (Cisternas et al., 2005; Lomnitz, 2004, 1970) as well as from seismoturbidites in at least three Chilean lakes (Moernaut et al., 2014) and in Fiordo Reloncaví (St-Onge et al., 2012). Tsunami deposits recorded inundation in coastal lowlands in Chucalén (Garrett et al., 2015), Maullín (Cisternas et al., 2005) and in Tirúa (Ely et al., 2014) (Fig. 4.1). The diatom assemblage reacted to co-seismic subsidence in Tirúa. All lines of evidence show the effect and size of the AD 1575 rupture are comparable with the AD 1960 M_W 9.5 earthquake, except for a potential lack of co-seismic subsidence in Chucalén (Garrett et al., 2015). One tsunami deposit in the Lake Huelde record is dated to AD 1467 to AD 1647 (median AD 1553) overlapping the AD 1575 event (Figs. 4.3, 4.4, 4.5; Tabs. 4.2, 4.3).

Sudden subsidence events and/or tsunami deposits in coastal lowlands suggest two megathrust earthquakes and tsunamis occurred after AD 1100 and before the beginning of historical documents in AD 1541 (Cisternas et al., 2005; Garrett et al., 2015). Correlated and varve-dated lacustrine seismoturbidites produced by strong shaking pinpoint the ages of the earthquakes to AD 1319 ± 9 and AD 1127 ± 44 (Moernaut et al., 2014). Both events appear to be represented in the Lake Huelde record as tsunami deposits (Figs. 4.2, 4.5). Two tsunami deposits older than AD 1127 are described in Maullín, to each of which we can correlate a tsunami deposit in Lake Huelde, with associated modelled ages of 1250 ± 50 and 1690 ± 90 cal. yrs BP and an direct IRSL age on the older of the two of 1565 ± 300 yrs BP. Another tsunami deposit from Lake Huelde matches a co-seismic subsidence event without unquestionable evidence of tsunami deposition in Maullín (Cisternas et al., 2005). Only one co-seismic subsidence event (event F) described in Maullín (no tsunami deposit reported) has no match in the Lake Huelde record (Fig. 4.5).

In summary, Lake Huelde has been a reliable recorder of large-scale tsunamis in the past ~900 yrs. The Lake Huelde record contains deposits of all three historically known tsunamis, including the AD 1960, AD 1837 and AD1575 tsunamis in Chile. Older tsunami deposits from Lake Huelde match all four known prehistoric tsunamis from south central Chile and one co-seismic subsidence event in Maullín over the last ~2 ka. The Lake Huelde record matches the historical and prehistoric record in all cases without either over- or underrepresentation (Fig. 4.5).

4.5.1 Recurrence pattern of tsunamis in south central Chile

Beyond the 7 historically and geologically known tsunami deposits and the one matched co-seismic subsidence event, we introduce 9 previously unknown tsunami deposits from 5.5 to 2 cal. ka BP (Fig. 4.5). The mean recurrence time over the entire period is ~325 yrs (or ~270 yrs for the latest 8 tsunamis), which is in broad agreement with the mean recurrence time of ~285 yrs of Cisternas et al. (2005). However, the recurrence times of all 17 dated tsunamis give a bimodal recurrence pattern with modes at ~115 yrs and ~490 yrs (Fig. 4.6). We tested the robustness of the bimodal pattern by randomly omitting one or two tsunami deposits from the input. The bimodal character of the recurrence pattern prevailed. The shorter recurrence mode of ~115 yrs is comparable to the historical 128 ± 62 (2σ) yrs mean recurrence time of megathrust earthquakes on the same seismic segment (Lomnitz, 2004, 1970; Nishenko, 1985), while ~490 yrs is in agreement with the expected ~500 yrs recurrence time of full segment ruptures with patches of ~40 m of slip, like the AD 1960 earthquake (Cifuentes, 1989; Moernaut et al., 2014; Moreno et al., 2009). The mean recurrence time loses meaning in face of this bimodal recurrence distribution of tsunamigenic subduction zone ruptures. In fact, in the case of tsunami inundation in Lake Huelde the mean is close to the least likely recurrence time (Fig. 4.6). The implications of the recurrence pattern are clear. The shortest recurrence time has a median of ~60 yrs showing that the subduction zone in south central Chile may already now have the potential to produce a tsunamigenic earthquake without redefining the extremes of the presented dataset.

The bimodal recurrence pattern of tsunamis can be explained in three different ways: Firstly, data may be missing, which, in our case, is unlikely, due to the strong agreement between the Lake Huelde record and the historical and sedimentary records from other areas without over- or underrepresentation. Secondly, two or more independent tsunamigenic processes with unimodal recurrence patterns are superimposed and differ sufficiently to produce a bimodal sum, which seems unlikely, too. We exclude meteorite impacts and purely landslide related triggers as tsunamigenic processes, because there are no known candidates and should it have occurred in the past 5500 yrs, it would most likely be a singular event in the record. It is possible that far-field tsunamis from other subduction zone segments across the Pacific are among the tsunami sources. However, in recent history, e.g. AD 1946 Aleutian Islands, AD 1952 Kamchatka, AD 1964 Alaska, AD 2010 Maule, AD 2011 Tōhoku, none of the giant tsunamis caused inundation into Lake Huelde or had a significant effect elsewhere on the coast of Isla de Chiloé. Furthermore, the youngest 8 tsunami deposits of the last ~2 ka from the Lake Huelde can be correlated to coastal subsidence, and therefor near-field events in Chucalén and Maullín. We do not consider far-field tsunamis, because of this absence of evidence. If tsunami deposits with far-field sources exist in the Lake Huelde record, it would make the recurrence of local tsunamigenic earthquakes longer. From a perspective of tsunami hazard assessment, the results would remain the same. Thirdly, the tsunamigenic earthquakes may be a process that is inherently bimodal in south central Chile, controlled by temporal and spatial variability in rupture modes. Shallow megathrust earthquakes, like the AD 2010 Mentawai tsunami earthquake, rupture the interface between the accretionary prism and the subducting plate. Low confining pressures and the presence of pore fluid in unconsolidated sediments at the up-dip fault allow anelastic deformation and aseismic sliding to occur between tsunami earthquakes (Lay et al., 2012). Central zone (15 to 35 km depth) and down-dip (35 to 55 km depth) megathrust earthquakes rupture the interface between the subducting and the overriding plates and the upper mantle, like the AD 2010 Maule earthquake. The greatest earthquakes rupture across the entire megathrust, extending their slip all the way to the trench, like the AD 2004 Sumatra and AD 2011 Tōhoku earthquakes (Lay et al., 2012). Complex recurrence patterns of tsunamis, like the one presented here, should be expected given the vast differences in physical environments along and across megathrust faults and in the amount of slip of tsunamigenic earthquakes at various depths. Classifying the earthquake of each tsunami deposit would allow an analysis of the recurrence patterns of separate rupture modes. However, additional paleoseismic information, such as rupture width and length, slip distribution, co-seismic vertical deformation etc. would be needed. This information may be acquired by integrating this and other paleotsunami records with new long records of shaking and coastal deformation.

Tsunamigenic subduction zone earthquakes around the globe pose a sizeable hazard, but they do so with differing variability. In south central Alaska, the recurrence pattern of 7 high magnitude megathrust earthquakes appears to be unimodal with a mean of ~595 yrs; only the last recurrence time is clearly longer (~880 yrs) than any other pair of predecessors (Shennan et al., 2014). However, to assess the variability in tsunami recurrence more than 7 tsunami deposits

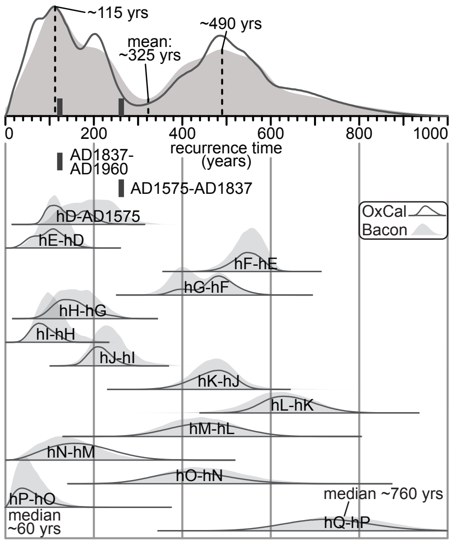

Figure 4.6: Tsunami recurrence in the Lake Huelde record has a bimodal average probability density function. The recurrence times (probability density functions in the box) were calculated using two different age-depth models, Bacon (Blaauw and Christen, 2011) and OxCal (Ramsey, 2008), which produce similar bimodal recurrence patterns (probability density function on top of the box).

are necessary in the record (McCaffrey, 2008). On the Cascadia subduction zone, a coastal lake record shows clustered tsunami recurrence, with extreme recurrence times as short as 22 yrs and gaps as long as ~1100 yrs (Kelsey et al., 2005). On the northeast Japanese Hokkaido coast, tsunami recurrence is described as aperiodic with a mean of ~400 yrs with recurrence times much shorter (~100 yrs) and much longer (~800 yrs) than the mean (Sawai et al., 2009). We expect other subduction zones to have similar ranges of variability. The commonly used mean recurrence time with a Poisson distribution recurrence pattern can misrepresent the reality of tsunamigenic earthquakes and therefore misrepresent the tsunami hazard (Geist and Lynett, 2014), as in the case of south central Chile. Consequently, it is necessary to re-examine seismic segments for their variability in tsunami recurrence time and the implications for the regional tsunami hazards mitigation measures.

Acknowledgements

PK acknowledges financial support by the Special Research Fund of Ghent University (BOF), JM from the Swiss National Science Foundation (SNF) grant 133481 and the Chilean Fondecyt projects no. 1150346 and 1150321, MVD and DV from the Research Foundation Flanders (FWO travel grant K201512N and FWO Post Doctoral grant G013915N). We thank Koen De Rycker and Gauvain Wiemer for fieldwork support, Dr. Claire Schepens and Dr. Eric Achten for CT-scanner support, and Marco Cisternas for constructive criticism on the manuscript.

References

Amante, C., Eakins, B.W., 2009. ETOPO1 1 Arc-Minute Global Relief Model: Procedures, Data Sources and Analysis. NOAA Technical Memorandom NESDIS NGDC-24. National Geophysical Data Center, NOAA.

Ando, M., 1975. Source mechanisms and tectonic significance of historical earthquakes along the nankai trough, Japan. Tectonophysics 27, 119–140.

Atwater, B.F., Cisternas, M., Yulianto, E., Prendergast, A.L., Jankaew, K., Eipert, A.A., Ignatius, W., Fernando, S., Tejakusuma, I., 2013. The 1960 tsunami on beach-ridge plains near Maullín, Chile: Landward descent, renewed breaches, aggraded fans, multiple predecessors. Andean Geology 40, 393–418.

Bertrand, S., Daga, R., Bedert, R., Fontijn, K., 2014. Deposition of the 2011–2012 Cordón Caulle tephra (Chile, 40°S) in lake sediments: Implications for tephrochronology and volcanology. Journal of Geophysical Research: Earth Surface 119, 2555–2573.

Blaauw, M., Christen, J.A., 2011. Flexible Paleoclimate Age-Depth Models Using an Autoregressive Gamma Process. Bayesian Analysis 6, 457–474.

Boës, X., Fagel, N., 2007. Relationships between southern Chilean varved lake sediments, precipitation and ENSO for the last 600 years. Journal of Paleolimnology 39, 237–252.

Fagel, N., Boës, X., Loutre, M.F., 2007. Climate oscillations evidenced by spectral analysis of Southern Chilean lacustrine sediments: the assessment of ENSO over the last 600 years. Journal of Paleolimnology 39, 253–266.

Bronk Ramsey, C., Lee, S., 2013. Recent and Planned Developments of the Program OxCal. Radiocarbon 55, 720–730.

Buylaert, J.-P., Jain, M., Murray, A.S., Thomsen, K.J., Thiel, C., Sohbati, R., 2012. A robust feldspar luminescence dating method for Middle and Late Pleistocene sediments. Boreas 41, 435–451.

Cifuentes, I.L., 1989. The 1960 Chilean Earthquakes. Journal of Geophysical Research 94, 665–680.

Cisternas, M., Atwater, B.F., Torrejón, F., Sawai, Y., Machuca, G., Lagos, M., Eipert, A., Youlton, C., Salgado, I., Kamataki, T., Shishikura, M., Rajendran, C.P., Malik, J.K., Rizal, Y., Husni, M., 2005. Predecessors of the giant 1960 Chile earthquake. Nature 437, 404–407.

Ely, L.L., Cisternas, M., Wesson, R.L., Dura, T., 2014. Five centuries of tsunamis and land-level changes in the overlapping rupture area of the 1960 and 2010 Chilean earthquakes. Geology 42, 995–998.

Fedorov, A. V, Brierley, C.M., Emanuel, K., 2010. Tropical cyclones and permanent El Niño in the early Pliocene epoch. Nature 463, 1066–1070.

Garrett, E., Shennan, I., Watcham, E.E.P., Woodroffe, S.S.A., 2013. Reconstructing paleoseismic deformation, 1: modern analogues from the 1960 and 2010 Chilean great earthquakes. Quaternary Science Reviews 75, 11–21.

Garrett, E., Shennan, I., Woodroffe, S.A.A., Cisternas, M., Hocking, E.P.P., Gulliver, P., 2015. Reconstructing paleoseismic deformation, 2: 1000 years of great earthquakes at Chucalén, south central Chile. Quaternary Science Reviews 113, 112–122.

Geist, E.L., Lynett, P.J., 2014. Source Processes for the Probabilistic Assessment of Tsunami Hazards. Oceanography 27, 86–93.

Goldfinger, C., Ikeda, Y., Yeats, R.S., Ren, J., 2013. Superquakes and Supercycles. Seismological Research Letters 84, 24–32.

Goldfinger, C., Nelson, C.H., Morey, a. E., Joel E, J., Patton, J., Karabanov, E., Gutierrez-Pastor, J., Eriksson, A., Gracia, E., Dunhill, G., Enkin, R., Dallimore, A., Valiier, T., 2012. Turbidite Event History — Methods and Implications for Holocene Paleoseismicity of the Cascadia Subduction Zone. U.S. Geological Survey Professional Paper 1661-F 170.

Gomez, B., Corral, Á., Orpin, A.R., Page, M.J., Pouderoux, H., Upton, P., 2015. Lake Tutira paleoseismic record confirms random, moderate to major and/or great Hawke's Bay (New Zealand) earthquakes. Geology 43, 103–106.

Goto, K., Hashimoto, K., Sugawara, D., Yanagisawa, H., Abe, T., 2014. Spatial thickness variability of the 2011 Tōhoku-oki tsunami deposits along the coastline of Sendai Bay. Marine Geology 358, 38–48.

Herrendorfer, R., van Dinther, Y., Gerya, T., Dalguer, L.A., 2015. Earthquake supercycle in subduction zones controlled by the width of the seismogenic zone. Nature Geoscience 8, 471–474.

Hogg, A.G., Hua, Q., Blackwell, P.G., Niu, M., Buck, C.E., Guilderson, T.P., Heaton, T.J., Palmer, J.G., Reimer, P.J., Reimer, R.W., Turney, C.S.M., Zimmerman, S.R.H., 2013. SHCal13 Southern Hemisphere Calibration, 0–50,000 Years cal BP. Radiocarbon 55, 1889–1903.

Kaneko, Y., Avouac, J.-P., Lapusta, N., 2010. Towards inferring earthquake patterns from geodetic observations of interseismic coupling. Nature Geoscience 3, 363–369.

Kelsey, H.M., Nelson, A.R., Hemphill-Haley, E., Witter, R.C., 2005. Tsunami history of an Oregon coastal lake reveals a 4600 yr record of great earthquakes on the Cascadia subduction zone. Geological Society of America Bulletin 117, 1009–1032.

Kempf, P., Moernaut, J., Van Daele, M., Vermassen, F., Vandoorne, W., Pino, M., Urrutía, R., Garrett, E., De Batist, M., 2015. The sedimentary record of the tsunami caused by the 1960 Great Chilean Earthquake in two coastal lakes on Chiloé Island, Chile. Sedimentary Geology 328, 73–86.

Lander, J.F., Lockridge, P., 1989. United States Tsunamis 1690 - 1988. Boulder, Colorado. National Geophysical Data Center publication, v. 41–42.

Lay, T., Kanamori, H., Ammon, C.J., Koper, K.D., Hutko, A.R., Ye, L., Yue, H., Rushing, T.M., 2012. Depth-varying rupture properties of subduction zone megathrust faults. Journal of Geophysical Research: Solid Earth 117, B04311.

Lomnitz, C., 2004. Major Earthquakes of Chile: A Historical Survey, 1535–1960. Seismological Research Letters 75, 368–378.

Lomnitz, C., 1970. Major Earthquakes and Tsunamis in Chile during the period 1535 to 1955. Geologische Rundschau 59, 938–960.

May, S.M., Pint, A., Rixhon, G., Kelletat, D., Wennrich, V., Brueckner, H., 2013. Holocene coastal stratigraphy, coastal changes and potential palaeoseismological implications inferred from geo-archives in Central Chile (29–32 degrees S). Zeitschrift für Geomorphologie 57, 201–228.

McCaffrey, R., 2008. Global frequency of magnitude 9 earthquakes. Geology 36, 263–266.

Messens, F., 2014. Luminescence dating of tsunami sand in south central Chile : a feasibility study. http://lib.ugent.be/nl/catalog/rug01:002163647. Ghent University, Belgium, pp. 98.

Moernaut, J., Van Daele, M., Heirman, K., Fontijn, K., Strasser, M., Pino, M., Urrutia, R., De Batist, M., 2014. Lacustrine turbidites as a tool for quantitative earthquake reconstruction: New evidence for a variable rupture mode in south central Chile. Journal of Geophysical Research: Solid Earth 119, 1607–1633.

Moreno, M.S., Bolte, J., Klotz, J., Melnick, D., 2009. Impact of megathrust geometry on inversion of coseismic slip from geodetic data: Application to the 1960 Chile earthquake. Geophysical Research Letters 36, L16310.

Nishenko, S.P., 1985. Seismic potential for large and great interplate earthquakes along the Chilean and Southern Peruvian Margins of South America: A quantitative reappraisal. Journal of Geophysical Research: Solid Earth 90, 3589–3615.

Pouderoux, H., Lamarche, G., Proust, J.-N., 2012. Building an 18 000-year-long paleo-earthquake record from detailed deep-sea turbidite characterisation in Poverty Bay, New Zealand. Natural Hazards and Earth System Sciences 12, 2077–2101.

Pouderoux, H., Proust, J.-N., Lamarche, G., 2014. Submarine paleoseismology of the northern Hikurangi subduction margin of New Zealand as deduced from Turbidite record since 16 ka. Quaternary Science Reviews 84, 116–131.

Ramsey, C.B., 2008. Deposition models for chronological records. Quaternary Science Reviews 27, 42–60.

Satake, K., Atwater, B.F., 2007. Long-Term Perspectives on Giant Earthquakes and Tsunamis at Subduction Zones. Annual Review of Earth and Planetary Sciences 35, 349–374.

Satake, K., Nishimura, Y., Putra, P., Gusman, A., Sunendar, H., Fujii, Y., Tanioka, Y., Latief, H., Yulianto, E., 2013. Tsunami Source of the 2010 Mentawai, Indonesia Earthquake Inferred from Tsunami Field Survey and Waveform Modeling. Pure and Applied Geophysics 170, 1567–1582.

Sawai, Y., Kamataki, T., Shishikura, M., Nasu, H., Okamura, Y., Satake, K., Thomson, K.H., Matsumoto, D., Fujii, Y., Komatsubara, J., Aung, T.T., 2009. Aperiodic recurrence of geologically recorded tsunamis during the past 5500 years in eastern Hokkaido, Japan. Journal of Geophysical Research: Solid Earth 114, L21309.

Shennan, I., Bruhn, R., Barlow, N., Good, K., Hocking, E., 2014. Late Holocene great earthquakes in the eastern part of the Aleutian megathrust. Quaternary Science Reviews 84, 86–97.

Sievers, H., Villegas, G.C., Barros, G., 1963. The seismic sea wave of 22 May 1960 along the Chilean coast. Bulletin of the Seismological Society of America 53, 1125–1190.

St-Onge, G., Chapron, E., Mulsow, S., Salas, M., Viel, M., Debret, M., Foucher, A., Mulder, T., Winiarski, T., Desmet, M., Costa, P.J.M., Ghaleb, B., Jaouen, A., Locat, J., 2012. Comparison of earthquake-triggered turbidites from the Saguenay (Eastern Canada) and Reloncavi (Chilean margin) Fjords: Implications for paleoseismicity and sedimentology. Sedimentary Geology 243–244, 89–107.

Tormann, T., Enescu, B., Woessner, J., Wiemer, S., 2015. Randomness of megathrust earthquakes implied by rapid stress recovery after the Japan earthquake. Nature Geoscience 8, 152–158.

"Der Natur gegenüberzustehen und seinen Scharfsinn an ihren Rätseln zu erproben,
gibt dem Leben einen ungeahnten Inhalt."
"To face nature and to try your brain against its conundrums,
gives an unforeseen meaning to life."

AD 1931, Alfred Wegener in *Tagebuch der Grönlandexpedition 1930/31*

5 Paleotsunami record in the dynamic coastal lake system of Lake Cucao

This chapter is intended for publication in a scientific journal after the age control on the sedimentary record has been improved as:

Paleotsunami record in the dynamic coastal lake system of Lake Cucao, south central Chile

Kempf, P., Moernaut, J., Van Daele, M., Vandoorne, W., Pino, M., Urrutia, R., De Batist, M.

Abstract: In AD 1960 Lake Cucao on Isla de Chiloé, south central Chile, was inundated by the tsunami of the Great Chilean Earthquake (M_W 9.5). The area of the lake basin has been submerged since the postglacial sea-level rise and may have recorded tsunami inundations in its sedimentary record since then. Sub-bottom profiles reveal a tidal delta with a crosscutting channel in Lake Cucao. A radiocarbon date from a sediment core and internal acoustic reflectors, which converge towards the channel, indicate that tidal currents were active at least sporadically over the last 3700 yrs. Little vertical displacement over the last 3700 yrs maintained the ability of Lake Cucao to record tsunamis in its sedimentary record. In a total of 21 sediment cores, 15 detrital layers are interpreted as tsunami deposits with a varying level confidence. The level of confidence depends on five criteria; there are site-specific criteria, i.e. i) high magnetic susceptibility of the sediment indicating high detrital content, ii) core correlation, iii) acoustic reflector correlation to the sedimentary record (both indicate traceability of the detrital layer in the sedimentary record), and general criteria, e.g. iv) presence of mud clasts and v) age correlation to known paleotsunamis in the area. In this way 8 detrital layers are interpreted as tsunami deposits with a high level of confidence, 4 with a medium level of confidence and 3 with a relatively low level of confidence. In comparison, the paleotsunami record of Lake Huelde, a mere 2 km north of Lake Cucao, contains 14 or 15 tsunami deposits in the same time interval. This study adds a long paleotsunami record on a coastline, where extreme tsunamis occur relatively frequently and where long paleotsunami records are still sparse. This study demonstrates how indispensible acoustic imagery can be in understanding the depositional environment, especially in lakes as dynamic as the coastal Lake Cucao. Imaging tsunami deposits in coastal lakes with sub-bottom profiles can now be added to the growing list of tools in the toolkit to observe, describe and recognise tsunami deposits.

Contributions: The manuscript was written by PK. Fieldwork was conducted by PK, JM, MVD and WV, and facilitated by MP and RU. Discussion of results and interpretation were done by PK, JM, MVD and MDB. All analyses were done by PK.

5.1 Introduction

Long sedimentary records of infrequent large-scale tsunamis are essential in understanding recurrence patterns, because documented history often does not cover the necessary time span. During the past decades the scientific means to research the sedimentary record of tsunamis have grown in quantity and quality (Chagué-Goff et al., 2011). Connecting tsunami deposits with tsunamis from documented history is needed to calibrate tools in paleotsunami research. However, the primary reason for sedimentological investigations is to extend the historical record. This is a challenging task, because long and continuous sedimentary records in coastal areas are rare.

The Valdivia seismic segment is notorious for having produced the strongest earthquake on instrumental record in AD 1960 (M_W 9.5). The region's written history begins with the Spanish invasion in AD 1541 (Cisternas et al., 2005; Lomnitz, 2004, 1970). In the 475 yrs since then, four major earthquakes were chronicled in AD 1575, 1737, 1837 and 1960. According to reports of damage, for all but the AD 1737 earthquake, tsunamis damaged coastal towns. Recent sedimentological investigations produced evidence for tsunami inundation for all three documented tsunamis in a multitude of coastal areas of Chile (Atwater et al., 2013; Cisternas et al., 2005, in prep.; Dura et al., 2015; Ely et al., 2014; Garrett, 2013; Garrett et al., 2015, 2013; Kempf et al., 2015; Nentwig et al., 2015; Reinhardt et al., 2010). In addition, five sites, i.e. Maullín (Cisternas et al., 2005), Caulle (Atwater et al., 2013), Chucalén (Garrett et al., 2015), Cocotué (Cisternas et al., in prep.) and Lake Huelde (see chapter 4) are known to have recorded tsunami inundation before written history began (Fig. 5.1). Of these five, only the Maullín and Lake Huelde records extend the tsunami history further back in time than a thousand years.

One of the difficulties, when researching tsunami deposits on millennial timescales, is the relative sea-level change, which plays a key role in tsunami deposition and preservation (Kelsey et al., 2015). Relative sea-level rise creates the needed accommodation space for tsunami deposit preservation in coastal lowlands. However, with too much relative sea-level rise or fall, the horizontal shoreline displacement shifts the area of tsunami deposition in respect to the previous tsunami deposit, which makes long and continuous paleotsunami records impossible. Coastal lakes provide excess accommodation space, however, their sensitivity to horizontal shoreline displacement experiences variability, too.

This study will present a coastal lake record with multiple tsunami deposits reaching back ~3700 yrs BP. The tsunami deposits are the first to be acoustically imaged in this way. The method proves to be essential in understanding the sedimentary environment and gives a crude, but crucial, insight into the relative sea-level change during the time span of the sedimentary record. Sub-bottom profiles in coastal lakes should therefore be included in the growing toolkit of paleotsunami research.

5.2 Setting

Lake Cucao (074.09°W, 42.63°S) is a coastal lake located on the west coast of Isla de Chiloé in south central Chile (Fig. 5.1a). Lake Cucao is connected to the Pacific Ocean by its outlet river

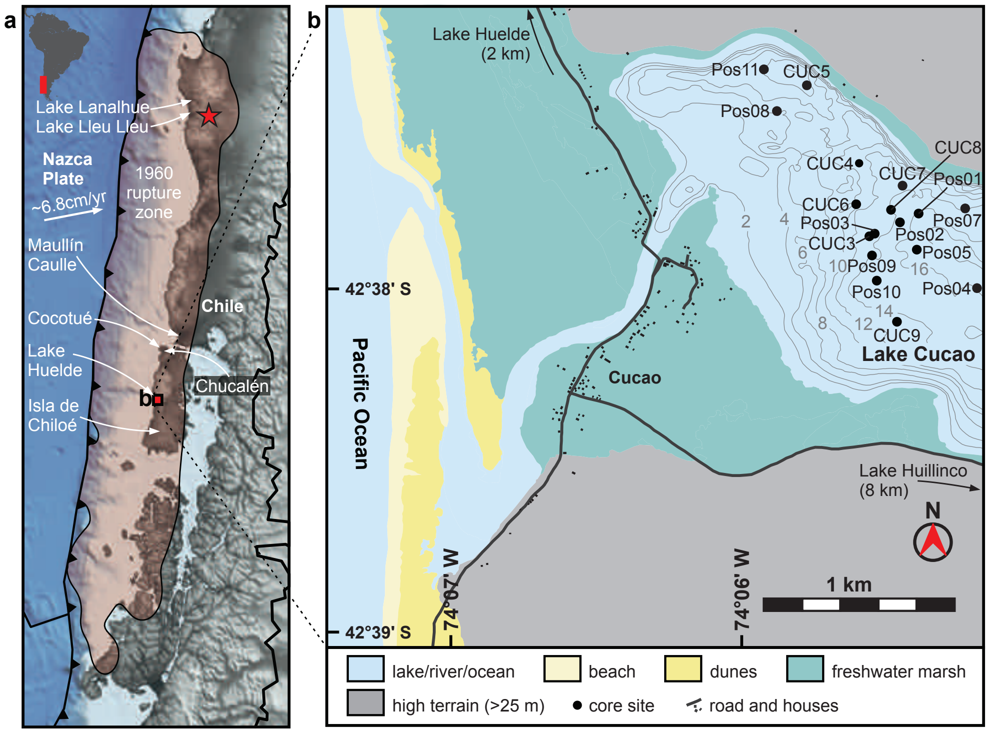

Figure 5.1: a) Topographic and bathymetric overview of south central Chile. The digital elevation model is based on the ETOPO1 dataset (Amante and Eakins, 2009). The epicentre and the 1 m slip contour line representing the rupture zone (Moreno et al., 2009) of the AD 1960 earthquake are drawn in red. b) detailed map of the study area. The geomorphological units are based on field observations and are extended using satellite imagery (Google Earth). The lake bathymetry map is based on side scan sonar bottom tracks (Kempf et al., 2015).

channel, which crosses the 1.3 km wide barrier. The barrier consists of an up to 250 m wide beach, a narrow belt of dunes followed by freshwater marshland (Fig. 5.1b). Lake Cucao is 7.9 km long east-west oriented elongated lake. It is 10.6 km² large and up to 25 m deep (Villalobos et al., 2003). The outlet channel of the lake facilitates water exchange between lake and ocean in both directions, because Lake Cucao lies in the intertidal zone (Kempf et al., 2015; Villalobos et al., 2003). The daily exchange of water forms a stable saline bottom water body in Lake Cucao and the upstream adjacent Lake Huillinco (Fig. 5.1) (Villalobos et al., 2003). With the transport of water comes transport and deposition of sediment, which produced a tidal delta around the outlet channel in Lake Cucao. Fresh mega-ripples on the tidal delta and a crosscutting channel through the delta are the sedimentary expression of strong tidal currents at present (Fig. 5.2, 5.3) (Kempf et al., 2015).

5.3 Methods

5.3.1 Acousting imaging

To understand the complex coastal lake environment of Lake Cucao, we used a side scan sonar, Klein 3000. Side scan sonar data reveals the acoustic reflectivity of the lake floor surface. In sandy surface areas the reflectivity is relatively high, while in muddy areas the reflectivity is rel-

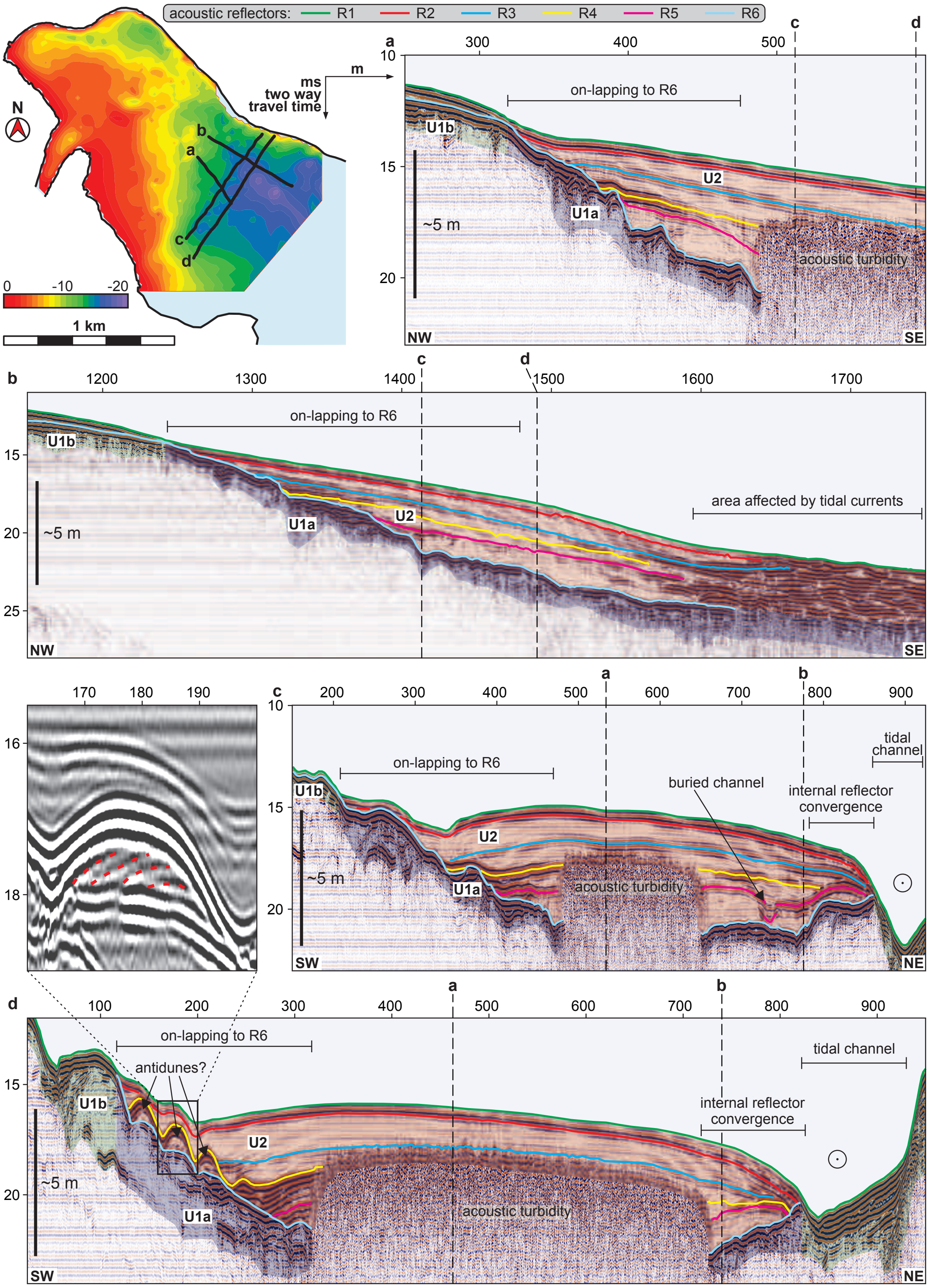

Figure 5.2: Sub-bottom profiles show the seismic stratigraphy of Lake Cucao with seismic units U1a (blue), U1b (green) and U2 (red). Profiles a) and b) parallel to the lake's long axis image the on-lapping of the internal acoustic reflectors R1–R5 onto acoustic reflector R6. Profiles in cross-direction to the lake's long axis c) and d) show the same on-lapping in the southeast and convergent internal reflectors towards the tidal channel. Reflector R4 expresses three hummocks (see inset), which are tentatively interpreted as antidunes.

atively low. Areas of recent sand deposition and areas of mud-winnowing can be identified in this manner. The data was processed to a map view mosaic with the software SonarWizMap v4. The bottomtrack of the side scan sonar survey provided the data base for the bathymetric map of Lake Cucao. The subsurface of Lake Cucao was imaged with sub-bottom profiles, for which we used a Geopulse Pinger, with a source frequency of 3.5 kHz. In the deeper parts of the lake basin, biogenic gas blanks the acoustic signal. The result is a chaotic seismic signature. Where gas blanking is not a problem, continuous high-amplitude horizons were mapped within the acoustically nearly transparent background sediment. Subaqueous geomorphological features The sub-bottom profile data was processed (band-pass filtering) and interpreted with the IHS Kingdom Suite v8.8 software.

5.3.2 Sediment analysis

In sediment cores we recovered up to 8 m of lake sediment. Every coring site consists of a Swiss gravity core at the top for an undisturbed sediment sample of the soft lake floor. The core sites with long cores are achieved by overlapping 3-m-long UWITEC piston hammer cores. The inner core diameter of both gravity and piston hammer cores is 6.0 cm.

All cores were analysed with several tools to reveal subtle sedimentary differences on the otherwise often homogeneous-appearing split core. Some physical properties were measured with a Geotek multi-sensor core logger (MSCL), measuring γ-ray attenuation density and magnetic susceptibility every 2 mm of each core. Split core surface images were taken with a line scan camera mounted on the MSCL. Several cores were CT-scanned with a Siemens Flash medical CT-Scanner with a voxel size of 0.15 mm $\times$ 0.15 mm $\times$ 0.6 mm (xyz). The results of these analyses facilitated sediment description, correlation and interpretation, which are visualised in the core logs. To differentiate sandy deposits of what we will interpret as tsunami deposits from sandy deposits of tidal delta foresets we analysed the grain size distribution with a lasergranulometer, Malvern 3000.

5.3.3 Age-depth modelling

The age-depth relationship of core Pos04 is based on sparse age-depth information. The surface of the core is from AD 2012. The topmost detrital layer was identified as the AD 1960 tsunami deposit in Kempf et al. (2015). And the very base of the core was radiocarbon date on a leaf at 3560–3830 cal. yrs BP. In light of the sparse age-depth information, we chose the classical age-depth model algorithm Clam v2.2 (Blaauw, 2010), which is based in an R-software environment. Clam produces a mathematical solution to the input data and keeps the model simple, which is often more successful in age-depth models, which rely on few data points (Telford et al., 2004). The uncertainty displayed in the model at depths far from age information is strongly underestimated, because the model considers only the uncertainty of the radiocarbon analysis and its calibration. The model has no information about the uncertainty of accumulation rate changes.

5.4 Results

5.4.1 Sub-bottom profiles

Two seismostratigraphic units can be differentiated on sub-bottom data from Lake Cucao, U1 and U2 (Kempf et al., 2015). U1 (a and b) describes the acoustic base of the lake basin. U1a is covered by the lake's sedimentary infill in relatively deep areas. U1b is at least sporadically reworked by tidal currents entering and exiting the lake in shallow areas near a tidal channel (Fig. 5.2). U2 is the lacustrine sediment infill. The basal contact of U2 to U1a creates an unconformity (reflector R6) characterized by on-lapping reflector terminations. The internal reflector geometry of U2 is parallel to sub-parallel with nearly acoustically transparent sediment with infrequent high amplitude and continuous reflectors. (Fig. 5.2c). The presence of shallow gas in the sediment of the central basin causes acoustic turbidity, which hides the internal reflector geometry of U2 at depths greater than ~1.5 m (~2 ms two-way-travel time, TWT). In total five parallel to sub-parallel reflectors (R1–R5) can be traced within U2. R1 coincides with the lake floor and is a continuous, strong reflector, with decreasing amplitude towards the southwest (Fig. 5.2). R2–R5 are high-amplitude, continuous internal reflectors and lap out onto to either R6 or onto one of the other internal reflectors, e.g. R4 laps out onto R5 in some areas. Of all internal reflectors, R4 has the highest amplitude and marks the top of a hummocky paleorelief in the south of the surveyed area (Fig. 5.2d). The hummocks are ~30 m long and ~1 m high with up-slope dipping internal reflections. The two lowermost internal reflectors, R4 and R5, exhibit erosion of the underlying acoustically transparent lake sediment in the form of a few now buried channels (Fig. 5.2c).

The tidal channel incises the shallow delta up to 3.5 m deep and ~100 m wide, at its upper western end as a prolongation of the outlet river channel (Fig. 5.3a). The channel continues towards the northeastern shore (Fig. 5.3b, c) and bends southeastward along the long axis of the lake from where it follows the northeastern shoreline (Fig. 5.3d, e). On its basin-facing side, the channel appears to have caused a convergent geometry of the sedimentary packages between the strong continuous internal reflectors of U2 (R1–R5) (Fig. 5.2c, d). The convergent geometry affects the oldest to the youngest strata of U2. The bathymetric cross-profiles of the channel are asymmetric with a fatter slip-off slope on the inside and a steeper undercut bank on the outside of the channel (Fig. 5.3). The asymmetry alters along the channel. About 10 m wide and 0.5 m deep incised channels are common on the upper slip-off slope. Mega-ripples with about 8 m ripple length and ~0.4 m ripple height are abundant around the incised channel, with a concentric arrangement (Kempf et al., 2015).

5.4.2 Lacustrine sediment

On the intertidal delta and in the crosscutting channel, i.e. areas where U1b is the lake floor, the sediment consists of a well-sorted medium to fine sand with mostly quartz, feldspar, hornblende and mica minerals (Fig. 5.4, e.g. core CUC7). The coarse sediment prevented deeper penetration with the coring equipment in these locations. This sand is mostly massive with a sporadic occurrence of ~1 cm thick grey muddy layers. The magnetic susceptibility of this sand is very

high, sometimes exceeding 1000×10^{-5} SI.
Sediment from the lake basin consists mostly of brown to black homogenous, poorly sorted muddy gyttja. Black indicates hypoxic or anoxic conditions, while brown represents an oxic environment. The transition from black to brown sediment can be gradual or sharp. In the case of sharp transitions the brown sediment is typically on top, the black below. The organic content (loss on ignition) for both black and brown sediment is between 20 and 35 wt% and consists of seeds, fibrous plant material, pollen and fragments of bivalve periostraca without the calcareous shell. The periostraca are sometimes fully preserved with distinct growth rings. The periostraca are most probably of the sepcies *Diplodon Chilensis*. The gyttja smells strongly of sulphur, when the cores are opened the first time, indicating anoxic conditions. The magnetic susceptibility is low between 0 and 40×10^{-5} SI. One radiocarbon date was acquired from a leaf within gyttja near the base of core Pos04 (at depth 679 cm). The sample was analysed to be 3445 ± 34 ^{14}C yrs BP old, which was calibrated to 3560–3830 cal yrs BP using the southern hemisphere calibration curve, SHCal13 (Hogg et al., 2013).

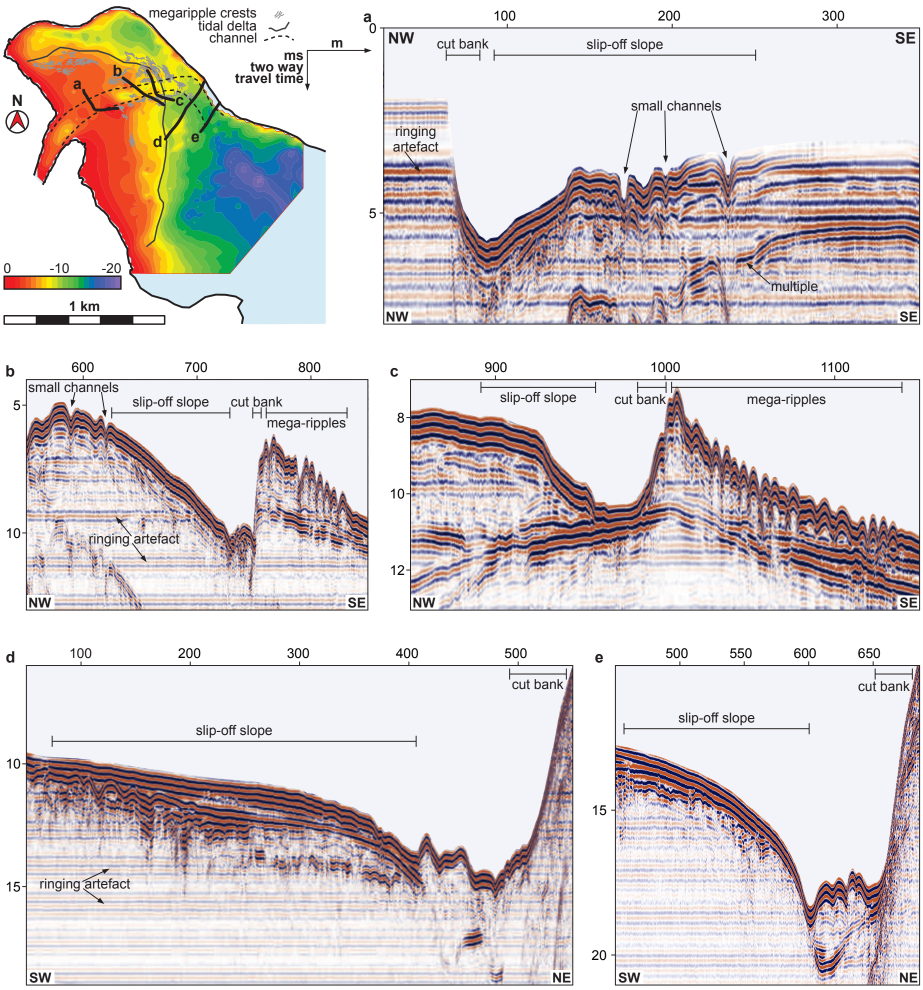

Figure 5.3: Sub-bottom profiles across the tidal channel expressing the asymmetry of the channel with alternating slip-off slopes and cut banks. Tidal currents produce mega-ripples outside the cut bank and small channels are present on the upper slip-off slope.

In all 9 long cores, there are 1 to 30 cm thick layers with high detrital content. The medium silt to fine sand of the detrital layers is coarser than the gyttja below and above. However, the detrital layers always contain a fraction of organic matter and clayey silt. The magnetic susceptibility signal of these layers ranges from relatively low, with values between 40 and 100 $\times 10^{-5}$ SI, to relatively high, with values up to 500 $\times 10^{-5}$ SI and higher (Fig. 5.4). The detrital layers are often visually indistinguishable from the gyttja on the split core surface, where no sedimentary structures other than the sometimes abrupt changes from black to brown were identified. CT-scans of the detrital layers reveal sharp lower contacts with highest X-ray attenuation at the base, gradually decreasing upwards (Fig. 5.5a, b). Some detrital layers bear 1–3 cm large mud clasts in a matrix of silt (Fig. 5.5b). If the detrital layers are brown, then they often coincide with a sharp colour transition from black to brown at their base. The detrital layers are labelled from cB to cO, where c stands for Lake Cucao and the capital letter is in alphabetical order down core. This is in analogy to the Lake Huelde record 2 km north of Lake Cucao (see chapter 4), where similar layers interpreted as tsunami deposits, are labelled hC, hD, and so on. The topmost detrital layer was identified in Kempf et al. (2015) as the tsunami deposit of the AD 1960 tsunami and is called AD 1960, instead of cA.

Seven of 9 long cores contain the detrital layer cN in the lowest part of the sedimentary record, which is markedly coarser (fine to medium sand) and exhibits higher magnetic susceptibility values than the rest of the detrital layers record, with peaks up to 2500 $\times 10^{-5}$ SI. Like in all other detrital layers, the sand of cN does not contain mica. The lack of mica distinguishes the sand of the detrital layers from the sand in samples from the tidal delta and the crosscutting channel. In cN, intervals of well-sorted massive sands are intercalated with intervals of mud clasts in a sandy matrix. The mud clasts can exceed the size of the core liner (6 cm) and are up to 11 cm thick (in down core direction). Smaller mud clasts are often arranged in layers (Fig. 5.5c). On the basis of the X-ray attenuation of the mud clasts, two types can be differentiated; one type with a low X-ray attenuation (black) and one type with an intermediate X-ray attenuation (grey). The sand of the matrix and intervals of massive sand contain mineralogenic grains of orthoclase, plagioclase, quartz, iron oxides (responsible for the high magnetic susceptibility), hornblende and rarely zircon, as well as lithic grains. The same composition of sand is reported for the AD 1960 deposit in Lake Huelde and for the beach sand, dunes sand and riverbed between Lake Cucao and the Pacific Ocean (Kempf et al., 2015).

Three cores (Pos02, -03 and -11) contain muddy sand at their base (Fig. 5.4). The muddy content makes this sand distinctly different in grain size from the well-sorted sand in the coarser detrital layers, e.g. detrital layers cC and cN. It consists of the same minerals (including mica) and lithic grains as the sand on the tidal delta and in the channel.

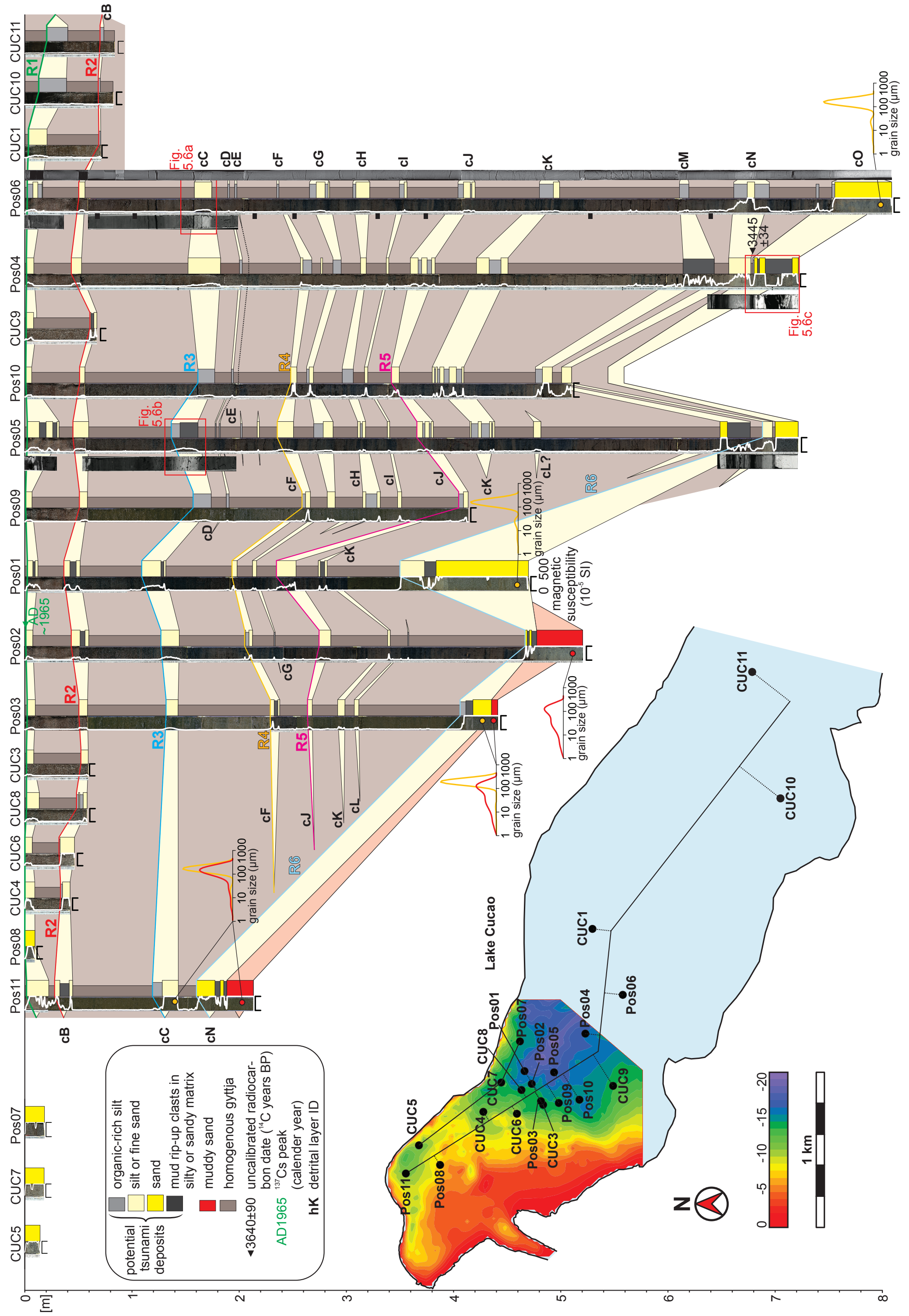

Figure 5.4: Core to core correlation of detrital layers in the gyttja dominated lake sediments. Cores are represented by a split core surface image, a sedimentological core log and in some cases CT-scans. The overview map shows two core transects through the lake. Cores CUC5, CUC7 and Pos07 are located in areas affected strongly by tidal currents. The white line on the split core surface images represents magnetic susceptibility. Grain size distribution are shown in 7 different positions to differentiate muddy sand of tidal delta foresets (red lines) from detrital layers (orange lines). Strong acoustic reflectors are drawn in the same colour as they are on sub-bottom profiles. The seismic to core correlation is captured in figure 5.5.

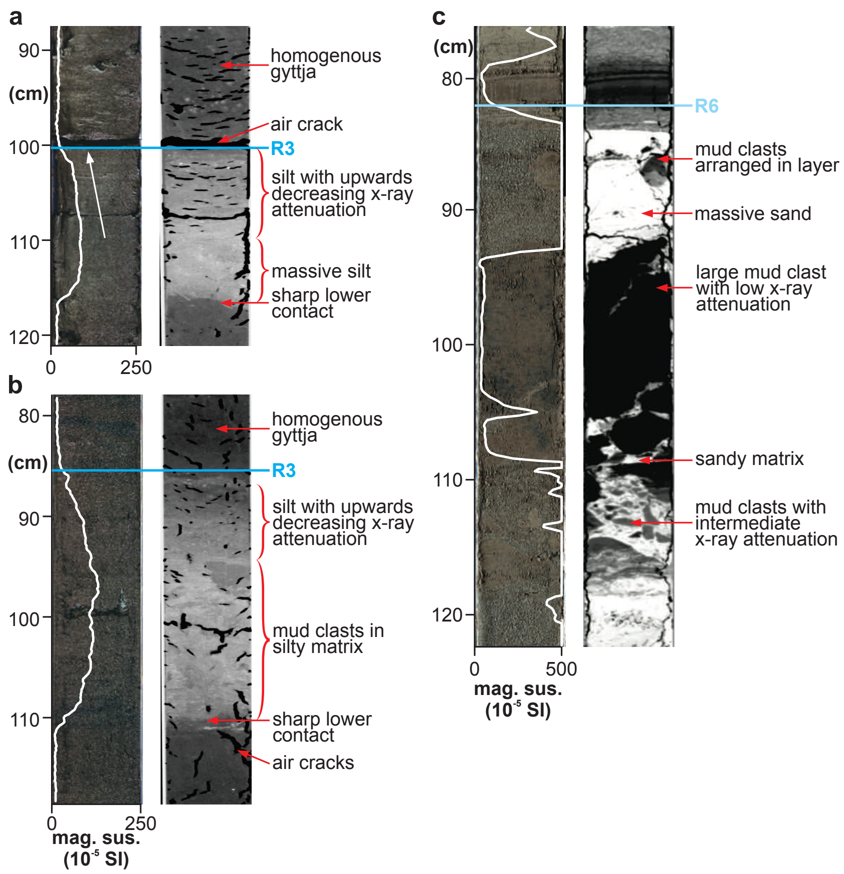

Figure 5.5: a) and b) CT-scans of detrital layer cC under acoustic reflector R3; c) detrital layer cN under acoustic reflector R6. All detrital layer exhibit a sharp contact at the bottom. CT-scans in a) and b) show upwards decreasing X-ray attenuation. In b) and c) Mud clasts with two differing X-ray attenuations are surrounded by silty (b) to sandy (c) matrix.

5.4.3 Seismics-to-core correlation

Six of the long cores can be plotted on sub-bottom profiles with acoustic penetration of the entire seismic unit U2 (Fig. 5.6). The correlation between cores and the sub-bottom profiles is performed under the assumption of a constant p-wave velocity in the entire sedimentary sequence. This is a simplification of the reality, however, realistic variability in p-wave velocity will produce negligible offsets. The six reflectors of U2 (R1 to R6) can be correlated to detrital layers in the cores (Fig. 5.4). The lake floor lies ≤ 3 cm above the top of the AD 1960 tsunami deposit (Kempf et al., 2015). The ≤ 3 cm between the lake floor surface and the AD 1960 tsunami deposit are below the vertical resolution of the sub-bottom profiles (vertical resolution ~10 cm). R1, the uppermost strong reflector therefore correlates to the lake floor as well as the top of the AD 1960 tsunami deposit. R2 correlates to detrital layer cB. R3 correlates to cC, R4 to cF and R5 to cJ, which are well traceable detrital layers in the sedimentary record of Lake Cucao. R6 is the reflector that sticks out, because reflectors R2 to R5 lap on to it. Even though on-lapping is difficult to observe in core samples, detrital layers cF–cM all appear to lap out onto cN in the core-to-core correlation (Fig. 5.4). Because of the on-lapping and the strong sedimentary contrast between gyttja and the medium sand of cN, we correlate the high-amplitude reflector R6 to the coarse detrital layer cN in most parts of the lake basin (Tab. 5.1).

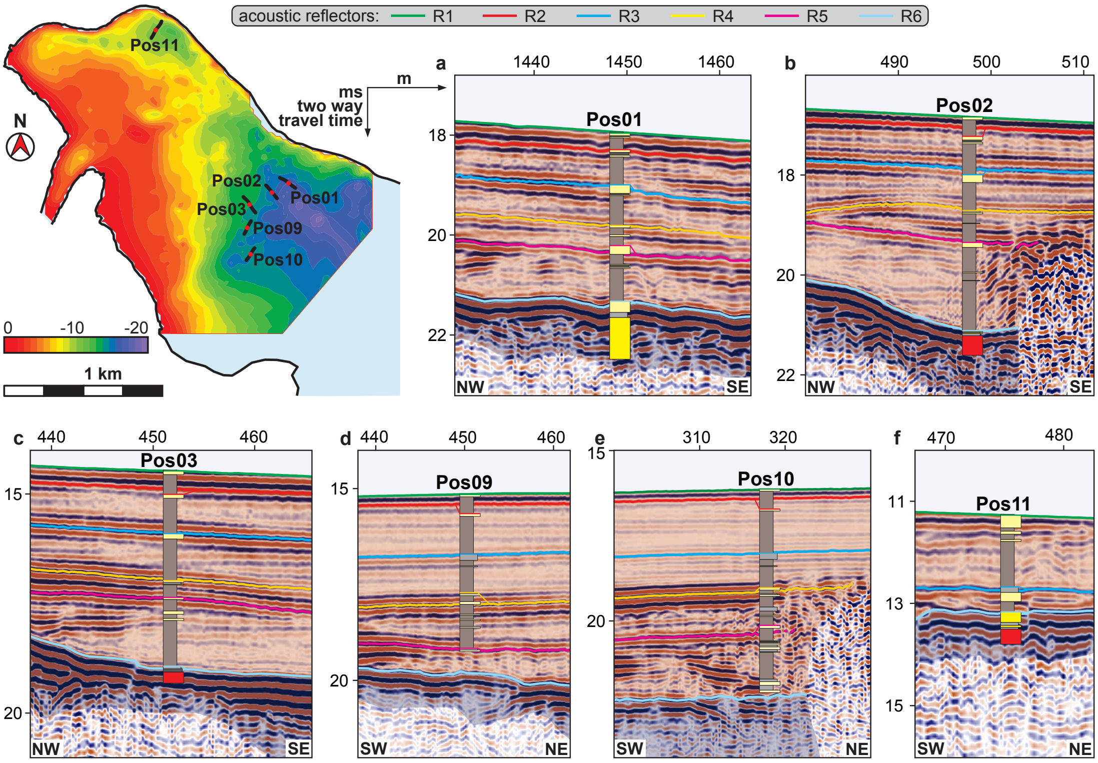

Figure 5.6: Seismic to core correlation of the AD 1960 tsunami deposit and detrital layers cB–cO with strong acoustic reflectors R1–R6. The assumption of uniform p-wave velocity within the entire lake infill and the piston coring process can cause minor offsets between cores and acoustic reflectors on sub-bottom profiles.

Table 5.1: Summary of confidence level towards the interpretation of tsunami deposits for each detrital layer, with maximum magnetic susceptibility, traceability of the detrital layers throughout the sedimentary record, correlation to acoustic reflections, content of mud rip-up clasts, age-correlation to a known tsunami. Characteristics written in green contribute to confidence, red denotes doubt and black stands for neutral or inconclusive characteristics.

detrital layer ID	max. magnetic susceptibility ($\times 10^{-5}$ SI)	traceability in the sedimentary record in cores / total cores	correlated to acoustic reflection	mud rip-up clasts	age-correlated to other tsunami deposits	confidence level
AD 1960	677	18/18	R1	yes	AD 1960	high
cB	695	17/17	R2	yes	AD 1575?	high
cC	1601	9/9	R3	yes	-	high
cD	57	5/9	-	not observed	-	low
cE	51	2/9	-	not observed	-	low
cF	581	8/9	R4	yes	-	high
cG	431	7/9	-	not observed	-	medium
cH	202	5/9	-	not observed	-	medium
cI	335	5/9	-	not observed	-	medium
cJ	306	8/9	R5	yes	-	high
cK	377	7/8	-	yes	-	high
cL	92	3/8	-	not observed	-	low
cM	585	4/8	-	yes	-	high
cN	2269	8/8	R6	yes	≥ 3560–3830 cal. yrs BP	high
cO	1656	3/3	-	not observed	-	medium

5.5 Discussion

5.5.1 Antidunes as a product of tsunami inundation in Lake Cucao

The hummocks with the up-slope dipping internal reflectors could be interpreted as antidunes due to their height and length in combination with the up-slope dipping internal reflectors. The length of antidunes is proportional to the square of the flow speed during formation. The relationship is described by Kennedy (1963) with

$$U^2 = \frac{gL}{2\pi} \tag{5.1}$$

Where U is the flow speed, g the gravitational acceleration on earth and L the wavelength of in-phase waves, e.g. antidunes. According to equation (5.1) the flow speed during antidune formation was 6.8 m s^{-1} – a reasonable flow speed for tsunami inundation (cf. Fritz et al., 2012). The position and WSW–ENE direction of the antidunes suggests that the freshwater marsh, which accommodates most inhabitants of the village of Cucao was washed over by very strong potentially destructive currents.

5.5.2 Age control and accumulation rate variability in Lake Cucao

The chronology of the five other regional paleotsunami records from south central Chile is based primarily on radiocarbon dates of plants flattened by the tsunami, rootlets in soil or terrestrial plant fragments from the pre- and post-tsunami lacustrine sediment (Atwater et al., 2013; Cisternas et al., 2005, in prep.; Garrett et al., 2015; see chapter 4).

There is no strong spatial variability in accumulation rate between long cores from the western part of the basin, which is indicated by sub-parallel detrital layers in the core-to-core correlation. This is confirmed by parallel to sub-parallel reflectors R1 to R5 on sub-bottom profiles. Exceptions are confined areas of erosional truncation in form of small channels and the area close to the crosscutting channel, where the sedimentary infill becomes significantly thinner or is non-existent (Fig. 5.2). However, all long core sites are outside these areas. In short cores CUC10 and CUC11, located 2–3 km southeast of most other cores (Fig. 5.4), and where tidal currents are probably very limited or absent, up to 21 cm of gyttja accumulated above the AD 1960 tsunami deposit. In all other cores further west the same interval is either missing or ≤ 4 cm thick. This thickness is comparable to 20–30 cm of post-1960 sediment accumulation in Lake Huelde (Kempf et al., 2015), which is also unaffected by tidal currents. Even though significant spatial accumulation rate variations are neither expected nor observed in the long cores, it cannot be excluded that sediment of strongly variable accumulation rate was retrieved in deeper parts of long cores, towards the on-lapping onto R6. Strong temporal variations in accumulation rate exist, at least in the uppermost part of the sedimentary record. The post-1960 sediment in the western part of the basin is ≤ 4 cm thick, on average 2 cm. The average accumulation rate in Pos04 is 1.88 mm yr^{-1}. The post-1960 sediment would be ~9.8 cm thick, or more, if the lack of compaction would be included.

The detrital layers exhibit characteristics of event deposition, e.g. mud clasts and decreasing upwards X-ray attenuation, which reflects fining upwards (cf. Van Daele et al., 2014). The intervals of the detrital layers are therefore likely to have been deposited with a different accumulation rate, probably quasi-instantaneously.
Given the sparse age-depth information and the potentially complex accumulation rate variations, it is most adequate to use a simplistic age-depth model, while being aware of the limitations of the model (Telford et al., 2004). The age-depth information, i.e. the radiocarbon date and the radionuclide analysis, that led to the AD 1960 tsunami deposit interpretation (Kempf et al., 2015), are the basis of a linear regression from near the bottom of core Pos04 to the top, which is the equivalent of a constant accumulation rate (Fig. 5.7). The intervals of detrital layer were considered as instantaneous deposits in this model's input.

5.5.3 Age of the crosscutting channel and constraints on Lake Cucao's vertical displacement history

Coastal areas on subduction zones are known to deform vertically throughout the seismic cycle (Wesson et al., 2015), which causes shoreline displacement. The AD 1960 Great Chilean Earthquake caused the area around Lake Cucao to subside co-seismically by ~1 m (Plafker and Savage, 1970), which put Lake Cucao into an intertidal position, if the lake level was above the intertidal zone before. The intertidal currents entering the lake during high tide caused the formation of the intertidal delta, the crosscutting channel and the mega-ripples. If the channel is a recently formed feature, it would truncate the mostly parallel to sub-parallel internal reflectors of seismic unit U2. This is not the case; all internal reflectors, R1 to R5, in U2 converge towards the channel (Fig. 5.2c), which indicates that intertidal currents were active at least episodically during the period represented by the sedimentary infill visible on sub-bottom profiles in Lake Cucao. This constrains the vertical displacement of Lake Cucao in the last 3700 yrs (3560–3830 cal. yrs BP) to a narrow window around its current position. This probably means that the beach, dunes and freshwater marshes on the barrier between the Pacific Ocean and Lake Cucao experienced limited horizontal shoreline displacement. Consequently, Lake Cucao may have been a reliable tsunami recorder in the past 3700 yrs and potentially longer.

5.5.4 Identifying tsunami deposits in the Lake Cucao sedimentary record

The detrital layers share similar sedimentary characteristics with the tsunami deposit of AD 1960. However, other causative processes have to be excluded before the interpretation of tsunami origin can be made. Tsunami deposits have several sedimentary characteristics, however, few are unique to tsunami deposits and none of them are found in all tsunami deposits. For example, landwards thinning and fining sand sheets can be produced by storm surges and tsunamis alike (Kortekaas and Dawson, 2007). Other causative processes typically associated with the formation of detrital layers can be excluded. For example, flood turbidites, which are common in Chilean lakes (Van Daele et al., 2015), can be excluded, because upstream adjacent Lake Huillinco traps riverine flood input to Lake Cucao, except for a small creek entering Lake Cucao from the

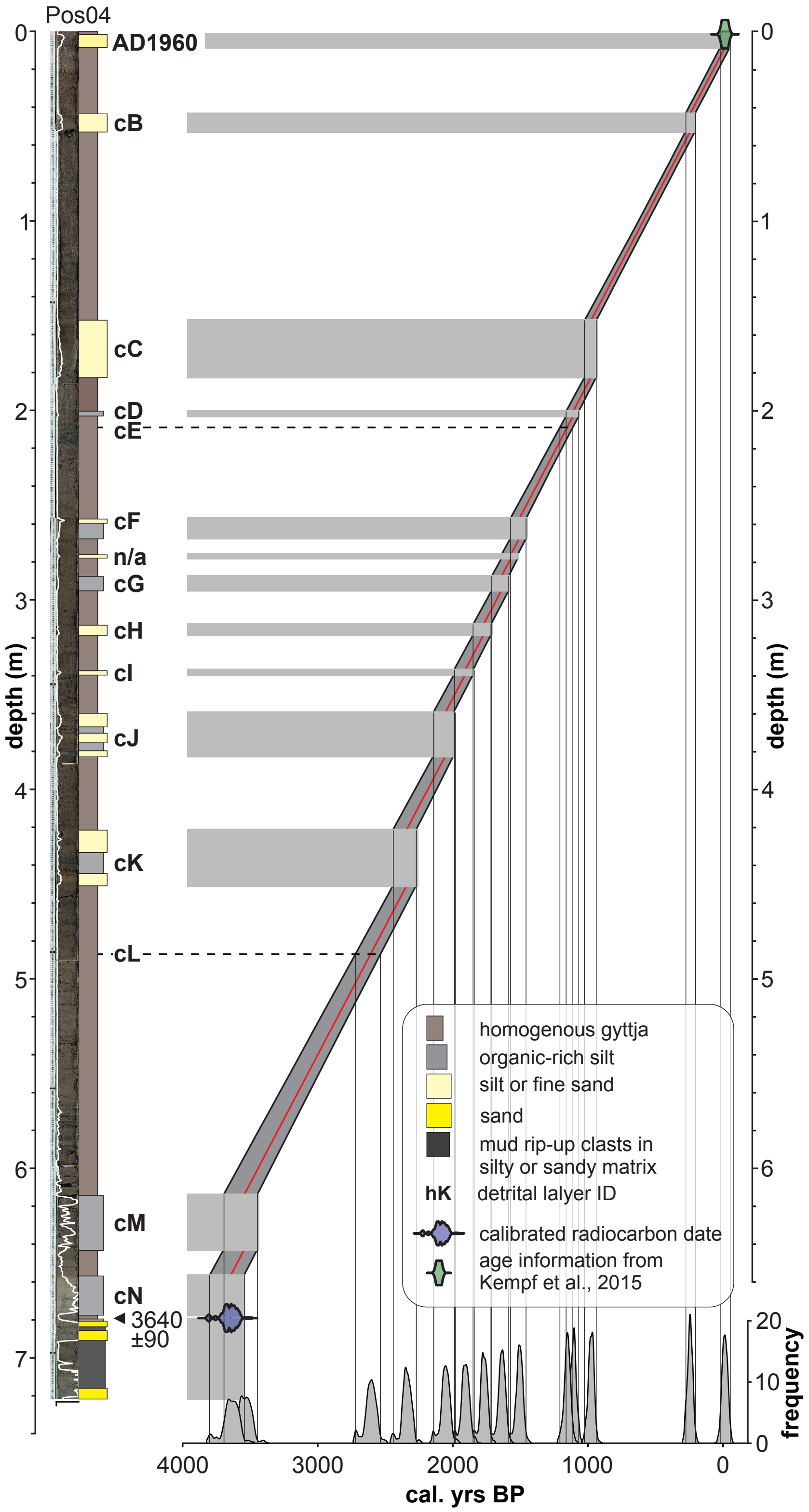

Figure 5.7: Classical age-depth model of core Pos04 calculated with Clam (Blaauw, 2010). The uncertainty (grey area) of 95 % around the modelled median (red line) is underestimated, which is an inherent problem with age-depth models with little age information. The grey probability density functions (PDFs) at the bottom show the calculated ages of detrital layers.

south. Hence, for each setting, criteria need to be developed specifically. We define the following five different criteria tailored to the sedimentary environment of Lake Cucao, each of which are indicative of tsunami deposition or are excluding other processes.

i **High magnetic susceptibility** – Magnetic susceptibility is controlled by the mineral content. High magnetic susceptibility in Lake Cucao means the sediment contains ferrimagnetic minerals, such as iron oxides (e.g. hematite and magnetite). Secondarily, concentrations of ferrimagnetic minerals content can be increased by organic matter depletion and compaction. The low magnetic susceptibility values of gyttja indicate that the layers with high magnetic susceptibility values are detrital. The detrital layers are interpreted as events, during which high amounts of terrigenous material (i.e. from the tidal delta and from outside the lake) is introduced quasi-instantaneously into the lake basin.

ii **Traceability in the sedimentary record** – Tsunami deposits on coastal lowlands are spatially variable in thickness (Goto et al., 2014). Tsunami deposits are often continuous deposits to where they wedge out towards their maximum lateral extent. When tsunamis inundate coastal lakes, the water flow contains and deposits sand, remobilises muddy lake sediment and redistributes it within the lake basin (Kelsey et al., 2005; Kempf et al., 2015). Areas beyond the zone of sandy deposition can receive exclusively muddy tsunami sediment (Kelsey et al., 2005; Kempf et al., 2015). Therefore tsunami deposits should be traceable in the sedimentary record throughout large areas of the lake, if not the entire lake basin. Storms occur on the south central Chilean coast, however, tropical cyclones with the potential to create deposits kilometres inland and in coastal lakes, have not been documented and are unlikely to happen, even under strong El Niño conditions (Fedorov et al., 2010). The criterion is given as a fraction of the number of cores, in which the detrital layer occurs over the number of cores, in which the detrital layer could occur in the stratigraphy. Complete or nearly complete representation in the sedimentary archive is treated as indicative for tsunami deposition (Tab. 5.1, Fig. 5.4).

iii **Acoustic reflector correlation** – The six strong reflectors (R1–R6) on the sub-bottom profiles represent strong contrasts in acoustic impedance, i.e. differences in p-wave velocity and/or density. In a gyttja dominated environment high acoustic impedance contrast can be associated with detrital layers. Not every detrital layer will necessarily produce a high-amplitude reflector. However, if a detrital layer can be correlated to a high-amplitude acoustic reflector, then this points towards basin wide distribution and high detrital content, which is expected of a tsunami deposit.

iv **Mud rip-up clasts** – Mud rip-up clasts are generated by high-energy processes in otherwise low-energy environments. In sub-aquatic landslides, mud rip-up clasts occur on the spectrum of disintegration of the sliding sediment from slumps, to debris flows, to turbidity currents (cf. Lee et al., 2013). Onshore landslides that impact muddy fjord sediment have also produced mud rip-up clasts, which may show paleo flow by imbrication (Van Daele et al., 2014). In coastal environments, mud rip-up clasts are most commonly associated with tsunami deposition (Peters et al., 2007), however, storm surges reportedly can produce mud rip-up clasts, too (Phantuwongraj et al., 2013). In Lake Cucao, two types of mud rip-up clasts can be differentiated by their X-ray attenuation. One type has the same X-ray attenuation as gyttja from lake sediment and is interpreted as such. The other type has higher X-ray attenuation and could represent soil from the lake-surrounding freshwater marshes. Specifically for Lake Cucao, the presence of both types of mud rip-up clasts excludes strong tidal currents as the depositional process for the detrital layers. However, mud rip-up clasts in the sedimentary record were difficult to impossible to identify on split core surfaces with an exception for detrital layer cN. All other mud rip-up clasts were identified on X-ray CT-scans (Fig. 5.5).

v **Age-correlation** – Tsunamis with a megathrust earthquake trigger hit long stretches of coastline. Tsunami deposits can be correlated over long distances using their chronology (Cisternas et al., in prep.; Peters et al., 2007; see chapter 4). If a detrital layer potentially correlates to an identified tsunami deposit from the Valdivia segment, then this consolidates the interpretation as a tsunami deposit. The age control in the Lake Cucao record is weak, due to little age information. However, two detrital layers, cA (i.e. AD 1960) and cN, have been dated sufficiently for correlation with other tsunami deposits. The AD 1960 deposit was dated using radionuclide analyses (Kempf et al., 2015) and correlated to the AD 1960 Great Chilean Earthquake and its tsunami, as well as other tsunami deposits in the coastal area closest to the entire rupture zone (Cisternas et al., 2005; Ely et al., 2014; Garrett et al., 2013; Reinhardt et al., 2010). The lowermost detrital layer in core Pos04, cN, is dated by the age-depth model to 3690 ± 130 cal. yrs BP, which correlates to the tsunami deposit hM (3740 ± 150 cal. yrs BP) in the Lake Huelde record (see chapter 4).

Three of the 15 detrital layers (cD, cE, and cL) fulfil only one or no criterion sufficiently. The confidence of an interpretation as a tsunami deposit in these cases is questionable, however, not excluded (Tab. 5.1). Eight detrital layers fulfil three or more criteria, for which the confidence level for the tsunami deposit interpretation is high. The remaining 4 detrital layers either fulfil one or two criteria sufficiently; however, absence of evidence for fulfilling further criteria only leads to a medium confidence level for the interpretation as a tsunami deposit.

5.5.5 Origin and evolution of the lake basin

The topographical depression that is now occupied by Lake Cucao, is a glacifluvial river valley (Glasser et al., 2008), which was submerged during the last global post-glacial eustatic sea-level rise (Siddall et al., 2003). During this transgression, the glacifluvial valley must have become an estuary, similar to lakes Lanalhue and Lleu Lleu ~500 km further north (Fig. 5.1) (Stefer et al., 2010). The sedimentary record retrieved above the radiocarbon date in core Pos04 is lacustrine, indicating that the barrier, which makes Lake Cucao a coastal lake, rather than an estuary, has been in place longer than 3700 yrs.

Coastal along-shore currents and aeolian sediment transport and deposition silled off the estuary and created the enclosed lake basin. When exactly this happened is unclear, however, one possibility is that the expanding westerlies between 8.5 and 5.5 ka (Lamy et al., 2010; Van Daele et al., 2016) may have effected the coastal current patterns and triggered aeolian processes to create the sill. Currently, Lake Cucao lies in the intertidal zone (Kempf et al., 2015; Villalobos et al., 2003), with saline water flowing into the lake from the Pacific during high tide. This process has built up a tidal delta in Lake Cucao around the outlet. The conceptual model of the basin infill and evolution includes foresets of the tidal delta interfingering with basin sediment of the estuary and later of the lake (Fig. 5.8). One of these foresets may explain the muddy sand at the base of cores Pos02, Pos03 and Pos11. Detrital layer cN, interpreted as tsunami deposit, is in direct contact to the muddy sand in all cores of the western part of the basin (not at Pos06). It appears that the formation of cN disrupted the deposition of muddy sand at the mentioned core locations. Detrital layer cN is thicker and coarser than all other detrital layers in most core locations. Additionally, the deposit correlates chronologically to either hM or hN, which are both among the thicker and coarser tsunami deposits from the Lake Huelde paleotsunami record (see chapter 4). The overall more extreme character of cN and hM/hN may point towards an unusually high tsunami. The end of foreset sedimentation after deposition of cN could be due to a large amount of either co-seismic uplift or subsidence. In the uplift scenario the lake system may stop interacting with the Pacific Ocean altogether. Tidal inflows into the lake would not occur and the processes, which form topsets and foresets on the tidal delta, would stop. Large amounts of co-seismic uplift can occur on the Chilean coast, e.g. in AD 1960 on Isla Guafo (Sievers et al., 1963). However, the geometry of the crust on and off Isla de Chiloé probably needs splay fault slip to generate said uplift, as neither AD 1960, 1837 nor 1575 created large co-seismic uplift (Garrett et al., 2015; Plafker and Savage, 1970; Sievers et al., 1963). The subsidence scenario is more plausible, because of the example given by co-seismic subsidence around Cucao (~1 m) during the 1960 earthquake (Plafker and Savage, 1970).

The subsidence would create accommodation space, which would favour aggradation at the cost of progradation of the delta. While the delta aggradates, the lake basin accumulates gyttja. Once aggradation used up the newly available accommodation space, the lake system would switch back to progradation and begin forming the next interfingering foreset. In both examples, the presence of the tidal delta would be less dominant in the more basinal sediments.

In the Lake Cucao paleotsunami record presented in this study, there are 8 (with the highest degree of confidence) to potentially 15 tsunami deposits in the last 3700 yrs. During the same time interval the Lake Huelde paleotsunami record contains 14 or 15 tsunami deposits. If all or all but one detrital layer in the Lake Cucao record are of tsunami origin, then Lake Huelde and Lake Cucao can be considered in broad agreement and recorded the same number of tsunamis over the last 3700 yrs.

5.6 Conclusions

Sub-bottom profiles from Lake Cucao show strong continuous reflectors in the otherwise acoustically semi-transparent lake sediment. The strong reflectors correlate to detrital layers in the sedimentary record. These and other detrital layers exhibit several characteristics indicative of tsunami deposition and were therefore interpreted as tsunami deposits. The tsunami deposit

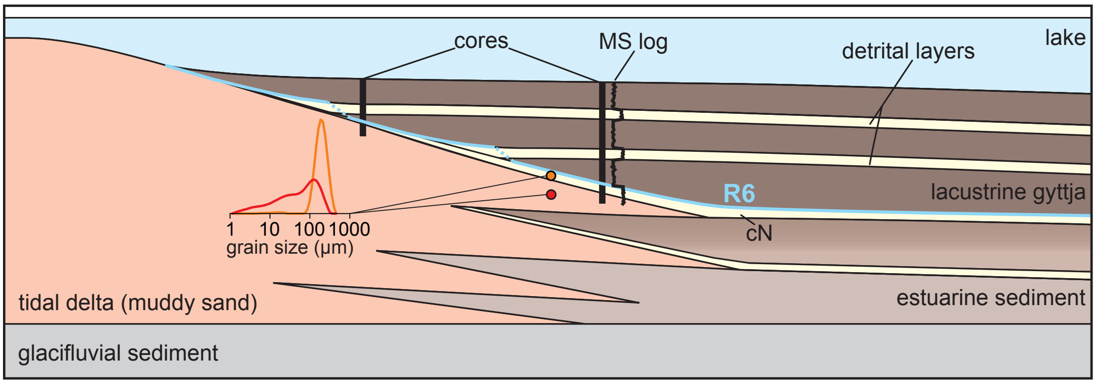

Figure 5.8: Conceptual model of Lake Cucao's sedimentary infill.

interpretation was made on the basis of five criteria concerning the sedimentary characteristics (i.e. magnetic susceptibility, presence of mud clasts and correlation throughout the lake basin), acoustic properties (i.e. correlation to strong acoustic reflectors) and age correlation to known paleotsunamis of the regional records. Eight detrital layers are interpreted as tsunami deposits with a high level of confidence, five with a medium level of confidence and three with a low level of confidence. However, the comparison to the same time interval in the neighbouring Lake Huelde suggests that all or all but one detrital layer may correlate to an identified tsunami deposit from Lake Huelde.

Acknowledgements

PK acknowledges financial support by the Special Research Fund of Ghent University (BOF), JM from the Swiss National Science Foundation (SNF) grant 133481 and the Chilean Fondecyt projects nr. 1150346 and 1150321, MVD from the Research Foundation Flanders (FWO travel grant K201512N). We thank Koen De Rycker and Gauvain Wiemer for fieldwork support, Dr. Clair Schepens and Dr. Eric Achten for CT-scanner support.

References

Amante, C., Eakins, B.W., 2009. ETOPO1 1 Arc-Minute Global Relief Model: Procedures, Data Sources and Analysis. NOAA Technical Memorandom NESDIS NGDC-24. National Geophysical Data Center, NOAA.

Atwater, B.F., Cisternas, M., Yulianto, E., Prendergast, A.L., Jankaew, K., Eipert, A.A., Ignatius, W., Fernando, S., Tejakusuma, I., 2013. The 1960 tsunami on beach-ridge plains near Maullín, Chile: Landward descent, renewed breaches, aggraded fans, multiple predecessors. Andean Geology 40, 393–418.

Blaauw, M., 2010. Methods and code for "classical" age-modelling of radiocarbon sequences. Quaternary Geochronology 5, 512–518.

Chagué-Goff, C., Schneider, J.-L., Goff, J.R., Dominey-Howes, D., Strotz, L., 2011. Expanding the proxy toolkit to help identify past events — Lessons from the 2004 Indian Ocean Tsunami and the 2009 South Pacific Tsunami. Earth-Science Reviews 107, 107–122.

Cisternas, M., Atwater, B.F., Torrejón, F., Sawai, Y., Machuca, G., Lagos, M., Eipert, A., Youlton, C., Salgado, I., Kamataki, T., Shishikura, M., Rajendran, C.P., Malik, J.K., Rizal, Y., Husni, M., 2005. Predecessors of the giant 1960 Chile earthquake. Nature 437, 404–407.

Cisternas, M., Carvajal, M., Gorigoitía, N., Garrett, E., Wesson, R., Dura, T., Ely, L., in prep. Dissimilar ancestors to a giant earthquake: Geologic and historical evidence for great and smaller earthquakes and tsunamis in the 1960 Chile earthquake region since A.D. 1000.

Dura, T., Cisternas, M., Horton, B.P., Ely, L.L., Nelson, A.R., Wesson, R.L., Pilarczyk, J.E., 2015. Coastal evidence for Holocene subduction-zone earthquakes and tsunamis in central Chile. Quaternary Science Reviews 113, 93–111.

Ely, L.L., Cisternas, M., Wesson, R.L., Dura, T., 2014. Five centuries of tsunamis and land-level changes in the overlapping rupture area of the 1960 and 2010 Chilean earthquakes. Geology 42, 995–998.

Fedorov, A. V, Brierley, C.M., Emanuel, K., 2010. Tropical cyclones and permanent El Niño in the early Pliocene epoch. Nature 463, 1066–1070.

Fritz, H.M., Phillips, D.A., Okayasu, A., Shimozono, T., Liu, H., Mohammed, F., Skanavis, V., Synolakis, C.E., Takahashi, T., 2012. The 2011 Japan tsunami current velocity measurements from survivor videos at Kesennuma Bay using LiDAR. Geophysical Research Letters 39, 6.

Garrett, E., 2013. Biostratigraphic constraints on megathrust earthquake deformation history in south central Chile. Doctoral Dissertation, Durham University, UK.

Garrett, E., Shennan, I., Watcham, E.E.P., Woodroffe, S.S.A., 2013. Reconstructing paleoseismic deformation, 1: modern analogues from the 1960 and 2010 Chilean great earthquakes. Quaternary Science Reviews 75, 11–21.

Garrett, E., Shennan, I., Woodroffe, S.A.A., Cisternas, M., Hocking, E.P.P., Gulliver, P., 2015. Reconstructing paleoseismic deformation, 2: 1000 years of great earthquakes at Chucalén, south central Chile. Quaternary Science Reviews 113, 112–122.

Glasser, N.F., Jansson, K.N., Harrison, S., Kleman, J., 2008. The glacial geomorphology and Pleistocene history of South America between 38°S and 56°S. Quaternary Science Reviews 27, 365–390.

Goto, K., Hashimoto, K., Sugawara, D., Yanagisawa, H., Abe, T., 2014. Spatial thickness variability of the 2011 Tōhoku-oki tsunami deposits along the coastline of Sendai Bay. Marine Geology 358, 38–48.

Hogg, A.G., Hua, Q., Blackwell, P.G., Niu, M., Buck, C.E., Guilderson, T.P., Heaton, T.J., Palmer, J.G., Reimer, P.J., Reimer, R.W., Turney, C.S.M., Zimmerman, S.R.H., 2013. SHCal13 Southern Hemisphere Calibration, 0–50,000 Years cal BP. Radiocarbon 55, 1889–1903.

Kelsey, H.M., Engelhart, S.E., Pilarczyk, J.E., Horton, B.P., Rubin, C.M., Daryono, M.R., Ismail, N., Hawkes, A.D., Bernhardt, C.E., Cahill, N., 2015. Accommodation space, relative sea-level, and the archiving of paleo-earthquakes along subduction zones. Geology 43, 675–678.

Kelsey, H.M., Nelson, A.R., Hemphill-Haley, E., Witter, R.C., 2005. Tsunami history of an Oregon coastal lake reveals a 4600 yr record of great earthquakes on the Cascadia subduction zone. Geological Society of America Bulletin 117, 1009–1032.

Kempf, P., Moernaut, J., Van Daele, M., Vermassen, F., Vandoorne, W., Pino, M., Urrutía, R., Garrett, E., De Batist, M., 2015. The sedimentary record of the tsunami caused by the 1960 Great Chilean Earthquake in two coastal lakes on Chiloé Island, Chile. Sedimentary Geology 328, 73–86.

Kennedy, J., 1963. The mechanics of dunes and antidunes in erodible-bed channels. Journal of Fluid Mechanics 16, 521–544.

Kortekaas, S., Dawson, A., 2007. Distinguishing tsunami and storm deposits: An example from Martinhal, SW Portugal. Sedimentary Geology 200, 208–221.

Lamy, F., Kilian, R., Arz, H.W., Francois, J.-P., Kaiser, J., Prange, M., Steinke, T., 2010. Holocene changes in the position and intensity of the southern westerly wind belt. Nature Geoscience 3, 695–699.

Lee, S.H., Jung, W.-Y., Bahk, J.J., Gardner, J.M., Kim, J.K., Lee, S.H., 2013. Depositional features of co-genetic turbidite–debrite beds and possible mechanisms for their formation in distal lobated bodies beyond the base-of-slope, Ulleung Basin, East Sea (Japan Sea). Marine Geology 346, 124–140.

Lomnitz, C., 2004. Major Earthquakes of Chile: A Historical Survey, 1535–1960. Seismological Research Letters 75, 368–378.

Lomnitz, C., 1970. Major Earthquakes and Tsunamis in Chile during the period 1535 to 1955. Geologische Rundschau 59, 938–960.

Moreno, M.S., Bolte, J., Klotz, J., Melnick, D., 2009. Impact of megathrust geometry on inversion of coseismic slip from geodetic data: Application to the 1960 Chile earthquake. Geophysical Research Letters 36, L16310.

Nentwig, V., Tsukamoto, S., Frechen, M., Bahlburg, H., 2015. Reconstructing the tsunami record in Tirúa, Central Chile beyond the historical record with quartz-based SAR-OSL. Quaternary Geochronology 30, 299–305.

Peters, R., Jaffe, B., Gelfenbaum, G., 2007. Distribution and sedimentary characteristics of tsunami deposits along the Cascadia margin of western North America. Sedimentary Geology 200, 372–386.

Phantuwongraj, S., Choowong, M., Nanayama, F., Hisada, K.-I., Charusiri, P., Chutakositkanon, V., Pailoplee, S., Chabangbon, A., 2013. Coastal geomorphic conditions and styles of storm surge washover deposits from Southern Thailand. Geomorphology 192, 43–58.

Plafker, G., Savage, J.C., 1970. Mechanism of the Chilean Earthquakes of May 21 and 22 , 1960. Geological Society of America Bulletin 81, 1001–1030.

Reinhardt, E.G., Nairn, R.B., Lopez, G., 2010. Recovery estimates for the Río Cruces after the May 1960 Chilean earthquake. Marine Geology 269, 18–33.

Siddall, M., Rohling, E.J., Almogi-Labin, A., Hemleben, C., Meischner, D., Schmelzer, I., Smeed, D.A., 2003. Sea-level fluctuations during the last glacial cycle. Nature 423, 853–858.

Sievers, H., Villegas, G.C., Barros, G., 1963. The seismic sea wave of 22 May 1960 along the Chilean coast. Bulletin of the Seismological Society of America 53, 1125–1190.

Stefer, S., Moernaut, J., Melnick, D., Echtler, H.P., Arz, H.W., Lamy, F., De Batist, M., Oncken, O., Haug, G.H., 2010. Forearc uplift rates deduced from sediment cores of two coastal lakes in south-central Chile. Tectonophysics 495, 129–143.

Telford, R.J., Heegaard, E., Birks, H.J.B., 2004. All age–depth models are wrong: but how badly? Quaternary Science Reviews 23, 1–5.

Van Daele, M., Cnudde, V., Duyck, P., Pino, M., Urrutia, R., De Batist, M., 2014. Multidirectional, synchronously-triggered seismo-turbidites and debrites revealed by X-ray computed tomography (CT). Sedimentology 61, 861–880.

Van Daele, M., Moernaut, J., Doom, L., Boes, E., Fontijn, K., Heirman, K., Vandoorne, W., Hebbeln, D., Pino, M., Urrutia, R., Brümmer, R., De Batist, M., 2015. A comparison of the sedimentary records of the 1960 and 2010 great Chilean earthquakes in 17 lakes: Implications for quantitative lacustrine palaeoseismology. Sedimentology 62, 1466–1496.

Van Daele, M., Bertrand, S., Meyer, I., Moernaut, J., Vandoorne, W., Siani, G., Tanghe, N., Ghazoui, Z., Pino, M., Urrutia, R., De Batist, M., 2016. Late Quaternary evolution of Lago Castor (Chile, 45.6°S): Timing of the deglaciation in northern Patagonia and evolution of the southern westerlies during the last 17 kyr. Quaternary Science Reviews 133, 130–146.

Villalobos, L., Parra, O., Grandjean, M., Jaque, E., Woelfl, S., Campos, H., 2003. A study of the river basins and limnology of five humic lakes on Chiloé Island. Revista Chilena de Historia Natural 76.

Wesson, R.L., Melnick, D., Cisternas, M., Moreno, M., Ely, L.L., 2015. Vertical deformation through a complete seismic cycle at Isla Santa Maria, Chile. Nature Geoscience advance on.

"Es irrt der Mensch solang er strebt."
"Man errs as long as he strives."

AD 1808, Johann Wolfgang Goethe in *Faust. Eine Tragödie*

6 Potential of lake sediments for quantitative paleotsunami research

Contributions: The manuscript was written by Philipp Kempf. Fieldwork was conducted by Philipp Kempf, Jasper Moernaut, Maarten Van Daele and Willem Vandoorne, and facilitated by Mario Pino and Roberto Urrutia. Discussion of results and interpretation was done by Philipp Kempf, Jasper Moernaut, Maarten Van Daele and Marc De Batist.

6.1 Introduction

For tsunami hazard assessment to be successful, tsunami research needs to determine how often tsunamis occur and how strong the tsunamis are. The recurrence pattern of tsunamis in south central Chile is addressed in chapter 4. The tsunami size lies outside of the scope of this thesis and is a lot more difficult to determine. Paleotsunami intensity analyses require tools for quantitative paleotsunami interpretation.

Tsunami deposits are a direct product of tsunami inundation and reflect the hydrodynamic energy during the event. However, tsunami deposits pose the problem of equifinality, i.e. every deposit can be created by a multitude of conditions and every set of conditions can form a multitude of deposits. The range of causative conditions for tsunami deposits is wide and tsunami deposits exhibit a high degree of variability (Goto et al., 2014). It is in principle possible to estimate the tsunami size by investigating the deposit, however, the uncertainty that comes with such an estimation may be large (e.g. Jaffe et al., 2012). Collecting quantitative information about a tsunami deposit, e.g. grain size or deposit thickness, is straightforward. Quantifying flow characteristics of a tsunami from a tsunami deposit is complex and requires a model. The field of modelling in tsunami research is quickly growing, because of its potential to answer questions related to the quantification of tsunamis (Goff et al., 2012) and because of the detailed observations made during the 2004 Indian Ocean Tsunami and especially during the AD 2011 Tōhoku tsunami. The observations from these two tsunamis provide an unprecedented database for model validation.

In contrast to quantitative methods, relative and semi-quantitative methods appear easier to apply, i.e. comparing one tsunami deposit with another. Relative methods, in general, require objective criteria. These criteria can be quantitative or threshold-based. For example in lacustrine paleoseismology the length along the central Chilean megathrust fault where earthquake-induced turbidites were recorded, or the cumulative turbidite thickness in a single lake (Moernaut et al., 2014) are quantitative criteria. Lake slope failures in lakes along the Alpine Fault in New Zealand are indicative of strong shaking (seismic intensity >VI), and a combination of lake slope failures and subaerial slope failures is indicative of violent shaking (seismic intensity >IX) (Howarth et al., 2014), which is an example of a threshold-based criterion. Potential criteria for relative tsunami sizes are discussed below.

6.2 Quantitative tsunami research

To infer quantitative information about tsunamis models are necessary. There are two principally different ways to model tsunamis, forward modelling and inverse modelling. Of the forward models there are two, physical and numerical models.
In forward modelling, a tsunami source model is determined, either through making assumptions or through crustal deformation model results. A hydrodynamic model translates the tsunami source to a flow field. The flow leads to a simulation of sediment transport, which in turn leads to a erosion-deposition simulation (Sugawara et al., 2014). The forward model can be validated or falsified by comparing the simulated flow field or the simulated deposit to field observations. In the case of paleotsunamis, the tsunami deposits may be available for validation or falsification, while flow field observations usually are not.
In inverse modelling the direction of modelling is reversed. Sedimentary data is the input, to which an inverse sediment transport model is applied. The result estimates characteristics of the flow field during deposition. Inverse modelling can only be validated in cases with existing flow field observations. This excludes all paleotsunamis.

6.2.1 Physical forward modelling

Most physical models are models of subaerial landslide-induced tsunamis. The wavelength and wave period of earthquake-induced tsunamis is long and difficult to model to scale (Rossetto et al., 2011). However, the focus on landslide-induced tsunamis allows modelling of the tsunami type that poses a great threat on coastlines with bays, for example in Norwegian fjords (e.g. Harbitz et al., 2014; Lindstrøm et al., 2014), or in the vicinity of volcanoes, for example in the Mediterranean (e.g. De Girolamo et al., 2014). In general, scaling is a difficult issue with physical models. Smaller scale models will have more unrealistic artefacts. In long flumes, 2D physical modelling of earthquake induced tsunami waves may only now become affordable (Rossetto et al., 2011). However, there is a key difference in energy dissipation in 2D models versus 3D models. The 2D models will generally produce a higher wave with the same source (Heller and Spinneken, 2015). As a consequence, scaling remains problematic in large 2D flume experiments.

6.2.2 Numerical forward modelling

Numerical modelling is not confined to size limitations, unlike the physical models. The rapidly evolving computational power allows increasingly high-resolution models. Numerical models are tailored for their purpose and can focus on parts of the cause and effect chain from earthquake to tsunami deposition, instead of modelling the entire process from earthquake to tsunami deposition. For example, there are analytical solutions from elastic models, which translate coseismic slip on the fault surface into crustal deformation, modelling only the tsunami source (e.g. Okada, 1985).
There are examples of numerical forward modelling case studies to match physical forward models of landslide induced tsunamis, e.g. in Norwegian fjords (e.g. Løvholt et al., 2015). How-

ever, more commonly, forward modelling case studies are matched with geological or historically recorded observations. For example, the Lituya Bay tsunami – notorious for being the highest eye-witnessed wave on record with 524 m (Fritz et al., 2009) – has puzzled researchers and has changed some of the underlying physical formulas used in models (Weiss et al., 2009). Subaqueous landslide-induced tsunami models have been applied to geologically and sometimes historically known tsunamis in oceans, e.g. Storegga Slide tsunami (Bondevik et al., 2005), or in lake basins, e.g. in Swiss lakes (Hilbe and Anselmetti, 2015; Kremer et al., 2014), to assess the hazard associated to specific events.
Several tsunami-related numerical forward models estimate the erosional and depositional effect of tsunami wave trains in coastal areas. Like all other numerical forward models, these models need either a real or an assumed topography and bathymetry as data input, as these parameters strongly influence the hydrodynamics near shore and onshore (Sugawara et al., 2014). For example, these kind of models noted that deposited grain sizes may not necessarily represent tsunami flow conditions and that flow reversal between run-up and backwash does not occur simultaneously along the landward extent of the wave, as the backwash can begin near the coastline, while the tsunami run-up front is still advancing (Apotsos et al., 2011). Overall trends common to tsunami deposits, like landward fining and landward thinning, are in reality often obscured by the onshore topography. In numerical models with idealized topography, these trends have been reconstructed (Sugawara et al., 2014). In this and similar ways, numerical models are able to address questions that are difficult to answer with purely geological tools, such as how to differentiate tsunami deposits from storm deposits, what are the sediment sources of tsunami deposits or what are the effects of tsunamis on the geomorphology in the inundated area (Sugawara et al., 2014).

6.2.3 Inverse modelling

Inverse models are tailored for specific use, just like forward models. As they unravel the cause and effect chain in reversed order, they all begin with an observation of the tsunami product, e.g. deposit grain size or deposit thickness etc., in order to calculate characteristics of the tsunami inundation, e.g. flow speed, inundation limit or flow depth. The application of inverse models bears great potential in tsunami hazard assessment. Most famously, the AD 869 Jōgan tsunami deposit was known north and south of the area of the Fukushima Daiichi nuclear power plant before the AD 2011 Tōhoku tsunami (Minoura et al., 2001). Tsunami hazard assessment with the use of current state-of-the-art inverse models on the AD 869 Jōgan tsunami deposit may have prevented the construction of a delicate piece of infrastructure, such as a nuclear power plant, in the tsunami inundation zone. It would have prevented the nuclear reactor meltdown catastrophe and will prevent similar catastrophes in the future.
All existing inverse models are for onshore deposits – not for offshore, i.e. marine tsunami deposits, and not for coastal lake tsunami deposits (Sugawara et al., 2014). Grain size of the deposit dictates which models can be applied. The different styles of transport of sand in suspension and boulders as bed load (transport by either sliding or overturning) require different models. Currently, there are 4 main inverse models for sandy tsunami deposits. They are reviewed in

detail in Sugawara et al. (2014). They all work under the assumption of transport in suspension and deposition out of suspension. The settling column model (Soulsby et al., 2007), for example, estimates run-up height and run-up distance of a tsunami. In order to do this, the settling column model needs the input of bulk distribution of settling velocities at multiple locations and the fractional thickness of grain size components. Apart from transport in suspension, this model assumes that the tsunami is heavily and uniformly loaded with sediment in suspension, when the tsunami hits the shoreline, and that particles are not resuspended after deposition (single trajectory). What unites this model with the other three models, i.e. particle trajectory model (Moore et al., 2007), particle settling model (Smith et al., 2007) and equilibrium suspension model (Jaffe et al., 2011, 2012; Jaffe and Gelfenbuam, 2007) (Tab. 6.1), are the extreme simplifications in the assumptions and in the physical principles at work.

The equations in inverse models for boulder transport and deposition need to be fundamentally different from sandy tsunami models, because boulders are transported in the bed load (Goff et al., 2010) and the size of the boulders (typically >1 m) is larger than the flow boundary layer as the base of the water column's velocity profile. Dimensionless coefficients of drag, lift and inertia need to be determined for the shape, size and density of the boulders (e.g. Buckley et al., 2011), while particles in the sandy tsunami models are treated as spherical. The inverse tsunami boulder models typically calculate the minimum flow depth and minimum flow speed to move the boulders found in the field (e.g. Nott, 2003). This could help to discriminate boulders moved by extreme storm waves from tsunami boulders. However, this method bears uncertainties, among other reasons, because the ranges of flow depth and speed in storms and tsunami overlap (tsunamis are capable of the higher flow depth and flow speed) and because models can significantly underestimate the flow depth and speed, if larger boulders were not available for entrainment in the source area.

An example of how various models could be used is given by the investigation of the AD 2011 Tōhoku tsunami, which led to an estimation of the AD 869 Jōgan tsunami. This investigation was possible, because of extensive flow depths reports during the AD 2011 Tōhoku tsunami (Mori et al., 2011). The co-seismic seafloor deformation and fault slip were calculated from, among other methods, tsunami waveform data (Satake et al., 2013), from high-rate GPS data alone (Yue and Lay, 2011) or in combination with seismic waveform data (Yue and Lay, 2013). These results were then fed into forward models, which calculated tsunami generation, propagation and inundation, i.e. flow depth, for the same event and compared it to the observed data (Namegaya and Satake, 2014). The difference between simulated and observed flow depths was minimal, validating the used parameters. Using these validated parameters, various forward models were run to recreate the tsunami deposit of the AD 869 Jōgan tsunami in an iterative way (Sawai et al., 2012). The best matching paleotsunami flow depth scenario was then reversed to estimate the magnitude of the AD 869 Jōgan earthquake ($M_W > 8.6$) (Namegaya and Satake, 2014).

Table 6.1: Overview of the four main inverse models for sandy tsunami deposits after Sugawara et al. (2014) (from Jaffe and Gelfenbuam, 2007; Jaffe et al., 2012; Moore et al., 2007; Smith et al., 2007; Soulsby et al., 2007).

approach	tsunami characteristics estimated	inputs	assumptions	references
particle trajectory	Product of tsunami height at shore and average speed (discharge), can use Law of the Wall or Froude number assumptions to calculate each parameter separately	settling velocity of a larger (D90 or D95) particle, distance particle travelled	- transport in suspension - particle not resuspended after deposition (single trajectory) - large particles suspended throughout the water - law of the wall applies (2007 paper)	Moore et al. 2007
particle settling	minimum flow depth of water	settling velocity of slowest settling particle	- transport in suspension - particles settle individually - muds settle as flocs - wave period of tsunami can be estimated	Smith et al. 2007
settling column	inundation limit and run-up distance	bulk distribution of settling velocities at multiple locations, fractional thickness of grain size components	- transport in suspension - wave heavily and uniformly charged with sediment at shoreline - particles not resuspended after deposition (single trajectory)	Soulsby et al. 2007
equilibrium suspension	Shear velocity at a point, tsunami flow speed at a point calculated using bottomroughness (high sensitivity to choice) and flow depth (low sensitivity to choice) estimates	bulk distribution of settling velocities of suspension graded interval, bottom roughness, flow depth (not a strong constraint)	- transport in suspension - steady flow formulation for turbulence - sediment available for suspension - equilibrium suspension - portions of deposit formed from clearing of the water column - no erosion by backwash	Jaffe and Gelfenbaum 2007, Jaffe et al. 2012

This was possible, because of detailed historical information of the paleo-coastline and numerous geophysical data types collected during the AD 2011 Tōhoku tsunami, e.g. high-rate GPS and seismic waveform data etc. Most of these observations and datasets are not available for south central Chile, the study area of this thesis.

6.3 Uncertainties in quantitative paleotsunami research in coastal lakes

Currently, there are no inverse models that are applicable to tsunami deposits from coastal lakes. The extreme simplifications of inverse models idealise the interaction of the tsunami inundation with the environment. Inundating a coastal lake changes the frictional regime. Basal drag may decrease, because of smoother surfaces and the slope towards the lake basin. However, loose sediment would be available for erosion increasing the ground-water interaction and the standing water body of the lake would need to be displaced by the tsunami water; both of these processes require large amounts of energy. All of these changes are unaccounted for in the existing inverse models.

For both coastal lakes and coastal lowlands, applying inverse numerical models to paleotsunamis is problematic, because the present coastal environment may not be the same as the contemporary coastal environment. The presented inverse models derive the tsunami flow depth, flow speed or run-up distance from the tsunami deposit at the site, where the tsunami deposit was sampled. While the result (e.g. flow depth) of the inverse model may be correct within the limits of uncertainty that comes with the method at the sampling site, it does not estimate the overall intensity of the paleotsunami, because it cannot account for the differences in the environment between the events. The shoreline may have been displaced horizontally and vertically since then (e.g. Bondevik et al., 1997; Fruergaard et al., 2015). In addition, vegetation or geomorphology are subject to changes, too, and affect tsunami inundation (e.g. Tang et al., 2013). In other words, inverse models (as well as relative methods) fail to answer the question whether a difference between tsunami deposits is due to a difference in the associated tsunamis (tsunami intensity) or if it is due to changes in the environment. For hazard-oriented studies the local tsunami intensity should be the key objective. Because of the strong influence by the environment, relative interpretations of tsunami deposits cannot be treated as relative information about tsunamis until all environmental factors are accounted for.

6.3.1 Sea-level change (vertical shoreline displacement)

Sea-level change displaces the shoreline vertically and with it the area of interaction between the tsunami and the environment. Relative sea-level change over thousands of years is a process governed by eustatic, isostatic, tectonic, local and unspecified processes (Shennan et al., 2012). Eustatic sea-level change is controlled by ocean crust production, sedimentation in the ocean basins, continental collisions, groundwater and lakes on continents, thermal expansion of the oceans and continental ice volume. Of these factors, continental ice volume has the highest potential amplitude on the time scale that most paleotsunamis are discussed on (~8000 yrs) (Miller et al., 2011). Oxygen isotopes can be used to estimate continental ice volume (e.g. Zachos et al., 2001).

Isostatic sea-level change can be dramatic on coastlines in postglacial environments with rapidly shrinking ice sheets (Boex et al., 2013). However, all paleotsunamis discussed here are from the Mid- to Late Holocene. Glacial isostatic adjustment during the last ~5500 yrs in northern Patagonia has not been researched directly.

Tectonic sea-level change or rather co-seismic and interseismic vertical deformation of the continental crust is very well documented. In fact, it was the co-seismic subsidence and uplift pattern that led to the understanding of megathrust earthquakes after the AD 1960 Great Chilean Earthquake and the AD 1964 Great Alaskan Earthquake (Plafker and Savage, 1970; Plafker, 1972). Co-seismic vertical deformation causes a sudden shift in near-coast environments. Such sudden shifts can be detected by analysing e.g. barnacle lines along the coastline (e.g Plafker, 1972) or diatom assemblages in the coastal deposits (Garrett et al., 2015). With the use of transfer functions, which quantify the difference of pre- and post-seismic diatom assemblages and modern analogues, the sea-level change can be determined with an uncertainty of a few decimetres (Shennan et al., 2012). The relative sea-level curve closest to the study area of this thesis (~85 km north of Cucao) was produced with a diatom transfer function (Garrett et al., 2015). This method has the potential to produce several thousand years of local relative sea-level data and is limited by the applicability of modern analogous diatom species and by the time-span and continuity of the sedimentary record. However, long diatom assemblage records archive relative sea-level change and do not differentiate between the causes. When diatom transfer functions cannot be used, the post-seismic and interseismic vertical deformation is less obvious to quantify. However, with networks of GPS antennas (e.g. Ding et al., 2015) or repeated observations through documented history (Wesson et al., 2015) this component can be measured with high precision.

There are no detailed records about relative sea-level change in the study area. However, in Chucalén, ~85 km north of the study area, there was no significant net change in sea-level over the past ~1000 yrs (Garrett et al., 2015), while in Maullín, 120 km north of the study area, a net relative sea-level fall was recognised for the late Holocene (Atwater et al., 1992). The global sea-level model ICE5G simulates net sea-level fall in the past 5500 on the southern South American Pacific coast, too (cf. Garrett, 2013 after Peltier, 2004).

6.3.2 Coastal landform evolution (horizontal shoreline displacement)

Coastal landform evolution affects tsunami inundation, because flow energy mostly dissipates through interaction with the surface, e.g. basal drag (friction) and erosion. The shallower the flow depth, the stronger the relative amount of friction becomes. For example, a prograding shoreline will gradually shift the area of potential tsunami inundation seaward in respect to older tsunami inundation areas. Some studies find that sand extent equals ~90 % of the inundation limit in low-lying coastal areas (MacInness et al. 2009). Others (Goto et al. 2011a, Abe et al. 2012) found only 50–60 % of the inundation area to be covered by tsunami deposits. Cheng and Weiss (2013) looked into the parameters that control this difference and found it is more dependent on the offshore wave height and on the onshore slope than the transported grain size. Nevertheless, even in post-tsunami surveys (not paleotsunami surveys) the relation between deposit limit and inundation limit varies (e.g. Szczuciński et al., 2012a, 2012b).
Over time coasts can experience horizontal shoreline displacement as a direct effect of vertical crustal deformation, e.g. on subsiding slopes the shoreline migrates landwards. The other way to produce horizontal shoreline displacement is to either deposit or erode sediment, e.g. deltaic sedimentation or coastal cliff erosion, respectively. Both processes need to be quantified, when accurate paleotsunami reconstructions are attempted reaching back as far as ~5500 yrs. However, both processes are not at all or not sufficiently reported on near Lake Huelde and Lake Cucao.

6.3.3 Vegetation and geomorphologic changes

The surface roughness in the inundation area influences a tsunami. The rougher the surface, the more basal drag it produces. In numerical models this roughness is called Manning's-n or Manning's roughness coefficient. The roughness coefficient (n) is part of the empirical formula for flow velocity of liquids in un-enclosed conduits

$$V = \frac{k}{n} R_h^{2/3} S^{1/2} \tag{6.1}$$

Where V is the cross-sectional average velocity, k is a constant, R_h is the hydraulic radius of the conduit and S is the slope of the hydraulic grade line. For example, in a numerical model study comparing the AD 2011 Tōhoku tsunami with its predecessor the AD Jōgan tsunami, Manning's-n was estimated to be lower (less rough) for the AD 869 Jōgan tsunami, because of fewer contemporary artificial structures (Namegaya and Satake, 2014). Similarly, with more geomorphologic features and more vegetation Manning's-n increases (Jaffe et al., 2012). However, coastal geomorphology and vegetation are subject to change. In a paleotsunami study Manning's-n can only be estimated. The highly active environment on the south central Chilean coast, and more specifically around Cucao, may be prone to strong changes over time. Reliable information on the geomorphologic history and the vegetation changes in the study area are not available.

6.4 Relative size of tsunami deposits

Respecting all confounding factors described above, it is still worth attempting a relative size analysis of the investigated tsunami deposits. However, the results of this analysis are relevant only in their relative size within their respective depositional environment, i.e. the lakes, and should be treated as tentative. The term "tsunami size" is used liberally, loosely referring to a group of parameters, e.g. inundation distance, inundation height, flow depth, flow speed, etc.

There are a few quantitative observations of the described and discussed tsunami deposits from the previous chapters, which lend themselves to comparative analyses. Namely, these parameters are i) maximum magnetic susceptibility, ii) average magnetic susceptibility, iii) traceability (lateral extent), iv) average tsunami deposit thickness and v) relative thickness of intervals of mud rip-up clasts (Tabs. 6.2, 6.3).

i **Maximum magnetic susceptibility** was used in chapters 4 and 5 as a criterion to interpret the detrital layers as tsunami deposits. The argument was that high magnetic susceptibility values represent sediment sources outside of the lake basin. The minerals accountable for the partially extreme values were identified as the high-density ferrimagnetic iron oxides hematite and magnetite. For erosion and transport, these dense mineral grains need higher flow speeds than lighter grains of the same shape and volume. Primarily, higher magnetic susceptibility means higher concentrations of the heavy and ferrimagnetic minerals, which in turn could be representative of stronger inundation (Fig. 6.1).

Table 6.2: Overview of tsunami deposit sizes in Lake Cucao in terms of maximum and average magnetic susceptibility, traceability (lateral extent), average deposit thickness and percentage of mud rip-up clast intervals. The tsunami deposits are ranked according to the presented objective criteria and they are compared to their subjective relative size (< means relatively smaller value, ≈ means similar and > means greater).

tsunami deposit ID	**max. magnetic susceptibility** ($\times 10^{-5}$ SI) and (rank)	**avg. magnetic susceptibility** ($\times 10^{-5}$ SI) and (rank)	**traceability (lateral extent)** (in cores/total cores) and (rank)	**avg. deposit thickness** (cm) and (rank)	**percentage of mud clast intervals** (%) and (rank)	**overall rank**	**subjective relative size to the AD 1960 tsunami deposit**
AD 1960	677 (5)	121 (6)	18/18 (1)	12,3 (7)	5,5 (9)	6	-
cB	695 (4)	184 (4)	17/17 (1)	9,0 (8)	19,3 (3)	4	≈
cC	1601 (3)	136 (5)	9/9 (1)	19,9 (4)	10,8 (7)	5	≈
cD	57 (14)	42 (14)	5/8 (3)	1,2 (14)	0 (11)	14	<
cE	51 (15)	37 (15)	2/8 (5)	0,4 (15)	0 (11)	15	<
cF	581 (7)	99 (7)	8/8 (1)	7,8 (10)	15,7 (5)	7	≈
cG	431 (8)	63 (10)	7/8 (2)	7,9 (9)	0 (11)	10	<
cH	202 (12)	45 (13)	5/8 (3)	6,9 (11)	18,8 (4)	11	<
cI	335 (10)	86 (9)	5/8 (3)	2,3 (12)	0 (11)	12	<
cJ	306 (11)	87 (8)	8/8 (1)	13,0 (6)	10,6 (8)	8	≈
cK	377 (9)	59 (11)	7/7 (1)	16,9 (5)	3,4 (10)	9	<
cL	92 (13)	58 (12)	3/7 (4)	1,7 (13)	0 (11)	13	<
cM	585 (6)	216 (3)	4/4 (1)	20,5 (3)	61,7 (1)	2	≈
cN	2269 (1)	671 (2)	8/8 (1)	32,6 (2)	12,2 (6)	2	>
cO	1656 (2)	816 (1)	3/3 (1)	39,8 (1)	22,6 (2)	1	>

ii **Average magnetic susceptibility** is representative of the overall concentration of sediment from sources outside of the lakes. Deposits with large mud caps, i.e. large amounts of reworked lake sediments, may be underrepresented in this criterion. However, this criterion is complementary to the maximum magnetic susceptibility, because it avoids the strong variability (Fig. 6.2).

iii **Traceability (lateral extent)** represents the minimum lateral reach of a tsunami. However, the lateral extent of the tsunami deposit is not solely dependent on the tsunami. Eroded mud is transported further by the tsunami than sand (Kempf et al., 2015). The traceability (lateral extent) of tsunami deposits in lakes therefore depends on the fine-grained fraction of the tsunami's sediment load, which forms the mud cap. The traceability (lateral extent) therefore depends partially on the availability of mud in areas, where the tsunami has the potential to erode. The availability of mud in the inundation area may change and the inundation pathways may vary between tsunamis. However, these changes are probably not drastic from tsunami to tsunami and the traceability should give some measure of relative tsunami size (Figs. 6.1, 6.2).

iv **Average tsunami deposit thickness** is influenced by flow speed and duration. Higher flow speeds are more erosional and longer erosional phases produce more material that enters the coastal lake. The total volume of reworked material is here represented as the average thickness in all cores. It was calculated by also including cores, in which the tsunami deposit was not observed, i.e. 0 cm tsunami deposit thickness). Direct volume estimates were not attempted, because of too few core samples in combination with high spatial variability in thickness associated with tsunami deposit (Goto et al., 2014) (Fig. 6.1).

v The **percentage of mud rip-up clast intervals** may correlate to tsunami size, because the presence of mud rip-up clasts is indicative of extreme flow speeds. Not all tsunami inundations were powerful enough to erode, transport and deposit mud rip-up clasts, or not in all cases were rip-up clasts recovered. In first order, this is therefore a threshold-based criterion. However, a high percentage of mud-rip clasts in the tsunami deposit could mean that the threshold for eroding soil and gyttja in form of mud rip-up clasts is exceeded for longer periods and/or in larger areas, which in turn may represent relative tsunami size (Fig. 6.2).

Each criterion for itself may not reflect the relative size of the tsunami deposits and their associated tsunamis sufficiently well. However, together the criteria create an objective measure to rank the relative size of the tsunami deposits (Tabs. 6.2, 6.3).

6.4.1 Relative size of tsunami deposits in Lake Cucao

The sedimentary record of Lake Cucao contains 15 detrital layers, which are interpreted as tsunami deposits with varying degree of confidence (chapter 5; Tab. 5.1 on page 99). Deposit thickness, coarsest grain size distributions and magnetic susceptibility were described and discussed for the uppermost tsunami deposit, interpreted as the AD 1960 tsunami deposit in chapter 3.

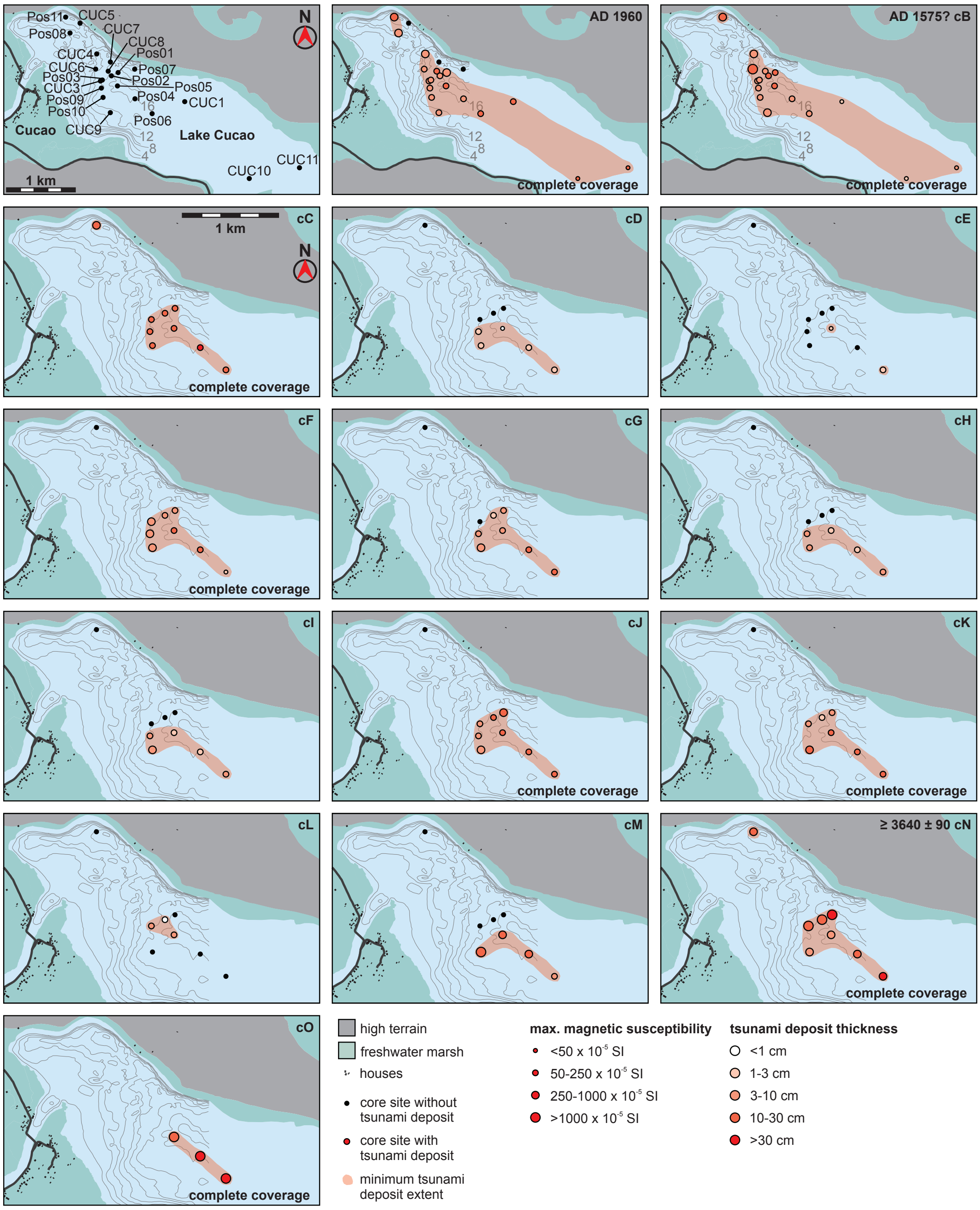

Figure 6.1: Lake Cucao tsunami deposit maps with maximum magnetic susceptibility and deposit thickness represented in size and colour of the circle, respectively.

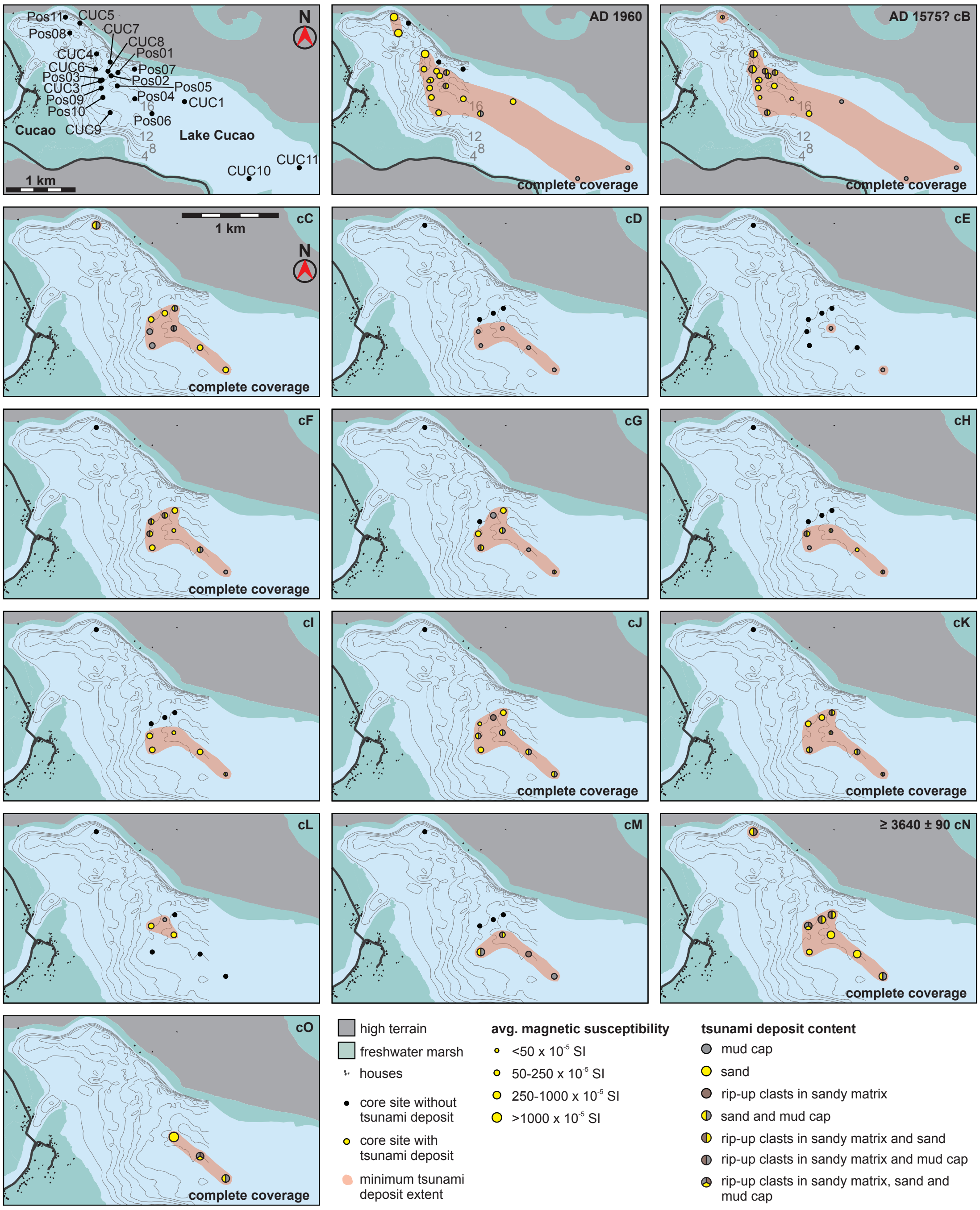

Figure 6.2: Lake Cucao tsunami deposit maps with average magnetic susceptibility and deposit content represented in size and colour of the circle, respectively.

Table 6.3: Overview of tsunami deposit sizes in Lake Huelde in terms of maximum and average magnetic susceptibility, traceability (lateral extent), average deposit thickness and percentage of mud rip-up clast intervals. The tsunami deposits are ranked according to the presented objective criteria and they are compared to their subjective relative size (« means much lower values, < means lower and ≈ means similar).

tsunami deposit ID	max. magnetic susceptibility ($\times 10^{-5}$ SI) and (rank)	avg. magnetic susceptibility ($\times 10^{-5}$ SI) and (rank)	traceability (lateral extent) (in cores/total cores) and (rank)	avg. deposit thickness (cm) and (rank)	percentage of mud clast intervals (%) and (rank)	overall rank	subjective relative size to the AD 1960 tsunami deposit
AD1960	1794 (3)	390 (5)	12/12 (1)	27.8 (1)	36.4 (4)	1	-
AD 1837	1585 (4)	676 (2)	5/8? (4)	5.5 (9)	3.7 (9)	8	<
AD 1575	763 (11)	201 (10)	1/8 (9)	1.4 (15)	60.9 (1)	11	<
hD	865 (8)	238 (7)	3/8 (6)	8.1 (6)	51.4 (3)	9	<
hE	816 (9)	211 (8)	5/8 (4)	8.0 (7)	51.43 (2)	6	<
hF	92 (17)	67 (13)	2/8 (8)	0.2 (17)	0 (11)	17	«
hG	1367 (5)	365 (6)	6/8 (3)	8.2 (5)	32.9 (5)	5	<
hH	773 (10)	193 (11)	7/8 (2)	4.1 (11)	0 (11)	10	<
hI	310 (12)	42 (15)	4/7 (5)	1.5 (14)	0 (11)	15	<
hJ	1030 (6)	206 (9)	6/6 (1)	5.9 (8)	16.9 (7)	7	<
hK	162 (15)	43 (14)	5/5 (1)	2.4 (12)	0 (11)	13	<
hL	172 (14)	77 (12)	2/5 (7)	0.8 (16)	0 (11)	16	«
hM	2480 (2)	519 (3)	5/5 (1)	16.0 (3)	2.5 (10)	3	≈
hN	3791 (1)	891 (1)	5/5 (1)	9.5 (4)	26.1 (6)	2	≈
hO	200 (13)	37 (16)	3/3 (1)	4.2 (10)	0 (11)	12	<
hP	132 (16)	35 (17)	2/2 (1)	1.8 (13)	0 (11)	14	<
hQ	877 (7)	463 (4)	1/1 (1)	20.7 (2)	9.7 (8)	4	≈

Subjectively, out of the 14 tsunami deposits predating the AD 1960 in Lake Cucao, there are 7, which generally appear smaller than the AD 1960 tsunami deposit; 5 are comparable to the AD 1960 tsunami deposit and 2 are overall larger, namely tsunami deposits cN and cO (Figs. 6.1, 6.2; Tab. 6.2). The subjective ranking matches the overall ranking of the objective criteria. Tsunami deposits cN and cO are objectively the two highest ranked tsunami deposits. The 5 tsunami deposits subjectively comparable in size to the AD 1960 deposit objectively rank from 2nd (cM shares 2nd rank with cN) to 8th rank. All other 7 tsunami deposits are objectively ranked 9th or lower and are subjectively smaller tsunami deposits (Tab. 6.2). Tsunami deposits cN and cO contain well sorted medium sand and in proximal cores they consist of mud clasts in a sandy matrix (5.4 on page 97). The radiocarbon date in Pos04 was retrieved from gyttja between cN and cO. The calibrated date determined that cN was deposited shortly before and cO shortly after 3560–3830 cal. yrs BP.

6.4.2 Relative size of tsunami deposits in Lake Huelde

The sedimentary record of Lake Huelde contains 17 tsunami deposits. The uppermost tsunami deposit was identified as the AD 1960 tsunami deposit, which is described and discussed in terms of thickness, grain size and magnetic susceptibility in chapter 3. As it is possible to distinguish single pulses within the AD 1960 tsunami deposit in Lake Huelde, areas of 1, 2 or 3 fining-up pulses were mapped for older tsunami deposits, too (cf. Fig. 3.11 on page 57; Fig. 6.4). Similar to the paleotsunami record of Lake Cucao, older tsunami deposits were not analysed for grain size with the same amount of detail as the AD 1960 tsunami deposit. The AD 1960 tsunami deposit in Lake Huelde is the single largest deposit in terms of thickness and evident lateral extent (Figs. 4.2 on page 73, 6.3, 6.3), its grain size is among the coarsest (subjective) and the magnetic susceptibility values are also among the highest of all tsunami deposits in Lake Huelde (Tab. 6.3; Figs. 6.3, 6.4). The relative abundance of mud-rip clasts in the AD 1960 tsunami deposit is among the highest in the stratigraphic record of Lake Huelde, too, and it is the only tsunami deposit with clear evidence of a strong erosional hiatus at the base (Figs. 4.3, 4.4 on pages 75 and 76, respectively). To summarise, there are more than the objective criteria and the subjective relative sizes in table 6.3, which indicate the AD 1960 tsunami was the largest event in Lake Huelde in the last 5500 yrs.

Subjectively, there are 13 of the 16 older tsunami deposits that are smaller or much smaller and only 3 that are of similar size compared to the AD 1960 tsunami deposit (Tab. 6.3). Remarkable about the lateral extent of the tsunami deposits predating the AD 1960 event is that all 7 tsunami deposits with complete coverage in the sampled lake basin are from as old as or older than 2200 ± 90 cal. yrs BP (age of tsunami deposit hJ; Tab. 4.2 on page 74). The subjective relative sizes match the objective ranking in Lake Huelde, too (Tab. 6.3). The two subjectively smallest tsunami deposits (hF and hL) are objectively ranked the two lowest. Three tsunami deposits (hM, hN and hQ) are of comparable size to the AD 1960 tsunami deposit, which is objectively the largest tsunami deposit in the Lake Huelde record. However, hQ is only represented in a single core (Pos18), which only allows a very limited comparison. Tsunami deposits hM and hN were dated to 3740 ± 150 cal. yrs BP and 3890 ± 140 cal. yrs BP, respectively (Tab. 4.2 on page 74).

6.4.3 Intergrating two adjacent coastal lake paleotsunami records

In contrast to the Lake Huelde sedimentary record, in the Lake Cucao record the AD 1960 tsunami deposit does not represent the largest tsunami. This discrepancy could be caused by not recording the proximal record in Lake Cucao (chapter 3). Even with regard of that discrepancy, the AD 1960 tsunami is undoubtedly one of the major events in the last 5500 yrs, when we take both coastal lakes' sedimentary records into account. Lake Huelde shows a trend of decreasing sensitivity to record tsunamis. Spatially more confined tsunami deposits express this trend since 2200 cal. yrs BP (age of tsunami deposit hJ). In total, 7 out of 8 tsunamis before and only once (AD 1960) out of 9 tsunamis after 2200 cal. yrs BP reach complete coverage within the lake basin (Fig. 6.3, 6.4 Tab. 6.3). Either this trend in sensitivity was reversed before the AD 1960 tsunami or the AD 1960 tsunami was exceptionally large. With detailed descriptions of extreme damages along the Chilean coast (Sievers et al., 1963) and also descriptions of the tsunami in Hawaii (Lander and Lockridge, 1989) and Japan (Nanayama et al., 2007), the AD 1960 tsunami can be regarded as an extreme tsunami. This suggests that the AD 1960 tsunami was unusually large even in light of ~5500 yrs of sedimentary record. Co-seismic subsidence was probably ~1 m in the vicinity of Lake Cucao and Lake Huelde (Plafker and Savage, 1970), which may have instantly increased the sensitivity of Lake Huelde to record tsunamis relative to previous inundations. However, ~1 m is probably not a lot in comparison to the relative sea-level change throughout the ~5500 yrs record, especially when considering the estimated tsunami height of 10–20 m north and south of the study area (Sievers et al., 1963). The uniqueness of the AD 1960 tsunami deposit in Lake Huelde suggests environmental changes were not the controlling factor for the tsunami deposit size of the AD 1960 tsunami.

In Lake Cucao the trend of decreasing sensitivity is not as evident. However, the two most ex-

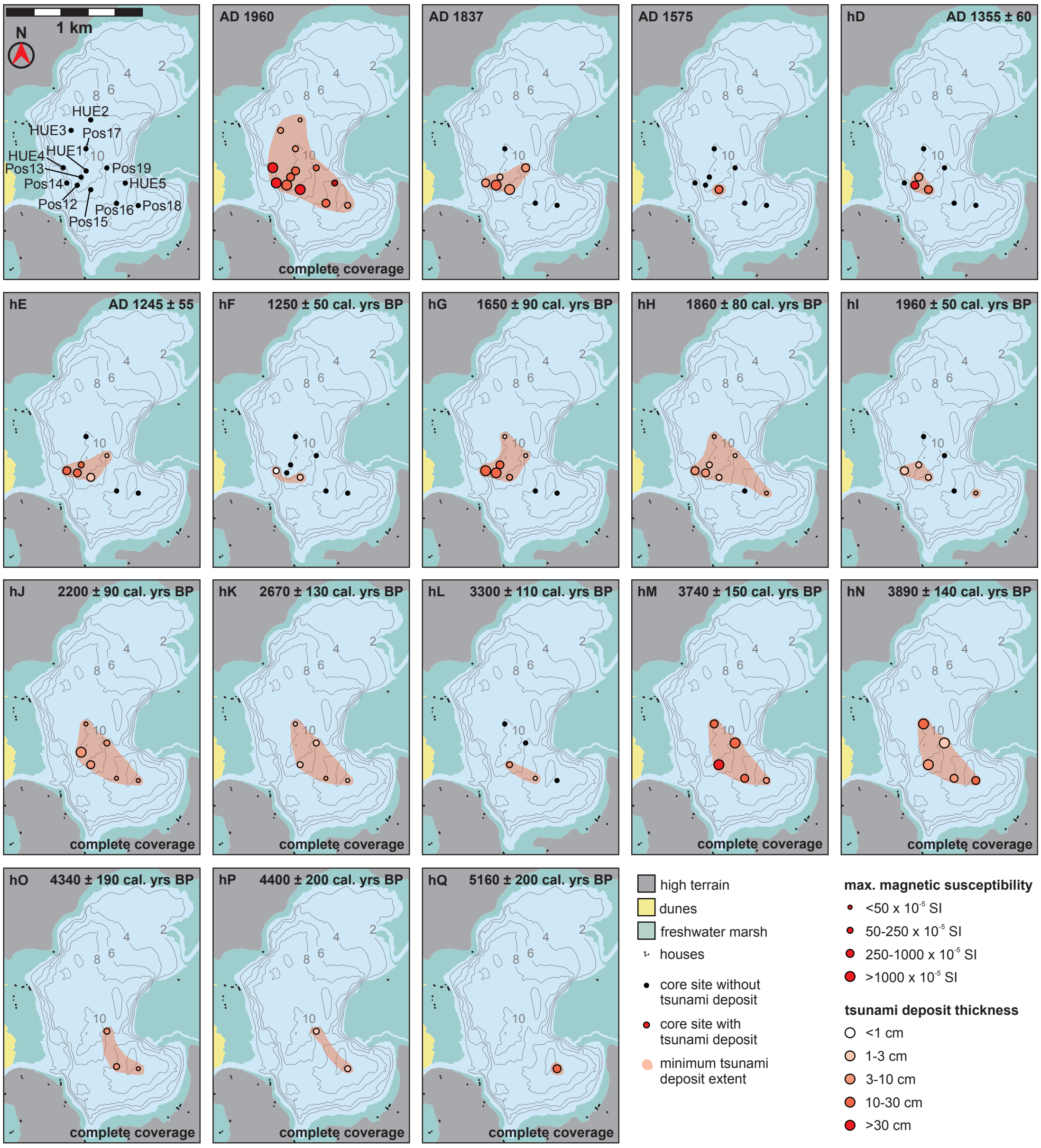

Figure 6.3: Lake Huelde tsunami deposit maps with maximum magnetic susceptibility and deposit thickness represented in size and colour of the circle, respectively.

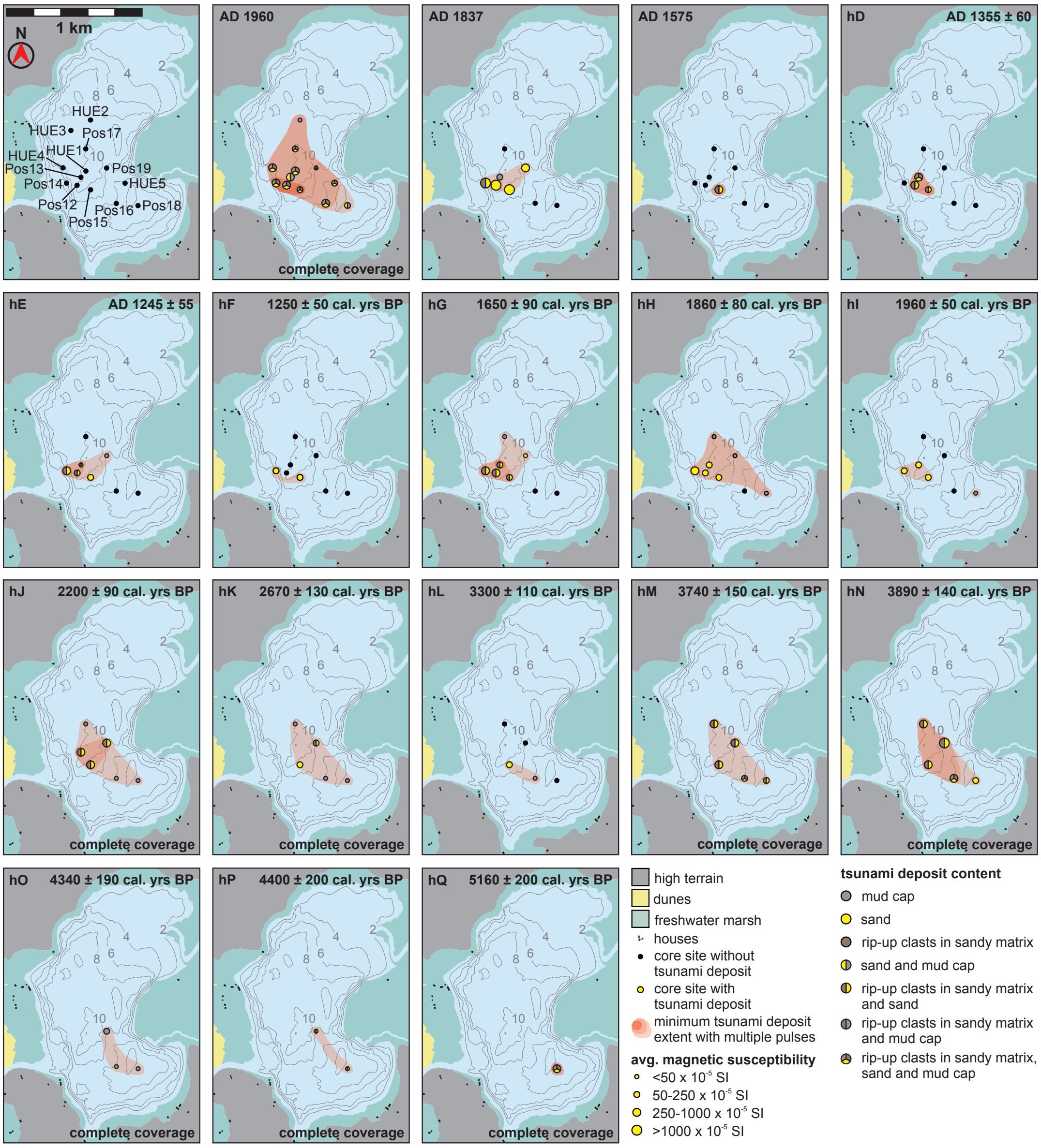

Figure 6.4: Lake Huelde tsunami deposit maps with average magnetic susceptibility and deposit content represented in size and colour of the circle, respectively.

treme tsunami deposits in Lake Cucao (cN and cO) are also the two oldest, which could indicate a similar trend in decreasing sensitivity. Events like the AD 1960 tsunami appear to occur on average every ~740–1720 yrs (the period between the oldest AD 1960-like deposit divided by the number of AD 1960-like deposits for both lakes, i.e. 5170 yrs divided by 3 for Lake Huelde and ~3700 yrs divided by 5 for Lake Cucao). However, given the low number of AD 1960-like tsunamis and the uneven distribution through time this 'average' should be considered with caution.

The two largest tsunami deposits in Lake Cucao, cN and cO, coincide chronologically with two major tsunami deposits from Lake Huelde, hM and hN. The two tsunami deposits can be tentatively correlated across the two lakes. If this correlation is correct, then they represent two major tsunami inundations closely spaced in time. However, a different environment, e.g. a higher sea-level, at the time of deposition could have favoured in-lake deposition. The higher sea-level is plausible, due to documented net uplift of ~2 m in the last ~4000 yrs in Maullín (~120 km north of the study area) (Atwater et al., 1992) and due to ~4 m of uplift in the last ~4000 yrs in the study area according to the global glacial isostasy model ICE-5G (Peltier, 2004). What this means in respect to the size of the tsunamis relative to the AD 1960 tsunami is unclear, because of competing factors, i.e. extreme tsunami deposits in Lake Cucao and major tsunami deposition in Lake Huelde on one side versus higher sea-level and closer shoreline etc. on the other. There are no tsunami deposits known from other records of the region to compare cN, cO, hM and hN, because other paleotsunami records of the region do not reach as far back in time.

The relative tsunami deposit sizes represent the in-lake sedimentary effect of the tsunamis, which does not necessarily represent the relative tsunami intensity, because environmental factors, which may change over time, are unaccounted for. The way forward is to assess the environmental factors together with the tsunami deposits. The relevant competing factors are discussed below. When more information is available about the inundation influencing factors and about the tsunami deposits, it is reasonable to apply models to learn about the tsunami in absolute values. This constitutes moving from qualitative to quantitative tsunami research.

6.5 Conclusions

The AD 1960 tsunami was one of the three major tsunami inundations in the area of Cucao in the last ~3700 yrs. Tsunamis with the sedimentary effect of the AD 1960 tsunami occur on average 740–1720 yrs. However, they can occur closely spaced in time.

Only two tsunami deposits rival the AD 1960 tsunami deposit in size. In Lake Cucao they are cN and cO and in Lake Huelde they are hM and hN. They coincide chronologically and are tentatively correlated with each other across the lakes. The relative tsunami deposit sizes represent the in-lake sedimentary effect of the tsunamis, which does not necessarily represent the relative tsunami intensity, because environmental factors, which may change over time, are unaccounted for.

In general, it appears that the sensitivity to record tsunamis in the Lake Cucao and especially in Lake Huelde decreased over the last 3700 and 5500 yrs, respectively. This decreasing trend is reflected less clearly in the sedimentary record of Lake Cucao, which may be connected to the

lack of a proximal sedimentary record.
Downsized, but otherwise realistic physical models exist for subaerial landslide-induced tsunamis. For earthquake-induced tsunamis the physical models have to be too large to be affordable. Long flumes are beginning to explore earthquake induced tsunami waves in 2D.
Numerical forward modelling is a research subject with a very promising outlook. However, to model tsunami or paleotsunami inundation in the study area would encompass another research project on its own. Tsunami inundation into a coastal lake has not been modelled before, partially because necessary data for validation is not yet existent.
Currently, there is no inverse numerical model, which could be applicable to the data that this thesis made available. The existing inverse models only apply to onshore sand and boulder deposits, while the tsunami deposits presented in this thesis are all from coastal lakes.
The sedimentary records presented in chapter 4 and 5 range from ~5500 yrs BP to ~3,700 yrs BP, respectively. The environmental changes in sea-level, landforms and vegetation since then can be estimated in some cases from regionally close studies, but have to be studied in the study area itself with great detail, before numerical models can make sense of the presented sedimentary data, in order to estimate the size of paleotsunamis.

References

Apotsos, A., Gelfenbaum, G., Jaffe, B., 2011. Process-based modeling of tsunami inundation and sediment transport. Journal of Geophysical Research: Earth Surface 116, F01006.

Atwater, B.F., Núñez, H.J., Vita-Finzi, C., 1992. Net Late Holocene emergence despite earthquake-induced submergence, south-central Chile. Quaternary International 15/16, 77–85.

Boex, J., Fogwill, C., Harrison, S., Glasser, N.F., Hein, A., Schnabel, C., Xu, S., 2013. Rapid thinning of the late Pleistocene Patagonian Ice Sheet followed migration of the Southern Westerlies. Science Reports 3, 2118.

Bondevik, S., Løvholt, F., Harbitz, C., Mangerud, J., Dawson, A., Inge Svendsen, J., 2005. The Storegga Slide tsunami—comparing field observations with numerical simulations. Marine and Petroleum Geology 22, 195–208.

Bondevik, S., Svendsen, J.I., Johnsen, G., Mangerud, J., Kaland, P.E., 1997. The Storegga tsunami along the Norwegian coast, its age and runup. Boreas 26, 29–53.

Buckley, M.L., Wei, Y., Jaffe, B.E., Watt, S.G., 2011. Inverse modeling of velocities and inferred cause of overwash that emplaced inland fields of boulders at Anegada, British Virgin Islands. Natural Hazards 63, 133–149.

Cheng, W., Weiss, R., 2013. On sediment extent and runup of tsunami waves. Earth and Planetary Science Letters 362, 305–309.

De Girolamo, P., Di Risio, M., Romano, A., Molfetta, M.G., 2014. Landslide Tsunami: Physical Modeling for the Implementation of Tsunami Early Warning Systems in the Mediterranean Sea. Procedia Engineering 70, 429–438.

Ding, K., Freymueller, J.T., Wang, Q., Zou, R., 2015. Coseismic and Early Postseismic Deformation of the 5 January 2013 Mw 7.5 Craig Earthquake from Static and Kinematic GPS Solutions. Bulletin of the Seismological Society of America 105, 1153–1164.

Fritz, H.M., Mohammed, F., Yoo, J., 2009. Lituya Bay Landslide Impact Generated Mega-Tsunami 50(th) Anniversary. Pure and Applied Geophysics 166, 153–175.

Fruergaard, M., Piasecki, S., Johannessen, P.N., Noe-Nygaard, N., Andersen, T.J., Pejrup, M., Nielsen, L.H., 2015. Tsunami propagation over a wide, shallow continental shelf caused by the Storegga slide, southeastern North Sea, Denmark. Geology 43, 1047–1050.

Garrett, E. 2013. Biostratigraphic constraints on megathrust earthquake deformation history in south central Chile. PhD Thesis, Durham University, UK.

Garrett, E., Shennan, I., Woodroffe, S.A.A., Cisternas, M., Hocking, E.P.P., Gulliver, P., 2015. Reconstructing paleoseismic deformation, 2: 1000 years of great earthquakes at Chucalén, south central Chile. Quaternary Science Reviews 113, 112–122.

Goff, J., Chagué-Goff, C., Nichol, S., Jaffe, B., Dominey-Howes, D., 2012. Progress in palaeotsunami research. Sedimentary Geology 243–244, 70–88.

Goff, J., Weiss, R., Courtney, C., Dominey-Howes, D., 2010. Testing the hypothesis for tsunami boulder deposition from suspension. Marine Geology 277, 73–77.

Goto, K., Hashimoto, K., Sugawara, D., Yanagisawa, H., Abe, T., 2014. Spatial thickness variability of the 2011 Tōhoku-oki tsunami deposits along the coastline of Sendai Bay. Marine Geology 358, 38–48.

Harbitz, C.B., Glimsdal, S., Løvholt, F., Kveldsvik, V., Pedersen, G.K., Jensen, A., 2014. Rockslide tsunamis in complex fjords: From an unstable rock slope at Åkerneset to tsunami risk in western Norway. Coastal Engineering 88, 101–122.

Heller, V., Spinneken, J., 2015. On the effect of the water body geometry on landslide–tsunamis: Physical insight from laboratory tests and 2D to 3D wave parameter transformation. Coastal Engineering 104, 113–134.

Hilbe, M., Anselmetti, F., 2015. Mass Movement-Induced Tsunami Hazard on Perialpine Lake Lucerne (Switzerland): Scenarios and Numerical Experiments. Pure and Applied Geophysics 172, 545–568.

Howarth, J.D., Fitzsimons, S.J., Norris, R.J., Jacobsen, G.E., 2014. Lake sediments record high intensity shaking that provides insight into the location and rupture length of large earthquakes on the Alpine Fault, New Zealand. Earth and Planetary Science Letters 403, 340–351.

Jaffe, B., Buckley, M., Richmond, B., Strotz, L., Etienne, S., Clark, K., Watt, S., Gelfenbaum, G., Goff, J., 2011. Flow speed estimated by inverse modeling of sandy sediment deposited by the 29 September 2009 tsunami near Satitoa, east Upolu, Samoa. Earth-Science Reviews 107, 23–37.

Jaffe, B.E., Gelfenbuam, G., 2007. A simple model for calculating tsunami flow speed from tsunami deposits. Sedimentary Geology 200, 347–361.

Jaffe, B.E., Goto, K., Sugawara, D., Richmond, B.M., Fujino, S., Nishimura, Y., 2012. Flow speed estimated by inverse modeling of sandy tsunami deposits: results from the 11 March 2011 tsunami on the coastal plain near the Sendai Airport, Honshu, Japan. Sedimentary Geology 282, 90–109.

Kempf, P., Moernaut, J., Van Daele, M., Vermassen, F., Vandoorne, W., Pino, M., Urrutía, R., Garrett, E., De Batist, M., 2015. The sedimentary record of the tsunami caused by the 1960 Great Chilean Earthquake in two coastal lakes on Chiloé Island, Chile. Sedimentary Geology 328, 73–86.

Kremer, K., Marillier, F., Hilbe, M., Simpson, G., Dupuy, D., Yrro, B.J.F., Rachoud-Schneider, A.-M., Corboud, P., Bellwald, B., Wildi, W., Girardclos, S., 2014. Lake dwellers occupation gap in Lake Geneva (France–Switzerland) possibly explained by an earthquake–mass movement–tsunami event during Early Bronze Age. Earth and Planetary Science Letters 385, 28–39.

Lander, J.F., Lockridge, P., 1989. United States Tsunamis 1690–1988 (including United States possession). National Geophysical Data Center, Boulder, Colorado, pp. 41–42 (publication, v).

Lindstrøm, E.K., Pedersen, G.K., Jensen, A., Glimsdal, S., 2014. Experiments on slide generated waves in a 1:500 scale fjord model. Coastal Engineering 92, 12–23.

Løvholt, F., Glimsdal, S., Lynett, P., Pedersen, G., 2015. Simulating tsunami propagation in fjords with long-wave models. Natural Hazards and Earth System Sciences 15, 657–669.

Miller, K.G., Mountain, G.S., Wright, J.D., Browning, J.V., 2011. A 180-million-year record of sea-level and ice volume variations from continental margin and deep-sea isotopic records. Oceanography 24, 40–53.

Minoura, K., Imamura, F., Sugawara, D., 2001. The 869 Jogan tsunami deposit and recurrence interval of large-scale tsunami on the Pacific coast of northeast Japan. Journal of Natural Disaster Science 23, 83–88.

Moernaut, J., Van Daele, M., Heirman, K., Fontijn, K., Strasser, M., Pino, M., Urrutia, R., De Batist, M., 2014. Lacustrine turbidites as a tool for quantitative earthquake reconstruction: New evidence for a variable rupture mode in south central Chile. Journal of Geophysical Research: Solid Earth 119, 1607–1633.

Moore, A.L., McAdoo, B.G., Ruffman, A., 2007. Landward fining from multiple sources in a sand sheet deposited by the 1929 Grand Banks tsunami, Newfoundland. Sedimentary Geology 200, 336–346.

Mori, N., Takahashi, T., Yasuda, T., Yanagisawa, H., 2011. Survey of 2011 Tōhoku earthquake tsunami inundation and run-up. Geophysical Research Letters 38.

Namegaya, Y., Satake, K., 2014. Reexamination of the A.D. 869 Jogan earthquake size from tsunami deposit distribution, simulated flow depth, and velocity. Geophysical Research Letters 41, 2297–2303.

Nott, J., 2003. Waves, coastal boulder deposits and the importance of the pre-transport setting. Earth and Planetary Science Letters 210, 269–276.

Okada, Y., 1985. Surface deformation due to shear and tensile faults in a half-space. Bulletin of the Seismological Society of America 75, 1135–1154.

Peltier, W.R., 2004. Global glacial isostasy and the surface of the earth: The ICE-5G (VM2) Model and GRACE. Annual Review of Earth and Planetary Sciences 32, 111–149.

Plafker, G., 1972. Alaskan earthquake of 1964 and Chilean earthquake of 1960: Implications for arc tectonics. Journal of Geophysical Research 77, 901–925.

Plafker, G., Savage, J.C., 1970. Mechanism of the Chilean Earthquakes of May 21 and 22 , 1960. Geological Society of America Bulletin 81, 1001–1030.

Rossetto, T., Allsop, W., Charvet, I., Robinson, D.I., 2011. Physical modelling of tsunami using a new pneumatic wave generator. Coastal Engineering 58, 517–527.

Satake, K., Fujii, Y., Harada, T., Namegaya, Y., 2013. Time and Space Distribution of Coseismic Slip of the 2011 Tōhoku Earthquake as Inferred from Tsunami Waveform Data. Bulletin of the Seismological Society of America 103, 1473–1492.

Sawai, Y., Namegaya, Y., Okamura, Y., Satake, K., Shishikura, M., 2012. Challenges of anticipating the 2011 Tōhoku earthquake and tsunami using coastal geology. Geophysical Research Letters 39.

Shennan, I., Milne, G., Bradley, S., 2012. Late Holocene vertical land motion and relative sea-level changes: lessons from the British Isles. Journal of Quaternary Science 27, 64–70.

Sievers, H., Villegas, G.C., Barros, G., 1963. The seismic sea wave of 22 May 1960 along the Chilean coast. Bulletin of the Seismological Society of America 53, 1125–1190.

Smith, D.E., Foster, I.D.L., Long, D., Shi, S., 2007. Reconstructing the pattern and depth of flow onshore in a palaeotsunami from associated deposits. Sedimentary Geology 200, 362–371.

Soulsby, R., Smith, D., Ruffman, A., 2007. Reconstructing Tsunami Run-Up from Sedimentary Characteristics: A Simple Mathematical Model, in: Coastal Sediments '07. American Society of Civil Engineers, pp. 1075–1088.

Sugawara, D., Goto, K., Jaffe, B.E., 2014. Numerical models of tsunami sediment transport — Current understanding and future directions. Marine Geology 352, 295–320.

Szczuciński, W., Kokociński, M., Rzeszewski, M., Chagué-Goff, C., Cachão, M., Goto, K., Sugawara, D., 2012a. Sediment sources and sedimentation processes of 2011 Tōhoku-oki tsunami deposits on the Sendai Plain, Japan — Insights from diatoms, nannoliths and grain size distribution. Sedimentary Geology 282, 40–56.

Szczuciński, W., Rachlewicz, G., Chaimanee, N., Saisuttichai, D., Tepsuwan, T., Lorenc, S., 2012b. 26 December 2004 tsunami deposits left in areas of various tsunami runup in coastal zone of Thailand. Earth, Planets and Space 64, 843–858.

Tang, J., Causon, D., Mingham, C., Qian, L., 2013. Numerical study of vegetation damping effects on solitary wave run-up using the nonlinear shallow water equations. Coastal Engineering 75, 21–28.

Weiss, R., Fritz, H.M., Wünnemann, K., 2009. Hybrid modeling of the mega-tsunami runup in Lituya Bay after half a century. Geophysical Research Letters 36.

Wesson, R.L., Melnick, D., Cisternas, M., Moreno, M., Ely, L.L., 2015. Vertical deformation through a complete seismic cycle at Isla Santa Maria, Chile. Nature Geoscience 8, 547–551.

Yue, H., Lay, T., 2013. Source Rupture Models for the Mw 9.0 2011 Tōhoku Earthquake from Joint Inversions of High Rate Geodetic and Seismic Data. Bulletin of the Seismological Society of America 103, 1242–1255.

Yue, H., Lay, T., 2011. Inversion of high-rate (1 sps) GPS data for rupture process of the 11 March 2011 Tōhoku earthquake (Mw 9.1). Geophysical Research Letters 38.

Zachos, J., Pagani, M., Sloan, L., Thomas, E., Billups, K., 2001. Trends, Rhythms, and Aberrations in Global Climate 65 Ma to Present. Science 292, 686–693.

"En avslutning bør alltid være virkningsfull."
"An exit should always be effective."

AD 1879, Henrik Ibsen in *Et Dukkehjem*

7 Conclusions and outlook

This thesis compiles work on tsunami deposits on two coastal lakes, which are located behind the same beach system. Research questions were defined for this thesis in the introduction and will be re-addressed here. The conclusions from each chapter are summarized below.

Are Chilean coastal lakes suited for tsunami research?

This thesis demonstrates that coastal lakes in Chile can be excellent recorders of tsunami inundations over long periods of time. The quality of the continuous sedimentary record ranks among the most outstanding sedimentary tsunami records worldwide. The next logic step is to widen the search and investigate other coastal lakes in Chile or elsewhere on subduction zone coasts for equally good records. Such a project has become reality in October 2015, when the Renard Centre of Marine Geology began a PhD project with the title: "Assessing the potential of coastal lakes and lagoons to record a history of tsunami inundation along tectonically active plate boundaries: a comparative study and establishment of a generally applicable methodology". Other than applying the developed methods to other areas each chapter could be expanded by conducting further research.

Can particular tsunami deposits in coastal lakes in Chile be assigned to known tsunami inundation from documented history?

The AD 1960 tsunami deposits was the central object of investigation of the published chapter 3. Further historical tsunamis, from AD 1837 and AD 1575, were matched with respective tsunami deposits in chapters 4 and 5.

How often and with which recurrence pattern do large-scale tsunamis occur on the south central Chilean coast?

The recurrence pattern of tsunamis on the south central Chilean coast is found to be bimodal in chapter 4. The mean recurrence time of 325 yrs matches the recurrence time of other regional tsunami records, but is found to be meaningless due to the bimodality in the recurrence pattern.

Can tsunami size be inferred from tsunami deposits in coastal lakes?

Inferring tsunami size from coastal lakes is attempted, however, quantitative information is not extracted from the coastal lake records. Relative size of the sedimentary effect of the tsunamis is discussed in chapter 6 and a across-lake correlation appears feasible once Lake Cucao has a more reliable age-depth model to its sedimentary record.

Can the growing toolkit for tsunami research be expanded with the tools used in this thesis?

The less usual lake environment for tsunami deposits allowed usage of typical tools for lake research, which are new techniques in tsunami research. Most notably the side scan sonar and the sub-bottom profiler proved extremely useful in imaging the sedimentary environment and the tsunami deposits in the lakes' sedimentary infill. Especially in chapter 5 sub bottom profiles are used to correlate tsunami deposits with high-amplitude continuous acoustic reflectors.

7.1 Summary of conclusions

In **chapter 3**, sub-bottom profiles and side scan sonar mosaics as well as sediment cores were analysed for radionuclides (dating), magnetic susceptibility, γ-ray attenuation density, and grain size. The data describe a tsunami deposit of the 1960 Great Chilean Earthquake in the coastal lakes Lake Cucao and Lake Huelde on the west coast of Isla de Chiloé in south central Chile. The mode of grain size distributions was used to distinguish between subaerial and lacustrine sediment sources of the 1960 tsunami deposit within the lakes. In the proximal area, the subaerial component dominates. After 100–200 m of in-lake transport, lacustrine sediment is part of the tsunami deposit. The maximum in-lake transport distance of the subaerial component is 1.3 km. Beyond this distance, the tsunami deposit consists entirely of reworked lacustrine gyttja. From Lake Huelde cores it is possible to map and infer a minimum of three lake-inundating waves during the AD 1960 tsunami, which is in agreement with eyewitness reports north and south of the study area. Side scan sonar maps revealed that the AD 1960 tsunami inundated both lakes over the barrier and through the river channel. A sediment fan at the outflow in Lake Huelde reaches far across the lake and highlights the dominant role of existing tidal delta channels as a pathway for sediment transport by the tsunami, despite the overspill of the barrier. By plotting grain size modes against distance from ocean and against distance from outflow, the dominating role of the river channel was described, without the use of acoustic geophysical data. Lake Cucao and Lake Huelde present two different settings for recording tsunami inundation despite their shared beach system and similar barrier topography. In Lake Cucao, the proximal record is lost due to constant reworking on the shallow tidal delta by tidal currents. Valuable paleotsunami information can be retrieved from the distal record. In Lake Huelde, both the proximal and distal records are preserved. This study demonstrates that it is paramount to understand the depositional environment of coastal lakes and the tsunami deposit characteristics in its spatial variability before records become meaningful.

In **chapter 4**, 17 detrital layers were interpreted as tsunami deposits in Lake Huelde sediment. The tsunami deposit interpretation was made on the basis of five criteria concerning the sedimentary characteristics (i.e. magnetic susceptibility, presence of mud clasts and correlation throughout the lake basin), acoustic properties (i.e. correlation to strong acoustic reflectors) and age correlation to known paleotsunamis of the regional records. IRSL dating revealed that the last tsunami in AD 1960 eroded into the tsunami deposit of its predecessor from AD 1837. Extensive radiocarbon dating was performed on a master core, which represents the sedimentary stratigraphy of Lake Huelde. Combining all available age information, i.e. radionuclide analyses from Kempf et al (2015), IRSL dating and radiocarbon dates, we modelled the age-depth relationship in the master core using Bacon and OxCal's P_Sequence. Modelled ages were extracted for all 17 tsunami deposits. The modelled variations in accumulation rate were independently confirmed by comparison to varve-counted sediment intervals. The oldest tsunami deposit was dated to 5160 ± 200 cal. yrs BP. The youngest 7 regionally known tsunamis – known through either historical documents (AD 1960, AD 1837 and AD 1575) or regional sedimentary evidence of shaking, co-seismic vertical deformation or tsunami inundation – were all matched with a tsunami deposit in Lake Huelde without over- or underrepresentation. The exact representation of tsunamis over the last ~2000 yrs validates the completeness of the record in the upper part and makes a complete record in the lower part likely. Recurrence times were extracted between each tsunami pair from the modelled tsunami deposit ages and convoluted the probability density functions to reveal the overall bimodal recurrence pattern of tsunamis on the coast of south central Chile. The two modes are at 115 yrs and 490 yrs. The lowest recurrence time probability coincides with the mean recurrence time at ~325 yrs. The mean recurrence time should therefore be used with caution in probabilistic tsunami hazard models.

In **chapter 5**, sub-bottom profiles from Lake Cucao show strong continuous reflectors in the otherwise acoustically semi-transparent lake sediment. The strong reflectors correlate to detrital layers in the sedimentary record. These and other detrital layers exhibit several characteristics indicative of tsunami deposition and were therefore interpreted as tsunami deposits. Eight detrital layers are interpreted as tsunami deposits with a high level of confidence, five with a medium level of confidence and three with a low level of confidence. However, the comparison to the same time interval in the neighbouring Lake Huelde suggests that all or all but one detrital layer may correlate to an identified tsunami deposit from Lake Huelde.

Chapter 6 discusses the size of older tsunami deposits from Lake Cucao and Lake Huelde relative to the size of the AD 1960 tsunami deposit. Maximum and average magnetic susceptibility, traceability, deposit thickness and percentage of mud rip-up clasts in the sedimentary record are used as tools to facilitate the comparison. Chapter 6 reveals that the AD 1960 event was one of 3 major events in the past ~4000 yrs in the lakes. These results determine the relative size of the sedimentary effect of tsunamis in the lakes, which does not translate to tsunami intensity. The associated uncertainties are factors including vertical and horizontal shoreline displacement and landscape evolution. Over the last 5500 yrs a net relative sea-level fall is documented 120 km north of the study area. Net relative sea-level fall is also modelled for the entire southern South American Pacific coast for the same time period. Therefore, it is likely that a net sea-level fall in the past 5500 yrs occurred near Cucao, which would be an influential factor for the sensitivity of the lakes to record tsunamis in their sedimentary records. Horizontal shoreline displacement is considered likely, too, as well as landscape evolution. However both of the latter processes are not studied at the study site. Quantitative research will be possible, when there are more tsunami deposits available and when the history of the inundation influencing factors is known. The quantitative research would involve numerical forward modelling.

7.2 Outlook

The sedimentary record of the AD 1960 tsunami in Lake Cucao and Lake Huelde (chapter 3) is a published article in Sedimentary Geology. However, there is more to investigate and discuss. The co-seismic vertical deformation of the AD 1960 Great Chilean Earthquake in the study area was reported in Plafker and Savage (1970) with ~1 m of subsidence. In this publication the subsidence value is annotated with a question mark, because the data was unclear. This issue might be addressed with a high-resolution sea-level reconstruction using diatom transfer functions, as was done ~80 km north near the northern tip of Chiloé. To confirm or improve this data point could be a starting point of a post-/interseismic deformation analysis on the western coast of Chiloé. The uncovered long term trends could be compared to the current locking state in south central Chile of the Pacific and American plates, as it was derived from stationary GPS data (Moreno et al., 2011). The current locking state gives information, where the subduction zone accumulates stress most efficiently and therefore where the most co-seismic slip would be expected. The post-/interseismic deformation analysis could be accompanied with making a digital elevation model of the area and collections of direct tide observations, to quantify the influence of the tides in Lake Cucao and possibly to model how much lower Lake Huelde needed to be to form the small intertidal delta at its outflow. Finally, if the coastal environment of Lake Cucao and Lake Huelde were to be put into a numerical forward model, it would be interesting to see whether the sedimentary expression of the AD 1960 tsunami deposit in Lake Huelde and Lake Cucao could be reproduced by the model. If yes, then the estimated parameters should be validated in the field. If not, an investigation as to why these differences occur would be valuable, too.

The long paleotsunami record of Lake Huelde, is in the process of becoming a publication. A previous reviewer remarked that it lacks a "null-hypothesis" test. The chapter claims that tsunamis occur time-dependently with a bimodal recurrence pattern. To test for the null-hypothesis in this case means to test, if the same or similar recurrence patterns can be reproduced with a unimodal distribution, e.g. with a Poisson distributed process. This is the equivalent of asking the question, whether the number of recurrence times ($n = 16$) can be trusted enough to determine time-dependency. The doubts are justified and I intend to test for the null-hypothesis after this thesis. The result of the null-hypothesis test would be the answer to the question: how many records of a high number of simulated recurrence time records have a similarly bimodal recurrence time pattern as the presented paleotsunami record of Lake Huelde, despite being part of a unimodally distributed process. Is the percentage very low, then the conclusion of chapter 4 remains the same, i.e. that the tsunami recurrence pattern is time-dependent and bimodal in south central Chile. If, on the other hand, the percentage is high, then the paleotsunami record of Lake Huelde does not answer the question, whether tsunamis recur time-dependently or not in south central Chile. In which case, it might be worth trying to recover deeper sections of the lake stratigraphy to increase the number of tsunami deposits. Lake Huelde was an open estuary before it became a lake. Estuarine sediments were not described in the deepest stratigraphic position in Lake Huelde, meaning that there remain lacustrine strata with the potential of containing older tsunami deposits.

To better understand the longer term impact of tsunami inundation on the coastal lake, it would be interesting to investigate the varved intervals above some of the tsunami deposits. Similar varved sediments were subject to research from a coastal lake in Oregon, USA, and it was concluded that these varves were caused by the presence of trapped saline water in the lake basin after the tsunami. To test for this hypothesis the content of the varves need to be studied, which could be done by the means of i) thin sections for a view into the fabrics and sedimentary microstructures (cf. Kilfeather et al., 2007), ii) scanning electron microscopy (SEM) for identifying the content of the varves (cf. Dean et al., 1999), iii) digital image analysis of photographs, line scans or X-radiographs (Zolitschka et al., 2015) and iv) micro-X-ray fluorescence (μXRF) scanning for semi-quantitative chemical element analysis (cf. Marshall et al., 2012).
The thin tephra layers in the Lake Huelde stratigraphy could be analysed for their chemical composition using XRF and microprobe analyses. The results could be compared to regionally known tephras and possibly volcanoes of origin could be identified (cf. Fontijn et al., 2016). In the case that some of the tephra layers can be linked to dated eruptions, the age information could be used as age information in order to refine the age-depth model.
The long paleotsunami record of Lake Cucao is eventually intended for publication. The geophysical and sedimentary data is excellent, however the record lacks the much needed age control that the Lake Huelde record has. With a robust age-depth model the record could become more meaningful and could be compared to the paleotsunami record of Lake Huelde. Together, the two records could validate and complement each other and tsunami deposit correlation could go beyond tentatively correlating tsunami deposits cN and cO with hM and hN, respectively. The ideal core for radiocarbon dating appears to be Pos06. It is furthest in the lake and therefore furthest away from complex tidal current processes exhibited by the crosscutting channel and by the convergent high-amplitude reflectors within seismic unit U2. In addition, Pos06 contains no indication of erosional effects in the sediment, the tsunami deposits are sufficiently spaced and the core boasts the longest record of all cores retrieved from Lake Cucao. However, the tsunami deposits in Pos06 are not easy to detect. A CT-scan of the entire core would avoid misinterpretations. Exactly how old the deepest recovered strata of core Pos06 are is still unknown, but 5000 ± 500 yrs is the first order estimation, which would be equally long as the paleotsunami record from Lake Huelde at the moment – a good premise for a detailed correlation.

References

Dean, J.M., Kemp, A.E.S., Bull, D., Pike, J., Patterson, G., Zolitschka, B., 1999. Taking varves to bits: Scanning electron microscopy in the study of laminated sediments and varves. Journal of Paleolimnology 22, 121–136.

Fontijn, K., Rawson, H., Van Daele, M., Moernaut, J., Abarzúa, A.M., Heirman, K., Bertrand, S., Pyle, D.M., Mather, T.A., De Batist, M., Naranjo, J.-A., Moreno, H., 2016. Synchronisation of sedimentary records using tephra: A postglacial tephrochronological model for the Chilean Lake District. Quaternary Science Reviews 137, 234–254.

Kempf, P., Moernaut, J., Van Daele, M., Vermassen, F., Vandoorne, W., Pino, M., Ur-

rutía, R., Garrett, E., De Batist, M., 2015. The sedimentary record of the tsunami caused by the 1960 Great Chilean Earthquake in two coastal lakes on Chiloé Island, Chile. Sedimentary Geology 328, 73–86.

Kilfeather, A. a., Blackford, J.J., Meer, J.J.M., 2007. Micromorphological Analysis of Coastal Sediments from Willapa Bay, Washington, USA: A Technique for Analysing Inferred Tsunami Deposits. Pure and Applied Geophysics 164, 509–525.

Marshall, M., Schlolaut, G., Nakagawa, T., Lamb, H., Brauer, A., Staff, R., Ramsey, C.B., Tarasov, P., Gotanda, K., Haraguchi, T., Yokoyama, Y., Yonenobu, H., Tada, R., 2012. A novel approach to varve counting using μXRF and X-radiography in combination with thin-section microscopy, applied to the Late Glacial chronology from Lake Suigetsu, Japan. Quaternary Geochronology 13, 70–80.

Moreno, M., Melnick, D., Rosenau, M., Bolte, J., Klotz, J., Echtler, H., Baez, J., Bataille, K., Chen, J., Bevis, M., Hase, H., Oncken, O., 2011. Heterogeneous plate locking in the South–Central Chile subduction zone: Building up the next great earthquake. Earth and Planetary Science Letters 305, 413–424.

Plafker, G., Savage, J.C., 1970. Mechanism of the Chilean Earthquakes of May 21 and 22 , 1960. Geological Society of America Bulletin 81, 1001–1030.

Zolitschka, B., Francus, P., Ojala, A.E.K., Schimmelmann, A., 2015. Varves in lake sediments – a review. Quaternary Science Reviews 117, 1–41.

8 Appendix

Bacon source-file and command line

sampleID,	age,	er,	depth,	cc
surface,	-62,	1,	0,	0
137Cs peak,	-16,	2,	26,	0
210Pb model,	-10,	1,	30,	0
HU03-95.0,	317,	31,	31.1,	3
HUEL03A-88.5,	396,	36,	59.5,	3
HUEL03A-126.5,	760,	31,	85.5,	3
HUEL03B-30.5,	848,	31,	97.5,	3
HUEL04A-51.5,	1298,	29,	190,	3
HUEL04A-59.5,	1423,	32,	195.5,	3
HUEL04A-107.0,	1869,	29,	243,	3
HUEL04B-14.5,	2032,	32,	276.5,	3
HUEL04B-55.5,	2056,	30,	305.5,	3
HUEL05A-10.5,	2015,	27,	310,	3
HUEL05A-56.5,	2201,	31,	354,	3
HUEL04B-113.5,	2292,	43,	369,	3
HUEL27A-3.5,	2266,	34,	424.5,	3
HUEL27A-72.0,	2533,	35,	488.5,	3
HUEL27A-141.5,	3155,	31,	561,	3
HUEL27B-50.5,	3325,	34,	614,	3
HUEL27B-107.5,	3718,	38,	632.5,	3
HUEL27b,	3692,	35,	643,	3
HUEL22b,	4757,	36,	841,	3

Figure 8.1: Bacon source file with information about the sample-ID, radiocarbon dates and other age-depth information, the error (er) associated to each age-information, the depth and the calibration curve (cc) used (0 = no calibration, 3 = SHCal13).

Command line for the Bacon model:

Bacon("LakeHueldeNoSlumpDev", thick=5, d.min=0, d.max=900, d.by=10, acc.mean=6, acc.shape=1.5, mem.mean=0.37, mem.strength=50, hiatus.depth=31, hiatus.mean=250, hiatus.shape=12, ssize=10000, d.res=200, yr.res=200)

OxCal code and model results

```
Sequence()
{
Curve("atmospheric southern hemisphere","ShCal13.14c");
P_Sequence(0.3)
{Boundary("core bottom"){z=865; };
R_Date("HUEL22b", 4757, 36){z=864; };
        Date("E16"){z=822.5; };
        Date("E15"){z=710; };
                Difference("E16-E15","E15","E16");
        Date("E14"){z=701; };
                Difference("E15-E14","E14","E15");
R_Date("HUEL27b", 3692, 35){z=643; };
        Date("E13"){z=635; };
                Difference("E14-E13","E13","E14");
R_Date("HUEL27B-107.5", 3718, 38){z=632.5; };
                Difference("E13-E12","E12","E13");
        Date("E12"){z=623.1; };
R_Date("HUEL27B-50.5", 3325, 34){z=614; };
        Date("E11"){z=563; };
                Difference("E12-E11","E11","E12");
R_Date("HUEL27A-141.5", 3155, 31){z=561; };
R_Date("HUEL27A-72", 2533, 35){z=488.5; };
        Date("E10"){z=481.5; };
                Difference("E11-E10","E10","E11");
R_Date("HUEL27A-3.5", 2266, 34){z=424.5; };
        Date("E09"){z=369; };
                Difference("E10-E09","E09","E10");
R_Date("HUEL04B-113.5", 2292, 43){z=369; };
R_Date("HUEL05A-56.5", 2201, 31){z=354; };
R_Date("HUEL05A-10.5", 2015, 27){z=310.5; };
        Date("E08"){z=307; };
                Difference("E09-E08","E08","E09");
R_Date("HUEL04B-55.5", 2056, 30){z=305.5; };
        Date("E07"){z=278; };
                Difference("E08-E07","E07","E08");
R_Date("HUEL04B-14.5", 2032, 32){z=276.5; };
Date("E06"){z=247; };
                Difference("E07-E06","E06","E07");
R_Date("HUEL04A-107.0", 1863, 29){z=243; };
R_Date("HUEL04A-59.5", 1423, 32){z=195.5; };
        Date("E05"){z=191; };
                Difference("E06-E05","E05","E06");
R_Date("HUEL04A-51.5", 1298, 29){z=190; };
R_Date("HUEL03B-30.5", 848, 31){z=97.5; };
        Date("E04"){z=96; };
                Difference("E05-E04","E04","E05");
R_Date("HUEL03A-126.5", 760, 31){z=78; };
        Date("E03"){z=78; };
                Difference("E04-E03","E03","E04");
R_Date("HUEL03A-88.5", 396, 36){z=59.5; };
        Date("E02"){z=52.5; };
                Difference("E03-E02","E02","E03");
R_Date("HU03-95.0", 317, 31){z=31.1; };
Boundary ("end_hiatus01"){z=31; };
};

Interval("hiatus01_period");
P_Sequence(0.3)
{Boundary("start_hiatus01"){z=31; };
        Date("E01"){z=30.5; };
Date("210Pb_model", N(AD(1960),2)){z=30; };
Date("137Cs_peak", N(AD(1966),1)){z=26; };
Date("surface", AD(2012)){z=0; };
Boundary("core top"){z=0; };
};
};
```

Figure 8.2: OxCal code for P_Sequence model run with 0.3 k-value.

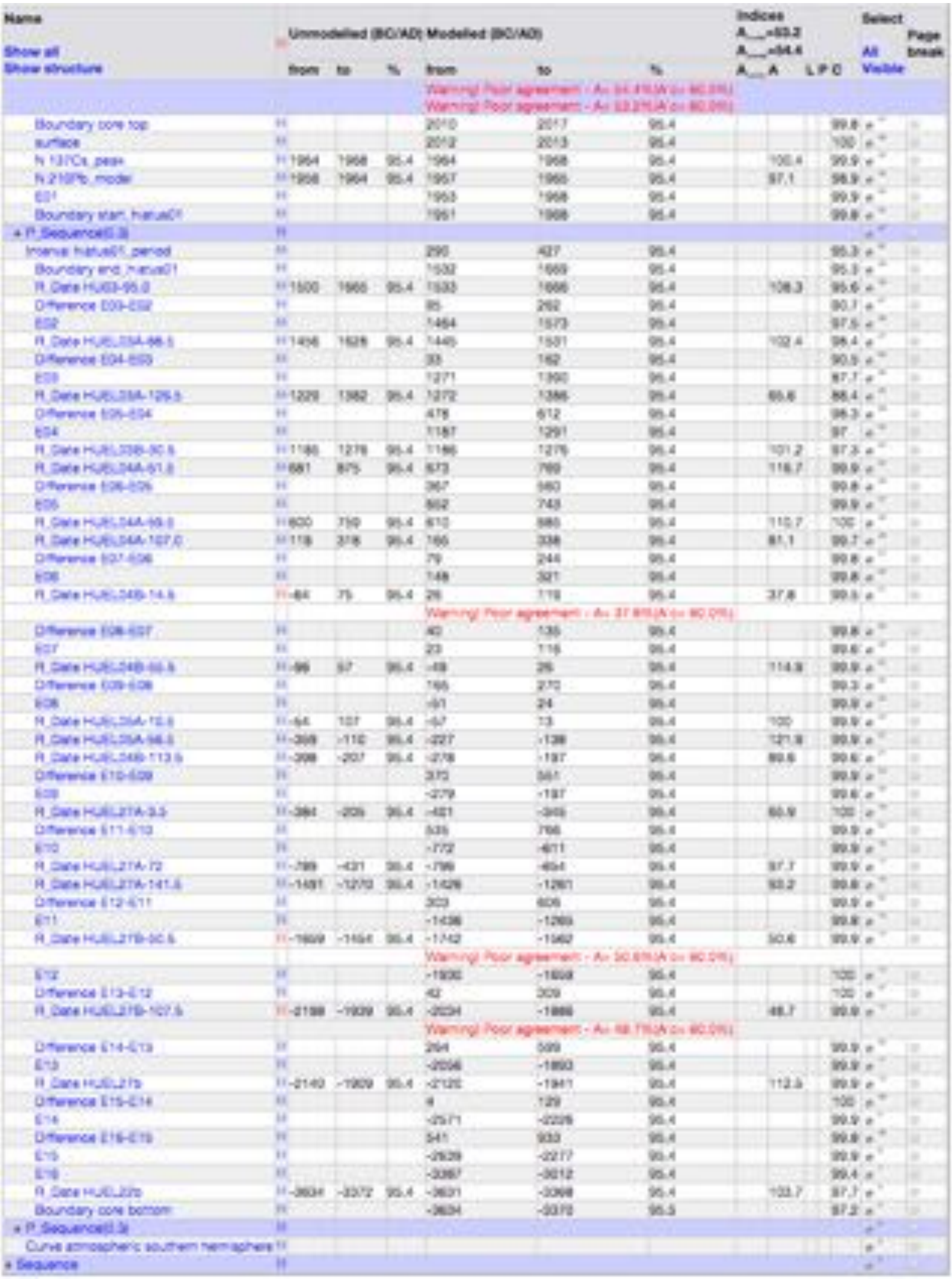

Name	Unmodelled (BC/AD) from	to	%	Modelled (BC/AD) from	to	%	Indices A_{model}=53.2 $A_{overall}$=54.4 A_{comb}	A	L	P	C
Show all / Show structure				Warning! Poor agreement - A= 54.4%(A'c= 60.0%) Warning! Poor agreement - A= 53.2%(A'c= 60.0%)							
Boundary core top				2010	2017	95.4					99.8
surface				2012	2013	95.4					100
N 137Cs_peak	1964	1968	95.4	1964	1968	95.4		100.4			99.9
N 210Pb_model	1958	1964	95.4	1957	1966	95.4		97.1			98.9
E01				1953	1968	95.4					99.9
Boundary start_hiatus01				1951	1968	95.4					99.8
+ P_Sequence(0.3)											
Interval hiatus01_period				290	427	95.4					95.3
Boundary end_hiatus01				1532	1669	95.4					95.3
R_Date HU03-95.0	1500	1665	95.4	1533	1666	95.4		108.3			95.6
Difference E03-E02				85	262	95.4					90.7
E02				1464	1573	95.4					97.5
R_Date HUEL23A-88.5	1456	1628	95.4	1445	1531	95.4		102.4			98.4
Difference E04-E03				33	162	95.4					90.5
E03				1271	1390	95.4					87.7
R_Date HUEL23A-126.5	1229	1382	95.4	1272	1386	95.4		65.6			88.4
Difference E05-E04				478	612	95.4					98.3
E04				1187	1291	95.4					97
R_Date HUEL23B-30.5	1186	1276	95.4	1186	1276	95.4		101.2			97.3
R_Date HUEL24A-61.0	681	875	95.4	673	769	95.4		116.7			99.9
Difference E06-E05				367	560	95.4					99.8
E05				662	743	95.4					99.9
R_Date HUEL24A-69.0	600	759	95.4	610	680	95.4		110.7			100
R_Date HUEL24A-107.0	119	318	95.4	166	338	95.4		81.1			99.7
Difference E07-E06				79	244	95.4					99.8
E06				148	321	95.4					99.8
R_Date HUEL24B-14.5	-64	75	95.4	26	119	95.4		37.8			99.5
				Warning! Poor agreement - A= 37.8%(A'c= 60.0%)							
Difference E08-E07				40	135	95.4					99.8
E07				23	116	95.4					99.6
R_Date HUEL24B-60.5	-99	57	95.4	-49	26	95.4		114.9			99.9
Difference E09-E08				166	270	95.4					99.3
E08				-91	24	95.4					99.9
R_Date HUEL25A-12.5	-54	107	95.4	-57	13	95.4		100			99.9
R_Date HUEL25A-58.5	-358	-110	95.4	-227	-138	95.4		121.9			99.9
R_Date HUEL24B-113.5	-398	-207	95.4	-278	-197	95.4		89.6			99.6
Difference E10-E09				373	561	95.4					99.9
E09				-279	-197	95.4					99.6
R_Date HUEL27A-3.5	-384	-205	95.4	-421	-345	95.4		60.9			100
Difference E11-E10				535	766	95.4					99.9
E10				-772	-611	95.4					99.9
R_Date HUEL27A-72	-799	-431	95.4	-796	-654	95.4		97.7			99.9
R_Date HUEL27A-141.5	-1491	-1270	95.4	-1426	-1261	95.4		93.2			99.8
Difference E12-E11				303	606	95.4					99.9
E11				-1436	-1269	95.4					99.8
R_Date HUEL27B-30.5	-1609	-1454	95.4	-1742	-1562	95.4		50.6			99.9
				Warning! Poor agreement - A= 50.6%(A'c= 60.0%)							
E12				-1930	-1659	95.4					100
Difference E13-E12				42	309	95.4					100
R_Date HUEL27B-107.5	-2198	-1939	95.4	-2034	-1886	95.4		48.7			99.9
				Warning! Poor agreement - A= 48.7%(A'c= 60.0%)							
Difference E14-E13				264	599	95.4					99.9
E13				-2096	-1893	95.4					99.9
R_Date HUEL27b	-2140	-1909	95.4	-2120	-1941	95.4		112.3			99.9
Difference E15-E14				4	129	95.4					100
E14				-2571	-2226	95.4					99.9
Difference E16-E15				541	933	95.4					99.8
E15				-2639	-2277	95.4					99.9
E16				-3367	-3012	95.4					99.4
R_Date HUEL22b	-3634	-3372	95.4	-3631	-3368	95.4		103.7			97.7
Boundary core bottom				-3634	-3370	95.5					97.2
+ P_Sequence(0.3)											
Curve atmospheric southern hemisphere											
+ Sequence											

Figure 8.3: OxCal model results.

Core list

Split Core List - Campaign: Chile 2012

Core Name	open	core type	lake	position	longitude	latitude	date	composite depth	Comments	photo	split core MSCL?	x-ray med2D, med3D and high-res 3D
CC01	yes	gravity core	Lago Cucao	Pos01	-074,08975156 E	-42,62946845 N	17/01/12	0 - 0,490 cm		yes	yes	med2D
CC02	yes	gravity core	Lago Cucao	Pos01	-074,08975156 E	-42,62946845 N	17/01/12	?		yes	yes	no
CUCA01A	yes	piston core	Lago Cucao	Pos01	-074,08975156 E	-42,62946845 N	17/01/12	0,225 - 1,67 m				med2D
CUCA01B	yes	piston core	Lago Cucao	Pos01	-074,08975156 E	-42,62946845 N	17/01/12	1,67 - 3,15 m				med2D
CUCA02	yes	piston core	Lago Cucao	Pos01	-074,08975156 E	-42,62946845 N	20/01/12	3,000 - 4,500 m	core was stuck for 2 days. The sandy sediment turned solid under the tensional forces applied and held on to the corer. Got it out with tension on an extra kevlar rope and hammering with the regular rope on 19.1.2012 but managed to extract the liner only on 20.1.2012 because of the sand between liner and core tube. Lost ca. 50 cm of sediment at base and shook the remaining core.	yes	yes	no
CUCA03A	yes	piston core	Lago Cucao	Pos01	-074,08975156 E	-42,62946845 N	21/01/12	0 - 1,075 m	slight doubts about top and base. Oasis definitely marks the top			med2D
CUCA03B	yes	piston core	Lago Cucao	Pos01	-074,08975156 E	-42,62946845 N	21/01/12	1,075 - 2,115 m	slight doubts about top and base. Oasis definitely marks the top			med2D
CUCA04A	yes	piston core	Lago Cucao	Pos01	-074,08975156 E	-42,62946845 N	21/01/12	1,296 - 2,726 m	Lost a bit at base and a bit at top			med2D
CUCA04B	yes	piston core	Lago Cucao	Pos01	-074,08975156 E	-42,62946845 N	21/01/12	2,726 - 3,361 m	Lost a bit at base and a bit at top			med2D
CUCA04b	yes	piston core	Lago Cucao	Pos01	-074,08975156 E	-42,62946845 N	21/01/12	3,361 - 3,601 m	Lost a bit at base and a bit at top			med2D
CUCA04a	yes	piston core	Lago Cucao	Pos01	-074,08975156 E	-42,62946845 N	21/01/12	above CUCA04				no
CC03	yes	gravity core	Lago Cucao	Pos02	-074,09083113 E	-42,62992812 N	21/01/12	0 - 0,585 m		yes	yes	med2D
CUCA05A	yes	piston core	Lago Cucao	Pos02	-074,09083113 E	-42,62992812 N	21/01/12	0,180 - 1,600 m	the core's base def. At 2 m depth. There is more sediment in the liner, probably because the weight of the ground plate pressed sediment up its tube.			no
CUCA05B	yes	piston core	Lago Cucao	Pos02	-074,09083113 E	-42,62992812 N	21/01/12	1,600 - 2,545 m	the core's base def. At 2 m depth. There is more sediment in the liner, probably because the weight of the ground plate pressed sediment up its tube.			med2D
CUCA06A	yes	piston core	Lago Cucao	Pos02	-074,09083113 E	-42,62992812 N	22/01/12	1,645 - 3,095 m				no
CUCA06B	yes	piston core	Lago Cucao	Pos02	-074,09083113 E	-42,62992812 N	22/01/12	3,095 - 4,585 m				med2D
CUCA07A	yes	piston core	Lago Cucao	Pos02	-074,09083113 E	-42,62992812 N	22/01/12	2,640 - 3,790 m	some sand fell out of the core catcher during raising the core. Liner was cut at base.			med2D
CUCA07B	yes	piston core	Lago Cucao	Pos02	-074,09083113 E	-42,62992812 N	22/01/12	3,790 - 5,290 m	some sand fell out of the core catcher during raising the core. Liner was cut at base.			no
CC04	yes	gravity core	Lago Cucao	Pos03	-074,0922922 E	-42,63052137 N	22/01/12	0 - 0,615 m		yes	yes	no
CUCA08A	yes	piston core	Lago Cucao	Pos03	-074,0922922 E	-42,63052137 N	22/01/12	0,135 - 1,545 m	more sediment then there should be. Base should be at 2 m depth. Probably the groundplate pushed sediment up the tube	yes	yes	no
CUCA08B	yes	piston core	Lago Cucao	Pos03	-074,0922922 E	-42,63052137 N	22/01/12	1,545 - 2,730 m	more sediment then there should be. Base should be at 2 m depth. Probably the groundplate pushed sediment up the tube	yes	yes	no
CUCA09A1	yes	piston core	Lago Cucao	Pos03	-074,0922922 E	-42,63052137 N	23/01/12	1,735 - 3,200 m	ca. 30 cm of sand fell out at base.	yes	yes	no
CUCA09A2	yes	piston core	Lago Cucao	Pos03	-074,0922922 E	-42,63052137 N	23/01/12	1,735 - 3,200 m	ca. 30 cm of sand fell out at base.			med2D, med3D, high-res3D
CUCA09A3	yes	piston core	Lago Cucao	Pos03	-074,0922922 E	-42,63052137 N	23/01/12	1,735 - 3,200 m	ca. 30 cm of sand fell out at base.	yes	yes	no
CUCA09B	yes	piston core	Lago Cucao	Pos03	-074,0922922 E	-42,63052137 N	23/01/12	3,200 - 4,495 m	ca. 30 cm of sand fell out at base.	yes	yes	no
CUCA10A	yes	piston core	Lago Cucao	Pos04	-074,08657810 E	-42,63323400 N	23/01/12	0,000 - 1,433 m		yes	yes	med2D
CUCA10B	yes	piston core	Lago Cucao	Pos04	-074,08657810 E	-42,63323400 N	23/01/12	1,433 - 2,903 m		yes	yes	med2D
CUCA11A	yes	piston core	Lago Cucao	Pos04	-074,08657810 E	-42,63323400 N	24/01/12	2,019 - 3,444 m		yes	yes	med2D
CUCA11B	yes	piston core	Lago Cucao	Pos04	-074,08657810 E	-42,63323400 N	24/01/12	3,444 - 4,944 m		yes	yes	med2D
CUCA12A	yes	piston core	Lago Cucao	Pos04	-074,08657810 E	-42,63323400 N	24/01/12	4,313 - 5,718 m	lost ca. 5 cm at base during lifting and did not penetrate completely with the corer	yes	yes	med2D
CUCA12B	yes	piston core	Lago Cucao	Pos04	-074,08657810 E	-42,63323400 N	24/01/12	5,718 - 6,973 m	lost ca. 5 cm at base during lifting and did not penetrate completely with the corer	yes	yes	med2D, med3D
CC06	yes	gravity core	Lago Cucao	Pos05	-074,08983037 E	-42,63132468 N	24/01/12	0 - 0,630 m		yes	yes	med2D
CUCA13A	yes	piston core	Lago Cucao	Pos05	-074,08983037 E	-42,63132468 N	25/01/12	0,115 - 1,565 m	Willem dropped the bucket on the coring site and Koen dropped a 17-key into the water. So if something strange is in the core it is probably related.	yes	yes	med2D, med3D
CUCA13B	yes	piston core	Lago Cucao	Pos05	-074,08983037 E	-42,63132468 N	25/01/12	1,565 - 3,040 m	Willem dropped the bucket on the coring site and Koen dropped a 17-key into the water. So if something strange is in the core it is probably related.	yes	yes	med2D
CUCA14A	yes	piston core	Lago Cucao	Pos05	-074,08983037 E	-42,63132468 N	25/01/12	2,115 - 3,565 m	lost 3 to 5 cm at top. Perfect 14C material at the very base.	yes	yes	med2D
CUCA14B	yes	piston core	Lago Cucao	Pos05	-074,08983037 E	-42,63132468 N	25/01/12	3,565 - 5,045 m	lost 3 to 5 cm at top. Perfect 14C material at the very base.	yes	yes	med2D
CUCA15A	yes	piston core	Lago Cucao	Pos05	-074,08983037 E	-42,63132468 N	25/01/12	4,235 - 5,680 m	ca. 30 cm missing at base due to lack of penetration.	yes	yes	med2D
CUCA15B	yes	piston core	Lago Cucao	Pos05	-074,08983037 E	-42,63132468 N	25/01/12	5,680 - 6,820 m	ca. 30 cm missing at base due to lack of penetration.	yes	yes	med2D

Figure 8.4: Core list with all meta data for all obtained cores on Lake Cucao and Lake Huelde.

CC07	yes	gravity core	Lago Cucao	Pos06	-074,08207000 E	-42,63561000 N	25/01/12	0 - 0,650 m		yes	yes	med2D
CUCA16A	yes	piston core	Lago Cucao	Pos06	-074,08207000 E	-42,63561000 N	25/01/12	0,000 - 1,475 m		yes	yes	med2D, med3D
CUCA16B	yes	piston core	Lago Cucao	Pos06	-074,08207000 E	-42,63561000 N	25/01/12	1,475 - 2,935 m		yes	yes	med2D
CUCA17A	yes	piston core	Lago Cucao	Pos06	-074,08207000 E	-42,63561000 N	25/01/12	4,075 - 5,545 m	base was pushed out by degasing (ca. 5 cm)	yes	yes	med2D
CUCA17B	yes	piston core	Lago Cucao	Pos06	-074,08207000 E	-42,63561000 N	25/01/12	5,545 - 7,015 m	base was pushed out by degasing (ca. 5 cm)	yes	yes	med2D
CUCA17a	yes	piston core	Lago Cucao	Pos06	-074,08207000 E	-42,63561000 N	25/01/12	-	it is the pushed out base of CUCA17	yes	yes	med2D
CUCA18A	yes	piston core	Lago Cucao	Pos06	-074,08207000 E	-42,63561000 N	26/01/12	2,025 - 3,500 m		yes	yes	med2D
CUCA18B	yes	piston core	Lago Cucao	Pos06	-074,08207000 E	-42,63561000 N	26/01/12	3,500 - 4,955 m		yes	yes	med2D
CUCA19A	yes	piston core	Lago Cucao	Pos06	-074,08207000 E	-42,63561000 N	26/01/12	6,160 - 7,545 m	did not penetrate the full corer.	yes	yes	med2D
CC08	yes	gravity core	Lago Cucao	Pos07	-074,08730139 E	-42,62915754 N	26/01/12	0 - 0,210 m		yes	yes	no
CC09	yes	gravity core	Lago Cucao	Pos09	-074,09243164 E	-42,63164331 N	01/02/12	0 - 0,685 m		yes	yes	no
CUCA20A	yes	piston core (s	Lago Cucao	Pos09	-074,09243164 E	-42,63164331 N	01/02/12	0,525 - 1,995 m	the top 10 cm were water so top should be lakefloor	yes	yes	no
CUCA20B	yes	piston core (s	Lago Cucao	Pos09	-074,09243164 E	-42,63164331 N	01/02/12	1,995 - 3,425 m	the top 10 cm were water so top should be lakefloor	yes	yes	no
CUCA21A	yes	piston core (s	Lago Cucao	Pos09	-074,09243164 E	-42,63164331 N	01/02/12	2,665 - 4,185 m	hit the sand and penetrated ca. 40 cm of it. Lost all of the sand on retraction, but there was a lot of sand between the core catcher and the vore tube -> unconformity was definitely reached and is at base of CUCA21	yes	yes	no
CC10	yes	gravity core	Lago Cucao	Pos10	-074,09213722 E	-42,63293580 N	02/02/12	0 - 0,625 m	the valve didn't close, but the sediment was stuck by ist own stickiness. A bit of resuspension in the top 1 cm due to the winching up with the open valve.	yes	yes	med2D
CUCA22A	yes	piston core (s	Lago Cucao	Pos10	-074,09213722 E	-42,63293580 N	02/02/12	0,000 - 1,460 m		yes	yes	med2D
CUCA22B	yes	piston core (s	Lago Cucao	Pos10	-074,09213722 E	-42,63293580 N	02/02/12	1,460 - 2,930 m		yes	yes	med2D
CUCA23A	yes	piston core (s	Lago Cucao	Pos10	-074,09213722 E	-42,63293580 N	02/02/12	2,325 - 2,880 m	started coring at ca. 2,35 m, because the unconformity is 7 ms subsurface (5,25 m) -> base = unconformity	yes	yes	med2D
CUCA23B	yes	piston core (s	Lago Cucao	Pos10	-074,09213722 E	-42,63293580 N	02/02/12	2,880 - 4,350 m	started coring at ca. 2,35 m, because the unconformity is 7 ms subsurface (5,25 m) -> base = unconformity	yes	yes	med2D
CUCA23b	yes	piston core (s	Lago Cucao	Pos10	-074,09213722 E	-42,63293580 N	02/02/12	4,350 - 4,670 m	it is the sand below CUCA23. In it there are shells. -> Radiocarbondates!	yes	yes	med2D
CC11	yes	gravity core	Lago Cucao	Pos08	-074,09782906 E	-42,62425598 N	02/02/12	0 - 0,380 m	too sandy for piston coring (gully)	yes	yes	no
CC12	yes	gravity core	Lago Cucao	Pos11	-074,09856958 E	-42,62212082 N	02/02/12	?	half sandy, half organic	yes	yes	no
CUCA24A	yes	piston core (s	Lago Cucao	Pos11	-074,09856958 E	-42,62212082 N	02/02/12	0,000 - 1,465 m	penetration was difficult -> only 2 m of sediment.	yes	yes	no
CUCA24B	yes	piston core (s	Lago Cucao	Pos11	-074,09856958 E	-42,62212082 N	02/02/12	1,465 - 2,130 m	penetration was difficult -> only 2 m of sediment.	yes	yes	no
HU01	yes	gravity core	Lago Huelde	Pos12	-074,11282478 E	-42,59908659 N	06/02/12	0,155 - 0,790 m	sand at base	yes	yes	med2D
HU02	yes	gravity core	Lago Huelde	Pos12	-074,11282478 E	-42,59908659 N	06/02/12	0,000 - 0,824 m	sand at base. Didn't change position before coring.	yes	yes	med2D
HUEL01A	yes	piston core (s	Lago Huelde	Pos12	-074,11282478 E	-42,59908659 N	06/02/12	0,220 - 1,255 m	didn't change position before coring after HU02, so maybe there is disturbance from 0 to 75 cm.	yes	yes	no
HUEL01B	yes	piston core (s	Lago Huelde	Pos12	-074,11282478 E	-42,59908659 N	06/02/12	0,220 - 1,255 m	didn't change position before coring after HU02, so maybe there is disturbance from 0 to 75 cm.	yes	yes	med2D
HUEL01C	yes	piston core (s	Lago Huelde	Pos12	-074,11282478 E	-42,59908659 N	06/02/12	0,220 - 1,255 m	didn't change position before coring after HU02, so maybe there is disturbance from 0 to 75 cm.	yes	yes	med2D, med3D
HUEL02A	yes	piston core (s	Lago Huelde	Pos12	-074,11282478 E	-42,59908659 N	06/02/12	2,050 - 3,500 m	cut away ca. 30 cm at top, probably because of loss at base	yes	yes	no
HUEL02B	yes	piston core (s	Lago Huelde	Pos12	-074,11282478 E	-42,59908659 N	06/02/12	3,500 - 4,625 m	cut away ca. 30 cm at top, probably because of loss at base	yes	yes	no
HU03	yes	gravity core	Lago Huelde	Pos15	-074,11158913 E	-42,59937753 N	06/02/12	0,000 - 0,984 m		yes	yes	med2D
HUEL03A	yes	piston core (s	Lago Huelde	Pos15	-074,11158913 E	-42,59937753 N	06/02/12	0,310 - 1,770 m	cut away ca. 30 cm at top, probably because of loss at base	yes	yes	med2D, med3D
HUEL03B	yes	piston core (s	Lago Huelde	Pos15	-074,11158913 E	-42,59937753 N	06/02/12	1,770 - 3,230 m	cut away ca. 30 cm at top, probably because of loss at base	yes	yes	med2D
HUEL04A	yes	piston core (s	Lago Huelde	Pos15	-074,11158913 E	-42,59937753 N	08/02/12	2,530 - 3,865 m	cut away ca. 30 cm at top, probably because of loss at base	yes	yes	med2D
HUEL04B	yes	piston core (s	Lago Huelde	Pos15	-074,11158913 E	-42,59937753 N	08/02/12	3,865 - 5,225 m	cut away ca. 30 cm at top, probably because of loss at base	yes	yes	med2D
HUEL05A	yes	piston core (s	Lago Huelde	Pos15	-074,11158913 E	-42,59937753 N	08/02/12	4,395 - 5,850 m	cut away ca. 30 cm at top, probably because of loss at base	yes	yes	med2D, med3D
HUEL05B	yes	piston core (s	Lago Huelde	Pos15	-074,11158913 E	-42,59937753 N	08/02/12	5,580 - 7,040 m	cut away ca. 30 cm at top, probably because of loss at base	yes	yes	med2D, med3D
HUEL27A	yes	piston core (s	Lago Huelde	Pos15	-074,11158913 E	-42,59937753 N	08/02/12	5,595 - 7,055 m	piston got stuck immediately after opening. Didn't core anything. Gravel grains were the cause. Liner extraction was difficult (bridgetrick).	yes	yes	med2D
HUEL27B	yes	piston core (s	Lago Huelde	Pos15	-074,11158913 E	-42,59937753 N	08/02/12	7,055 - 8,290 m	piston got stuck immediately after opening. Didn't core anything. Gravel grains were the cause. Liner extraction was difficult (bridgetrick).	yes	yes	med2D, med3D
HUEL27b	yes	piston core (s	Lago Huelde	Pos15	-074,11158913 E	-42,59937753 N	08/02/12	-	completely sieved for radiocarbondates . All samples gone except for the macrofossils.	yes	yes	no
HU04	yes	gravity core	Lago Huelde	Pos13	-074,11248172 E	-42,59854045 N	08/02/12	0,000 - 0,400 m	sand at base	yes	yes	med2D

Figure 8.5: Core list continued.

HUEL07A	yes	piston core (s	Lago Huelde	Pos13	-074,11248172 E	-42,59854045 N	09/02/12	0,385 - 1,845 m	cut away ca. 30 cm at top, probably because of loss at base	yes	yes	med2D, med3D
HUEL07B	yes	piston core (s	Lago Huelde	Pos13	-074,11248172 E	-42,59854045 N	09/02/12	1,845 - 3,085 m	cut away ca. 30 cm at top, probably because of loss at base	yes	yes	med2D
HUEL08A	yes	piston core (s	Lago Huelde	Pos13	-074,11248172 E	-42,59854045 N	09/02/12	2,487 - 3,922 m	cut away ca. 30 cm at top, probably because of loss at base. Hammer pole arm broke off again (the one we had repaired).	yes	yes	med2D, med3D
HUEL08B	yes	piston core (s	Lago Huelde	Pos13	-074,11248172 E	-42,59854045 N	09/02/12	3,922 - 4,867 m	cut away ca. 30 cm at top, probably because of loss at base. Hammer pole arm broke off again (the one we had repaired).	yes	yes	med2D
HU05	yes	gravity core	Lago Huelde	Pos14	-074,11378594 E	-42,59894823 N	09/02/12	0,000 - 0,795 m		yes	yes	med2D
HUEL09A1	yes	piston core (s	Lago Huelde	Pos14	-074,11378594 E	-42,59894823 N	09/02/12	0,435 - 1,885 m	cut away ca. 30 cm at top, probably because of loss at base	yes	yes	med2D, med3D
HUEL09A2	no	piston core (s	Lago Huelde	Pos14	-074,11378594 E	-42,59894823 N	09/02/12	0,435 - 1,885 m	cut away ca. 30 cm at top, probably because of loss at base	yes	yes	med2D, med3D
HUEL09B	yes	piston core (s	Lago Huelde	Pos14	-074,11378594 E	-42,59894823 N	09/02/12	1,885 - 3,135 m	cut away ca. 30 cm at top, probably because of loss at base	yes	yes	med2D, med3D
HUEL10A	yes	piston core (s	Lago Huelde	Pos14	-074,11378594 E	-42,59894823 N	09/02/12	2,290 - 3,320 m	cut away ca. 30 cm at top, probably because of loss at base	yes	yes	med2D, med3D
HUEL10B1	yes	piston core (s	Lago Huelde	Pos14	-074,11378594 E	-42,59894823 N	09/02/12	3,320 - 4,280 m	cut away ca. 30 cm at top, probably because of loss at base	yes	yes	med2D, med3D
HUEL10B2	no	piston core (s	Lago Huelde	Pos14	-074,11378594 E	-42,59894823 N	09/02/12	3,320 - 4,280 m	cut away ca. 30 cm at top, probably because of loss at base	yes	yes	med2D, med3D
HUEL10 core	no	piston core (s	Lago Huelde	Pos14	-074,11378594 E	-42,59894823 N	09/02/12	-	it is just the material from the core catcher	yes	yes	no
HU06	yes	gravity core	Lago Huelde	Pos17	-074,11206491 E	-42,59662919 N	09/02/12	0,000 - 0,865 m	x-ray already exists. Core is in Bordeaux for Cs/Pb analysis	yes	yes	no
HUEL11A	yes	piston core (s	Lago Huelde	Pos17	-074,11206491 E	-42,59662919 N	09/02/12	0,505 - 1,970 m	cut away ca. 30 cm at top, probably because of loss at base	yes	yes	no
HUEL11B	yes	piston core (s	Lago Huelde	Pos17	-074,11206491 E	-42,59662919 N	09/02/12	1,970 - 3,275 m	cut away ca. 30 cm at top, probably because of loss at base	yes	yes	no
HUEL12A	yes	piston core (s	Lago Huelde	Pos17	-074,11206491 E	-42,59662919 N	09/02/12	2,485 - 3,935 m	cut away ca. 30 cm at top, probably because of loss at base	yes	yes	no
HUEL12B	yes	piston core (s	Lago Huelde	Pos17	-074,11206491 E	-42,59662919 N	09/02/12	3,935 - 5,100 m	cut away ca. 30 cm at top, probably because of loss at base	yes	yes	no
HUEL13A	yes	piston core (s	Lago Huelde	Pos17	-074,11206491 E	-42,59662919 N	10/02/12	4,345 - 5,785 m	cut away ca. 30 cm at top, probably because of loss at base	yes	yes	no
HUEL13B	yes	piston core (s	Lago Huelde	Pos17	-074,11206491 E	-42,59662919 N	10/02/12	5,785 - 7,045 m	cut away ca. 30 cm at top, probably because of loss at base	yes	yes	no
HUEL14A	yes	piston core (s	Lago Huelde	Pos17	-074,11206491 E	-42,59662919 N	10/02/12	6,190 - 7,635 m	cut away ca. 30 cm at top, probably because of loss at base. Sand at base is in sample HUEL14b	yes	yes	no
HUEL14B	yes	piston core (s	Lago Huelde	Pos17	-074,11206491 E	-42,59662919 N	10/02/12	7,635 - 8,895 m	cut away ca. 30 cm at top, probably because of loss at base. Sand at base is in sample HUEL14b	yes	yes	no
HUEL14b	yes	piston core (s	Lago Huelde	Pos17	-074,11206491 E	-42,59662919 N	10/02/12	-	it is the collected material from the bonnet and the core catcher. Sieved for radiocarbondates. Samples gone.	yes	yes	no
HU07	yes	gravity core	Lago Huelde	Pos16	-074,10922149 E	-42,60027907 N	10/02/12	0,000 - 0,885 m		yes	yes	med2D
HUEL15A	yes	piston core (s	Lago Huelde	Pos16	-074,10922149 E	-42,60027907 N	10/02/12	0,465 - 1,905 m	cut away ca. 30 cm at top, probably because of loss at base. Started coring on topmost sand layer, so there are ca. 30 to 40 cm missing at top. Correlation with HU07 should be easy.	yes	yes	me2D, med3D
HUEL15B	yes	piston core (s	Lago Huelde	Pos16	-074,10922149 E	-42,60027907 N	10/02/12	1,905 - 3,370 m	cut away ca. 30 cm at top, probably because of loss at base. Started coring on topmost sand layer, so there are ca. 30 to 40 cm missing at top. Correlation with HU07 should be easy.	yes	yes	no
HUEL16A	yes	piston core (s	Lago Huelde	Pos16	-074,10922149 E	-42,60027907 N	10/02/12	2,655 - 4,095 m	cut away ca. 30 cm at top, probably because of loss at base	yes	yes	no
HUEL16B	yes	piston core (s	Lago Huelde	Pos16	-074,10922149 E	-42,60027907 N	10/02/12	4,095 - 5,410 m	cut away ca. 30 cm at top, probably because of loss at base	yes	yes	no
HUEL17A	yes	piston core (s	Lago Huelde	Pos16	-074,10922149 E	-42,60027907 N	10/02/12	4,735 - 6,190 m	cut away ca. 30 cm at top, probably because of loss at base	yes	yes	no
HUEL17B	yes	piston core (s	Lago Huelde	Pos16	-074,10922149 E	-42,60027907 N	10/02/12	6,190 - 7,595 m	cut away ca. 30 cm at top, probably because of loss at base	yes	yes	no
HUEL18A	yes	piston core (s	Lago Huelde	Pos16	-074,10922149 E	-42,60027907 N	12/02/12	6,255 - 7,695 m	cut away ca. 20 cm at top, probably because of loss at base.	yes	yes	med2D
HUEL18B	yes	piston core (s	Lago Huelde	Pos16	-074,10922149 E	-42,60027907 N	12/02/12	7,695 - 9,025 m	cut away ca. 20 cm at top, probably because of loss at base.	yes	yes	med2D, med3D
HU08	yes	gravity core	Lago Huelde	Pos18	-074,10723512 E	-42,60040996 N	12/02/12	0,000 - 0,804 m		yes	yes	med2D
HUEL19A	yes	piston core (s	Lago Huelde	Pos18	-074,10723512 E	-42,60040996 N	12/02/12	0,365 - 1,820 m	cut away ca. 30 cm at top, probably because of loss at base. Too sticky and not enough water at top for actually being lake floor sediment	yes	yes	no
HUEL19B	yes	piston core (s	Lago Huelde	Pos18	-074,10723512 E	-42,60040996 N	12/02/12	1,820 - 3,300 m	cut away ca. 30 cm at top, probably because of loss at base. Too sticky and not enough water at top for actually being lake floor sediment	yes	yes	no
HUEL20A	yes	piston core (s	Lago Huelde	Pos18	-074,10723512 E	-42,60040996 N	12/02/12	2,393 - 3,843 m	cut away ca. 40 cm at top, probably because of loss at base. A lot of loss at base.	yes	yes	no
HUEL20B	yes	piston core (s	Lago Huelde	Pos18	-074,10723512 E	-42,60040996 N	12/02/12	3,843 - 5,078 m	cut away ca. 40 cm at top, probably because of loss at base. A lot of loss at base.	yes	yes	no
HUEL21A	yes	piston core (s	Lago Huelde	Pos18	-074,10723512 E	-42,60040996 N	12/02/12	4,292 - 5,742 m	cut away ca. 30 cm at top, probably because of loss at base. 2 to 4 mm thick grey/lightgrey silt or clay layer in the core catcher.	yes	yes	no
HUEL21B	yes	piston core (s	Lago Huelde	Pos18	-074,10723512 E	-42,60040996 N	12/02/12	5,742 - 7,017 m	cut away ca. 30 cm at top, probably because of loss at base. 2 to 4 mm thick grey/lightgrey silt or clay layer in the core catcher.	yes	yes	no
HUEL22A	yes	piston core (s	Lago Huelde	Pos18	-074,10723512 E	-42,60040996 N	12/02/12	6,055 - 7,455 m	cut away ca. 20 cm at top, probably because of loss at base. Sand and some gravel in the core catcher.	yes	yes	no?
HUEL22B	yes	piston core (s	Lago Huelde	Pos18	-074,10723512 E	-42,60040996 N	12/02/12	7,455 - 8,800 m	cut away ca. 20 cm at top, probably because of loss at base. Sand and some gravel in the core catcher.	yes	yes	no?
HUEL22b	yes	piston core (s	Lago Huelde	Pos18	-074,10723512 E	-42,60040996 N	12/02/12	-	bulk sample below HUEL22. Sieved for radiocarbon dates. Samples gone.	yes	yes	no

Figure 8.6: Core list continued.

HU09	yes	gravity core	Lago Huelde	Pos19	-074,11014044 E	-42,59790062 N	13/02/12	0,000 - 0,809 m		yes	yes	med2D
HUEL23A	yes	piston core (s	Lago Huelde	Pos19	-074,11014044 E	-42,59790062 N	13/02/12	0,000 - 1,190 m	cut away ca. 15 cm at top, probably because of loss at base.	yes	yes	med2D
HUEL23B	yes	piston core (s	Lago Huelde	Pos19	-074,11014044 E	-42,59790062 N	13/02/12	1,190 - 2,935 m	cut away ca. 15 cm at top, probably because of loss at base.	yes	yes	med2D
HUEL23C	yes	piston core (s	Lago Huelde	Pos19	-074,11014044 E	-42,59790062 N	13/02/12	1,190 - 2,935 m	cut away ca. 15 cm at top, probably because of loss at base.	yes	yes	no
HUEL24A	yes	piston core (s	Lago Huelde	Pos19	-074,11014044 E	-42,59790062 N	13/02/12	2,040 - 3,475 m	cut away ca. 10 cm at top, probably because of loss at base.	yes	yes	med2D
HUEL24B	yes	piston core (s	Lago Huelde	Pos19	-074,11014044 E	-42,59790062 N	13/02/12	3,475 - 4,690 m	cut away ca. 10 cm at top, probably because of loss at base.	yes	yes	med2D
HUEL25A	yes	piston core (s	Lago Huelde	Pos19	-074,11014044 E	-42,59790062 N	13/02/12	3,865 - 5,300 m	cut away ca. 30 cm at top, probably because of loss at base.	yes	yes	med2D
HUEL25B	yes	piston core (s	Lago Huelde	Pos19	-074,11014044 E	-42,59790062 N	13/02/12	5,300 - 6,450 m	cut away ca. 30 cm at top, probably because of loss at base.	yes	yes	med2D
HUEL25b	yes	piston core (s	Lago Huelde	Pos19	-074,11014044 E	-42,59790062 N	13/02/12	-	leaf sample for 14C dating	yes	yes	no
HUEL26A	yes	piston core (s	Lago Huelde	Pos19	-074,11014044 E	-42,59790062 N	13/02/12	5,615 - 6,540 m		yes	yes	med2D
HUEL26B	yes	piston core (s	Lago Huelde	Pos19	-074,11014044 E	-42,59790062 N	13/02/12	6,540 - 7,500 m		yes	yes	med2D, med3D
HUEL26C	yes	piston core (s	Lago Huelde	Pos19	-074,11014044 E	-42,59790062 N	13/02/12	7,500 - 8,425 m		yes	yes	no
HUEL26b	yes	piston core (s	Lago Huelde	Pos19	-074,11014044 E	-42,59790062 N	13/02/12	-	push out + bonnet + core catcher in moore or less the correct way up. Sieved for radiocarbon dates. Samples gone.	yes	yes	no
CUC1	yes	gravity core	Lago Cucao	CUC1	-74.07777	-42.63368	02/03/11	75cm	1 plomo, approx 5m free fall	yes	yes	no
CUC2	yes	gravity core	Lago Cucao	CUC2	-74.05780	-42.64252	03/03/11	55cm	"	yes	yes	no
CUC3	yes	gravity core	Lago Cucao	CUC3	-74.09260	-42.63066	03/03/11	60cm	"	yes	yes	no
CUC4	yes	gravity core	Lago Cucao	CUC4	-74.09325	-42.62691	03/03/11	40cm	"	yes	yes	no
CUC5	yes	gravity core	Lago Cucao	CUC5	-74.09619	-42.62292	03/03/11	17cm	"	yes	yes	no
CUC6	yes	gravity core	Lago Cucao	CUC6	-74.09339	-42.62902	03/03/11	45cm	"	yes	yes	no
CUC7	yes	gravity core	Lago Cucao	CUC7	-74.09078	-42.62802	03/03/11	20cm	"	yes	yes	no
CUC8	yes	gravity core	Lago Cucao	CUC8	-74.09136	-42.62929	03/03/11	60cm	"	yes	yes	no
CUC9	yes	gravity core	Lago Cucao	CUC9	-74.09093	-42.63504	03/03/11	70cm	"	yes	yes	no
CUC10	yes	gravity core	Lago Cucao	CUC10	-74.06666	-42.64549	03/03/11	85cm	"	yes	yes	no
CUC11	yes	gravity core	Lago Cucao	CUC11	-74.06374	-42.64335	03/03/11	85cm	"	yes	yes	no
HUE1	yes	gravity core	Laguna Huelde	HUE1	-74.11203	-42.59812	04/03/11	45cm	1 plomo, 3-5m free fall. H2S-smell	yes	yes	no
HUE2	yes	gravity core	Laguna Huelde	HUE2	-74.11166	-42.59468	04/03/11	60cm	"	yes	yes	no
HUE3	yes	gravity core	Laguna Huelde	HUE3	-74.11344	-42.59540	04/03/11	65cm	"	yes	yes	no
HUE4	yes	gravity core	Laguna Huelde	HUE4	-74.11412	-42.59792	04/03/11	70cm	"	yes	yes	no
HUE5	yes	gravity core	Laguna Huelde	HUE5	-74.10844	-42.59891	04/03/11	85cm	idem, taped liners	yes	yes	no

Figure 8.7: Core list continued.

Tsunami deposits in Lake Huelde

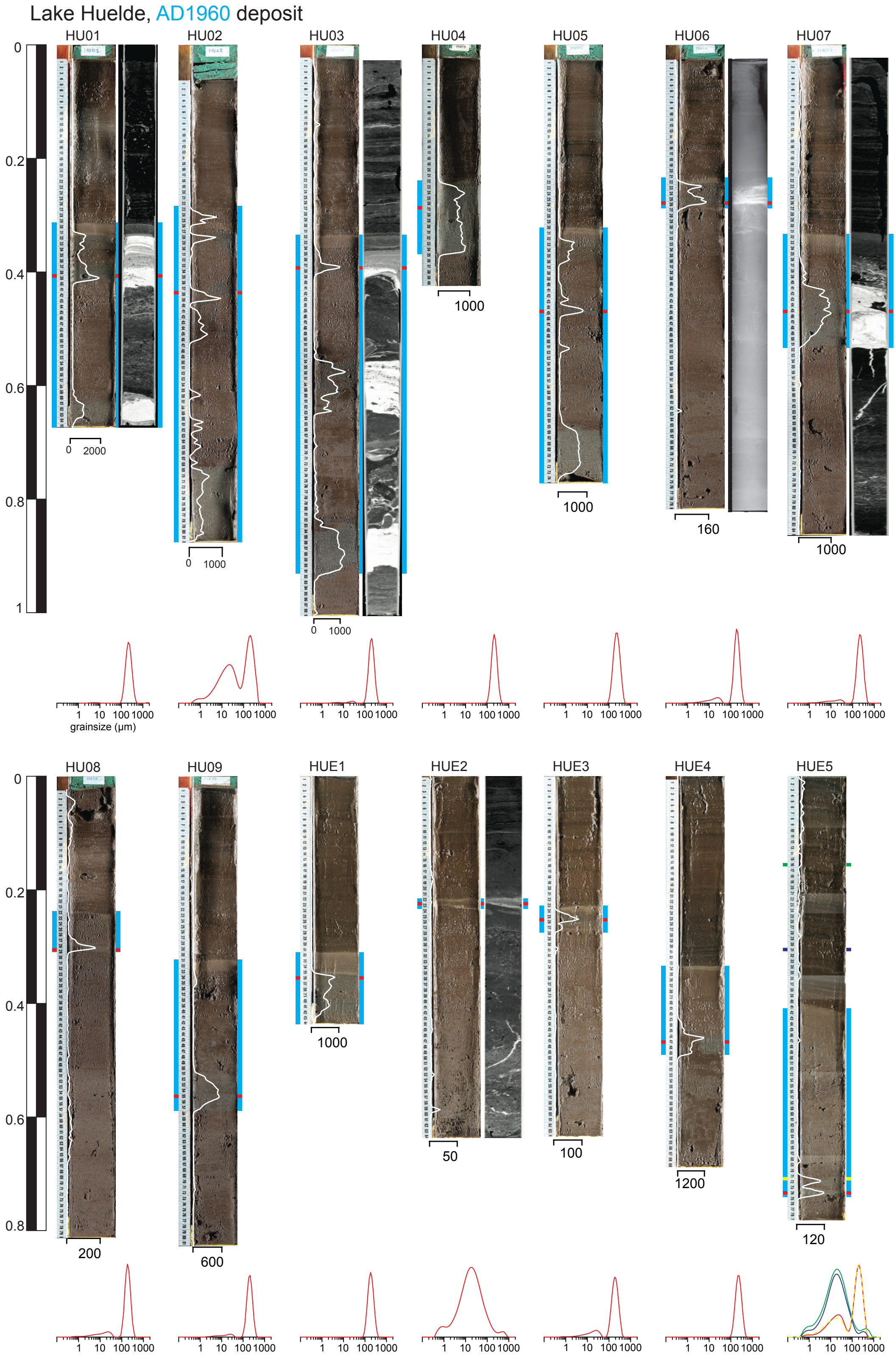

Figure 8.8: AD 1960 tsunami deposit in Lake Huelde.

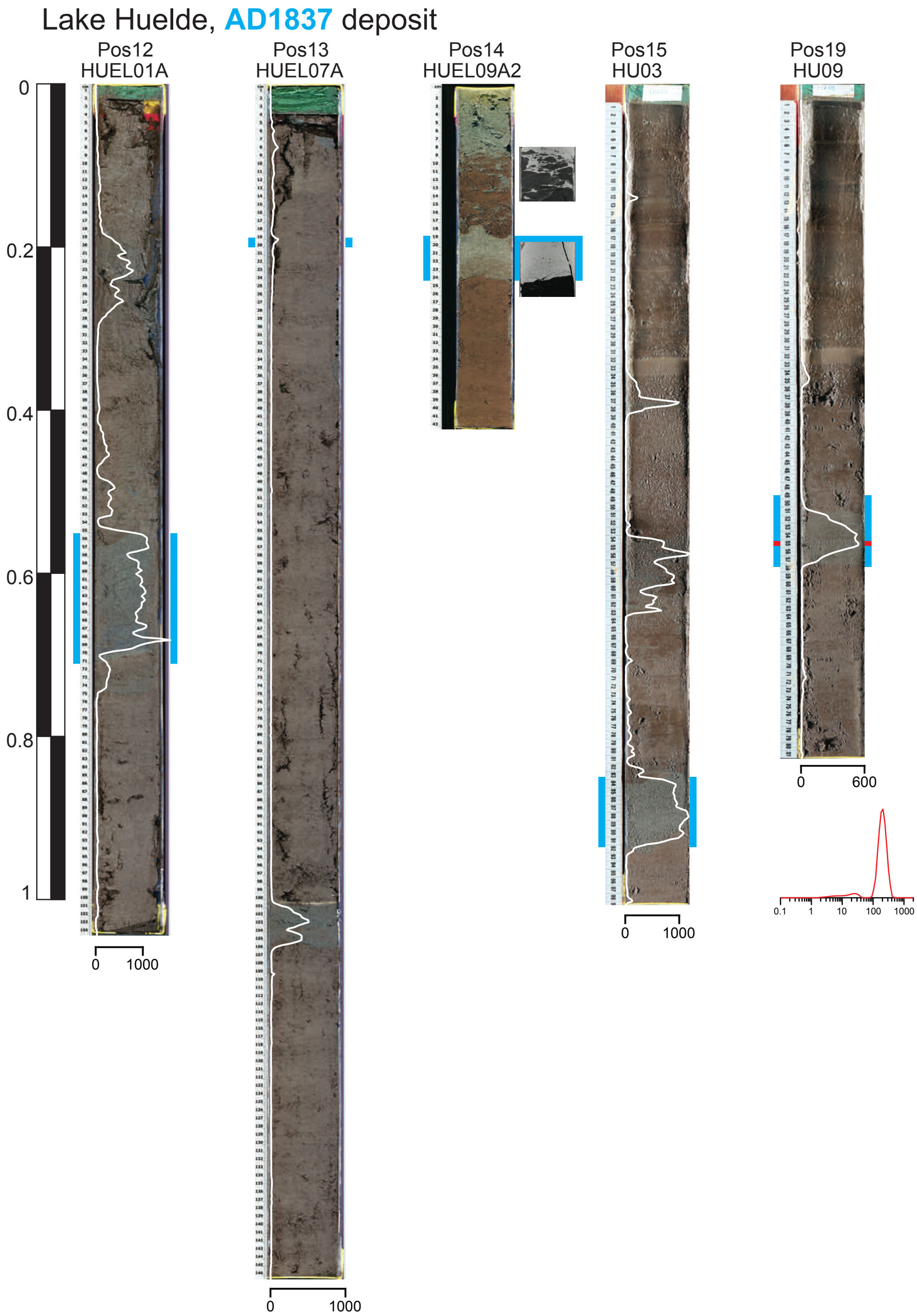

Figure 8.9: AD 1837 tsunami deposit in Lake Huelde.

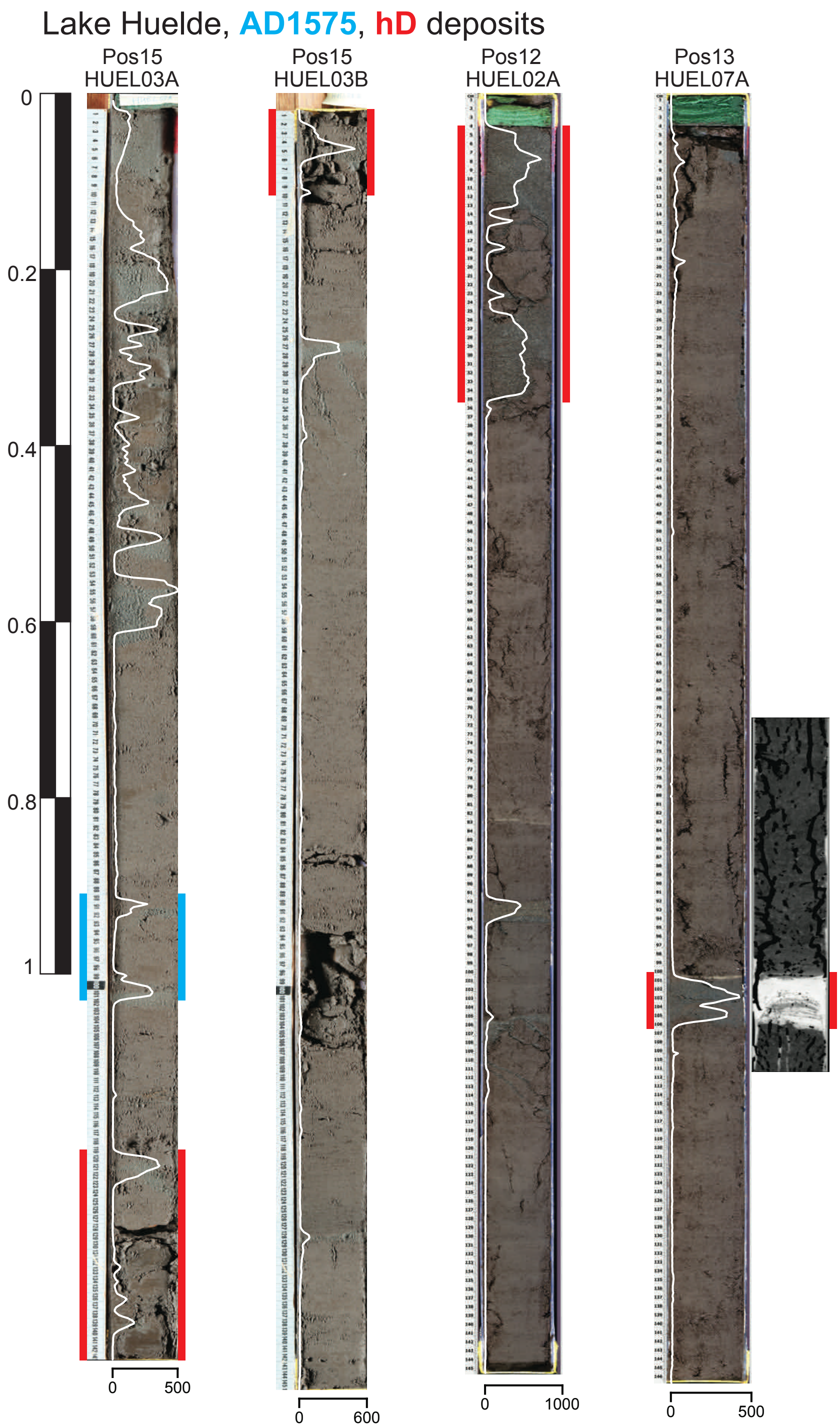

Figure 8.10: AD 1575 and hD tsunami deposit in Lake Huelde.

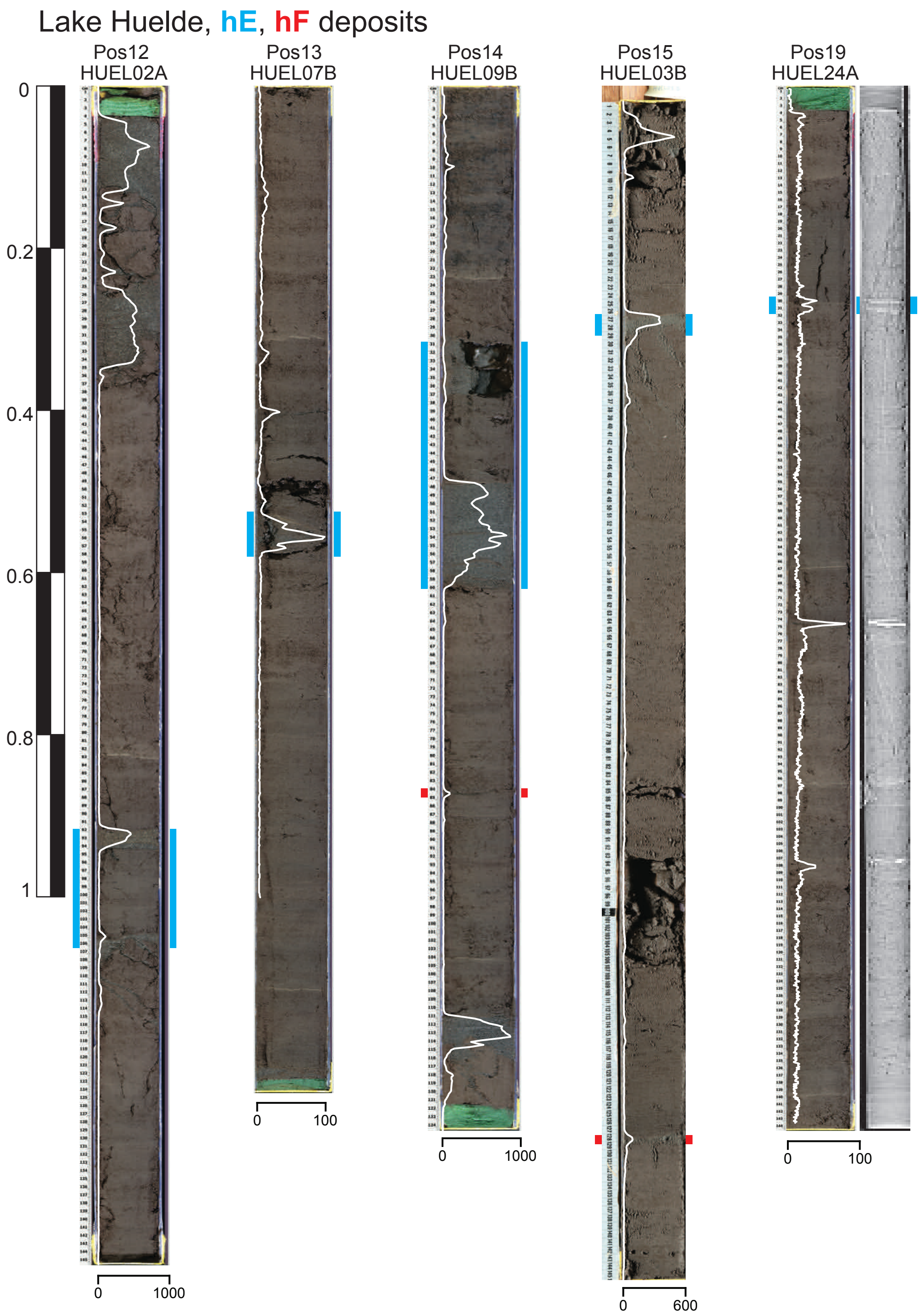

Figure 8.11: hE and hF tsunami deposits in Lake Huelde.

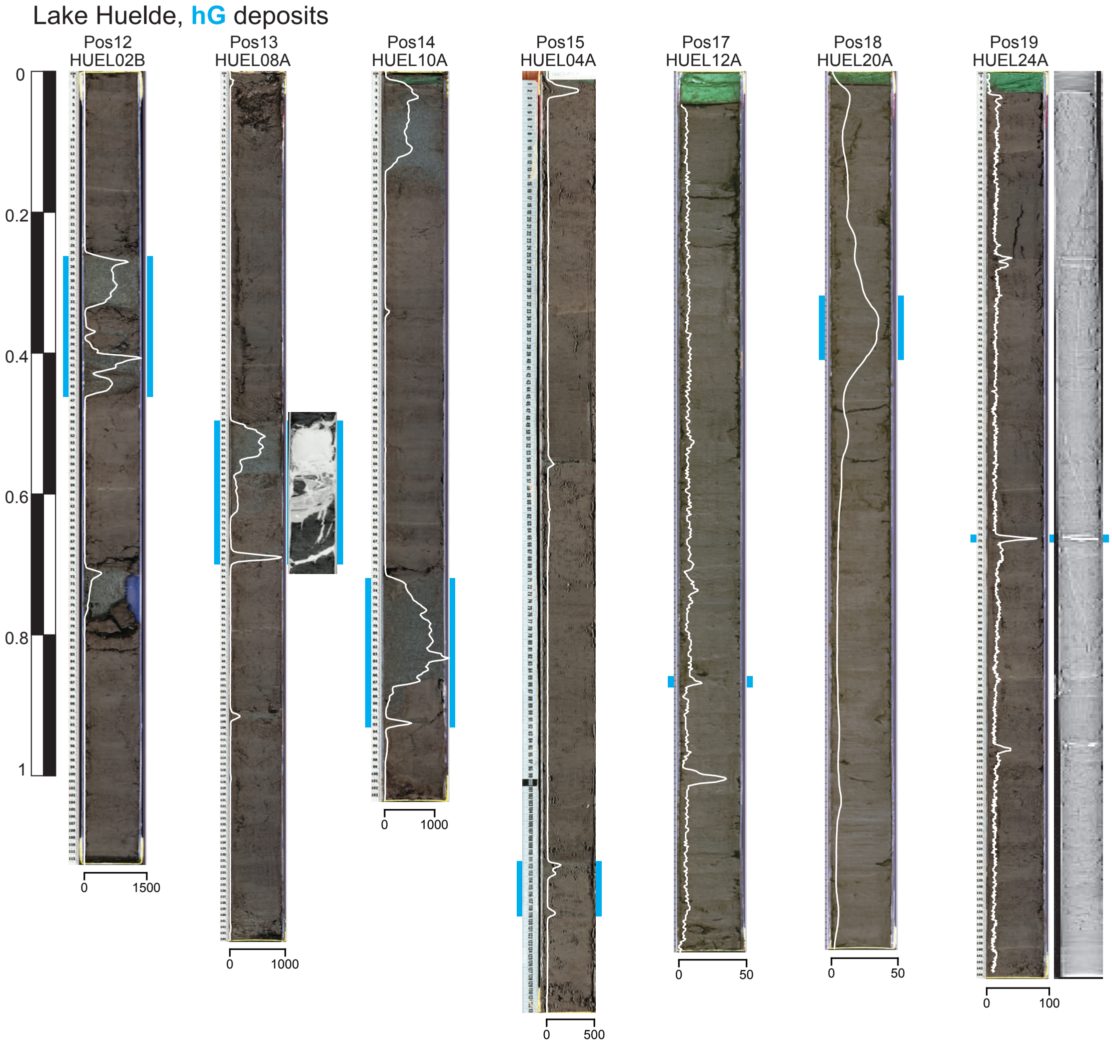

Figure 8.12: hG tsunami deposit in Lake Huelde.

Figure 8.13: hH tsunami deposit in Lake Huelde.

Figure 8.14: hI tsunami deposit in Lake Huelde.

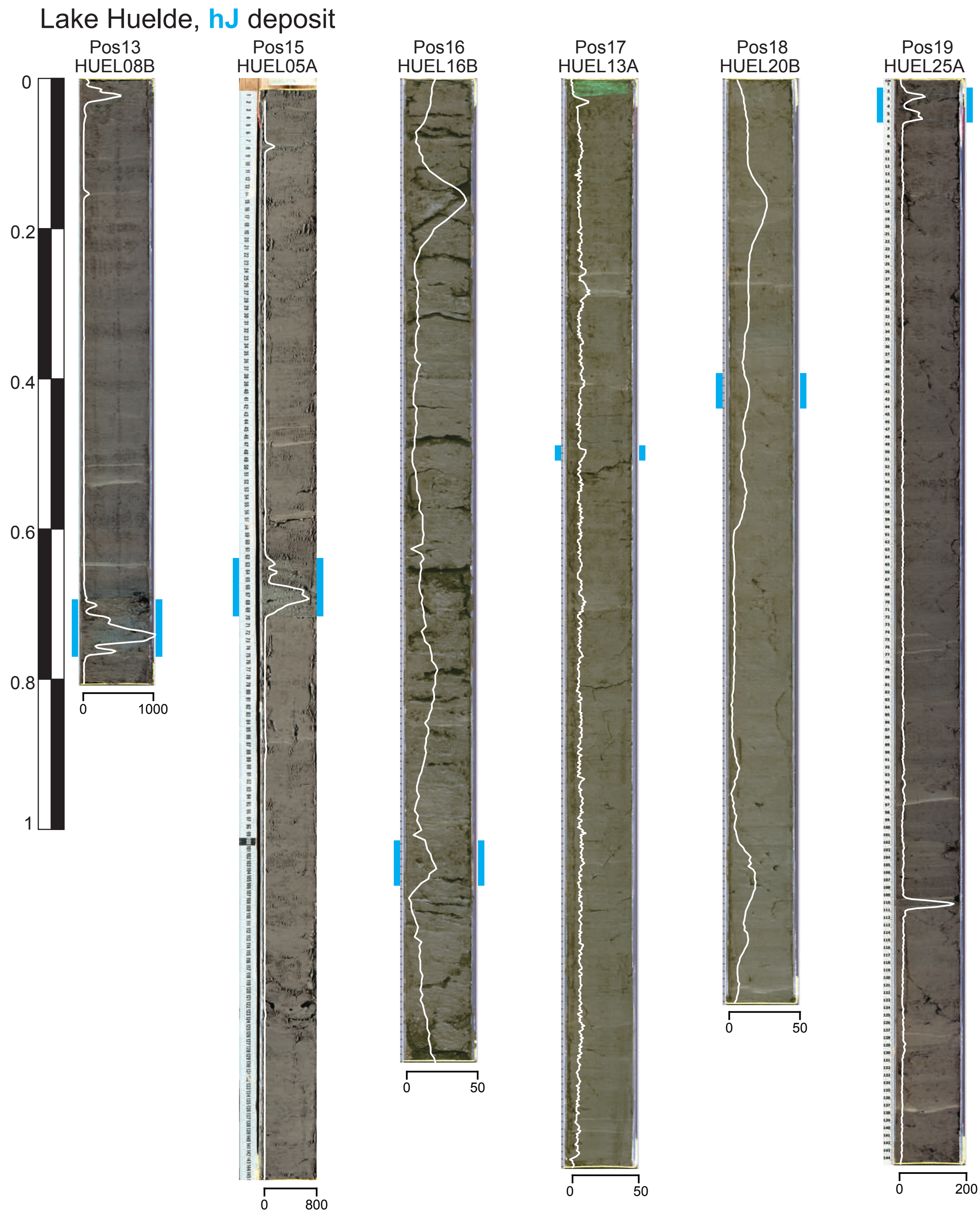

Figure 8.15: hJ tsunami deposit in Lake Huelde.

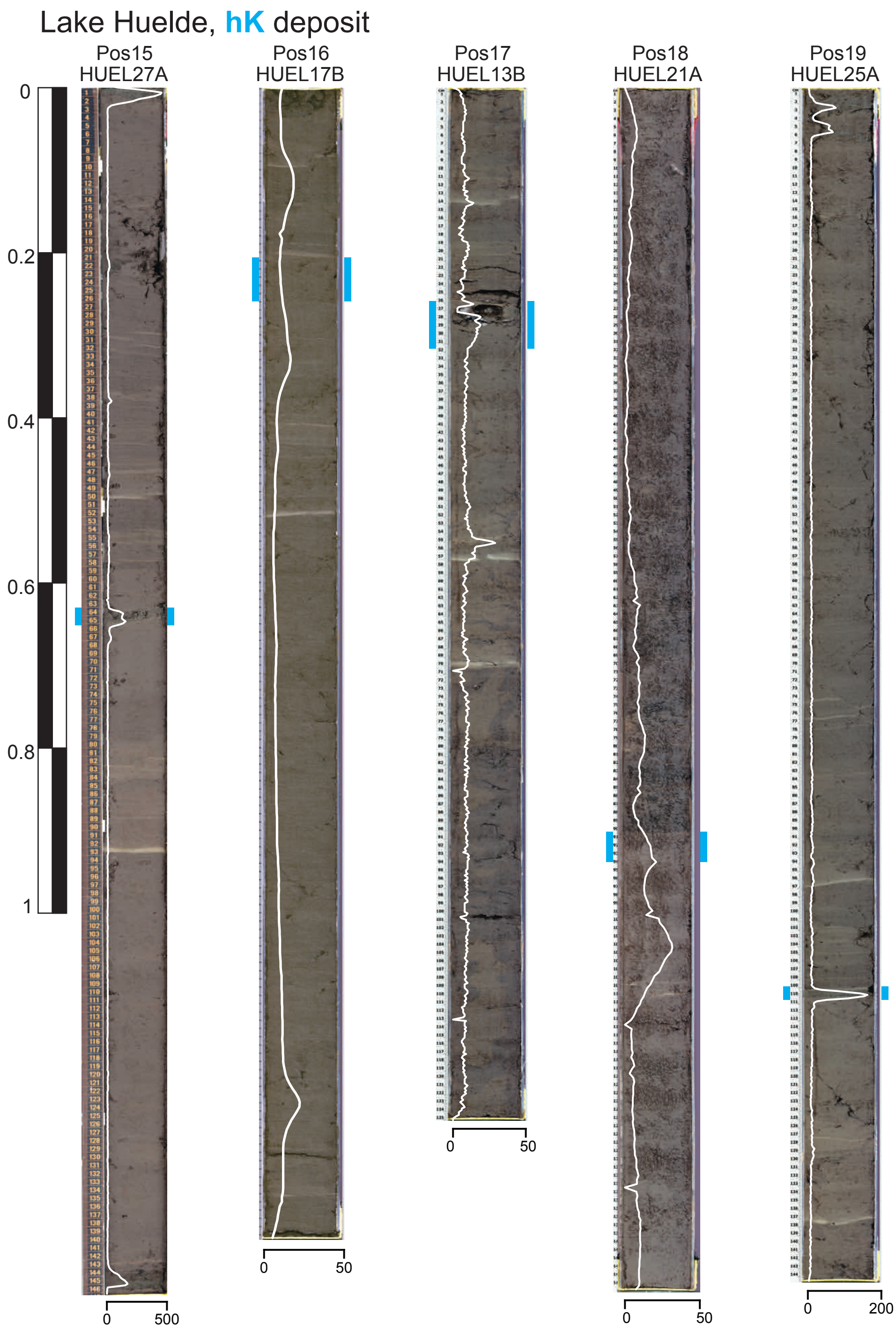

Figure 8.16: hK tsunami deposit in Lake Huelde.

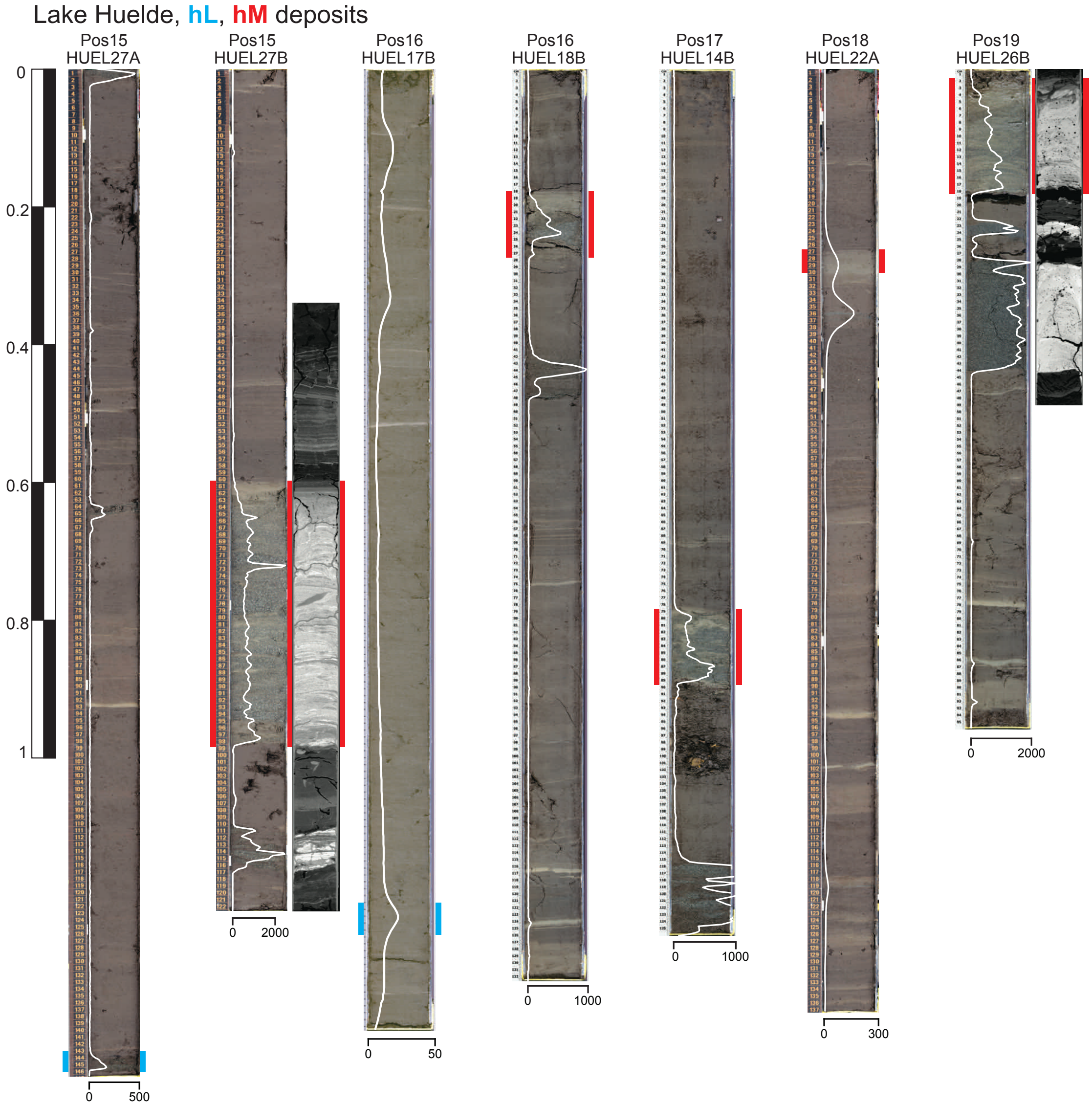

Figure 8.17: hl and hM tsunami deposit in Lake Huelde.

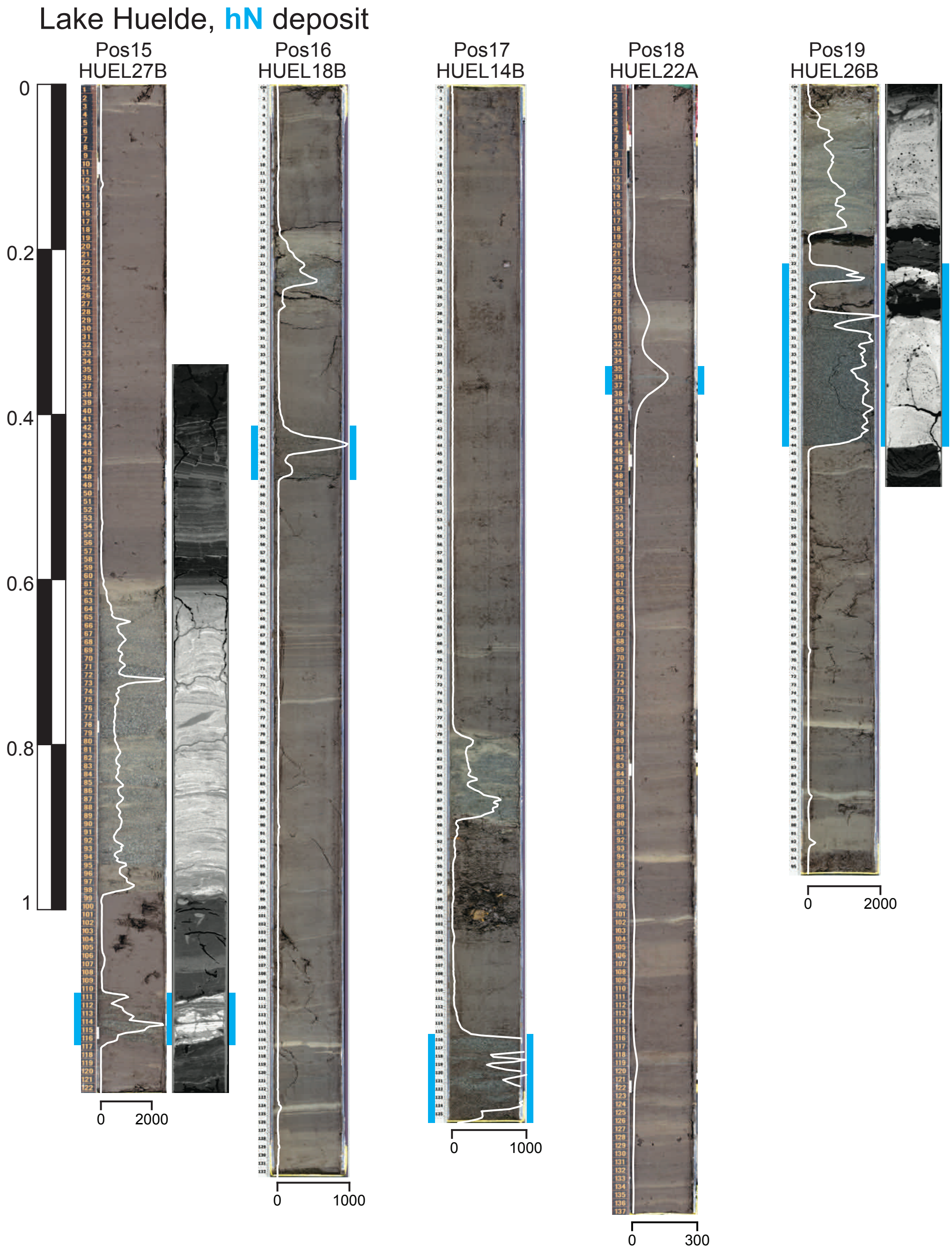

Figure 8.18: hN tsunami deposit in Lake Huelde.

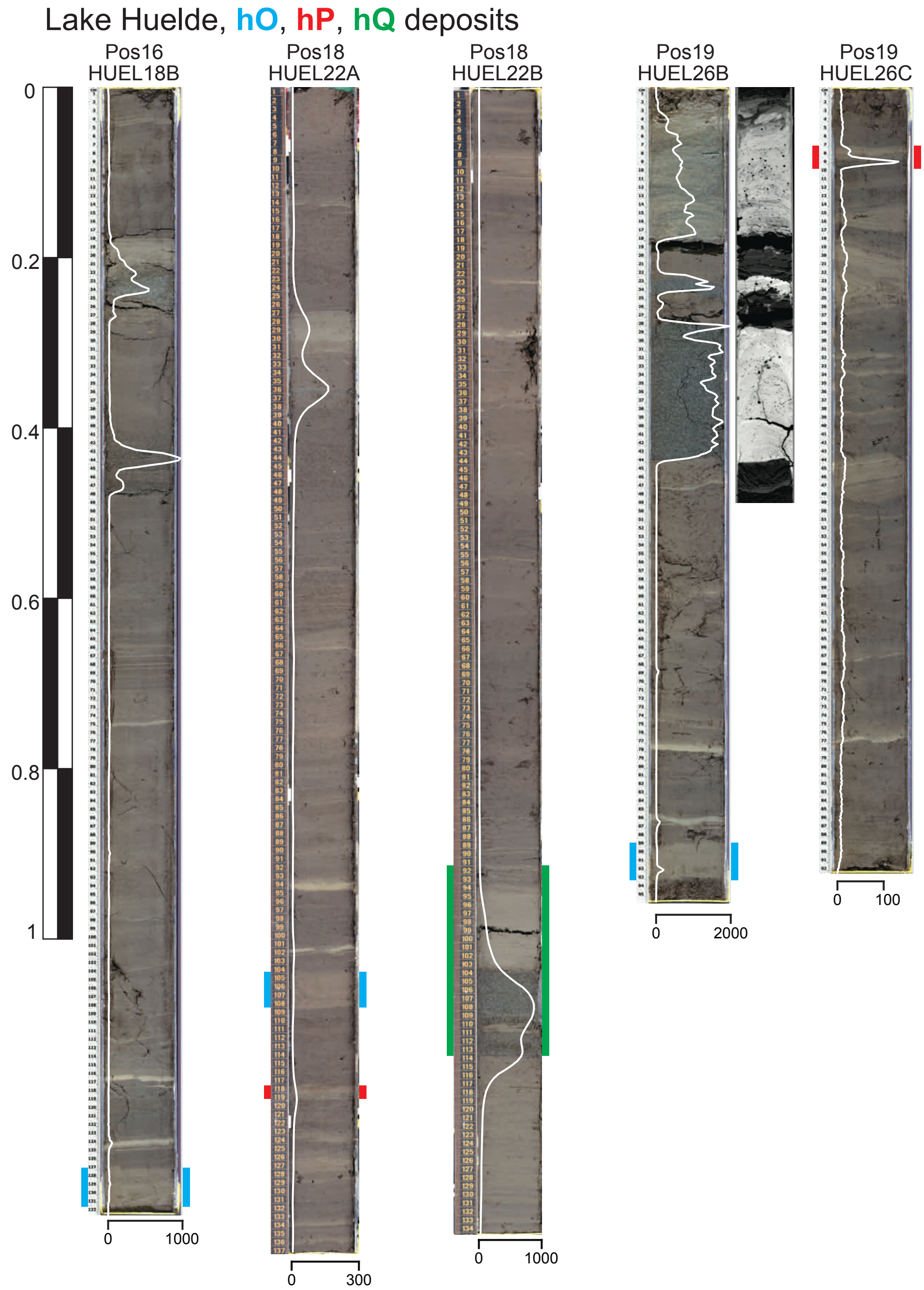

Figure 8.19: hO, hP and hQ tsunami deposits in Lake Huelde.

Tsunami deposits in Lake Cucao

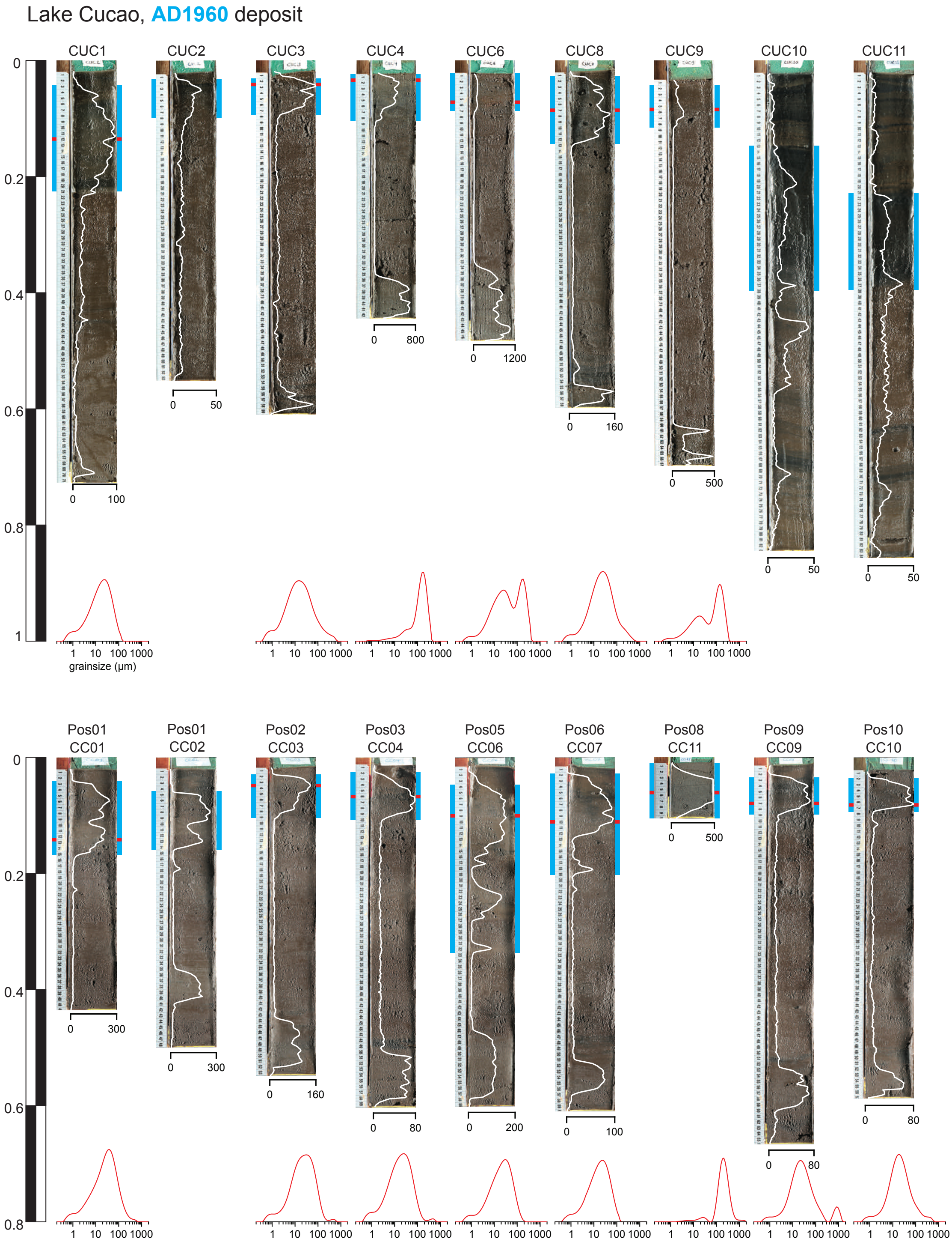

Figure 8.20: AD 1960 tsunami deposit in Lake Cucao.

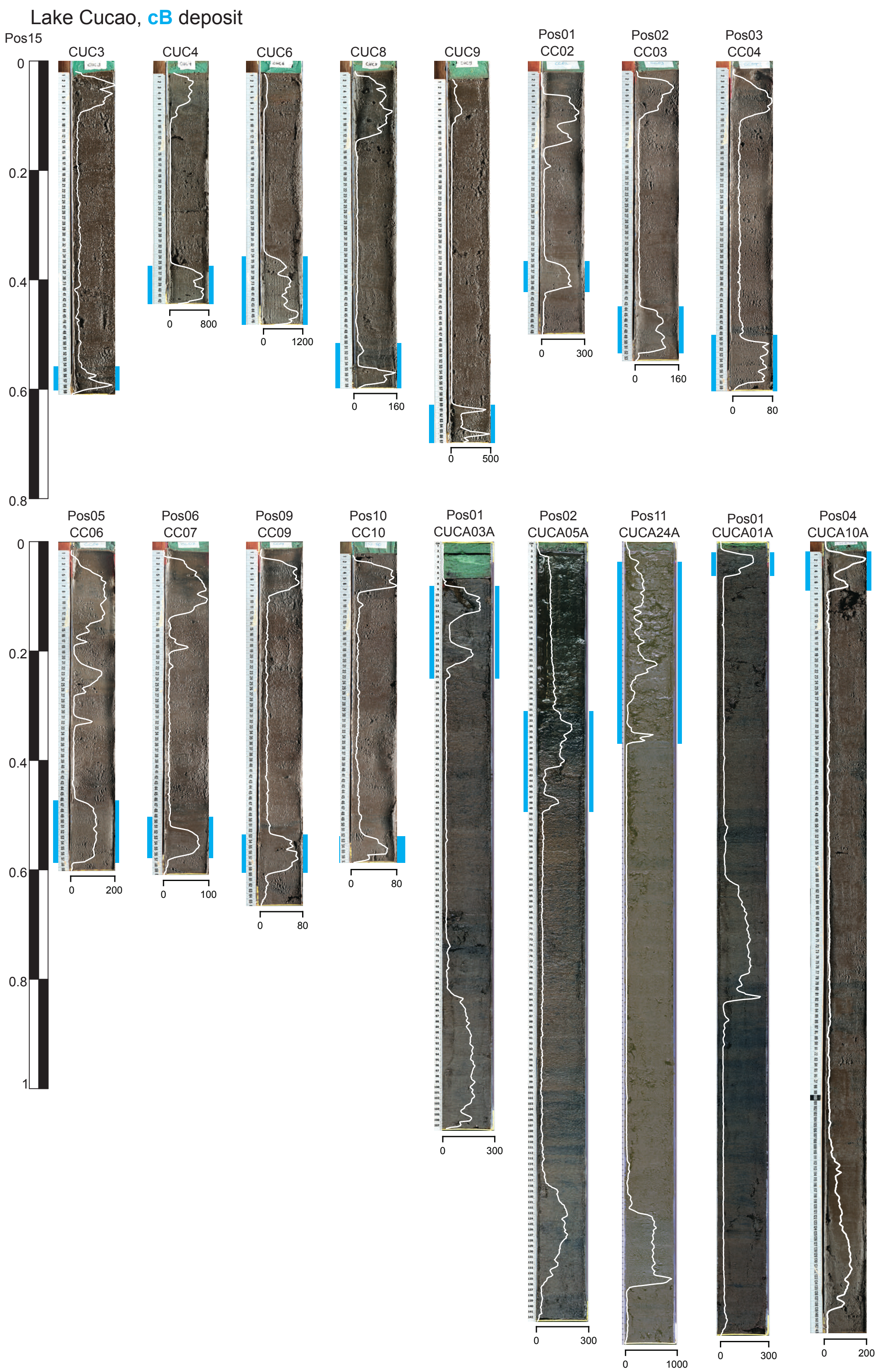

Figure 8.21: cB tsunami deposit in Lake Cucao.

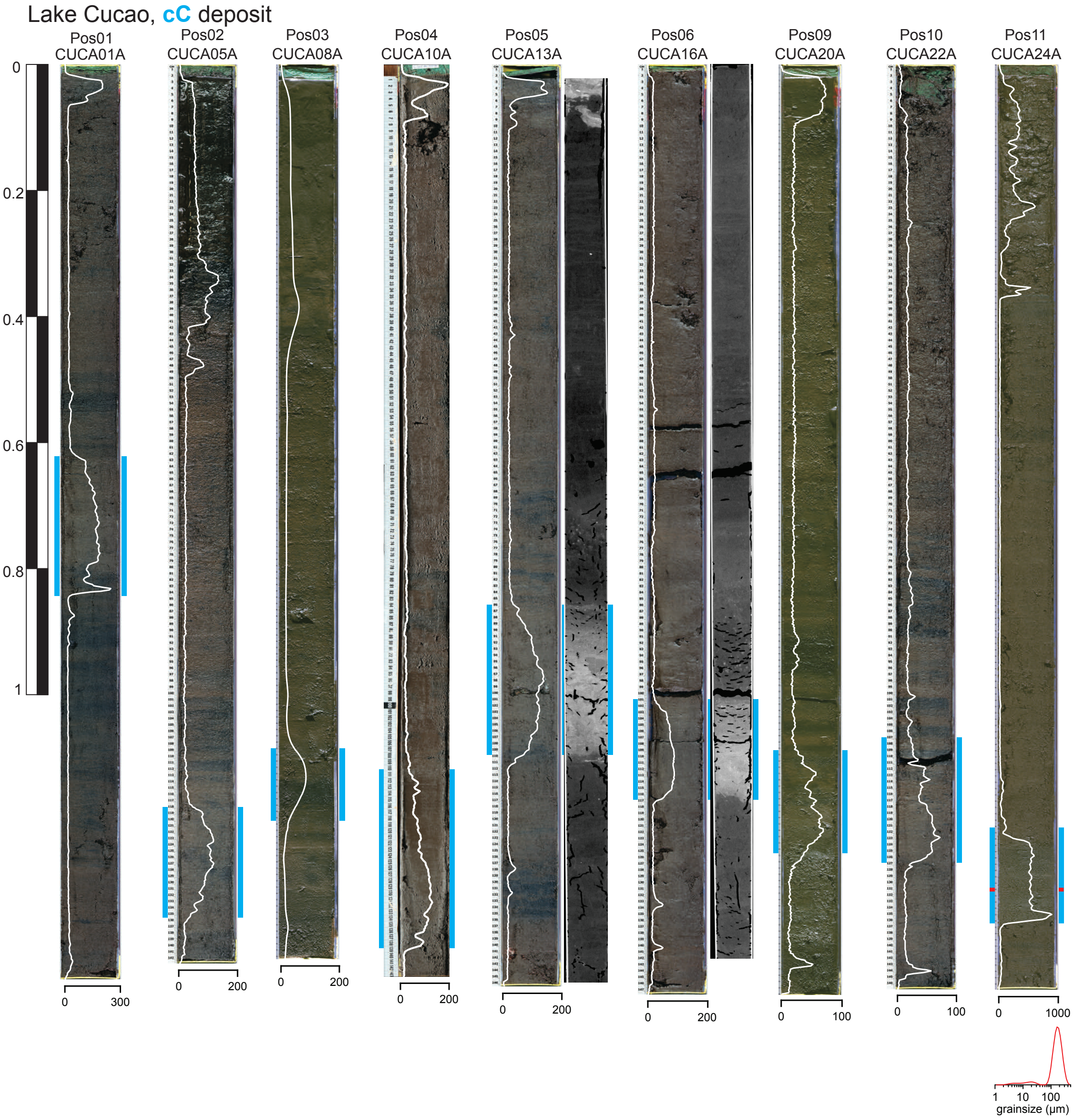

Figure 8.22: cC tsunami deposit in Lake Cucao.

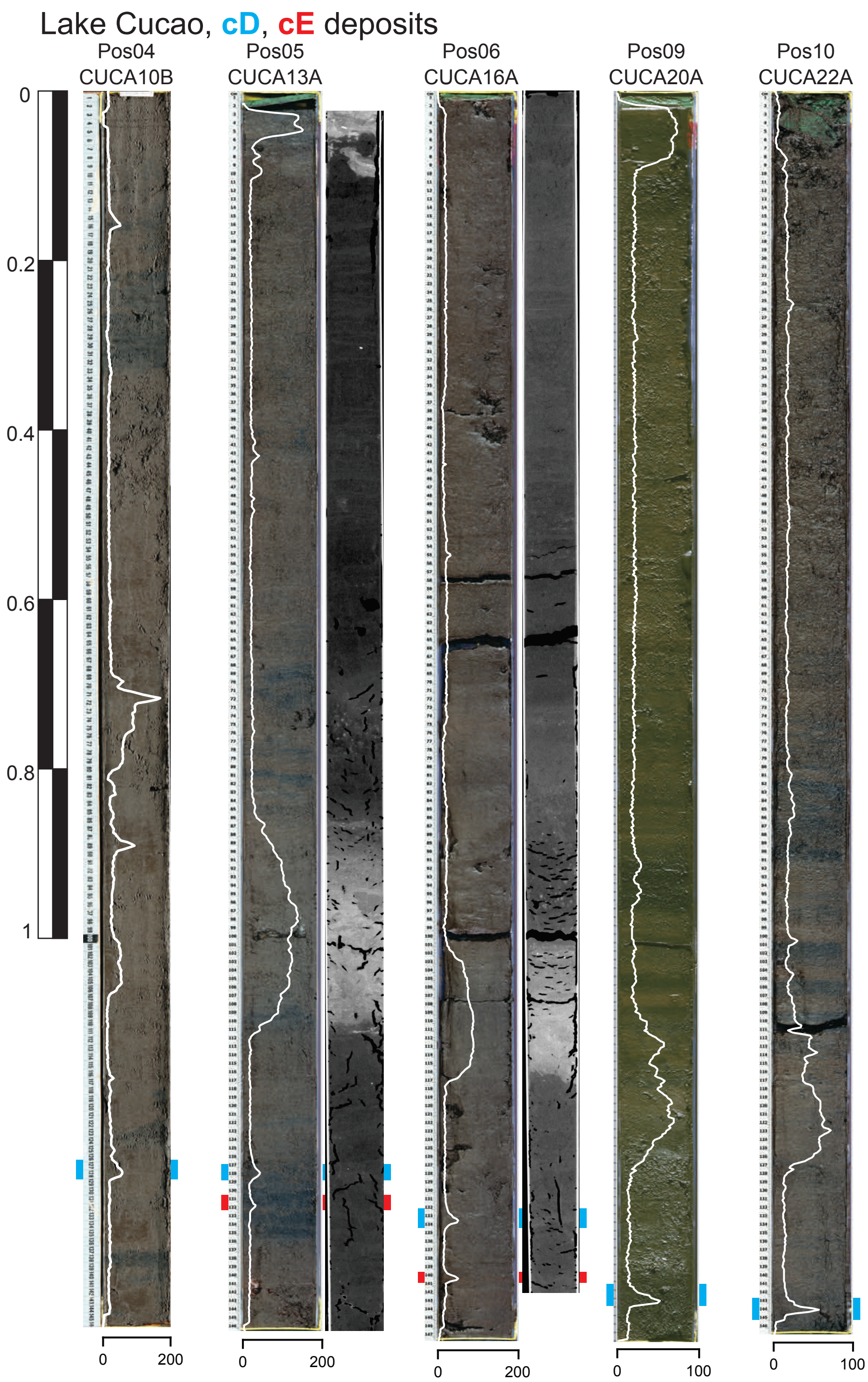

Figure 8.23: cD and cE tsunami deposits in Lake Cucao.

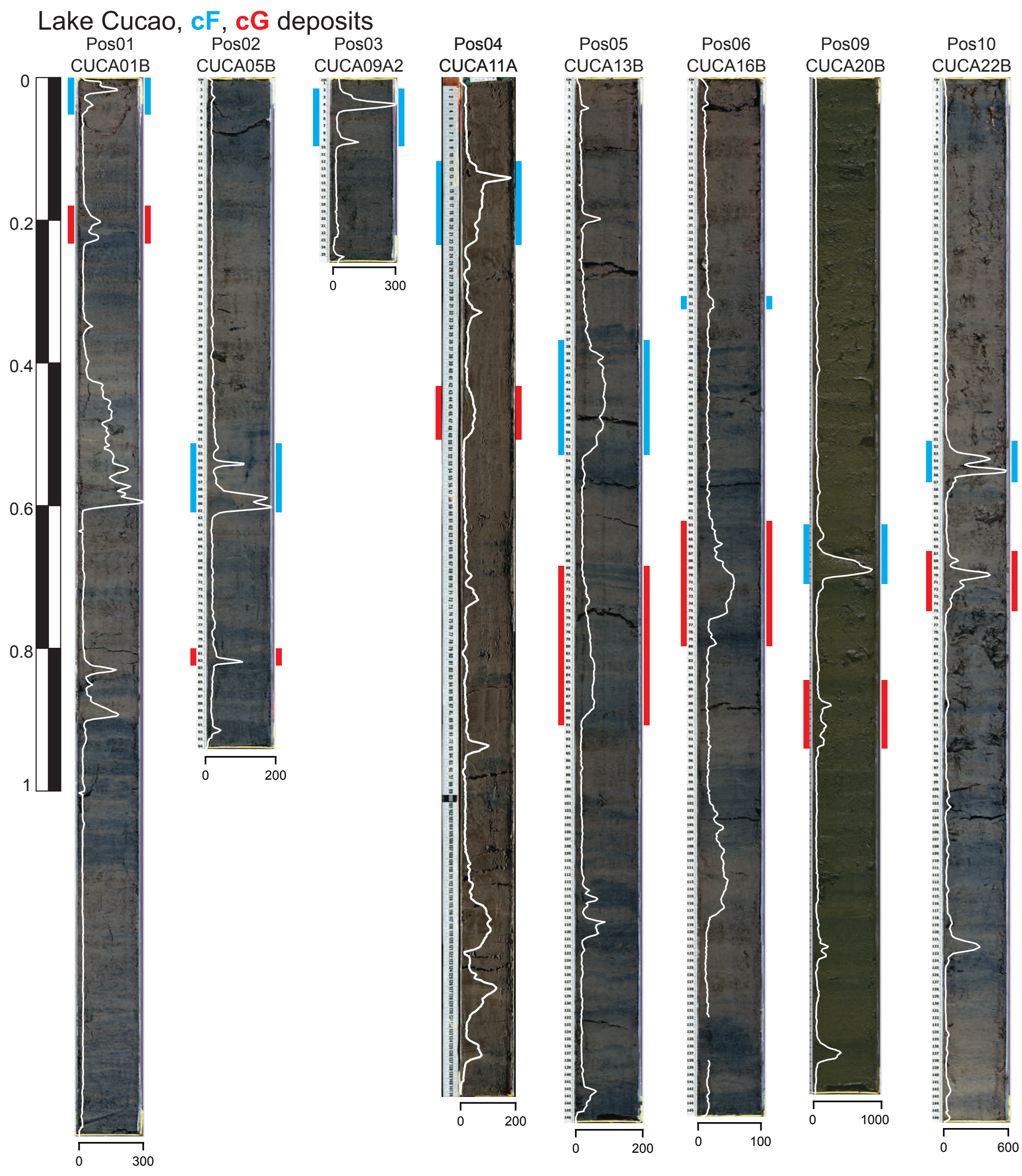

Figure 8.24: cF and cG tsunami deposits in Lake Cucao.

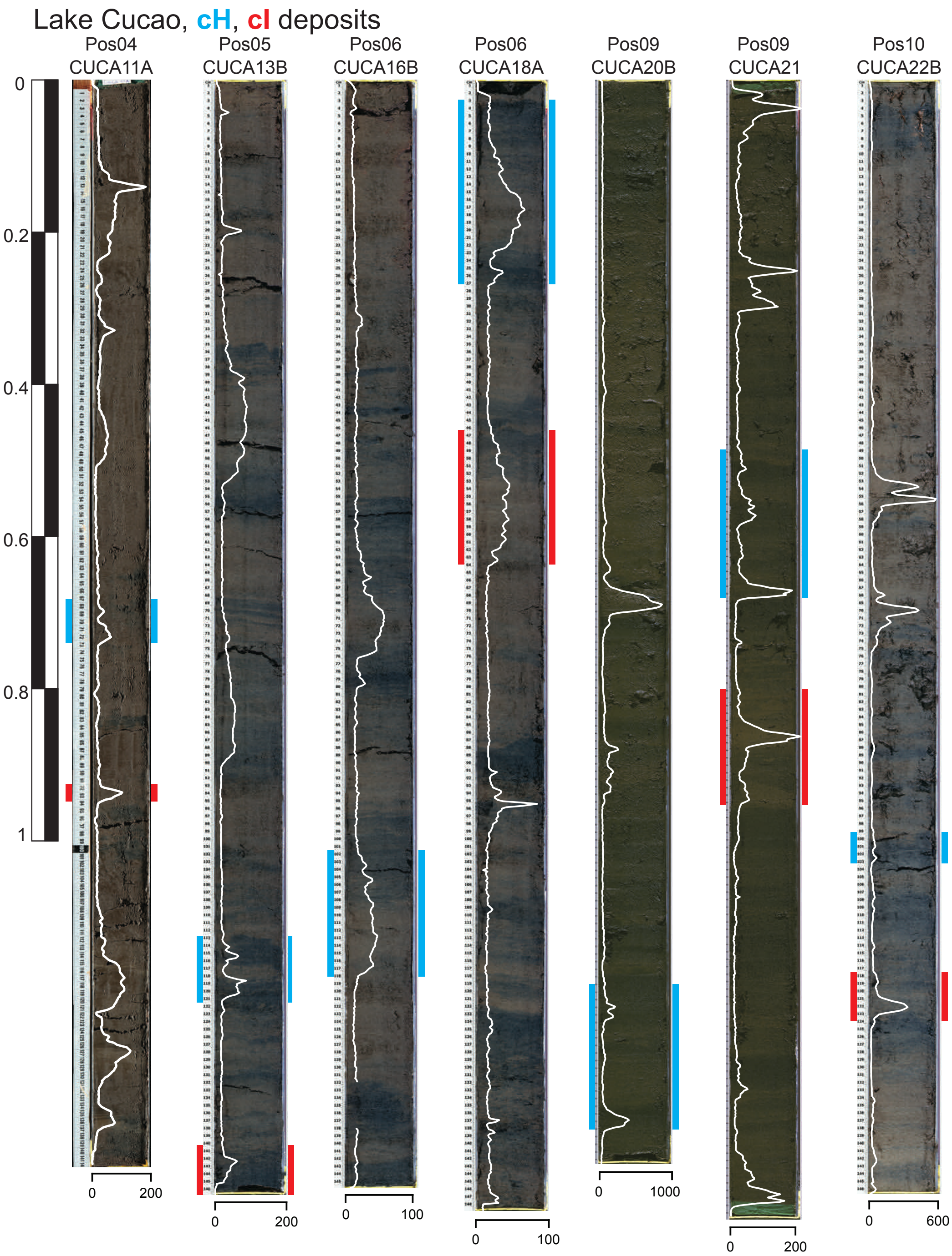

Figure 8.25: cH and cI tsunami deposits in Lake Cucao.

Figure 8.26: cJ tsunami deposit in Lake Cucao.

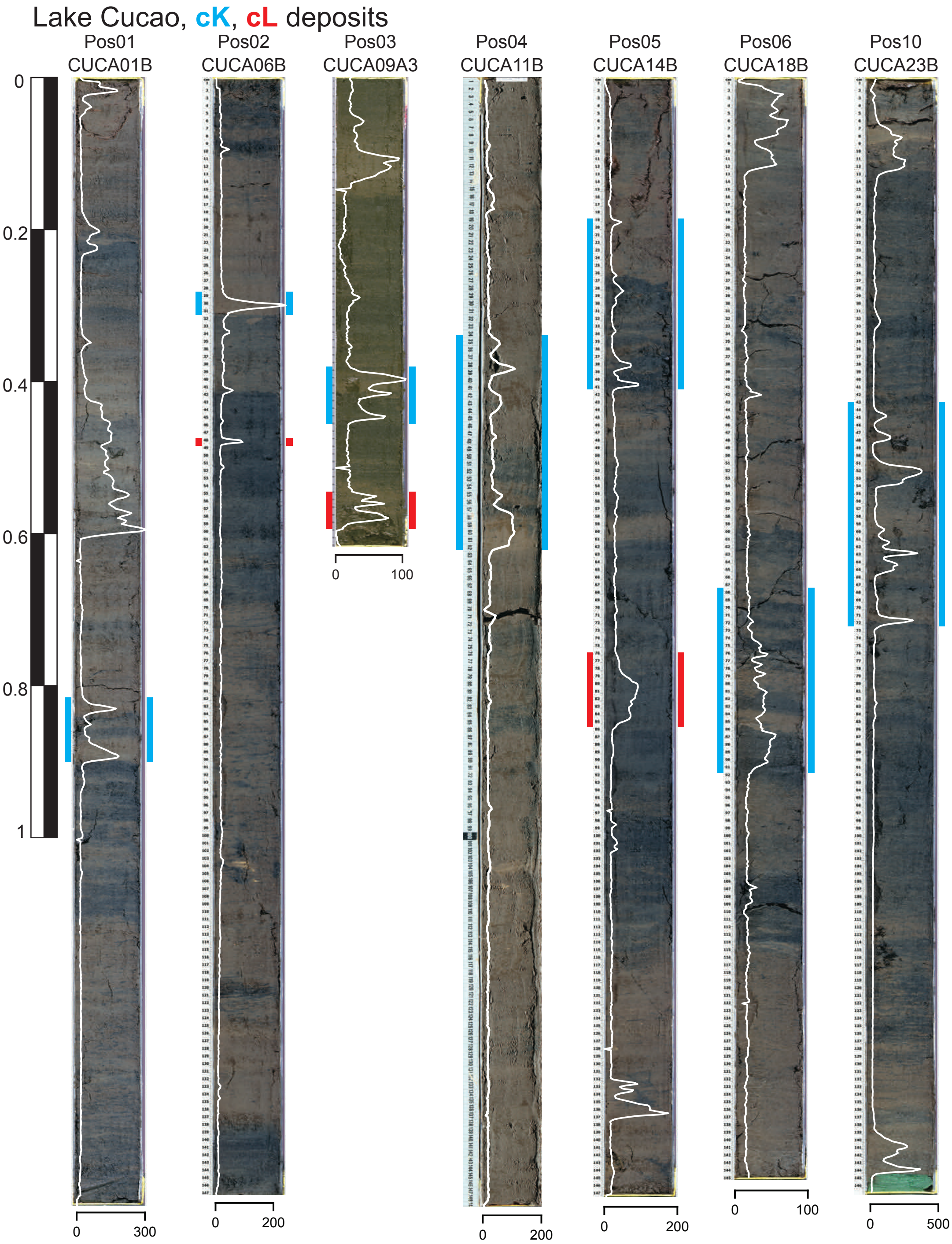

Figure 8.27: cK and cL tsunami deposits in Lake Cucao.

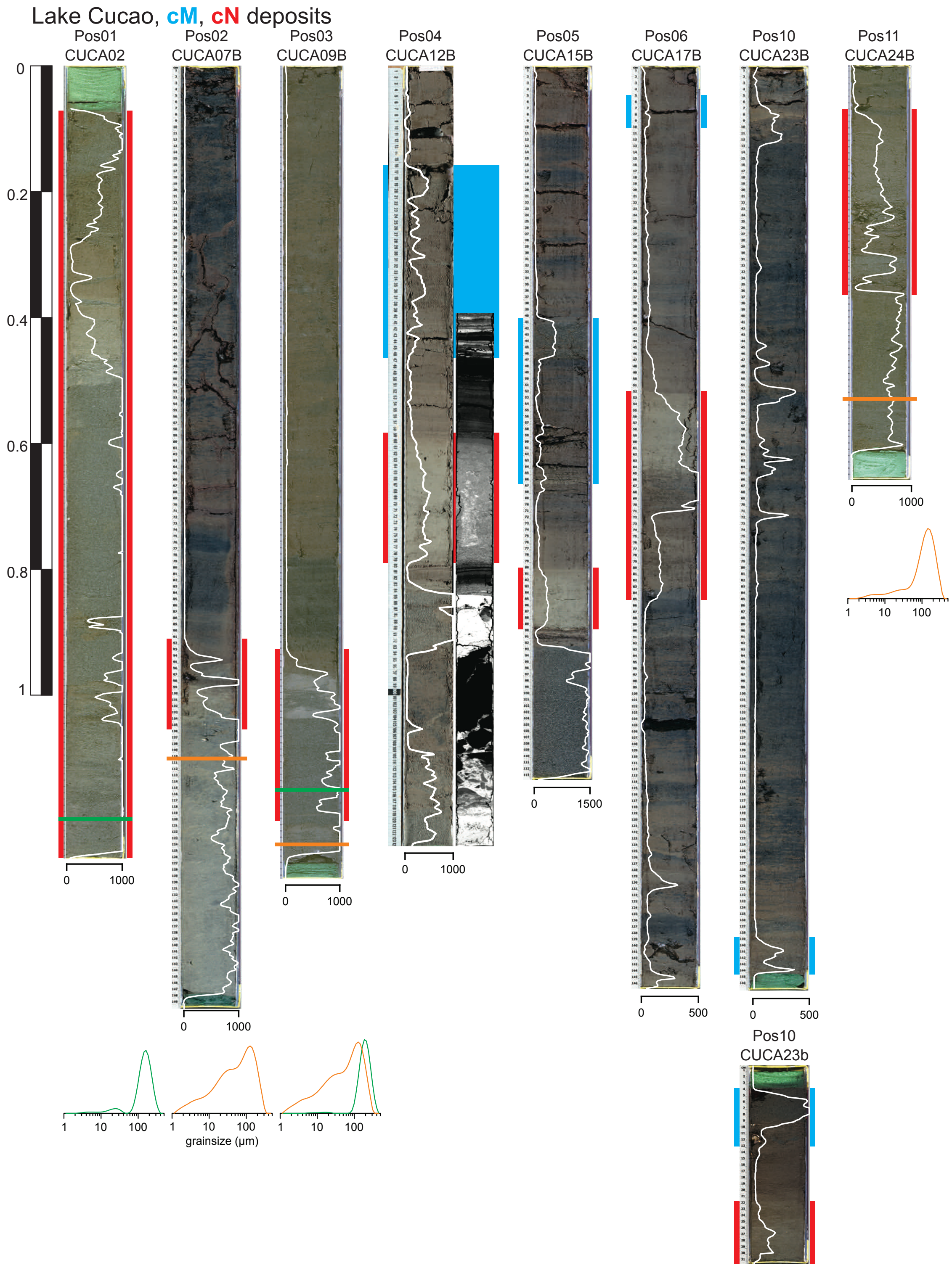

Figure 8.28: cM and cN tsunami deposits in Lake Cucao.

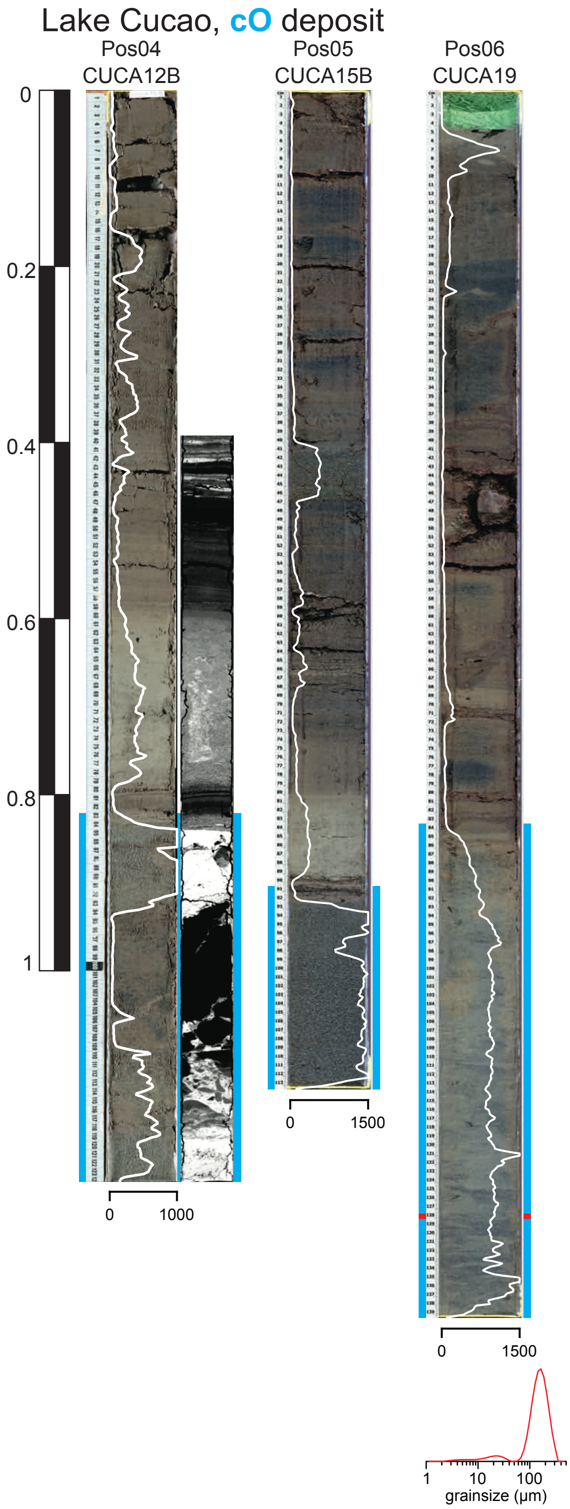

Figure 8.29: cO tsunami deposit in Lake Cucao.